ISSN 2699-1020

Maximilian Schoen Analysis of tunnel excavation in swellable clay shales 85

RUHR-UNIVERSITÄT BOCHUM

SFB 837
Interaction Modeling in Mechanized Tunneling

Maximilian Schoen

Numerical analysis of tunnel excavation in swellable clay shales

Bochum 2025 Heft 85

Schriftenreihe des Lehrstuhls für
Bodenmechanik, Grundbau und Umweltgeotechnik

Herausgeber: Torsten Wichtmann

ISSN 2699-1020

Ruhr-Universität Bochum
Schriftenreihe Bodenmechanik, Grundbau und Umweltgeotechnik
Heft 85

Herausgeber:
Prof. Dr.-Ing. habil. Torsten Wichtmann
Ruhr-Universität Bochum
Fakultät für Bau- und Umweltingenieurwissenschaften
Lehrstuhl für Bodenmechanik, Grundbau und Umweltgeotechnik
44801 Bochum
Telefon: 0234/ 3226135
Internet: www.bgu.ruhr-uni-bochum.de

ISSN 2699-1020

Numerical analysis of tunnel excavation in swellable clay shales

Dissertation

as a requirement of the degree of
Doktor-Ingenieur (Dr.-Ing.)

at the Faculty of
Civil and Environmental Engineering
Ruhr-Universität Bochum

submitted by
Maximilian Schoen
from Bochum, Germany

Reviewers
Prof. Dr.-Ing. habil. Torsten Wichtmann
Assoc. Prof. Dr.-Ing. Arash Alimardani Lavasan
Prof. Frédéric Collin

Bochum, 2025

Preface of the editor

Tunneling in swellable soils or rocks like clay shales may trigger swelling processes, due to the excavation-induced unloading and wetting by the transport of water or vapor to the swellable geomaterials. The transport of water from distant aquifers along the tunnel axis may occur in the so-called excavation damaged zone (EDZ), showing an increased permeability due to the formation or opening of cracks and dilative shear bands induced by the excavation. The diffusion of vapor in the direction perpendicular to the tunnel axis due to a hydraulic gradient is another source of additional humidity potentially evoking wetting-induced swelling processes. These processes may lead to the development of swelling pressures under constant-volume conditions and to swelling strains if free swelling is possible. The development of both swelling pressures and strains is expected under mixed boundary conditions allowing a certain amount of deformation.

For tunnel construction in swellable geomaterials mainly two different strategies can be followed. The first one uses a massive stiff lining capable of carrying large swelling pressures. The second involves a flexible tunnel support system, allowing some swelling deformations to occur and thus reducing the swelling pressures acting on it. Up to now tunnel construction in swellable soils or rocks has been mainly performed using conventional methods, since they can be more easily adapted to the local soil or rock conditions. However, mechanized tunneling is an attractive alternative, since it regularly allows more economical and time-efficient tunnel construction. For an application in swellable geomaterials, a flexible tunnel support system can be realized by deformable lining segments and / or a deformable grout. Extensive research on such deformable tunnel support systems was done in the framework of the collaborate research center SFB 837 "Interaction modelling in mechanized tunneling" funded by the German Research Council (DFG). Thereby, the sub-project A5 investigated the hydro-mechanical behavior of swellable clay shales, with a special focus on the development of swelling pressures and strains under tunnel-relevant boundary conditions, and its consideration in numerical models. The doctoral thesis of Maximilian Schoen is dedicated to the numerical part of that research project.

In his doctoral thesis Maximilian Schoen has developed adequate numerical models for the simulation of tunnel excavation in swellable clay shales. The swelling of the clay shale due to excavation-induced unloading and hydration was described by the Barcelona Basic model (BBM). The local second gradient model was used as regularization approach enabling the mesh-independent modeling of shear strain localization in the EDZ. Both

models were coupled and applied to the problem of mechanized tunneling in the FE code Lagamine for the first time. In the developed plane strain models the tunnel excavation is effectively simulated using the convergence-confinement method. The models represent the excavation of the new Belchen tunnel in northern Switzerland, which served as one of the reference projects in SFB 837.

The parameters of the BBM model were meticulously calibrated for both intact and remolded Opalinus clay shale, based either on data from the literature or on various types of laboratory tests with hydro-mechanical loading performed in the parallel doctoral thesis of Florian Christ within SFB 837. The excellent model performance, also for more complex boundary conditions like in the case of the deformation-controlled swelling pressure tests, was demonstrated by a comparison of element test simulations with the experimental data. After validation the numerical models for mechanized tunneling were used for detailed FE parametric studies, concentrating on the formation and evolution of the EDZ, the development of deformations as well as forces and bending moments in the tunnel lining. Maximilian Schoen developed suitable methods to reliably quantify the size of the EDZ and to predict the permeability increase in this zone based on deviatoric strains.

Maximilian Schoen demonstrates that the initial saturation state of the clay shale has a significant impact on the temporal evolution of the EDZ. While for initially saturated conditions the EDZ mainly develops during tunnel excavation, the majority of the EDZ forms after excavation if the clay shale is initially unsaturated. The latter is due to the time-dependent saturation process, leading to suction loss and material softening. The comparison of rigid and deformable support systems reveals the beneficial effect of the latter, particularly for initially unsaturated conditions. The compression of the deformable grout causes a considerable decrease of the swelling pressures acting on the tunnel lining, thereby reducing normal forces and bending moments in the lining. Meanwhile the deformations of the tunnel lining are only moderately larger in case of deformable tunnel support system. The results suggest that employing a deformable tunnel support system may enable a reduction in the amount and costs of materials. The numerical results thus confirm that for mechanized tunneling in swellable geomaterials a deformable support system represents an economical and ecologically friendly alternative.

This research has been done in the framework of the project A5 of Collaborate Research Center (SFB) 837 "Interaction Modeling in Mechanized Tunneling" at Ruhr-Universität Bochum. The funding of German Research Council (DFG) is gratefully acknowledged.

Torsten Wichtmann

Acknowledgments

I would like to sincerely thank everyone who supported me on this journey.

First, I'm especially grateful to my three reviewers: Prof. Wichtmann, Prof. Lavasan, and Prof. Collin. Prof. Wichtmann gave me the freedom to follow my own research path, while always being available when I needed guidance, something I truly appreciated.

Prof. Lavasan was always open for discussions and offered thoughtful insights that helped shape my work. Prof. Collin hosted me for a research stay and generously shared his time and expertise. I learned a great deal during that time, and I'm thankful for the support and attention he gave me.

My work was funded by the German Research Foundation (DFG) through Subproject A5 of the Collaborative Research Center 837 "Interaction Modeling in Mechanized Tunneling" at Ruhr-Universität Bochum. I'm thankful for this support, which made my research possible. In addition to the regular meetings and events within the Collaborative Research Center 837, the annual status seminars at Burg Schnellenberg were a real highlight, offering not only scientific exchange, but also a unique and inspiring atmosphere that I will always remember fondly.

I'd also like to thank the colleagues I had the pleasure to work with. Diethard König made it possible for me to join the chair at a time when things were uncertain, without him, this whole journey might not have started. Within Subproject A5, I had the opportunity to work closely with Florian Christ, whose laboratory experiments provided essential data for the calibration of my models. I'm grateful for the constructive collaboration. Sina Shivaei supported me as a student assistant and through his Master's thesis. Your help made a real difference.

Beyond direct collaboration, I'm also grateful to all my other colleagues at the chair for the friendly and enjoyable working environment. The many shared experiences, such as chair excursions, Christmas and summer parties, made this time truly special.

Most of my research was carried out at Ruhr University Bochum, but I also had the chance to spend time at the University of Liege and the University of Luxembourg. These stays were both productive and inspiring, and I'm grateful for the experiences and connections I made there.

Last but certainly not least, I want to thank my wife Stefanie and my parents. Their support, patience, and encouragement, especially during the tough phases, meant everything to me. This dissertation wouldn't exist without them.

Maximilian Schoen

Abstract

Tunnel excavation in swellable clay shales poses substantial challenges, as numerous tunnels have experienced damage in recent decades due to swelling phenomena. Excavation processes lead to stress redistribution and, consequently, to damage and a resulting permeability increase around the tunnel. This affected zone, known as the Excavation damaged Zone (EDZ), is particularly critical because swelling in clay shales can only occur when water is available. The resulting swelling pressure must be accounted for in the design of the tunnel support system. However, the evolution of this pressure is highly dependent on water ingress and the allowed deformations of the support system. To mitigate swelling, thereby reducing material usage and enhancing the long-term safety of the tunnel, mechanized tunnel excavation is preferred, as it imposes less disturbance on the clay shales compared to other methods.

Although efforts are made to minimize swelling, its complete prevention remains unachievable. In response to these geological conditions, two primary tunnel support strategies are employed: a rigid support system that resists deformation during swelling, requiring substantial material, and a deformable support system that accommodates deformations, thereby reducing swelling pressure. The deformable support system, still under development for mechanized excavations, offers promising potential for material efficiency, sustainability, and reduced CO_2 emissions. While previous studies have modeled the EDZ, none have thoroughly examined swelling in the context of mechanized tunnel excavation. This thesis aims to bridge that gap by investigating the integration of these concepts.

Given the complexity of tunnel excavation and the interactions between clay shales and tunnel support systems, this study employs finite element modeling to examine the excavation process and the evolution of the EDZ. The swelling behavior of Opalinus clay is modeled using the Barcelona Basic Model. The corresponding constitutive parameters are calibrated using laboratory tests to capture the mechanical behavior and swelling characteristics of the clay shales. Special attention is devoted to the dependency of swelling behavior on allowed deformations, which is critical for designing efficient tunnel support systems. The EDZ is modeled using shear strain localization, with the local second gradient model as a regularization technique to eliminate mesh dependency. Increased permeability within the EDZ is modeled by linking intrinsic permeability to shear strains. A comprehensive parameter study identifies the model parameters influencing the EDZ, followed by a comparative analysis of the two tunnel support strategies.

The study achieved mesh-independent simulations of the EDZ, confirming the effectiveness of the chosen methods. Among the parameters analyzed, the tunnel diameter proved to be the most influential factor affecting the EDZ. In contrast, parameters that are difficult to determine prior to excavation had minimal to negligible impact, underscoring the reliability of the modeling approach. Results reveal that, in case of an initially saturated conditions, the most substantial EDZ growth occurs during the excavation phase, emphasizing the importance of selecting an appropriate excavation method. Furthermore, the deformable support system demonstrated comparable tunnel deformations while reducing swelling pressure, showcasing its potential to enhance material efficiency and ensure long-term tunnel stability.

Zusammenfassung

Der Tunnelvortrieb in quellfähigem Tonstein stellt eine erhebliche Herausforderung dar, da in den letzten Jahrzehnten an zahlreichen Tunneln Schädigungen festgestellt wurden, die auf das Quellen des umliegenden Gesteins zurückzuführen sind. Der Vortriebsprozess führt zu Spannungsumlagerungen und in der Folge zur Ausbildung von Scherzonen und Rissbildungen im Tonstein, wodurch sich die Durchlässigkeit im Bereich um den Tunnel erhöht. Diese betroffene Zone, bekannt als Excavation Damaged Zone (EDZ), ist von besonderer Bedeutung, da ein Quellen des Tonsteins nur bei Wasserzutritt auftreten kann. Der daraus resultierende Quelldruck muss bei der Auslegung des Tunnelausbaus berücksichtigt werden. Die Entwicklung des Quelldrucks hängt jedoch stark vom Wasserzutritt sowie den zugelassenen Verformungen des Tunnelausbaus ab. Um das Quellen zu begrenzen und damit den Materialeinsatz des Tunnelausbaus zu reduzieren sowie die langfristige Standsicherheit des Tunnels zu erhöhen, wird der maschinelle dem konventionellen Tunnelvortrieb vorgezogen, da er dem Tonstein während des Tunnelvortriebes weniger Auflockerungen ermöglicht.

Obwohl Anstrengungen unternommen werden, das Quellen des Tonsteins zu minimieren, ist eine vollständige Vermeidung nicht möglich. In Reaktion auf diese geologischen Gegebenheiten werden zwei grundlegende Tunnelausbauarten angewendet: ein starrer Tunnelausbau, welcher Verformungen während der Volumenzunahme des Tonsteins infolge des Quellens widersteht, jedoch einen hohen Materialeinsatz erfordert, sowie ein verformbarer Tunnelausbau, welcher Verformungen explizit zulässt und dadurch den Quelldruck reduziert. Letzterer befindet sich für maschinelle Vortriebe noch in der Entwicklung, zeigt jedoch vielversprechendes Potenzial im Hinblick auf Materialeffizienz, Nachhaltigkeit und reduzierte CO_2-Emissionen. Während bereits frühere Studien die EDZ modellierten, wurde das Quellverhalten im Kontext des maschinellen Tunnelvortriebs bislang nicht umfassend untersucht. Ziel dieser Arbeit ist es, diese Forschungslücke durch eine integrative Betrachtung zu schließen.

Angesichts der Komplexität des Tunnelvortriebs sowie der Wechselwirkungen zwischen Tonstein und Tunnelausbau kommt in dieser Arbeit die Finite-Elemente-Methode zum Einsatz, um den Vortriebsprozess und die Entwicklung der EDZ zu analysieren. Das Quellverhalten des Opalinustons wird mittels des Barcelona Basic Models abgebildet. Die zugehörigen konstitutiven Parameter werden auf Grundlage von Laborversuchen kalibriert, um das mechanische Verhalten sowie die Quelleigenschaften des Tonsteins realitätsnah zu

erfassen. Besonderes Augenmerk liegt dabei auf der Abhängigkeit des Quellverhaltens von den zulässigen Verformungen, die für die Auslegung eines effizienten Tunnelausbaus von entscheidender Bedeutung ist. Die EDZ wird unter Annahme von lokalisierter Schädigung (Scherbänder) modelliert, wobei das lokale Second-Gradient-Modell als Regularisierungstechnik zur Vermeidung von Netzabhängigkeiten dient. Die erhöhte Durchlässigkeit innerhalb der EDZ wird durch eine Kopplung der intrinsischen Durchlässigkeit an die Scherdehnung berücksichtigt. Durch eine umfassende Parameterstudie wurden diejenigen Modellparameter identifiziert, welche den größten Einfluss auf die EDZ haben, gefolgt von einem Vergleich der beiden Tunnelausbauarten.

Die vorliegende Arbeit erreichte netzunabhängige Simulationsergebnisse der EDZ und bestätigte damit die Wirksamkeit der gewählten Methodik. Von den untersuchten Parametern zeigte der Tunneldurchmesser den größten Einfluss auf die Ausdehnung der EDZ. Dagegen wurden fü Parameter, die im Vorfeld der Vortriebsmaßnahme nur schwer zu bestimmen sind, nur geringe bis vernachlässigbare Auswirkungen festgestellt, was die Aussagekraft des Modellierungsansatzes unterstreicht. Die Ergebnisse belegen, dass die bedeutendste Ausdehnung der EDZ bei Annahme eines initial vollständig gesättigten Zustands bereits kurz nach dem Vortrieb erreicht wird, was die Relevanz einer geeigneten Wahl der Vortriebsmethode hervorhebt. Zudem zeigte der verformbare Tunnelausbau im Vergleich zum starren Ausbau ähnliche Tunnelverformungen bei gleichzeitig reduzierten Quelldrücken, womit er ein erhebliches Potenzial zur Verbesserung der Materialeffizienz aufweist bei gleichzeitiger Gewährleistung der langfristigen Tunnelstandsicherheit.

Contents

1. Introduction

1.1. Background and motivation

The tunneling process and the long-term safe operation of tunnel structures in swelling clay shales have posed significant challenges for engineers for decades. As highlighted by Amstad and Kovári (2001); Anagnostou et al. (2010); Einstein (1996); Steiner (1993), numerous tunnel projects have demonstrated swelling-induced deformations or damage throughout their lifespans. This challenge is particularly complex due to the inherent difficulties associated with tunneling, which involves multiple interacting subsystems such as the surrounding ground, the tunnel boring machine (TBM), and tunnel support systems. In this context, the hydro-mechanically coupled processes play a critical role.

During tunnel excavation, inevitable damage occurs to the surrounding formation, forming the so-called Excavation Damaged Zone (EDZ). Within this zone, the hydro-mechanical properties differ from those in the intact formation. The mechanical stiffness decreases, while the damage creates preferential flow paths for water transport from surrounding layers along the tunnel, thus increasing permeability. In the case of swelling clay shales, water transfer poses an immediate risk of swelling, which must be considered in tunnel design.

Two principal approaches for handling swelling soils in conventional tunneling method are known: the resistance principle and the yielding principle (Wittke, 2014). The resistance principle involves designing the tunnel support to be as rigid as possible, so it does not deform when swelling (volumetric increase) occurs. This method requires significant amounts of materials, including both concrete and steel, to ensure high stiffness. However, this approach leads to high material costs and, ecologically, to substantial CO_2 emissions due to concrete production. Alternatively, the yielding principle allows for the tunnel support to deform in a pre-defined manner when swelling of the ground occurs, reducing the swelling pressure exerted on the tunnel.

Mechanized tunnel excavation (using TBMs) offers several advantages compared to conventional tunneling methods, such as higher automation and better control over the deformations of the surrounding ground due to the ability to support it during excavation (Maidl et al., 2011). This results in generally smaller deformations compared to conventional tunneling methods. Since there is a correlation between deformations and the development of damage, mechanized tunneling could provide significant benefits in swelling clay shales, by limiting both, the extend and intensity of the EDZ. Unlike the conventional tunneling method, which has the ability to use a deformable tunnel support, no comparable approach has been developed for mechanized tunneling.

This thesis is conducted within the framework of the Collaborative Research Center 837 "Interaction Modeling in Mechanized Tunneling" where research is focused on adapting and implementing this concept for mechanized tunneling in swelling clay shales. Within the framework of the Collaborative Research Center 837, each subproject focuses on specific aspects of mechanized tunneling processes. Subproject A5, to which this thesis is associated, specifically addresses the challenges related to swelling clay shales. This focus is of particular importance, as the unique properties of clay shales, especially the hydro-mechanical interactions, have complex implications for tunnel construction and the long-term operation of tunnel structures.

A crucial aspect related to ground conditions is to analyze and understand the underlying processes that lead to swelling. With the insights gained, the magnitude of swelling pressure, and the swelling pressure-strain relationship during tunnel excavation can be derived. Understanding the formation of the EDZ is essential, as it governs not only the immediate mechanical behavior of the surrounding formation but also its long-term stability. The EDZ forms as a result of the tunneling process, and its characteristics evolve over time, influenced by factors such as excavation rate, support system design, and the inherent properties of swelling clay shales. Understanding the temporal development of the EDZ and its interactions with tunnel excavation is therefore critical for a comprehensive assessment of tunnel stability, as it is the key component which controls the water transfer in the nearfield of the tunnel and consequently the swelling of the clay shale.

The changes in the hydro-mechanical properties of the EDZ, particularly in terms of permeability and mechanical stiffness, have a significant impact on water transport. In swelling clay shales, this can lead to an increase in swelling pressure, which can damage the tunnel structure if not adequately considered in the design of the tunnel support system. In this context, the interaction between the EDZ and the tunnel support system becomes especially important. When a deformable tunnel support system is used, it allows

reduction of swelling pressure by allowing controlled deformations, thereby reducing the mechanical loads on the tunnel lining. Whereas further ground deformations could have a negative impact leading to a further increase in size of the EDZ. This dynamic interaction between the EDZ and the tunnel support system needs to be thoroughly investigated, as it is crucial for optimizing support systems that ensure both safety and economic feasibility in the tunneling process.

1.2. Objectives

The primary objective of this work is to develop a fundamental understanding of the hydro-mechanically coupled processes and interactions occurring during and after mechanized tunnel excavations in swelling clay shales. The study focuses on two main aspects: first, the modeling of clay shale swelling under various displacement boundary conditions, and second, the mesh-independent modeling of the Excavation Damaged zone (EDZ), which significantly influences the hydro-mechanical regime in the nearfield of the tunnel.

A key aim is to investigate which aspects of the model affect the feasibility of TBM-driven tunnel excavations in swelling clay shales. Particular emphasis is placed on analyzing different tunnel construction strategies to provide recommendations for a safe yet economically viable tunneling process in swelling clay shales.

The resulting objectives of this thesis are defined as follows:

- Calibration of constitutive parameters based on laboratory experiments on swellable clay shale conducted at Ruhr University Bochum (RUB), deriving both mechanical and hydraulic constitutive model parameters.
- Modeling and validation of swelling tests under various tunnel-relevant deformation boundary conditions using laboratory experiments conducted at RUB.
- Conducting an in-depth analysis of shear strain localization in swellable clay shales under well-controlled boundary conditions, including the identification of stress paths that lead to localization, determination of key model parameters influencing this behavior, and the comparison and selection of suitable modeling approaches for representing permeability increases in the EDZ.
- Numerical investigation of the growth of the EDZ during and after the completion of mechanized tunnel excavation in swelling clay shales, supported by parametric studies to identify key model parameters.

- Analyzing and comparison of the influence of tunnel support stiffness/deformability and the modeling approach for tunnel excavation on the temporal development of the EDZ.

1.3. Layout of the thesis

Following the introduction, Chapter 2 provides an overview of the swelling behavior of clay shales. This includes a discussion of the mechanisms driving swelling, laboratory experiments that investigate swelling behavior, and a review of existing swelling laws available in the literature. Additionally, the chapter presents the fundamentals of tunneling excavation techniques and explores the possibilities for numerically modeling the tunneling process. Particular emphasis is placed on the Excavation Damaged Zone (EDZ), its characteristics, and modeling approaches, including methods for increasing permeability within the EDZ. This chapter establishes the foundational knowledge required for the subsequent chapters.

Chapter 3 derives the hydro-mechanical properties of intact Opalinus clay through an extensive literature review. Furthermore, mechanical and hydraulic constitutive parameters are determined using laboratory experiments conducted at Ruhr University Bochum (RUB) on remolded Opalinus clay. Using these parameters, various swelling tests with tunnel-relevant boundary conditions, also performed at RUB, are simulated and validated against model results. The aim is to accurately replicate the hydro-mechanical behavior of Opalinus clay and to scale these findings from the laboratory level to the tunneling scale in subsequent chapters.

Chapter 4 focuses on the shear strain localization behavior of Opalinus clay. A numerical model with well-defined boundary conditions is developed to study various stress paths and their impact on shear strain localization. Based on this, multiple model parameters are investigated through a parameter study. Additionally, the approaches for permeability enhancement within the EDZ introduced in Chapter 2 are analyzed in detail.

Building on these insights, Chapter 5 addresses the modeling of tunneling processes with a focus on the formation and evolution of the EDZ. This is demonstrated through a case study, which is briefly introduced at the beginning of the chapter. Subsequently, the numerical modeling of tunnel excavation is presented. The systematic evaluation of the EDZ is emphasized, as several model parameters need to be analyzed for their influence on the EDZ. After identifying key parameters using simulations of unsupported tunnels,

different tunnel support systems are evaluated and compared. At the end of the chapter, the influence of a modified modeling approach for tunnel excavation on the development of the EDZ is introduced and analyzed.

Finally, Chapter 6 summarizes all findings of the thesis. The results are contextualized, and potential future research directions within the scope of this work are outlined.

2. State of the art

2.1. Introduction

In this chapter the fundamentals for the numerical modeling of mechanized tunnel excavations in swellable clay shales are outlined. Initially, the swelling phenomenon is examined, focusing on the various swell mechanisms, laboratory tests available to analyze swelling, and the possibilities of numerical modeling of swelling. Subsequently, the tunnel excavation techniques and the numerical modeling approach using a 2D plane strain model are discussed. The significance of the excavation damaged zone is explained, underlining its importance for this study and outlining methods for its modeling. Finally, the underlying methodologies and constitutive frameworks of this research are elaborated.

2.2. Swelling of clay shales

Swelling can cause serious damage to tunnel supports (Steiner, 1993; Berdugo et al., 2009*a*,*b*; Alonso and Olivella, 2008), which are the primary focus of this research, as well as to other infrastructural constructions, such as high-performance highways (Kleinert and Einsele, 1978) and bridges (Alonso and Ramon, 2013). Thus, it is crucial to comprehend the underlying swelling mechanisms and methods for identifying and idealizing swelling phenomena.

In this section, first the various swell mechanisms are described. Subsequently, different laboratory tests for investigating and quantifying swelling are introduced. Finally, an overview of available swelling laws to aid in the idealization of the investigated swelling phenomena are presented.

2.2.1. Introduction to rock swelling mechanisms

Rock swelling can manifest through a variety of mechanisms, broadly categorized into two groups: physical and chemical mechanisms, as noted by Pimentel (2015). Among the chemical swell mechanisms, anhydrite swelling stands out prominently. The swelling by chemical interactions in anhydrite arises from the hydration of the anhydrite minerals, leading to their transformation into gypsum and resulting in a substantial volume increase of up to 60% (Butscher et al., 2018). However, since this research primarily focuses on pure clay shales, chemical swelling will not be extensively discussed here, as it is not applicable to pure clay formations.

In the field of physical swelling mechanisms, three distinctive processes come to the forefront: pure mechanical swelling, innercrystalline swelling, and osmotic swelling (Pimentel, 2015). The subsequent section elaborates on these physical swelling mechanisms, explaining the details of each swell mechanism.

2.2.1.1. Pure mechanical swelling

Pure mechanical swelling is a phenomenon that arises from a reduction in negative pore pressure and can manifest in any argillaceous rock, also known as inverse consolidation (Pimentel and Anagnostou, 2013). During unloading, such as in the course of tunnel excavation, a decrease in total stress occurs. If the permeability of the material is low, the inflow of water is delayed, and negative pore water pressures develop. As a result, the effective stress remains largely unchanged initially. Over time, as water gradually re-enters the pore space and the negative pore pressure dissipates, the effective stress decreases, leading to a volume increase, which is called mechanical swelling. According to Pimentel (2015), its relevance in tunneling and foundation engineering is minimal due to its inherently low swelling potential compared to anhydrite swelling. For the swelling of clay shales this type of swelling should be considered.

2.2.1.2. Innercrystalline swelling

Clay minerals can swap the central cations in their tetrahedal and octahedral structures with other cations, often with lower valence. In the case of fully dry montmorillonite, the exchangeable interlayer cations are situated either on the surface of the layers or within the hexagonal holes of the tetrahedral sheets. The layers, negatively charged, are tightly bound together by the interlayer cations and the van der Waals forces operating

at this short distance. Upon contact with water, these interlayer cations undergo hydration and arrange themselves on a plane positioned midway between the clay layers. This rearrangement results in an expansion of the spacing between the layers, which is called innercrystalline swelling as can be seen in Figure 2.1. Notably, the volume of montmorillonite can undergo a significant increase, potentially doubling the volume, during the process of innercrystalline swelling.

However, the overburden pressures required to counteract innercrystalline swelling are typically so substantial, over 100 MPa according to Madsen and Müller-Vonmoos (1989), which are not reached at typical depths where tunnel excavation occurs.
Furthermore, it can be assumed that the innercrystalline swelling in the depths where construction activities take place is usually already completed, thus engineers commonly do not encounter or address this specific challenge (Ferrage, 2016; Madsen and Müller-Vonmoos, 1989; Massat et al., 2016).

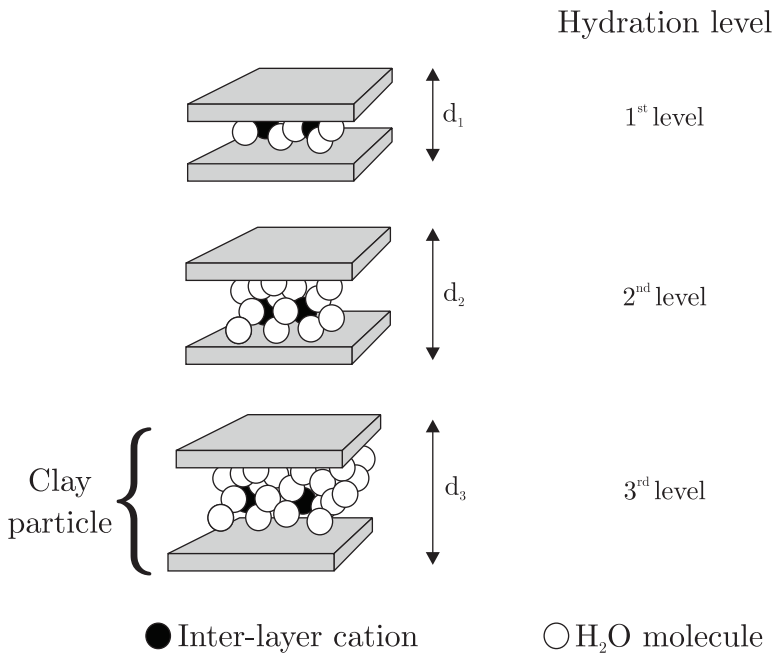

Figure 2.1.: Innercrystalline swelling of montmorillonite after Kraehenbuehl et al. (1987)

2.2.1.3. Osmotic swelling

Osmotic swelling is a distinctive type of swelling observed when clayey sedimentary rocks undergo unloading, such as during excavation, allowing them to absorb water. Unlike innercrystalline swelling, which primarily acts over small distances (up to 1 nm), osmotic swelling relies on the repulsion between electric double layers and can exert its influence over much larger distances (Madsen and Müller-Vonmoos, 1989).

Notably, the swelling stresses associated with osmotic swelling are significantly smaller compared to innercrystalline swelling, typically around 2 MPa rather than 100 MPa. The driving force behind osmotic swelling is the substantial difference in concentration between ions electrostatically held near the clay surface and those present in the pore water of the formation. Crystal lattice irregularities manifest as an excess negative charge, necessitating the presence of positive ions in close proximity to the clay surface. This results in an extremely high concentration of positive ions near the surface, contrasting with a very low concentration of negative ions. The positive ion concentration diminishes with increasing distance from the surface, while the concentration of negative ions rises. This interplay creates a diffuse electric double layer comprising the negatively charged clay surface and the surrounding ion cloud (Madsen and Müller-Vonmoos, 1989).

The observed swelling in clay occurs when two such negative potential fields overlap, leading to mutual repulsion and contributing to the phenomenon of osmotic swelling as depicted in Figure 2.2.

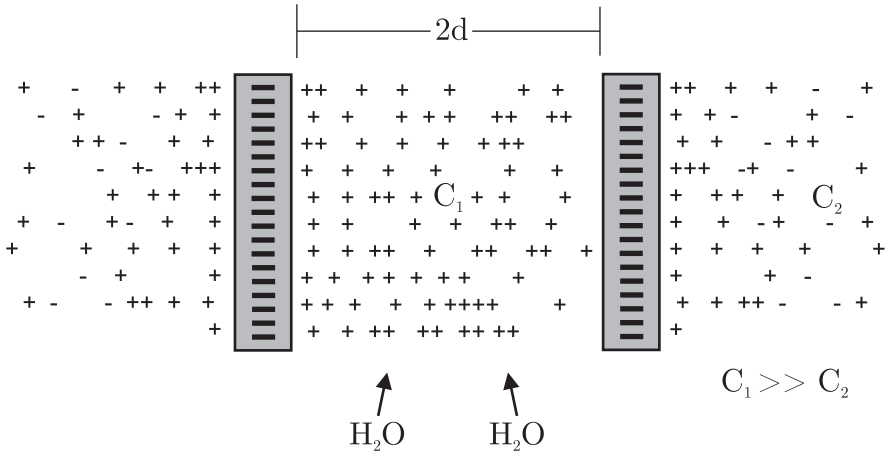

Figure 2.2.: Osmotic clay swelling after Madsen and Müller-Vonmoos (1989)

2.2.2. Laboratory tests for characterizing swelling of clays

Following the elaboration of different swelling mechanisms, the next crucial step involves evaluating the swelling potential of clays in a laboratory setting. The objective of these tests is to establish a stress-strain relationship, crucial for the formulation of a swelling law (see Section 2.2.3). All tests share the common procedure of preparing a sample, followed by hydration, leading to swelling of the sample.

Unfortunately, the determination of swelling potential in the laboratory presents a challenge due to the variety of available methods, each with different experimental procedures and standards, such as ISRM, DGGT and Swiss recommendations. Literature categorizes these tests based on various criteria. Pimentel (2015) proposes grouping based on the confinement conditions of the test apparatus, whereas Sridharan et al. (1986) groups them according to the test procedure into free swelling-load, swell-under-load, and constant volume categories. According to ISRM (1989, 1999), grouping is based on the results obtained, such as determining axial swelling pressure, free swelling strain, or swelling pressure as a function of axial swelling strain. Although analysis of the swelling phenomena in the laboratory is crucial, this thesis focuses on the numerical modeling of the swelling. Therefore, only a brief overview of the available laboratory tests is provided in the following subsection, categorized according to ISRM (1989, 1999). The main emphasis here is to highlight the different boundary conditions of the tests, which are crucial for the numerical modeling. For a more in-depth and critical review of the different swelling tests the author refers to Pimentel (2015).

2.2.2.1. Tests for determining free swelling strains

Free swelling strains represent the extent to which the sample can expand in one direction without encountering any external constraints. There are two prominent approaches in the literature to determine the free swelling strain.

The first, under unconfined conditions, measures the deformation of either cubic specimens in all three orthogonal directions after watering (ISRM, 1979) or of a disk in axial and radial direction ISRM (1989, 1999), both illustrated in Figure 2.3.

The second, known as the swell-heave test (DGGT, 2022), is performed in an oedometer device, determining the maximum swelling strain under a low dead load (e.g., 5 kPa), as shown in Figure 2.4.

It is important to emphasize that all mentioned tests aim to determine the maximum swelling strain, despite their significant differences in boundary conditions. It should be noted that methods outlined by ISRM (1979, 1989, 1999) may overestimate the resulting maximum swelling strain due to the unconfined nature of the test, where the sample could disintegrate. This may also result in non-homogeneous deformations, making the measurement of swelling strains challenging and less straightforward. According to Pimentel (2015), a test conducted under oedometric conditions should be preferred to accurately determine the maximum swelling strain for a swelling law.

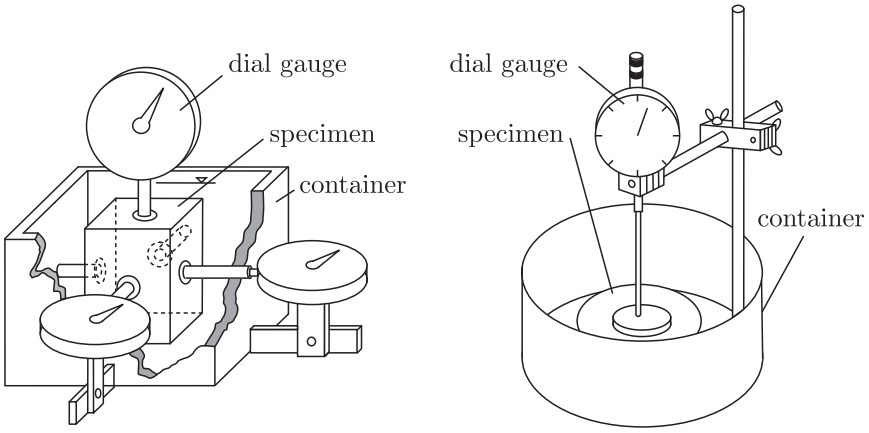

Figure 2.3.: Free swell test setup according to ISRM (1979) (left) and ISRM (1999) (right)

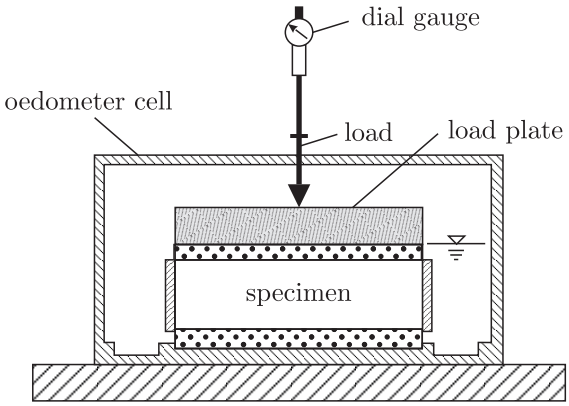

Figure 2.4.: Free swell test setup according to DGGT (2022)

2.2.2.2. Tests for determining axial swelling pressure

The definition of swelling pressure varies across different literature sources. Some define it as the pressure measured during the hydration of a sample under constant volume conditions, while others describe it as the load needed to maintain the volume constant. However, all standards agree that the maximum swelling pressure is determined within an oedometer device, as shown in Figure 2.4. In tests where swelling pressure is measured under constant volume conditions, either a rigid frame or a purpose-built apparatus is utilized. These tests aim to maintain nearly constant volume conditions by restricting axial and radial deformations.

Despite the use of a rigid frame, slight deformations may still occur. Therefore, ISRM (1989, 1999) recommend applying small deformations as compensation if necessary.

An alternative method, proposed by Henke et al. (1975) and adopted by DGGT (2022), involves placing the sample in an oedometer ring without axial constraints. The sample is then hydrated and allowed to freely swell in the axial direction until equilibrium is reached. Subsequently, stepwise loading is applied until all swelling strains are compensated. The maximum stress required for compensation is termed the equivalent swelling pressure.

2.2.2.3. Test for determining swelling pressure as a function of axial swelling strain

While the maximum swelling strain and swelling pressure are important parameters for characterizing the swelling phenomenon, it is the relationship between swelling pressure and swelling strain that is of paramount importance for construction projects. On site, deformations often occur, so construction projects typically operate in an equilibrium state between swelling strain and swelling pressure.

In the literature, this relationship is determined in several different ways, including variations in boundary conditions (e.g., constant load or constant volume), the number of tests conducted (e.g., single test or series of tests), and differences in initial loading procedures.

The swelling tests proposed by DGGT (2022) follow the methodology outlined by Huder and Amberg (1970), with a slight modification suggested by ISRM (1989, 1999). Conducted under oedometer conditions, these tests allow the sample to swell under a high constant load until equilibrium is achieved.

The load must be sufficiently high to minimize deformations due to swelling while avoiding excessive compaction or modifications of the initial structure that could falsify the results.

As the appropriate load is unknown prior to testing, it is often chosen based on the in situ overburden pressure, as suggested by Pimentel (2015). Subsequently, a stepwise unloading process records equilibrium swelling pressure and strain for each step, forming a swelling pressure-strain relationship, as shown in Figure 2.5 (right).
The key difference between the standards lies in the loading procedure, where the method of Huder and Amberg (1970) involves loading, unloading, and reloading before watering, while ISRM (1999) loads the sample only once before water hydration. It should be noted that in the previously mentioned tests, the swelling pressure-strain relationship is obtained from a single soil sample, and the maximum swelling pressure has to be extrapolated using the obtained curve.

Whereas, in the swelling-under-load method explained by Sridharan et al. (1986), at least three tests on identical samples under three different constant loads are needed. After hydration, when each sample reaches equilibrium, the resulting swelling strain is recorded alongside the applied vertical stress. Plotting the results of these individual tests in a semi-logarithmic stress-strain diagram provides a swell-under-load curve, as illustrated in Figure 2.5 (left). The maximum swelling pressure as well as the free swelling strain need to be extrapolated here as well.

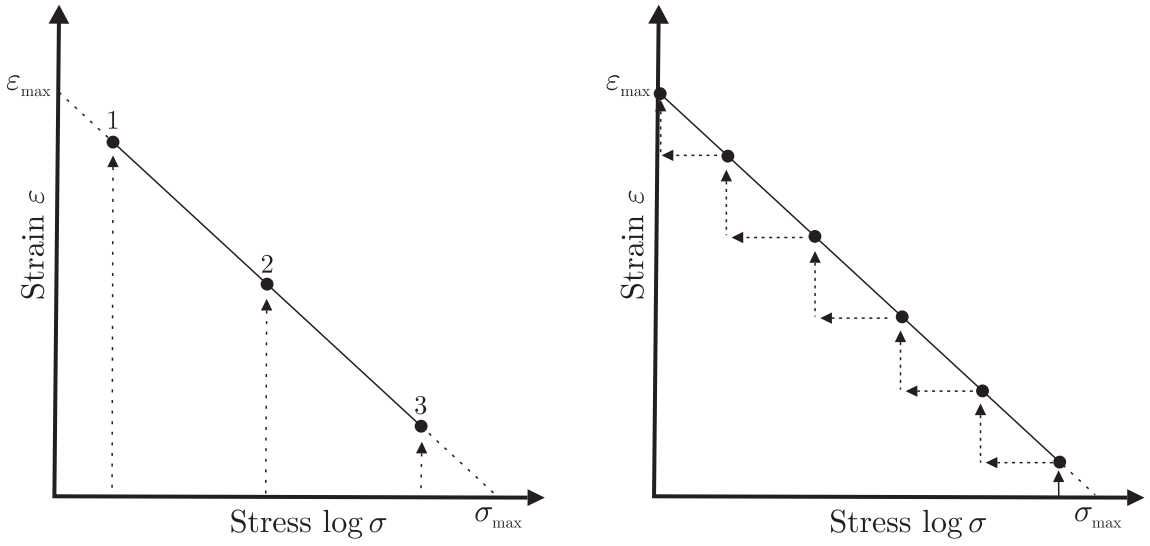

Figure 2.5.: Swell test procedure according to Sridharan et al. (1986) (left) and Huder and Amberg (1970) (right)

Additionally, in the work of Pimentel and Anagnostou (2013), a purpose-built swelling test apparatus is introduced along with an alternative testing procedure as seen in Figure 2.6. The sample is initially watered under constant volume conditions, requiring no compensation strains due to the high rigidity of the load frame. After equilibrium is attained, the sample undergoes stepwise unloading, with stress maintained constant in each step until equilibrium swelling strain is reached, as illustrated in Figure 2.6 (left). The initial strain increase at the beginning of each unloading step corresponds to the elastic heave.

According to Pimentel and Anagnostou (2013), these swelling tests can be conducted either in a load-controlled or, with slight modification, a deformation-controlled manner as shown in Figure 2.6 (right). The difference is that in the deformation-controlled method, the unloading is prescribed and maintained at a constant displacement until a steady swelling pressure is established.

The advantage of this test is that both the maximum swelling pressure and the free swelling strains can be determined with just one test, thus eliminating the extrapolation required by the tests of Huder and Amberg (1970) and Sridharan et al. (1986). Furthermore, Pimentel (2015) demonstrates that the interpolated maximum swelling pressure, using either ISRM (1989, 1999) or DGGT (2022) method, overestimate the maximum swelling pressure compared to the test procedure by Pimentel (2015).

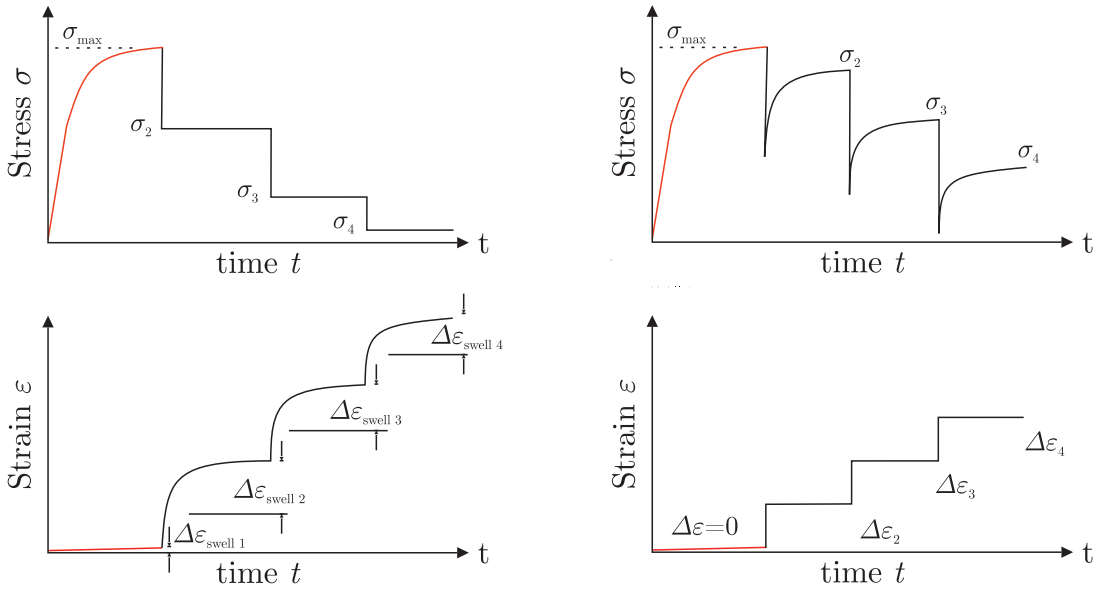

Figure 2.6.: Swell test procedure load-controlled (left) and deformation-controlled (right) according to Pimentel (2015)

2.2.3. Swelling laws

After discussing the available laboratory tests for analyzing the swelling potential, it is essential to simplify and model this potential using either analytical or numerical swelling laws to incorporate it into finite element simulations.

The literature incorporates a variety of swelling laws designed to elaborate the relationship between swelling pressure and strain. Broadly categorized, these laws fall into two main groups: analytical and process-based numerical swelling laws.

The subsequent sections will provide insights into each of these categories. While the primary focus of this work is on clay swelling and not anhydrite swelling, it is essential to discuss swelling laws designed for anhydrite (e.g., Kirschke's or Pimentel's swelling law) for the sake of completeness and comprehensive understanding. This inclusion ensures a thorough exploration of existing theories, even if their direct application may not align with the specific objectives of the current study.

2.2.3.1. Analytical swelling laws

The most prominent analytical swelling laws include Grob's swelling law, Kirschke's swelling law, and Pimentel's swelling law. These laws establish relationships between swelling pressure and swelling strain through analytical equations or other relationships, which will be explained in the following section.

Grob's Swelling Law:

Grob (1972) established a linear relationship between swelling strain and the logarithm of pressure, based on oedometric swelling experiments by Huder and Amberg (1970) (see Section 2.2.2). These experiments utilized drill core samples of Jurassic Opalinus Clay and Triassic Gipskeuper, collected from the Belchen tunnel in Switzerland.

The law is expressed as:

$$q = k - m \ \log p \tag{2.1}$$

Here, q represents the volumetric strain in percentage, and p is the pressure in kg/cm^2. The constants k and m are material-specific.

Given that the maximum swelling pressure p_0 corresponds to $q = 0\%$, the relationship can be further expressed as:

$$k = m \ \log p_0 \tag{2.2}$$

By substituting this expression for m back into Equation 2.1 and changing the notation of swelling strain and swelling stress, the law can be represented in the more common form:

$$\varepsilon = k \left(1 - \frac{\log \sigma}{\log \sigma_0}\right) \tag{2.3}$$

where, ε denotes the swelling strain, σ is the swelling stress, k represents the swelling strain when $\sigma = 1\,\text{kPa}$, and σ_0 characterizes the maximum swelling pressure (see Figure 2.7).

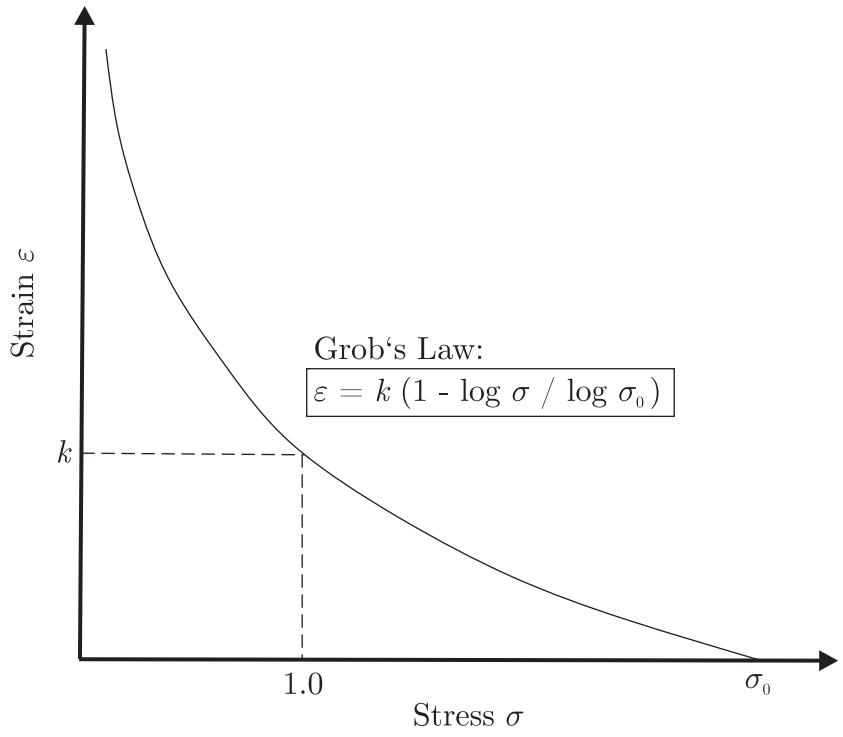

Figure 2.7.: Swelling law proposed by Grob (1972)

Kirschke's Swelling Law:

In a study conducted by Kirschke (1996) on Gipskeuper samples obtained from the Freudenstein tunnel in Germany, it was observed that the stress-strain relationship depends on the test duration. Notably, Kirschke reported that, unlike pure clay formations, experiments with claysulfate rocks did not reach a final equilibrium state. Grob's swelling law, which considers only equilibrium states and neglects any time dependence, is therefore unsuitable for claysulfate rocks. While Kirschke acknowledged that this assumption is acceptable for pure clay formations, he emphasized that anhydrite never reaches equilibrium, rendering the application of Grob's law inappropriate.

As depicted in Figure 2.8, the stress and corresponding strains demonstrate an upward trajectory over time. This led Kirschke (1996) to suggest that the constants k and σ_0 (see Equation 2.3) did not exclusively characterize the formation. Instead, Kirschke argued that these constants should be considered time-dependent.

It is important to note that the curves presented by Kirschke (1996) for extended swelling durations were derived by extrapolating stress-strain curves obtained at different time intervals to predict behavior for future timeframes. Consequently, Kirschke (1996) did not provide a specific formula.

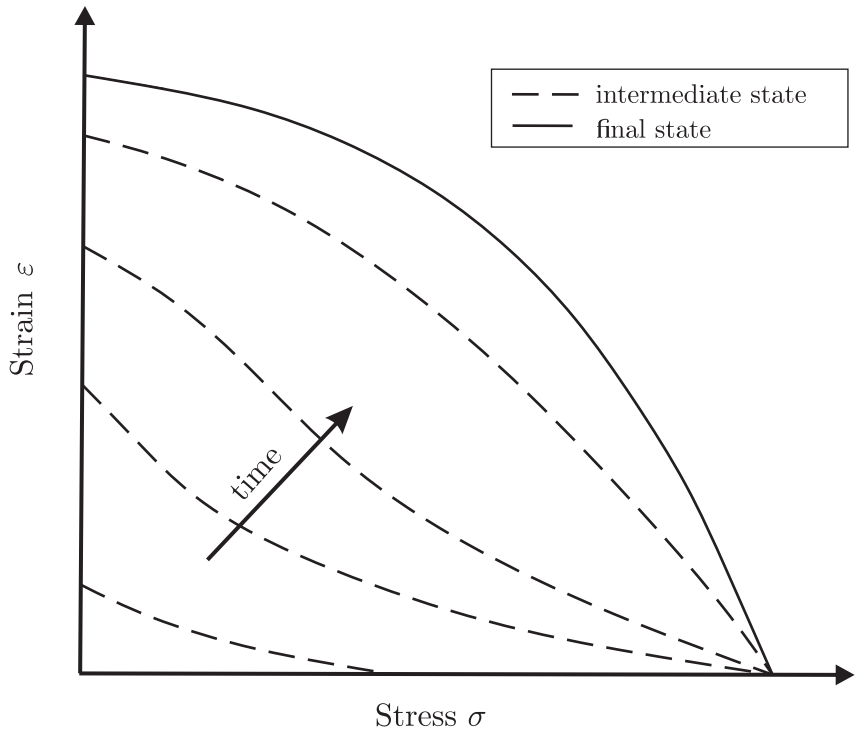

Figure 2.8.: Swelling law proposed by Kirschke (1996)

Pimentel's Swelling Law:

Pimentel (2007) conducted swelling tests with samples from the Gipskeuper formation obtained at a railway tunnel in southwest Germany, where he identified three distinct phases in the swelling behavior, each dependent on the applied stress conditions.

Pimentel observed minimal deformation under high pressures (>5.5 MPa) and explained this phenomenon by the prevention of gypsum crystallization. At medium pressures (4 – 5.5 MPa), he recorded large deformations, which he attributed to gypsum crystallization. Under low pressures (<4 MPa), he noted only a slight additional deformation compared to the deformations from the previous phase, which Pimentel interpreted as an effect of reduced stiffness due to the development of macropores (cracks) during swelling, possibly compounded by gypsum dissolution.

To describe these phases, Pimentel employed a "tri-linear" relation in a semi-logarithmic plot as shown in Figure 2.9, providing a visual representation of the intricate stress-strain relationships observed during swelling under varying pressure conditions.

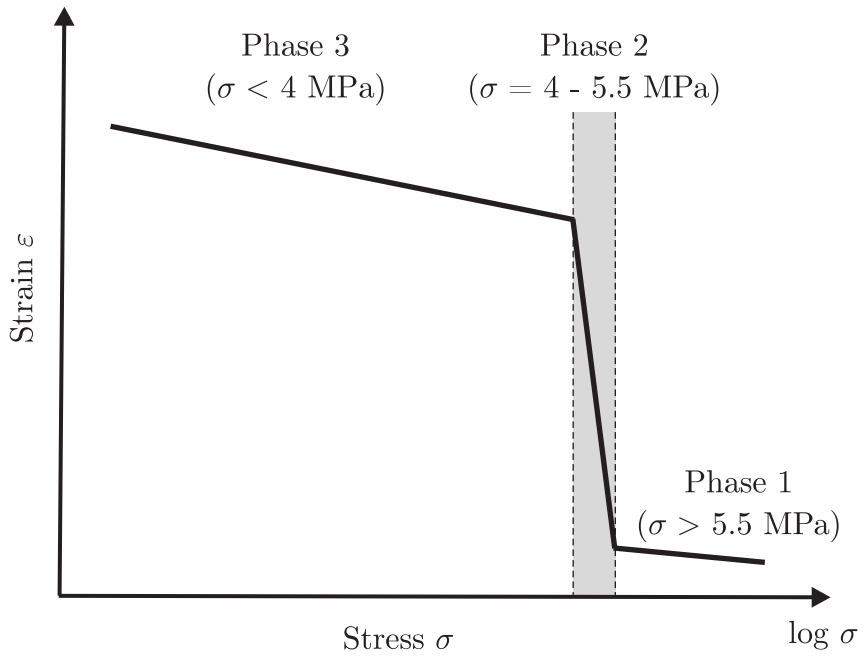

Figure 2.9.: Swelling law proposed by Pimentel (2007)

In summary, the swelling law of Grob provides a satisfactory description of the equilibrium states between swelling strain and swelling pressure for pure clay formations and is acceptable for pure clay shales when focusing solely on equilibrium states. However, an important limitation highlighted by Kirschke (1996) is the neglect of time in Grob's formulation. Furthermore, none of the existing laws considers water transfer, and the equations provided are typically formulated only in 1D. For application in models such as finite element models, these equations would need to be extended to 2D or 3D formulations. Additionally, it is worth noting that for anhydrite, other phenomena, such as those described in Pimentel (2007), must be considered, although anhydrite swelling is beyond the scope of this research.

2.2.3.2. Numerical representation of swelling

In the previous section, analytical swelling laws were discussed. This section shifts the focus to the numerical representation of swelling, starting with a quick overview of different modeling approaches and then proceeding to a detailed description of the method used in this research.

In the literature, three different categories of approaches can be found: models derived from the analytical swelling law proposed by Grob (1972), mechanical-chemically coupled approaches, and elasto-plastic models considering soil saturation.

The first group of models incorporates a dedicated swelling term using a 3D generalization of the analytical swelling law by Grob (1972) (see Equation 2.3). These models, such as those proposed by (Anagnostou, 1993; Heidkamp and Katz, 2002; Kiehl, 1990; Wittke-Gattermann, 2004), extend the original swelling law to include additional features like anisotropic or time-dependent behavior. These models provide a comprehensive understanding of swelling behavior without a coupled description of the material.

Another group of models employs a mechanical-chemically coupled approach, to simulate the process of hydration of anhydrite. For instance, in Alonso and Olivella (2008), the swelling strain caused by gypsum crystal growth in fractures is calculated using thermodynamic kinetic equations.

Lastly, the group of elasto-plastic models utilizes soil suction to characterize material behavior in the unsaturated state. Notable models in this category include the Barcelona Basic Model (BBM) by Alonso et al. (1990) and its successors formulated in $p - q - s$ space, where p represents the net stress, q the deviatoric stress, and s the suction, or using alternative parameters, such as the degree of saturation S_r, instead of suction.

These models can be further extended by expressing swelling on a microstructure level using a double-porosity approach. A prominent example is the Barcelona Expansive model (BExM) by Gens and Alonso (1992), which extends the Barcelona Basic Model to allow modeling of highly expansive soils.

All of the previously mentioned models are capable of simulating swelling. However, as the focus of this study is on swelling clay shales, mechanical-chemically coupled models are not considered, as they have been developed specifically for anhydrite swelling. These models include features such as crystallization of gypsum, which are not present in clay shales. While models based on Grob's model can simulate swelling, they often fail to accurately capture the mechanical behavior in unsaturated conditions. Therefore, only elasto-plastic models can be considered for this thesis.

As this thesis focuses on moderately swelling clay shales that do not exhibit dominant double porosity behavior, the use of the Barcelona Expansive Model (BExM) is not considered appropriate. Instead, the Barcelona Basic Model (BBM) and its extension, the Barcelona Basic Model for Expansive Soils (BBMEx), are selected for a more detailed investigation. The choice of BBM is supported by several considerations: it is a relatively simple and robust model with proven numerical stability and computational efficiency, which makes it well-suited for large-scale simulations. Furthermore, the model requires a limited set of material parameters, enabling a practical calibration based on available laboratory test data. The BBM has already been successfully applied to large-scale engineering problems (e.g. Rothfuchs et al. (2007), Sánchez et al. (2010), Lee et al. (2021), among many others). Importantly, the BBM is already implemented in the finite element framework Lagamine, which is employed throughout this thesis, further justifying its selection. Since the BBM is based on the Modified Cam-Clay model, it is necessary to first describe the latter, which is done in the following section.

Modified Cam-Clay (MCC) model

The Modified Cam-Clay model, developed by Roscoe and Burland (1968), is an elasto-plastic constitutive model widely employed in geotechnical engineering to simulate the mechanical behavior of clays. The model is grounded on the assumption of a logarithmic relationship between the mean stress p and the void ratio e, applicable both during virgin isotropic compression (normal compression line) but also during isotropic unloading and reloading, as shown in Figure 2.10.

The normal compression line is mathematically expressed as:

$$e - e_0 = -\lambda \ \ln\left(\frac{p}{p_{\text{ref}}}\right) \tag{2.4}$$

where λ represents the slope of the normal compression line (NCL), e_0 is the initial void ratio and p_{ref} denotes a reference stress. Concurrently, isotropic unloading and reloading are characterized by:

$$e - e_0 = -\kappa \ \ln\left(\frac{p}{p_{\text{ref}}}\right) \tag{2.5}$$

with κ denoting the slope of the unloading-reloading line, commonly known as the swelling line.

The Modified Cam-Clay model's yield surface takes the form of an ellipse in the $p - q$ plane, as illustrated in Figure 2.11. The yield function is defined by:

$$F = q^2 + M^2 p \ (p + p_c) = 0 \tag{2.6}$$

Here, p_c denotes the preconsolidation pressure, controlling the extent of the yield surface. Within the yield surface, the soil response is elastic, leading to only elastic strain increments upon a change in stress.

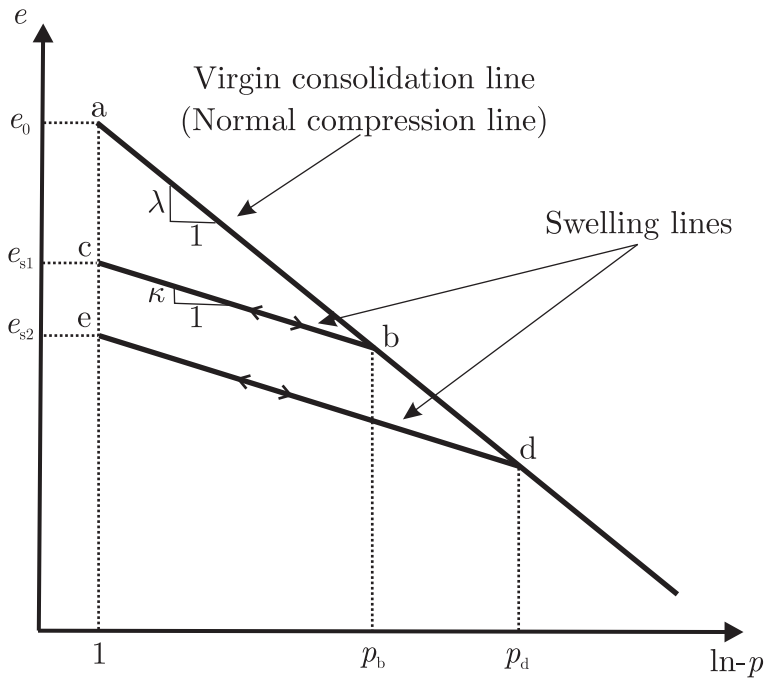

Figure 2.10.: Slopes of the virgin isotropic consolidation line and swelling line

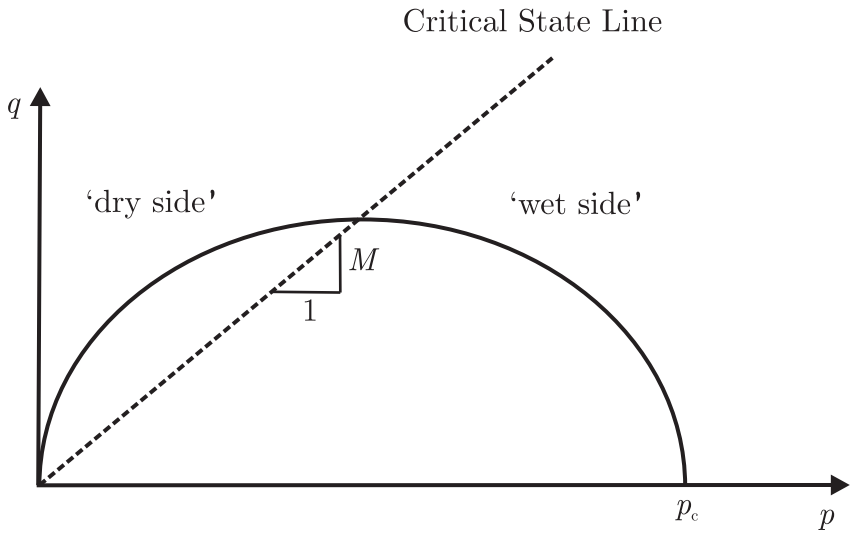

Figure 2.11.: Yield surface of Modified Cam-Clay model after Brinkgreve et al. (2017)

The parameter M influences the height of the ellipse and corresponds to the slope of the Critical State Line (CSL) in the $p-q$ plane. The CSL intersects the yield surface at the maximum q value, the CSL represents the stress states where the soil reaches the critical state. Additionally, it divides the yield surface into two segments, the left side referred to as the dry side and the right side as the wet side. During stress path crossings, the model generates plastic strain increments. On the dry side, the soil exhibits softening associated with dilatancy, while on the wet side, the response involves hardening accompanied by compression.

Barcelona Basic Model (BBM)

The Barcelona Basic Model is an extension of the previously explained Modified Cam-Clay Model (MCC) (Roscoe and Burland, 1968) and is a widely-used constitutive model for unsaturated soils. It was first proposed by Alonso et al. (1990) and is since then extensively applied in geotechnical engineering to predict the mechanical behavior of unsaturated soils under various loading conditions.

The BBM incorporates key features of unsaturated soil behavior, such as the influence of matric suction on the mechanical response and the coupling between hydraulic and mechanical processes. The model is formulated in the $p-q-s$ space, where p represents the net mean stress, q the deviatoric stress and s the matric suction. The net mean stress is defined as the difference between the mean total stress σ_t and the pore air pressure p_a,

while the matric suction represents the difference between the pore air pressure p_a and pore water pressure p_w.

The BBM has been developed in a conventional elasto-plastic framework, with the yield surface, illustrated in Figure 2.12, defined in the $p-q-s$ space. In the $p-q$ plane the yield curve is called the Loading-Collapse (LC) curve and is characterized by a Modified Cam-Clay type shape:

$$f_{LC} = q^2 - M^2(p+p_s)(p_0-p) = 0 \tag{2.7}$$

where M is the slope of the critical state line (CSL), p_0 is the preconsolidation pressure at the current suction level and p_s denotes the left lateral boundary of the yield surface.

Within the elastic domain, changes in the net mean stress generate volumetric strains for which the increment is given as:

$$\mathrm{d}\varepsilon^e_{v,p} = \frac{\kappa}{1+e}\frac{\mathrm{d}p}{p} \tag{2.8}$$

where e is the void ratio and κ represents the slope of the unloading-reloading line, as illustrated in Figure 2.13.

For changes in suction within the elastic domain the increment in volumetric strains is calculated by:

$$\mathrm{d}\varepsilon^e_{v,s} = \frac{\kappa_s}{1+e}\frac{\mathrm{d}s}{s+p_a} \tag{2.9}$$

where κ_s is the slope of the reversible wetting-drying line and p_a is the air pressure.

Once the net mean stress p exceeds the preconsolidation pressure p_0, plastic deformations are generated (see Figure 2.13). Incorporating the hardening law, the plastic strain increment is given by:

$$\mathrm{d}\varepsilon^p_v = \frac{\lambda(s)-\kappa}{1+e}\frac{\mathrm{d}p_0}{p_0} \tag{2.10}$$

where λ(s) denotes the slope of the virgin consolidation line, which is formulated as a function of suction:

$$\lambda(s) = \lambda(0)[(1-r)\exp(-\omega s)+r] \tag{2.11}$$

The maximum stiffness of the soil (for an infinite suction) is linked to the parameter r, while ω determines the rate at which the soil stiffness increases with suction.

Furthermore, the preconsolidation pressure p_0 as well as the left lateral boundary of the yield surface p_s are suction-dependent as shown in the following:

$$p_0(s) = p_c\left(\frac{p_0^*}{p_c}\right)^{\frac{\lambda(0)-\kappa}{\lambda(s)-\kappa}} \tag{2.12}$$

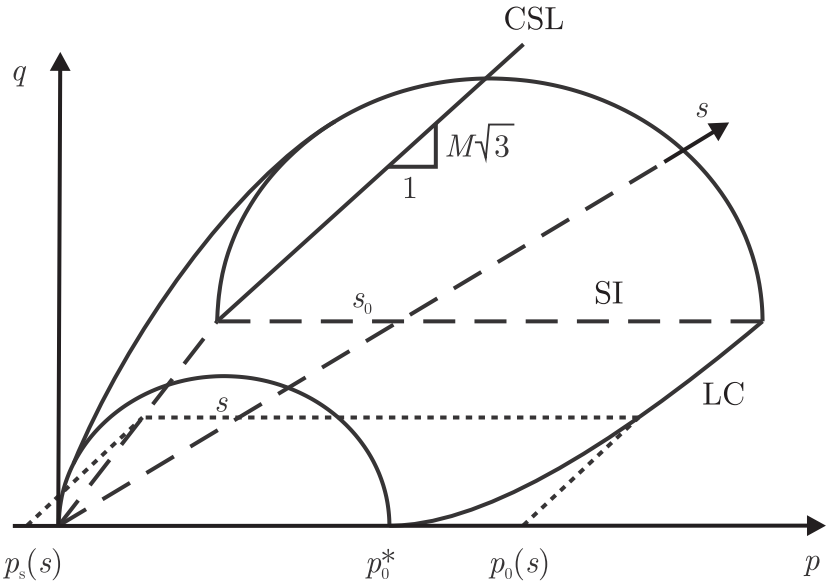

Figure 2.12.: Yield surface of the Barcelona Basic Model in $p-q-s$ space after Alonso et al. (1990)

where p_c is a reference net stress and p_0^* is the preconsolidation pressure at saturated conditions. And

$$p_s(s) = \frac{c_0 + ks}{\tan\varphi} \tag{2.13}$$

with the saturated cohesion c_0, the friction angle φ and the parameter k which controls the suction dependence of the cohesion.

The second yield curve is called the Suction-Increase (SI) curve and is defined in $p-s$ plane:

$$f_{SI} = s = s_0 \tag{2.14}$$

where s_0 is the threshold suction beyond which plastic deformations occur. The increment of the corresponding volumetric strain is given by the following expression:

$$\mathrm{d}\varepsilon_v^p = \frac{\lambda_s - \kappa_s}{1+e}\frac{\mathrm{d}s_0}{s_0 + p_a} \tag{2.15}$$

where κ_s is the slope of the virgin drying line.

The non-associated flow rule for the LC yield surface of the model is defined as:

$$g_{LC} = \alpha q^2 - M^2(p+p_s)(p_0-p) \quad \text{with} \tag{2.16}$$

$$\alpha = \frac{M(M-9)(M-3)}{9(6-M)} \cdot \frac{1}{1-\frac{\kappa}{\lambda(0)}} \tag{2.17}$$

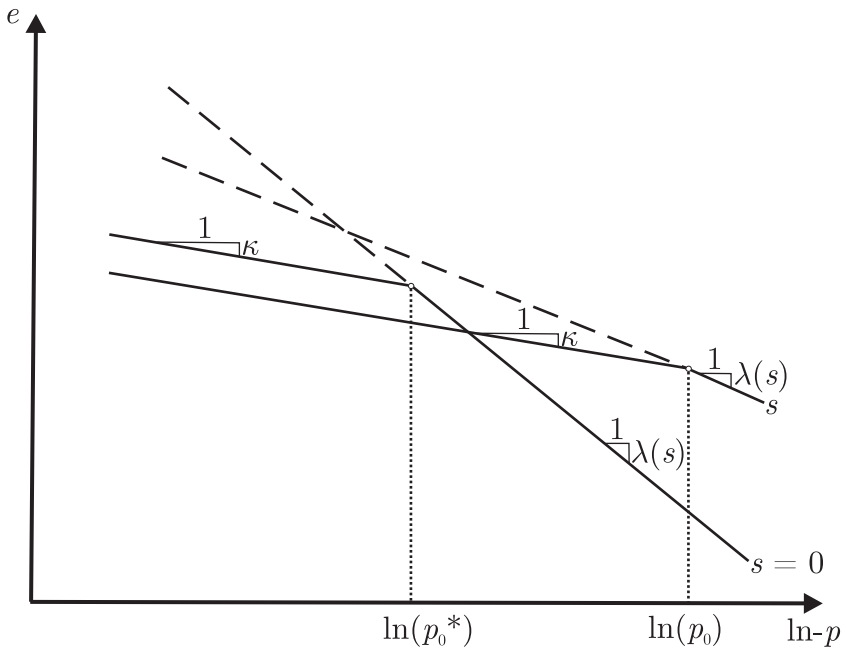

Figure 2.13.: Compression curves for saturated and unsaturated soil (Alonso et al., 1990)

It is important to note that α in Equation 2.16 is not an independent parameter in the model and is instead defined by Equation 2.17. This approach ensures zero lateral strain for stress states corresponding to Jaky's K_0 values.

While the BBM is a robust and versatile constitutive model for unsaturated soils, capable of capturing most key features, including changes in stiffness and shear strength with suction, certain limitations can affect its performance in specific scenarios.

As an extension of the MCC model, the BBM inherits some of its limitations, such as the inability to account for anisotropic behavior and viscous effects.

The BBM assumes a decrease in the slope of the normal compression line (NCL) with increasing suction ($r < 1$), based on tests conducted on compacted low-plasticity kaolin and a compacted sandy clay (Alonso et al., 1990).

According to Wheeler et al. (2002), experiments on compacted speswhite kaolin show an increase in the slope of the NCL with increasing suction ($r > 1$). Wheeler et al. (2002) highlight issues and possible solutions arising from $r < 1$, such as the necessity of using a high reference stress $p_c > p_0^*$ and the challenges in determining p_c.

Furthermore, the use of two intersecting yield surfaces in the BBM poses challenges for numerical solutions, particularly in the intersection regions.

Lastly, Dieudonne (2016) highlights the limitations in accurately predicting swelling pressures during swelling pressure tests using the BBM. To address this, the Barcelona research group incorporated suction- and/or stress-dependent elastic parameters (κ and κ_s) into the BBM, resulting in the Barcelona Basic Model for Expansive Soils (BBMEx), which will be explained in the following section.

Barcelona Basic Model for Expansive soils (BBMEx)

Following the original publication of the BBM, it was observed that swelling pressure tests could not be satisfactorily modeled (Gens and Sánchez, 2010; Dieudonne, 2016). Dieudonne (2016) reported unrealistically low swelling pressures for Febex bentonite, when using BBM with constant elastic parameters (κ and κ_s). To address this limitation, García-Fontanet (1998) extended the BBM to incorporate suction- and/or stress-dependent elastic parameters κ and κ_s. These parameters are critical in controlling the swelling pressure, and since swelling pressure tests involve changes in both suction and pressure, incorporating a dependency of κ and κ_s on net mean stress p and suction s is a reasonable approach.

The elastic parameter κ, giving the slope of the unloading-reloading line for changes in mean net stress, is in the BBMEx suction dependent:

$$\kappa(s) = \kappa_0 \left[1 + \alpha_1 + \alpha_2 \ln\left(\frac{s + p_a}{p_a}\right)\right] \tag{2.18}$$

where κ_0 is the elastic stiffness in saturated conditions, α_1 and α_2 are model parameters.

Additionally, for the elastic stiffness κ_s, describing the slope of the wetting-drying line during suction changes, was transformed into a function $\kappa_s(p, s)$ considering net pressure p and suction s:

$$\kappa_s(p, s) = \kappa_{s0} \left[1 + \alpha_p \ \ln\left(\frac{p}{p_{\text{ref}}}\right)\right] \exp(\alpha_s \cdot s) \tag{2.19}$$

where p_{ref} is the reference pressure and κ_{s0}, α_p and α_s are fitting parameters.

It has to be noted that the parameters α_1, α_2, α_p, and α_s introduced in the BBMEx do not have a direct physical meaning. Instead, they are fitting parameters determined through back-analysis of laboratory data. These parameters are calibrated by matching the model to experimental results, allowing for an accurate representation of the observed behavior in swelling pressure tests.

2.3. Tunnel excavation in swellable clay shales

The tunnel excavation and long-term maintenance of tunnels in swellable clay shales is a challenging task, and in the literature (Grob, 1972; Einstein, 1996; Steiner, 1993; Amstad and Kovári, 2001; Butscher et al., 2016), many cases where tunnels were damaged due to the swelling of the ground are reported. As the previous section already discussed the swelling mechanisms and modeling approaches for swelling, this section will focus on tunnel excavation in this type of ground.

Therefore, the following section presents the techniques relevant to tunnel excavation in swellable clay shales, with particular emphasis on their application in these. Furthermore, the numerical methods used in this thesis to model tunnel excavations are elaborated.

2.3.1. Tunnel excavation techniques

There are three primary tunnel excavation techniques, namely cut and cover, conventional tunnel excavation, and mechanized tunnel excavation. As the cut and cover method is only applicable to very shallow tunnels, this method is out of the scope of this thesis, which is focusing on deep tunnel excavations in clay shales.

In these geological conditions only the conventional and the mechanized tunneling method are relevant and both of them will be explained with focus on excavations in swellable clay shales.

2.3.1.1. Conventional tunnel excavation

Conventional tunnel excavation methods, such as the New Austrian Tunneling Method (NATM), involve the sequential excavation of small sections of the tunnel face, followed by the immediate installation of support systems. The tunnel support typically consists of a primary support, including shotcrete to stabilize the excavated walls and rock bolts to secure the surrounding ground, a drainage system to reduce ground water pressure, and a secondary lining made of concrete or reinforced concrete to provide permanent stability and protection. According to Amstad and Kovári (2001), the NATM method has been employed in several tunnel constructions in swellable formations.

In NATM, the highest and most critical swelling deformations are typically observed at the tunnel invert (Amstad and Kovári, 2001).

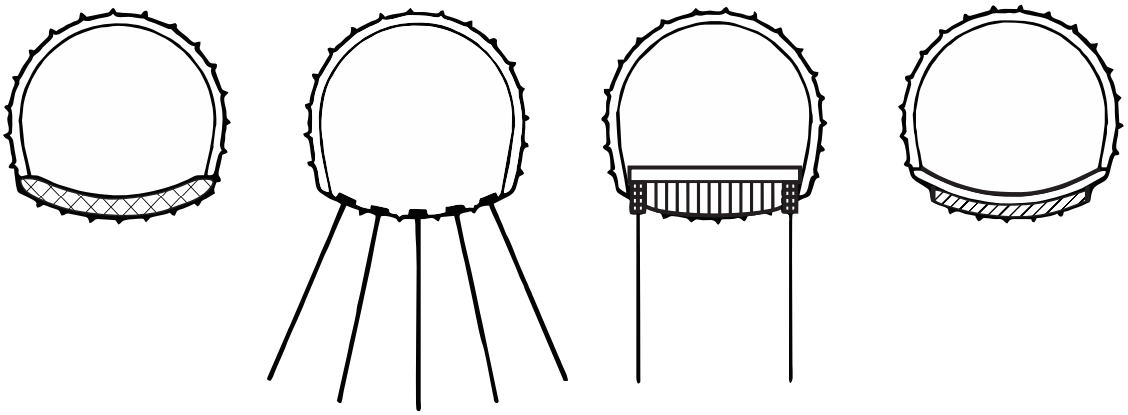

Figure 2.14.: Constructive measures in swellable rock (Kovári et al., 1987)

As a result, designs aimed at counteracting swelling primarily focus on the tunnel invert. According to Kovári et al. (1987), four different support systems are suitable for swellable rocks, as illustrated in Figure 2.14.

The first two approaches involve the installation of a rigid invert arch or an anchoring system to suppress swelling-induced heave, although these approaches may lead to significant swelling pressures. Another method uses a hollow invert, which creates a void beneath the road slab of a road tunnel to accommodate the swelling pressure. The fourth option involves a compressible layer, combining the advantages of the previous methods by mitigating heave while controlling the development of swelling pressure within the structure.

According to Kovári et al. (1987), water ingress into swellable rock is a critical factor, as no swelling can occur without water. Additionally, the rate of water ingress, which depends on the degree of damage to the ground, influences the ability to maintain the tunnel's design profile. Water ingress causes the rock to swell, which can lead to potential damage, such as lifting of the open inner lining (invert arch only) before ring closure or the failure of the outer lining before construction of the inner lining. Consequently, the excavation tools used for the excavation play a crucial role.

An excavation method is considered rock-preserving if it does not significantly affect the properties of the intact rock, particularly its strength and permeability. Non-rock-preserving excavation loosens the rock surrounding the cavity, facilitating water inflow in the invert area and potentially accelerating the swelling process. This affected area is referred to in the literature as the excavation damaged zone (EDZ) and is discussed in detail in Section 2.4 due to its critical importance.

In conventional tunnel excavation, the cavity can be created using blasting, drilling, or milling. Blasting is regarded as non-rock-preserving, whereas partial-face excavation machines are considered rock-preserving. Similarly, tunnel boring machines (TBMs), used in mechanized tunnel excavation, are also classified as rock-preserving methods.

2.3.1.2. Mechanized tunnel excavation

Mechanized tunneling plays a crucial role in modern tunnel construction, offering an efficient and reliable excavation method in different geological conditions. It provides several advantages, including high excavation speed, profile accuracy, minimal impact on existing structures, enhanced safety for the workforce, environmentally friendly construction methods (e.g. groundwater level increase, reduced noise), and the possibility of achieving high-quality and cost-effective lining (Maidl et al., 2011).

TBMs consist of a cutterhead equipped with tools specifically designed for the type of ground or rock to be excavated. Since clay shales exhibit high stability, support for the tunnel face is generally not required. However, in cases where such support becomes necessary, such as in non-cohesive soils, the tunnel face can be stabilized using a support medium, such as bentonite slurry.

In mechanized tunneling, TBMs are categorized into shielded TBMs and open TBMs. The latter use grippers to anchor themselves into the ground and steer the machine by pushing against the unreinforced sides of the tunnel. The forward advancement is achieved through hydraulic thrust cylinders that press the cutting head against the ground. Once the maximum stroke of the jack forces is reached, the grippers must be repositioned. Tunnel support in gripper TBMs is provided using steel reinforcement, shotcrete, and, if necessary, rock bolts.

Open TBMs are suitable exclusively for stable ground, such as intact rock, where the ground conditions allow for reliable anchoring and excavation without a protective shield. According to Kovári et al. (1987), tunneling with an open TBM is unlikely to be significantly affected by swelling pressure or heave. However, problems may arise due to rock softening. This was the case during the excavation of the pilot tunnel for the tunnel near Kreuzlingen. In certain sections, the gripper plates could no longer anchor effectively, reducing the advance rate to just a few meters per working day (Kovári et al., 1987).

In contrast, shield TBMs are primarily used in unstable ground conditions. The excavation steps for mechanized tunnel excavations using shield TBMs and selected cross sections are illustrated in Figure 2.15. In this method, precast concrete segments, known

as tubbings, are installed within the protection of a shield (cross section C-C), ensuring stability and safety during excavation. Hydraulic thrust cylinders, located between the tunnel lining and the thrust wall of the shield machine, advance the TBM during excavation. To allow precise steering, the cutterhead diameter is slightly larger than the tunnel lining diameter, also known as overcut (cross section B-B).

The gap between the tunnel lining and the surrounding ground behind the shield tail is continuously injected with grout at the shield tail. The grout material prevents unwanted soil ingress into the ring gap and ensures proper bedding of the tunnel lining within the surrounding ground (cross section D-D). Depending on the requirements, various materials can be used as grout, such as mortar, two-component grout, or pea gravel (Thewes and Budach, 2009*a*,*b*).
These materials differ in their mechanical properties, application range, backfilling system, and hardening time. By controlling the mixture, these properties can be optimized to suit the geological conditions, e.g., a very rigid or a deformable mortar.

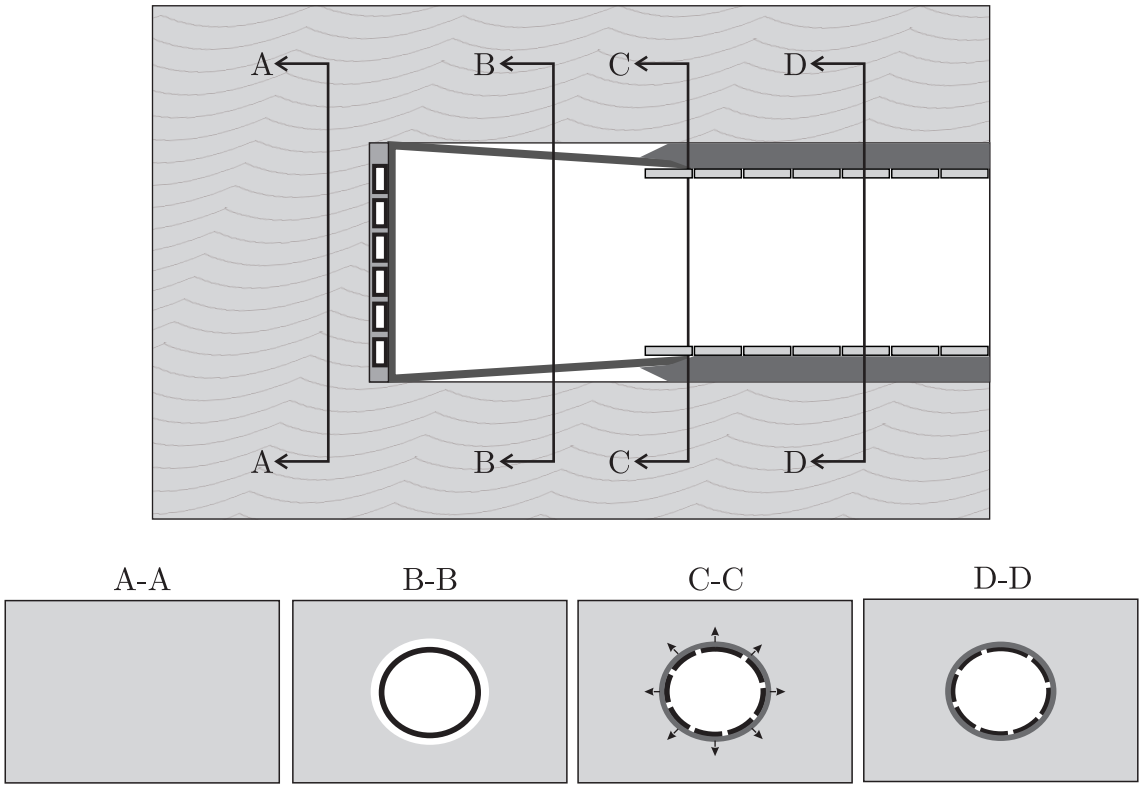

Figure 2.15.: Schematic representation of mechanized tunnel excavation

The use of shield TBMs in swellable rock offers several advantages, according to Kovári et al. (1987). These include high advance rates, mitigation of potential swelling-induced heave at the tunnel face due to the weight of the cutterhead and the shield, and a short ring closure time for the outer lining, achieved by installing the tubbings within the shield tail. The primary risk when using a shield TBM in swellable rock is the jamming of the shield due to swelling during excavation or during downtime. These risks can be mitigated through preventive measures, such as selecting a shorter or more conical shield design or increasing the bore diameter or overcut (Kovári et al., 1987). Due to these advantages, this thesis focuses on mechanized tunneling using shield TBMs.

2.3.2. Numerical modeling of mechanized tunnel excavation

Mechanized tunnel excavation requires advanced numerical methods to simulate stress-strain interactions and predict ground behavior (Möller, 2006). 2D and 3D finite element methods (FEM) are commonly employed, with each approach offering specific advantages depending on the complexity and focus of the simulation.

In 3D FEM, two primary approaches are commonly used: the single-step approach or the step-by-step approach. The single-step approach simplifies the process by simultaneously removing ground elements and activating lining elements along the entire tunnel length, as described by Lee and Rowe (1991); Corbetta (1990); Anagnostou (2007).

The step-by-step approach, introduced by Hanafy and Emery (1980); Katzenbach and Breth (1981) and further developed by others such as Hoefsloot and Verweij (2006), models excavation incrementally in discrete steps, allowing for a more detailed representation of the excavation sequence and the installation of linings. For both approaches, the specific simulation details can vary depending on the focus of the analysis, e.g., consideration of face pressure and grouting pressure. While 3D modeling of tunnel excavation enables highly detailed simulations, it is computationally demanding, making 2D modeling a popular alternative.

2D FEM simplifies the three-dimensional stress-strain behavior by approximating the effects of the missing third dimension. This can be achieved through the soil stiffness release method (α-method), the lining reduction method (δ-method), and the stress reduction method (β- or λ-method). The α-method reduces the stiffness of the soil located inside the tunnel core to simulate the unsupported section of the excavation. The δ-method activates the lining with reduced stiffness to account for load transfer. The β- or λ-method

uses a staged reduction of the initial ground pressure, simulating the redistribution of stresses during excavation.

While 2D methods are computationally efficient, they require calibration against real-world measurement data (e.g., settlement profiles) or 3D FEM results to ensure reliability. One common technique to incorporate 3D information into 2D models is the convergence-confinement method, which will be detailed in the following section.

2.3.2.1. Convergence-confinement method

The convergence-confinement method (Panet, 1995) is a widely used approach in tunneling engineering to predict the behavior of the ground and the support system during tunnel excavation. The method is based on the β- or λ-method, where a pressure σ is applied inside the tunnel wall, which is reduced when the TBM is approaching. In this method, the stress σ is related to the natural state of stress σ_0 by the equation:

$$\sigma = (1 - \lambda)\sigma_0 \tag{2.20}$$

Here, the coefficient λ is called the deconfinement ratio or stress release ratio. The deconfinement ratio λ will increase from no excavation ($\lambda = 0$) to full excavation ($\lambda = 1$). This coefficient is derived from the Longitudinal Displacement Profile (LDP) and the Ground Reaction Curve (GRC) illustrated in Figure 2.16. The former represents the evolution of the radial displacement u_r at the tunnel wall as a function of the distance x to the tunnel face:

$$f_{\mathrm{LDP}}(u_r, x) = 0. \tag{2.21}$$

The relationship between the support pressure σ and the radial displacement u_r at the wall of the tunnel gives the ground convergence, represented by the Ground Reaction Curve (GRC):

$$f_{\mathrm{GRC}}(\sigma, u_r) = 0. \tag{2.22}$$

The LDP can be obtained from settlement profiles along the tunnel excavation or derived from a 3D simulation, while the GRC is derived from a 2D plane strain model. By linking the LDP and GRC ($f_{\mathrm{LDP}} = f_{\mathrm{GRC}}$), the deconfinement ratio is now dependent on the distance to the tunnel face $\lambda(x)$. With knowledge of the excavation speed, the evolution of $\lambda(t)$ over time can be calculated.

In the context of supported tunnel, the mechanical behavior of the support can be described by the relationship between the stress at the outer face of the support σ and the radial displacement u_r:

$$f_{\mathrm{SCC}}(\sigma, u_r) = 0 \tag{2.23}$$

As the installed tunnel support needs some deformation to start limiting the tunnel convergence, an unsupported distance L is considered as illustrated in Figure 2.16, where the corresponding radial displacement is u_r^0. The equation for the support is then:

$$f_{\mathrm{SCC}}(\sigma, u_r - u_r^0) = 0 \tag{2.24}$$

The resulting curve is called the Support Confining Curve (SCC). The final static equilibrium of the interaction between the ground and the tunnel support can be found by solving the two equations ($f_{\mathrm{GRC}} = f_{\mathrm{SCC}}$), as shown in Figure 2.16.

The convergence-confinement method is developed analytically with restrictive assumptions, such as a tunnel with a circular section, full face excavation, homogeneous and isotropic ground, and an isotropic state of natural stress, but has been used successfully in Mousivand et al. (2017) for other cases as well.
According to Panet and Sulem (2022) the convergence-confinement method can be used for tunnel excavation with anisotropic initial stress states, however it is assumed that the deconfinement ratio λ is uniform around the tunnel.

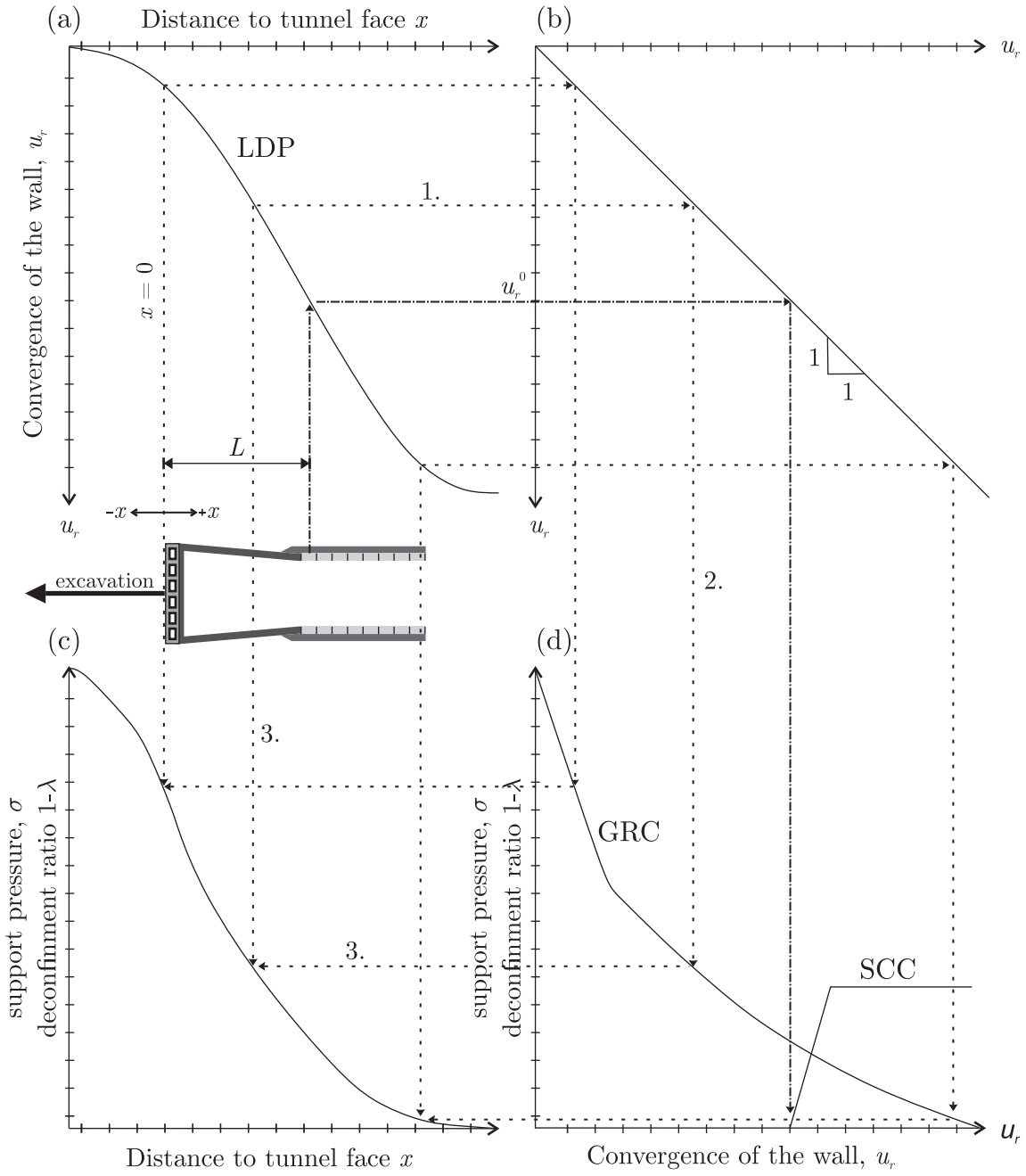

Figure 2.16.: Workflow of the convergence-confinement method

2.4. Excavation Damaged Zone (EDZ)

As previously explained in Section 2.3, the Excavation Damaged Zone (EDZ) is a critical factor for tunnel excavation in swellable clay shales, as it significantly influences water transport in the vicinity of the tunnel. This, in turn, substantially affects the temporal evolution of swelling acting on the tunnel support. Thus, the EDZ is one of the most important aspects of tunnel excavations in swellable clay shales and requires special attention. Consequently, this section provides a detailed discussion of the EDZ.

Tunnel excavation induces stress redistribution, leading to the development of damage in the surrounding material. Microcracks initiate upon surpassing the damage threshold, accumulating and propagating as distributed damage, eventually forming larger interconnected macrocracks. Two primary processes contribute to this phenomenon: (i) stress-induced microcracking in the short term and (ii) time-dependent microcracking that often develop in the long term (Golshani et al., 2007).

The damaged region, identified as the EDZ, experiences deformations and alterations in the hydro-mechanical properties of the clay shale. These alterations, including increased permeability and strength reduction, can pose challenges to tunnel safety, underscoring the importance of a comprehensive investigation into the short-term and long-term behavior of the rock within the EDZ.

According to Blümling et al. (2007), the geometry of the EDZ is influenced by various factors, such as the stress anisotropy, material anisotropy, the presence of natural fracture zones, tunnel geometry, and interactions between tunnel support and ground. In hard and brittle clays, discrete features in the EDZ result from short-term excavation-induced unloading, primarily exhibiting extensional or tensile failure, whereas weaker rocks or soft clay shales may experience shear failure instead. Anisotropic rocks may activate planes of weakness, leading to either extensional or shear failure (Blümling et al., 2007).

According to Blümling et al. (2007), within the EDZ, stress redistribution may lead to localized consolidation and swelling in the post-closure phase. For example, in regions of tangential stress concentration, the maximum stress may exceed the previous overconsolidation stress, causing the material to behave more like a normally consolidated sediment rather than an overconsolidated one. In unloaded areas, suction may attract moisture, leading to localized swelling of the materials.

The Mont Terri Underground Research Laboratory (URL) in Switzerland, focusing on Opalinus Clay for potential nuclear waste disposal, serves as a significant facility for EDZ

investigation (Bossart et al., 2002). The fractures under investigation were sampled using resin-injected overcores from the EDZ, yielding valuable data on fracture orientations, frequencies, and the extent of the EDZ.

To determine the hydraulic properties of these fractures, including permeability and transmissivity, pneumatic and hydrogeological tests were conducted. The synthesis of these data concluded in the development of a conceptual model for the EDZ in the Opalinus Clay, leveraging insights gained from observations at the Mont Terri URL as illustrated in Figure 2.17.

The conceptual model illustrates a plastic deformed zone extending a distance equivalent to the tunnel's radius. This zone is further divided into two regions: an inner zone spanning $0.5\,r$ (f_1), characterized by an air-filled interconnected fracture network, and an outer zone (f_2) dominated by a partially saturated and isolated fracture network, both highlighted in Figure 2.17. Within the inner zone (f_1), intrinsic permeability k_0 is significantly higher compared to the undisturbed rock k_0, particularly within the initial $0.2\,r$ distance from the tunnel wall. In contrast, the outer zone (f_2) exhibits considerably lower permeability evolution $\frac{k}{k_0}$ compared to the inner zone. This comprehensive model enhances our understanding of fracture network characteristics and permeability changes within the EDZ in the Opalinus clay shale.

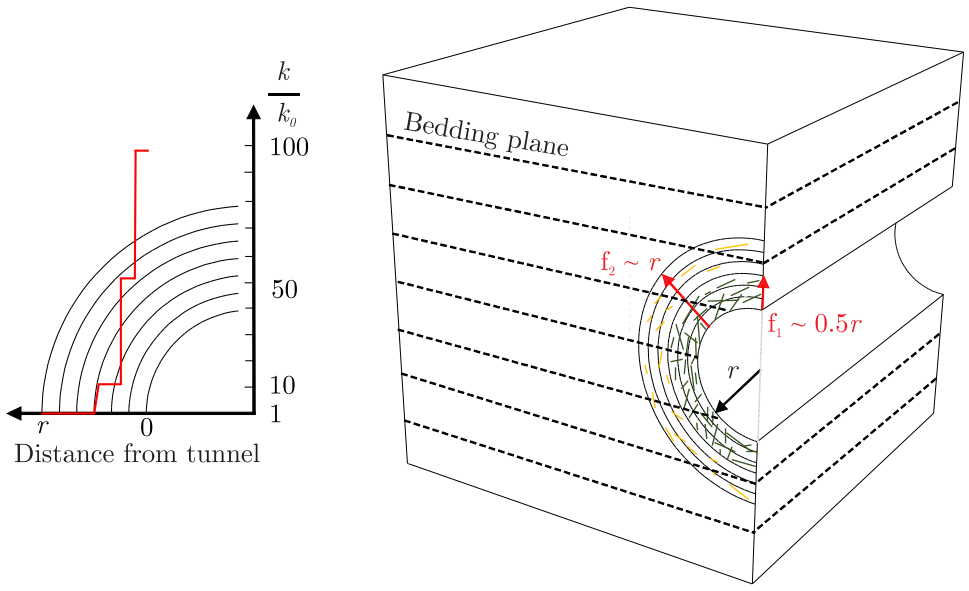

Figure 2.17.: Conceptual model of fracture network and permeability evolution within the EDZ in OPA after Bossart et al. (2002)

In the study conducted by Perras and Diederichs (2016), the Excavation Damaged Zone (EDZ) was categorized into four distinct zones, each reflecting varying levels of damage resulting from excavation activities, as depicted in Figure 2.18. These zones contribute to the understanding of the modeled fracture network and permeability evolution within the EDZ in Opalinus clay shale. The identified zones are as follows:

- **Construction Damaged Zone (CDZ):** CDZ is characterized by damage caused by construction methods, particularly the excavation process itself. The degree of damage in this zone can potentially be influenced and reduced by adjusting or altering construction techniques.
- **Highly Damaged Zone (HDZ):** HDZ represents the initial and unavoidable consequences of excavation, featuring interconnected macro-fractures within the rock mass. These fractures result from changes in geometry, structural alterations, and induced stress changes.
- **Excavation Damaged Zone (EDZ):** EDZ encompasses varying levels of damage and connectivity, including the HDZ and further subdivisions. This zone provides insights into the complex network of fractures and changes in the rock structure induced by the excavation process.
- **Excavation Influenced Zone (EIZ):** EIZ is characterized by primarily elastic changes and lies beyond the EDZs. It represents a transitional region between excavation-induced changes and undisturbed rock, primarily experiencing alterations in stress and strain rather than significant damage.

Ensuring precise modeling of hydro-mechanical interactions within the EDZ is essential for designing and ensuring the safety of underground structures. The following section describes different approaches for modeling the EDZ.

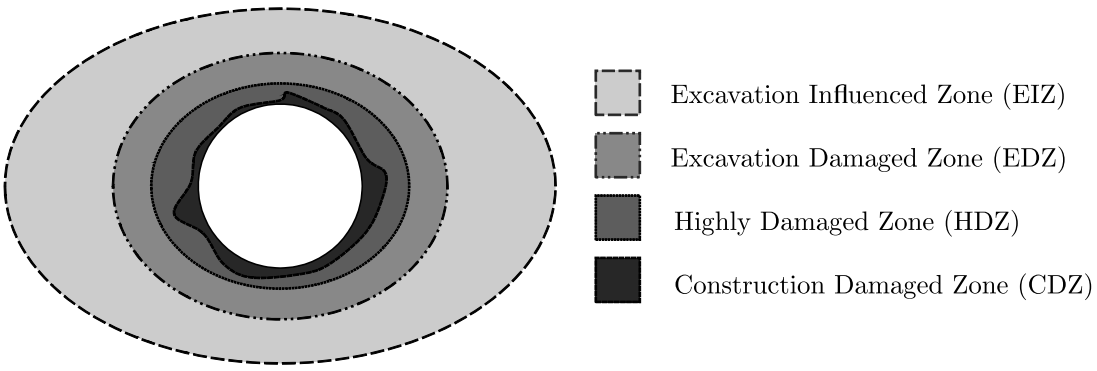

Figure 2.18.: Various damaged zones around the excavation (Perras and Diederichs, 2016)

2.5. Modeling approaches for the EDZ

The prediction of the Excavation Damaged Zone (EDZ) and its fracture structure is critical for tunneling in swellable clay shales, particularly regarding the long-term safety and stability of deep excavations. Various methods have been employed in the literature to determine the extent and characteristics of the EDZ.

Empirical and analytical methods, as utilized by researchers such as Tao et al. (2019); Xu et al. (2022); Martin et al. (1999); Diederichs (2007); Perras and Diederichs (2016), provide straightforward approaches and reasonable estimations of the EDZ. These models relate EDZ size to the tunnel radius and rely on various assumptions, such as employing the Mohr-Coulomb or Hoek-Brown failure criteria, or integrating UCS (Uniaxial Compressive Strength) or CI (Crack Initiation) values with the actual stress state. However, for complex tunnel-ground interactions, numerical methods are generally more suitable.

Numerical approaches encompass diverse techniques, each with unique capabilities. The Discrete Element Method (DEM), employed by Shen and Barton (1997); Zhao et al. (2020); Farahmand and Diederichs (2021); Dedecker et al. (2007), models joints and fractures in rock masses by representing the rock as discrete particles. This method excels in capturing the discrete nature of fractures and joint behavior, particularly in heavily fractured or jointed rock masses. However, its particle-based nature typically demands high computational resources compared to other methods.

Conversely, the Finite Element Method (FEM) offers advantages in simulating rock masses with advanced constitutive models, though it cannot directly model discrete fractures. FEM is widely applied in EDZ simulations using damage models (Golshani et al., 2007; Arson and Gatmiri, 2012; Mader et al., 2022; Xu and Arson, 2014) or strain localization techniques (Pardoen, Levasseur and Collin, 2015; Levasseur et al., 2013; Bertrand and Collin, 2017). Damage models simulate gradual material degradation, capturing the evolution of damage within the rock mass. In contrast, strain localization techniques are particularly suited to modeling localized deformation zones, such as shear bands.

Hybrid approaches, such as the Hybrid Finite-Discrete Element Method (FDEM), combine the strengths of DEM and FEM. These methods allow FEM to model intact rock masses while enabling DEM to capture discrete fractures and joint behavior. Studies like Lei et al. (2017) and Lisjak et al. (2016) highlight the utility of FDEM for complex fracture scenarios. However, the computational demands and specialized software requirements of hybrid approaches make them less practical for this thesis.

Given the complexity of tunnel excavation and the need for computational efficiency, this thesis adopts FEM. Among the FEM techniques, strain localization methods are selected due to their flexibility in incorporating constitutive models tailored to the swelling behavior of clay shales, due to the independence of a specific constitutive law.

To justify this choice, the following section elaborates on the significance of strain localization, demonstrating its occurrence in geomaterials both at the laboratory scale and in tunnel-scale applications.

2.6. Shear strain localization in geomaterials

In the context of geomaterials, localized deformations occur in a variety of forms, spanning from simple cracks to multiple fault planes. This diversity is particularly evident in geotechnical contexts like boreholes and tunnels. While some instances of failure demonstrate a diffuse pattern, the majority involve localized strains within specific shear bands, ultimately culminating in the creation of rupture zones (Salehnia, 2015).

It's widely acknowledged that materials often undergo localized damage before experiencing complete rupture. Initially, stress redistribution disperses damage throughout the material, which gradually concentrates over time. Once the damage threshold is surpassed, microcracks initiate, propagate, and coalesce, spreading throughout the material. The cumulative effect of distributed damage intensifies strain localization, prompting the initiation of interconnected fractures and the eventual development of macrocracks, leading to abrupt material rupture (Diederichs, 2003).

Fracture mechanics defines various fracture modes, including tensile (mode I), sliding shear (mode II), tearing shear (mode III), and a mixed mode (mode I-II) as illustrated in Figure 2.19 (Jenq, 1988). In tunnel excavation scenarios, clay shales commonly experience fracturing, primarily through shear fractures in mode II (Pardoen, 2015). Therefore, shear strain localization serves as a critical indicator of the fracturing process. Although the modeling approach for shear strain localization is continuous and does not explicitly depict fractures and their discontinuities, it often results in the formation of shear bands and non-uniform strain fields, leading to discontinuities in material displacement on both sides of a shear band (Pardoen, 2015).

After introducing shear strain localization, it becomes essential to explore practical examples of this phenomenon in geomaterials. Experimental studies provide compelling evidence of these localized strains, offering insights into how geomaterials behave under

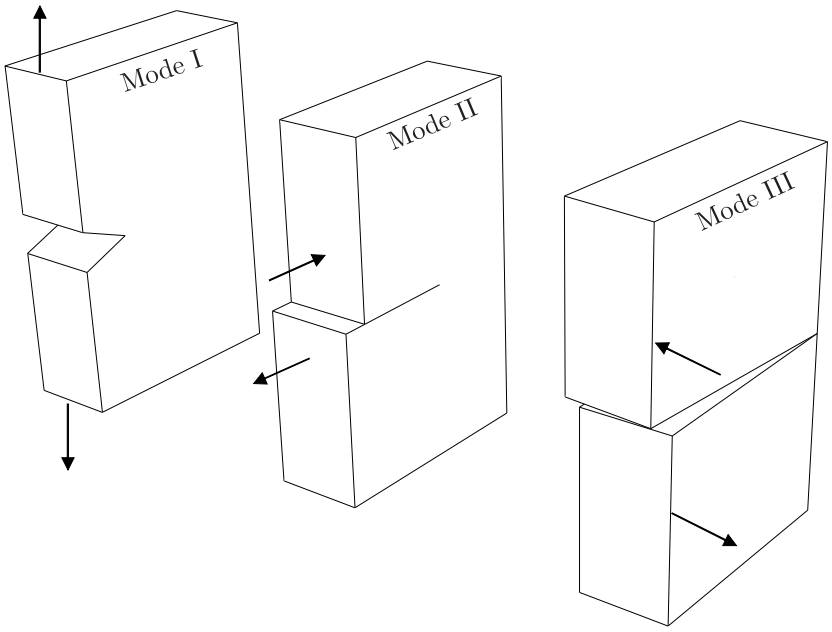

Figure 2.19.: Different fracture modes (Pardoen, 2015)

varying conditions, thereby bridging the gap between theory and practice. The subsequent sections will delve into experimental evidence of strain localization at both small and large scales.

2.6.1. Small-scale evidence of strain localization

In the past five decades, strain localization has been extensively investigated through various laboratory tests, including biaxial tests (Vardoulakis et al., 1978; Han and Vardoulakis, 1991; Finno et al., 1996, 1997; Desrues, 1984; Alshibli et al., 2003; Desrues and Viggiani, 2004; Mokni and Desrues, 1999; Roger et al., 1998; Tatsuoka et al., 1986, 1990), hollow cylinder tests (Labiouse et al., 2014), triaxial tests (Desrues et al., 1996; Bésuelle et al., 2000; Yu et al., 2012; Lenoir et al., 2007), and direct shear tests (Arthur et al., 1977). Various techniques, such as stereophotogrammetry, 3D digital image correlation, X-ray microtomography, and scanning electron microscopy (SEM), have been employed to visualize and analyze the development of shear bands in geomaterials (Desrues, 2005).

The collective findings from these laboratory experiments, as synthesized by Desrues (2005), reveal several key insights. Firstly, strain localization in the form of shear bands commonly occurs in most laboratory tests, ultimately leading to material rupture as illustrated in Figure 2.20.

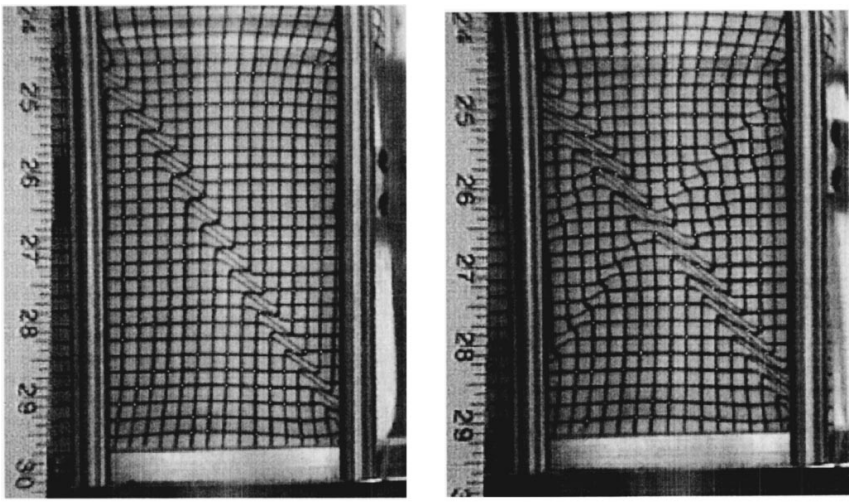

Figure 2.20.: Shear bands in sand specimen during biaxial testing (Alshibli et al., 2003)

The observed localization patterns can exhibit complexity, influenced by factors such as specimen geometry and loading conditions. Notably, well-defined stress peaks in stress-strain curves often serve as indicators of an established shear band system within the specimens.

Furthermore, investigations conducted on materials like loose and dense Hostun sand under plane strain undrained conditions have highlighted distinct localization patterns. Particularly in dense (dilatant) sand specimens, the occurrence of localization is contingent upon cavitation phenomena in the pore fluid.

By elucidating the existence and characteristics of shear bands through laboratory-scale experimentation, researchers have laid the groundwork for understanding these phenomena in real-world scenarios. The subsequent section will delve into the manifestation of shear bands in in-situ experiments, further bridging the gap between laboratory observations and field applications.

2.6.2. Large-scale observation of strain localization

In addition to small-scale observations of strain localization in the laboratory, there are also larger-scale observations, such as strain localization in railway tracks following earthquakes or during tunneling or drilling. Due to the fact that the EDZ, as a result of tunnel excavation, is the focus of this thesis, this section is limited to in situ observations within the context of tunneling or drilling.

As discussed in Section 2.4, the excavation process induces stress redistribution, leading to the formation of the Excavation Damaged Zone (EDZ), where the hydro-mechanical properties are altered. The significance of the EDZ extends beyond road and railway tunnel excavations to include nuclear waste repositories, where stricter regulations and significantly longer maintenance periods must be considered. Due to the high risks associated with the disposal of radioactive waste, numerous field observations have been conducted to analyze the EDZ. Notably, in three major European underground laboratories dedicated to nuclear waste disposal in clay shales, strain localization phenomena have been observed. These laboratories include the Bure underground research laboratory operated by the French National Radioactive Waste Management Agency (ANDRA), where the host rock is the Callovo-Oxfordian (COX) clay; the HADES underground research laboratory managed by the Belgian Agency for Radioactive Waste and Enriched Fissile Materials (NIRAS/ONDRAF), situated in the Boom Clay; and the Mont Terri Underground Laboratory overseen by the Swiss National Cooperative for the Disposal of Radioactive Waste (NAGRA), where the host rock is Opalinus Clay.

To gain insight into the fracture patterns encountered during tunnel excavation, small-scale field tests involving borehole drilling in the host rock formation are often conducted.

Figure 2.21 displays the herringbone structure of fractures observed in a COX borehole core at the Bure Underground Research Laboratory, induced by the drilling process. A similar pattern is evident in Figure 2.22 for a Boom Clay borehole at the HADES Underground Research Laboratory. Additionally, Figure 2.23 shows combined shear-extensional fracturing around a borehole in Opalinus clay.

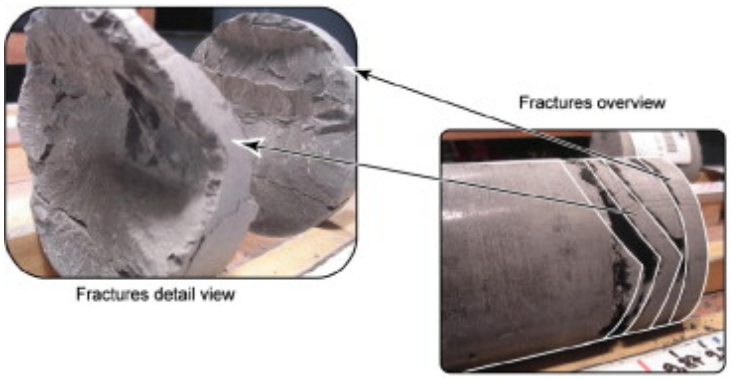

Figure 2.21.: Fractures pattern along a COX borehole core induced by the drilling process (Wileveau and Bernier, 2008)

Figure 2.22.: Fractures pattern along a Boom Clay borehole core induced by the drilling process (Wileveau and Bernier, 2008)

Figure 2.23.: Eye shaped combined shear-extensional fractures around a borehole in OPA (Thury and Bossart, 1999)

Transitioning to observations from actual tunnel excavations, similar phenomena were noted at the HADES Underground Research Facility. Stress redistribution led to the formation of shear-induced fractures both in the excavation front and on the tunnel sidewalls, as depicted in Figures 2.24 and 2.25.

By combining the fracture patterns obtained from borehole drilling with those observed during tunnel excavation, an idealized representation of the excavation-induced fracture network can be derived, as illustrated in Figure 2.26. According to Bastiaens et al. (2003), the observed fracture pattern typically comprises two main conjugated localized shear planes: one in the upper part, dipping towards the excavation direction, and the other in the lower part, dipping in the opposite direction. These fracture planes intersect at the mid-height of the gallery and exhibit curvature at their intersection with the vertical and horizontal planes passing through the gallery axis.

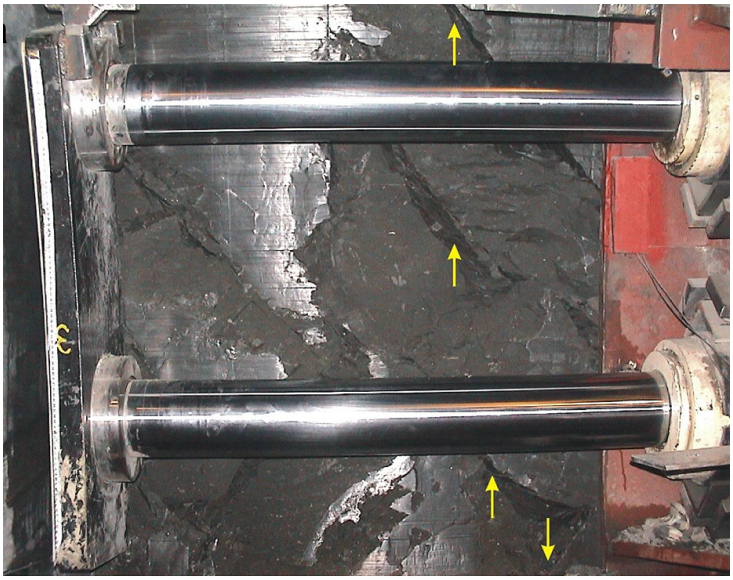

Figure 2.24.: Fractures observed on the sidewalls (Connecting Gallery) at the HADES URF (Van Marcke and Bastiaens, 2010)

Figure 2.25.: Fractures observed on the excavation front (Praclay Gallery) at the HADES URF (Van Marcke and Bastiaens, 2010)

This curvature is more pronounced vertically than horizontally due to the anisotropic stresses in the clay, with vertical stress exceeding horizontal stress.

Experimental and field observations offer valuable insights into strain localization, but both approaches face challenges that limit their ability to fully capture the complexities of the EDZ. Laboratory tests often require intact rock samples, which can be difficult to

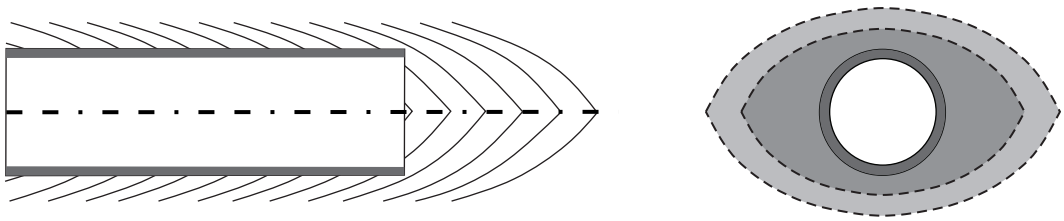

Figure 2.26.: Schematic representation of fracturing pattern modified from Bastiaens et al. (2003)

obtain, especially in weak or fractured rocks. Advanced techniques like stereophotogrammetry, 3D digital image correlation, X-ray microtomography, and scanning electron microscopy (SEM) are employed to visualize strain localization in the laboratory. While these methods provide high-resolution observations of deformation and microstructural changes, they are often constrained by sample size.

Field monitoring, in contrast, lacks access to these advanced imaging tools and typically relies on visual assessments or basic instrumentation. The heterogeneous nature of the rock mass and the inaccessibility of excavation zones further hinder the visualization of the EDZ's spatial extent and development.

To address these limitations and provide a comprehensive understanding across various conditions, computational modeling becomes a crucial tool. Simulating complex scenarios allows for a detailed analysis of strain localization, complementing experimental and field studies while offering predictions for conditions that may be difficult or impossible to replicate physically. The subsequent section will explore the methodologies and applications of computational modeling for strain localization.

2.7. Computational modeling of strain localization

Before discussing the challenges in computational modeling of strain localization with the support of regularization techniques in the subsequent section, it is essential to provide an explanation of the relevant theoretical concepts. These concepts are fundamental in the field of computational modeling, building the foundation for a comprehensive understanding of the challenges and approaches involved. In the context of computational modeling of strain localization, two main theoretical concepts are particularly significant: the bifurcation phenomenon and the Rice criterion.

2.7.1. Bifurcation phenomenon

From a theoretical perspective, strain localization is often conceptualized as a bifurcation phenomenon, indicating loss of a unique solution to a problem. This notion has been explored in studies by Rice (1976) and Chambon and Caillerie (1999). Although, the concept of bifurcation can manifest in various forms (e.g., diffused loss of homogeneity (Vardoulakis, 1981), surface wave (Triantafyllidis, 1980), or shear banding (Rice, 1976)), this study focuses on understanding strain localization in the shear band mode.

In numerical analysis, the conditions leading to the onset of localization are determined by identifying a critical point where the constitutive equations of the material suggest the potential for a bifurcation. At this critical point, the deformation becomes locally concentrated into a shear band. The occurrence of the bifurcation phenomenon in uniaxial compression tests is depicted in Figure 2.27.

Here, the absence of a distinct solution can result in the emergence of shear bands from various potential localized solutions. Upon observing a discontinuity in the material, elastic unloading occurs outside the shear band, while the material within the shear band undergoes plastic loading deformation. The post-peak response, as highlighted in Figure 2.27, is characterized by the degree of softening, represented by the comparison of the shear band thickness H_s to the complete height of the specimen H. Such conditions may introduce strong discontinuities, evident as very thin bands.

It is crucial to distinguish between instability and bifurcation, where the instability implies that minor initial perturbations amplify over time, as postulated by Lyapunov (1992), while bifurcation signifies the absence of a singular solution for a specified boundary problem, as described by Rice (1976) and Sulem (2010). This situation arises at a specific point in the physical process where an alternate solution emerges alongside the primary

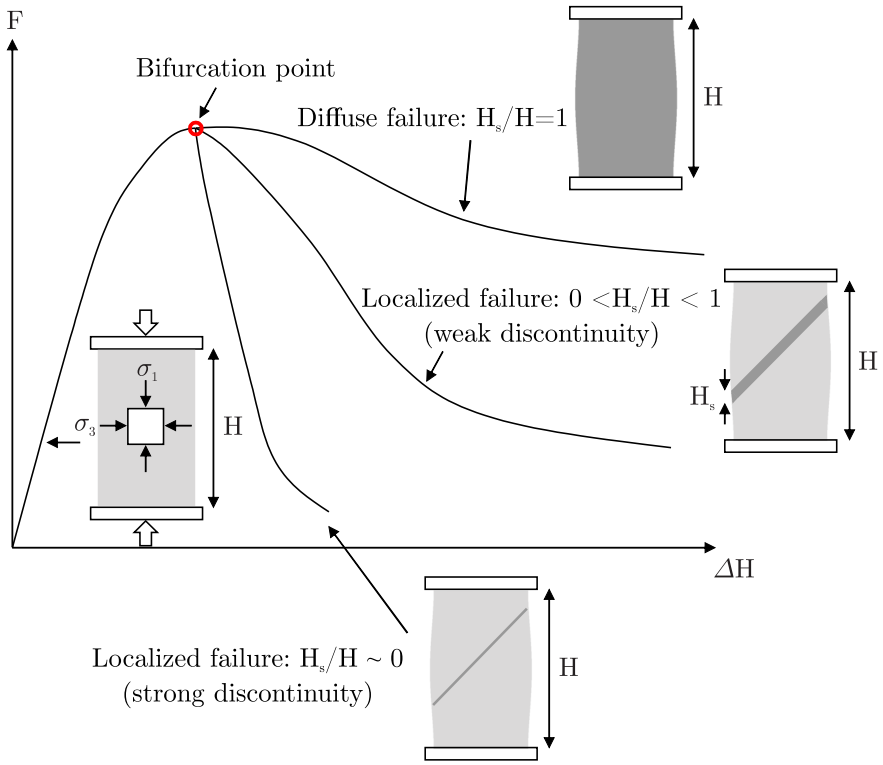

Figure 2.27.: Relationship between shear band thickness and post-peak response in a uniaxial compression test (Thakur, 2007).

solution for subsequent loading phases, leading to an abrupt shift in the deformation mode, such as deformation localized within a planar zone. Essentially, this represents the non-uniqueness of the solution due to the inherent instability in the material.

2.7.2. Rice criterion

Following prior works by Hadamar (1904); Hill (1958); Mandel (1966), a criterion for strain localization, specifically in shear band mode, was introduced by Rudnicki and Rice (1975) and Rice (1976). This theory analyzes conditions under which a system might transit from a homogeneous state of deformation to a localized state within a planar band. Figure 2.28 presents a theoretical scheme illustrating a shear band, distinguishing between variables outside (superscript 0) and inside the shear band (superscript 1). This criterion relies on a kinematical condition, a static condition, and the constitutive equation.

The kinematic condition evaluates the possibility of a non-homogeneous solution within the shear band by ensuring continuity in the velocity field $v_i(x)$ as the band forms.

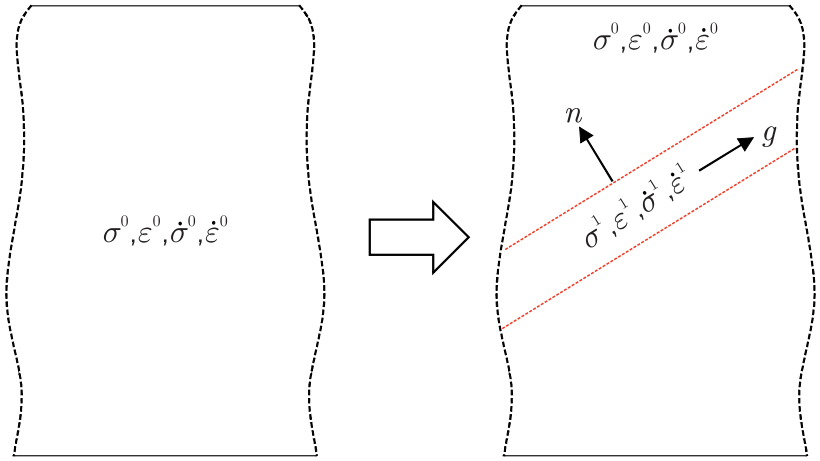

Figure 2.28.: A conceptual representation of the bifurcation within a localized shear band (Salehnia, 2015)

Mathematically, the strain jump across the band interface is represented as:

$$\dot{\varepsilon}^1_{ij} = \dot{\varepsilon}^0_{ij} + \frac{1}{2}(g_i n_j + g_j n_i) \tag{2.25}$$

where, $\dot{\varepsilon}_{ij}$, given by the symmetry of $\frac{\partial v_i}{\partial x_j}$, represents the deformation rate, while the vector g, defined by $g(x_i n_i)$, is arbitrary and oriented based on its direction and magnitude as it transverses the band, and n_i is the normal unit vector to the shear band.

The static condition ensures equilibrium at the band's interface, maintaining consistent stress rates inside and outside the band:

$$n_j(\dot{\sigma}^1_{ij} - \dot{\sigma}^0_{ij}) = 0 \tag{2.26}$$

The constitutive equation relates the stress rate to the strain rate through a constitutive tangent tensor C_{ijkl}. At the onset of bifurcation, the material's state is assumed homogeneous across the band, given by:

$$\dot{\sigma}_{ij} = C_{ijkl}\dot{\varepsilon}_{kl} \tag{2.27}$$

When different constitutive tensors are assumed inside and outside the band (discontinuous bifurcation), combining Equation 2.27 with Equations 2.25 and 2.26, the bifurcation condition is expressed as:

$$C^1_{ijkl}\left(\dot{\varepsilon}^0_{kl} + \frac{1}{2}(g_k n_l + g_l n_k)\right) n_j = C^0_{ijkl}\left(\dot{\varepsilon}^0_{kl}\right) n_j \tag{2.28}$$

The resulting equation system is a third-order system where the unknown is the vector g. The trivial solution, when $g = 0$, is possible, but leads to a uniform deformation without

shear band forming (see diffuse failure in Figure 2.27). For a non-trivial solution $g \neq 0$, the differences between the constitutive tensors inside and outside the band make the solution quite complicated. However, it has been demonstrated that continuous bifurcation, with continuous constitutive tensor along the shear band, always leads to discontinuous bifurcation. Therefore, by assuming continuous bifurcation:

$$C^1_{ijkl} = C^0_{ijkl} = C_{ijkl} \tag{2.29}$$

non-trivial solutions can be found when the determinant of the acoustic tensor is less than or equal to zero (Hill, 1958):

$$\det[n_i \cdot C^1_{ijkl} \cdot n_j] \leq 0 \tag{2.30}$$

The equation's solution determines the direction of the shear band, indicating potential multiple orientations rather than a single predefined direction. Theories regarding shear band orientation vary. Coulomb's criterion (Coulomb, 1773) suggests alignment with the maximum shear stress, corresponding to the maximal obliquity line of the stress vector. This implies the shear band's orientation is $\frac{\pi}{4} \pm \frac{\varphi}{2}$ relative to the principal directions of the total stresses, with φ denoting the friction angle.

However, experiments often demonstrate that shear planes follow zero extension lines, influenced by the dilatancy angle ψ (Desrues, 1984). According to this perspective, the shear band's orientation is $\frac{\pi}{4} \pm \frac{\psi}{2}$ with respect to the principal directions of the strain rate. The debate on whether shear bands follow maximal obliquity or zero extension lines introduces uncertainties in their direction (Pardoen, 2015). It is suggested that shear band orientation may vary between these theories, largely determined by the initial strain localization and tends to remain consistent during propagation. Additionally, this orientation is influenced by the friction and dilatancy angles present at the bifurcation state.

2.7.3. Regularization methods

Strain localization, characterized by discontinuities in strain rate and the emergence of localized shear bands, presents a significant challenge for modeling due to the inherent mesh dependency issues in classical finite element models (Collin et al., 2009). These challenges underscore the necessity for regularization methods that incorporate an internal length scale to effectively represent post-localization behavior without mesh dependency.

Various regularization methods have been proposed in the literature, broadly categorized into two main groups: enrichment of the constitutive law and enrichment of the kinematics.

Enrichment of the constitutive law:

One possibility is to introduce an internal length scale at the level of the constitutive model. The advanced analysis of localization phenomena has shown that constitutive equations with internal length are necessary to properly model the experimental results involving some localized patterns. Two well known groups of models are the non-local models and gradient plasticity.

The non-local approach (e.g., Pijaudier-Cabot and Bažant (1987); Peerlings et al. (2001)) ensures that a material's response at a given location depends not only on its immediate state but also on the states of its surrounding areas. This method employs integral equations over specific domains, introducing a defined material length scale to mitigate mesh dependency. However, it does not directly account for microstructural effects in its formulations.

On the other hand, gradient plasticity models (e.g., Aifantis (1984); De Borst and Mühlhaus (1992); Peerlings et al. (1996)) introduce gradients of internal variables into constitutive equations, providing flexibility by incorporating gradient variables into the yield function or plasticity flow rule. While this approach allows for adaptability to various materials and behaviors, it can be computationally complex and requires careful calibration.

Enrichment of the kinematics:

The previous approaches, which enrich the constitutive law, introduce the effect of microstructure through non-local or gradient terms, yet the microstructure itself remains imprecisely defined. Therefore, the enrichment of classical kinematics with additional descriptions of microstructure kinematics, resulting in a microstructure continuum medium, is another possibility. One of the first and well-known models of this group, is the Cosserat model (Cosserat and Cosserat, 1909), which introduces additional rotational degrees of freedom in addition to the classical continuum displacements. The Cosserat model is particularly relevant for granular media. However, this model may encounter challenges in prescribing microrotation boundary conditions and lacks broader applicability (Toupin, 1962; Mindlin, 1964).

In contrast, the second gradient model (Chambon et al., 1998, 2001), stemming from the works of Toupin (1962), Mindlin (1964) and Germain (1973), offers a detailed view of continuum mechanics by considering both macro- and micro-kinematics. This model

distinguishes between macro-deformation and micro-deformation, providing insights into the individual motion of microstructural elements. Despite introducing computational challenges related to secondary gradients, it excels in achieving a balanced approach between computational feasibility and physical accuracy.

In this research, the local second gradient method is used, as this method maintains local constitutive equations, offering a straightforward formulation of a second gradient extension applicable to most classical constitutive models. Further details on the numerical framework of this specific model are discussed in the subsequent section.

2.7.4. Framework of the coupled local second gradient model

In the subsequent section, the fundamentals of the second gradient model are elaborated. This encompasses the essential balance equations, necessary assumptions, and the microkinematic constitutive equations.

2.7.4.1. Balance equations of the coupled local second gradient model

In a classical continuous medium, a material particle with volume Ω is characterized at the macroscopic scale by its displacement field u_i. The classical kinematic fields are described as the macro-deformation field:

$$F_{ij} = \frac{\partial u_i}{\partial x_j} \tag{2.31}$$

The macro-strain and macro-rotation fields, which are the first gradients of the displacement field, are given by the symmetric and antisymmetric components of F_{ij}, respectively, as:

$$\varepsilon_{ij} = \frac{1}{2}(F_{ij} + F_{ji}) \tag{2.32}$$

$$r_{ij} = \frac{1}{2}(F_{ij} - F_{ji}) \tag{2.33}$$

Toupin (1962) and Mindlin (1964) introduced the concept of materials with microstructure. Within this framework, a macro-volume Ω is made up of several microscale particles Ω^m, represented as micro-volumes Ω^m embedded within the macro-volume Ω, as illustrated in Figure 2.29. The micro-displacement field u_i^m is established independently from the macro-displacement u_i, with its gradient defined as:

$$\upsilon_{ij} = \frac{\partial u_i^m}{\partial x_j} \tag{2.34}$$

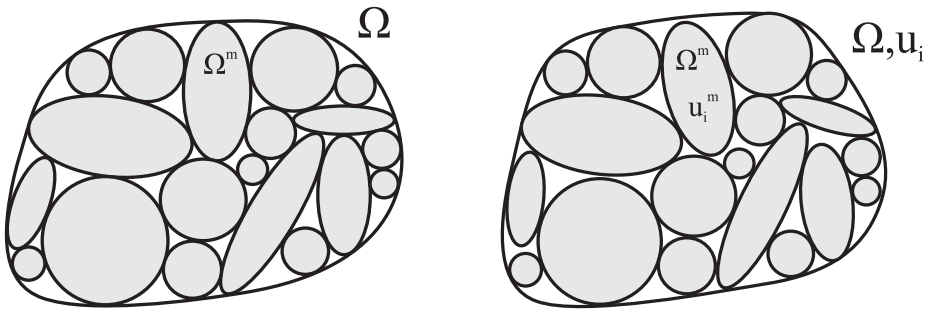

(a) Initial configuration (b) Deformed configuration

Figure 2.29.: Kinematics of microstructure continuum highlighting the microstructure's relative movement

The micro-deformation field is uniform within the micro-volume Ω^m but shows non-homogeneity within the macro-volume Ω. The symmetric and antisymmetric components of υ_{ij} correspond to the micro-strain and the micro-rotation, respectively, as given by the Equations 2.35 and 2.36:

$$\varepsilon_{ij}^m = \frac{1}{2}(\upsilon_{ij} + \upsilon_{ji}) \tag{2.35}$$

$$r_{ij}^m = \frac{1}{2}(\upsilon_{ij} - \upsilon_{ji}) \tag{2.36}$$

Furthermore, the micro second gradients, has been introduced and defined as follows:

$$h_{ijk} = \frac{\partial \upsilon_{ij}}{\partial x_k} = \frac{\partial^2 u_i^m}{\partial x_j \partial x_k} \tag{2.37}$$

The microstructure's relative deformation is expressed by the difference between the macro and micro-deformation fields:

$$\overline{\varepsilon}_{ij} = F_{ij} - \upsilon_{ij} \tag{2.38}$$

Based on the previously explained microstructure effects within an enriched continuum, Chambon et al. (2001) postulated the local second gradient model for monophasic continua. Subsequently, Collin et al. (2006) extended the model from monophasic to biphasic.

With respect to the classical continuum mechanics, additional terms needed to be added in the internal virtual work of a given body Ω (Germain, 1973):

$$W_{\text{int}}^* = \int_\Omega \left(\sigma_{ij} \frac{\partial u_i^*}{\partial x_j} - \tau_{ij} \overline{\varepsilon}_{ij}^* + \Sigma_{ijk} h_{ijk}^* \right) \mathrm{d}\Omega \tag{2.39}$$

Here, σ_{ij} is the Cauchy stress tensor, while the term τ_{ij} is an additional stress linked to the microstructure, often referred to as the microstress. In addition, h_{ijk}^* is the virtual micro second gradient (refer to Equation 2.37). $\overline{\varepsilon}_{ij}^*$ is the virtual relative deformation of

the microstructure (as outlined in Equation 2.38). Lastly, Σ_{ijk} is the double stress, dual of the virtual micro second gradient, which necessitates an additional constitutive law, as elaborated in Section 2.7.4.2.

The external virtual work is defined as:

$$W^*_{\text{ext}} = \int_{\Gamma_\sigma} (\overline{t}_i u^*_i + \overline{T}_i \mathrm{D} u^*_i)\, \mathrm{d}\Gamma \tag{2.40}$$

where $\overline{t}_i$ is the classical external traction force per unit area, while $\overline{T}_i$ represents an additional external double force per unit area. Both are acting on a segment Γ_σ of the boundary of Γ (see Figure 2.30).

One major assumption of the local second gradient model is the absence of relative deformation of the microstructure, $\overline{\varepsilon}_{ij} = 0$, implying equality between the micro- and macrokinematic gradients $F_{ij} = \upsilon_{ij}$ (refer to Equation 2.38). When analyzing the problem using finite element methods, C^{h-1} functions are typically considered within a finite element, with h denoting the highest order of derivation in the virtual work relation. Due to the second derivative of the virtual displacement field in the formulation, C^1 functions need to be used. As the direct integration of C^1 functions poses notable numerical challenges, an alternative approach is employed in the fine element formulation. Therein, C^0 functions along with a field of Lagrange multipliers, symbolized as λ_{ij}, are used (Chambon et al., 1998; Salehnia, 2015).

Consequently, the governing Equations for the local second gradient model are as follows:

$$\int_\Omega \left(\sigma_{ij} \frac{\partial u^*_i}{\partial x_j} + \Sigma_{ijk} \frac{\partial \upsilon^*_{ij}}{\partial x_k} - \lambda_{ij} \left(\frac{\partial u^*_i}{\partial x_j} - \upsilon^*_{ij} \right) \right) \mathrm{d}\Omega = \int_{\Gamma_\sigma} (\overline{t}_i u^*_i + \overline{T}_i \upsilon^*_{ik} u_{\perp,k})\, \mathrm{d}\Gamma \tag{2.41}$$

$$\int_\Omega \lambda^*_{ij} \left(\frac{\partial u_i}{\partial x_j} - \upsilon_{ij} \right) \mathrm{d}\Omega = 0 \tag{2.42}$$

In the context of coupled hydro-mechanical analyses, the local second gradient model incorporates the mass balance of the fluid (water) phase, as detailed in Equation 2.43, for every kinematically admissible virtual pore water pressure field p^*_{w} (Collin et al., 2006). The assumption made here is that the fluid has no effect on the microstructure, which implies that there is no relationship between the double stress Σ_{ijk} and the pore water pressure p_{w}.

$$\int_\Omega \left(\dot{M}_{\text{w}} p^*_{\text{w}} - m_{\text{w},i} \frac{\partial p^*_{\text{w}}}{\partial x_i} \right) \mathrm{d}\Omega = \int_\Omega Q_{\text{w}} p^*_{\text{w}}\, \mathrm{d}\Omega - \int_{\Gamma_q} \overline{q}_{\text{w}} p^*_{\text{w}}\, \mathrm{d}\Gamma \tag{2.43}$$

In Equation 2.43, $m_{\text{w},i}$ represents the water mass flow, $\dot{M}_{\text{w}}$ denotes the change in water mass, Q_{w} acts as a sink term, and Γ_q specifies the boundary segment where the input water mass per unit area $\overline{q}_{\text{w}}$ is prescribed (refer to Figure 2.30).

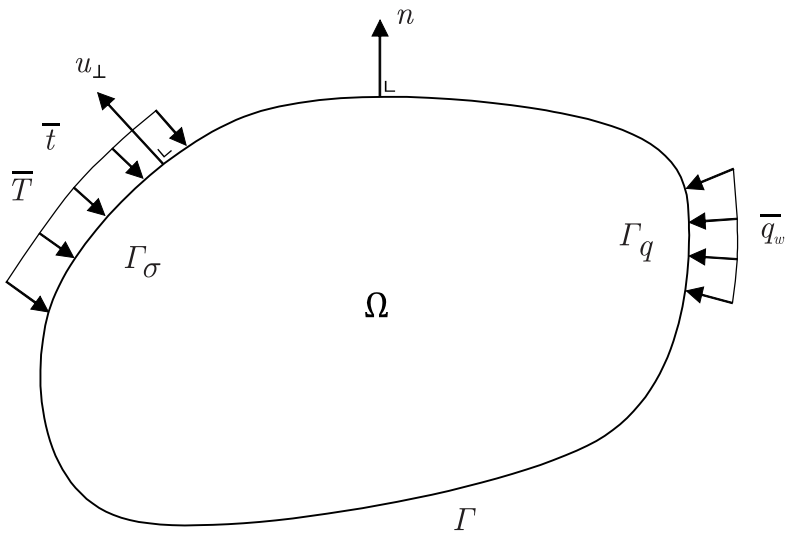

Figure 2.30.: Boundary conditions and the current configuration of the material for the second gradient model

Using Darcy's law, the water mass flow is defined as:

$$m_{\mathrm{w},i} = -\rho_{\mathrm{w}} \frac{k_{w,ij} k_{\mathrm{r,w}}}{\mu_{\mathrm{w}}} \frac{\partial p_{\mathrm{w}}}{\partial x_j} \tag{2.44}$$

where ρ_{w} represents the water density, $k_{w,ij}$ is the intrinsic hydraulic permeability tensor, $k_{\mathrm{r,w}}$ signifies the relative water permeability that varies based on the water's degree of saturation, and μ_{w} stands for the water dynamic viscosity. The water mass M_{w} is defined as:

$$M_{\mathrm{w}} = \rho_{\mathrm{w}} n S_{\mathrm{r,w}} \Omega \tag{2.45}$$

where $S_{\mathrm{r,w}}$ is the degree of saturation of water and n is the material porosity.

2.7.4.2. Second gradient constitutive equation

As mentioned in the previous section, a constitutive law is required to describe the relationship between the double stress and the microkinematics. This relationship is considered to be independent of both the conventional constitutive model of the macro scale (first gradient model) and the pore water pressure. Due to the limited information about the relationship between double stress and micro-deformation and the complexity of gathering this information at microstructure level, a linear elastic mechanical law has been selected in the local second gradient model for its inherent simplicity. It is based on an isotropic linear relationship proposed by Mindlin (1964):

$$\tilde{\Sigma}_{ijk} = D_{ijklmn} \frac{\partial \dot{v}_{lm}}{\partial x_n} \tag{2.46}$$

In consequence of the unclear physical interpretation of the material parameters within D_{ijklmn}, a more straightforward approach with only one parameter D was suggested by Matsushima et al. (2002). Expressed for two-dimensional problems, the linear elastic mechanical law introduced by Matsushima et al. (2002) can be written as:

$$\begin{bmatrix} \tilde{\Sigma}_{111} \\ \tilde{\Sigma}_{112} \\ \tilde{\Sigma}_{121} \\ \tilde{\Sigma}_{122} \\ \tilde{\Sigma}_{211} \\ \tilde{\Sigma}_{212} \\ \tilde{\Sigma}_{221} \\ \tilde{\Sigma}_{222} \end{bmatrix} = D \begin{bmatrix} 1 & 0 & 0 & 0 & 0 & \frac{1}{2} & \frac{1}{2} & 0 \\ 0 & \frac{1}{2} & \frac{1}{2} & 0 & -\frac{1}{2} & 0 & 0 & \frac{1}{2} \\ 0 & \frac{1}{2} & \frac{1}{2} & 0 & -\frac{1}{2} & 0 & 0 & \frac{1}{2} \\ 0 & 0 & 0 & 1 & 0 & -\frac{1}{2} & -\frac{1}{2} & 0 \\ 0 & -\frac{1}{2} & -\frac{1}{2} & 0 & 1 & 0 & 0 & 0 \\ \frac{1}{2} & 0 & 0 & -\frac{1}{2} & 0 & \frac{1}{2} & \frac{1}{2} & 0 \\ \frac{1}{2} & 0 & 0 & -\frac{1}{2} & 0 & \frac{1}{2} & \frac{1}{2} & 0 \\ 0 & \frac{1}{2} & \frac{1}{2} & 0 & 0 & 0 & 0 & 1 \end{bmatrix} \begin{bmatrix} \frac{\partial \dot{v}_{11}}{\partial x_1} \\ \frac{\partial \dot{v}_{11}}{\partial x_2} \\ \frac{\partial \dot{v}_{12}}{\partial x_1} \\ \frac{\partial \dot{v}_{12}}{\partial x_2} \\ \frac{\partial \dot{v}_{21}}{\partial x_1} \\ \frac{\partial \dot{v}_{21}}{\partial x_2} \\ \frac{\partial \dot{v}_{22}}{\partial x_1} \\ \frac{\partial \dot{v}_{22}}{\partial x_2} \end{bmatrix} \tag{2.47}$$

The constitutive elastic modulus D in Equation 2.47 represents the physical microstructure and the internal length scale that defines the shear band width (Kotronis et al., 2007).

2.8. Intrinsic hydraulic permeability evolution

As already highlighted in Section 2.4, the EDZ is a zone with increased permeability due to the occurrence of fractures. This is from special interest when dealing with swelling clay shales, as the water transfer due to the elevated hydraulic permeability in the EDZ might trigger the swelling process within the clay shale formation. The amount of the swelling is a crucial design parameter for the choice of the tunnel support system.

Therefore, in this section several possible methods to model that hypothetical permeability increase within the EDZ are discussed. Although the discrete modeling of the fracture flow allows in theory a good representation of the in situ behavior, only continuous approaches are discussed in the following, to be in line with the chosen EDZ modeling approach. Furthermore, since no damage model is applied in this study, the possibilities of linking the permeability evolution to the damage parameter (e.g., Levasseur et al. (2013)) have not been set in focus of this work.

A well-known and frequently used approach is the Kozeny-Carman relationship (Kozeny, 1927; Carman, 1997), which links the intrinsic hydraulic permeability $k_{w,ij}$ to the porosity ϕ given by:

$$k_{w,ij} = k_{w,ij,0} \frac{(1-\phi_0)^2}{\phi_0^3} \frac{\phi^3}{(1-\phi)^2} \tag{2.48}$$

where $k_{w,ij,0}$ represents the initial intrinsic water permeability, while ϕ_0 and ϕ denote the initial and current porosity, respectively. According to Chapuis and Aubertin (2003) this relationship is approximately valid for sands, but not for clay materials. Furthermore, using a porosity dependent relationship as the Kozeny-Carman relationship, a permeability increase is only possible for material with pronounced dilative behavior, which has to be considered for the choice of the permeability evolution approach.

Another commonly used approach is the cubic law. By assuming that the flow within a single crack is equivalent to a laminar flow between to two parallel plates, using Darcy's law, the permeability parallel to the fracture plane can be estimated as (Levasseur et al., 2010):

$$k = \frac{b^2}{12} \tag{2.49}$$

where b is the hydraulic aperture or in other words, the crack width.

Following the above equation, the permeability of a medium with a set of parallel fractures can be represented by a cubic law (Levasseur et al., 2010; Snow, 1969; Liu et al., 1999; Wittke, 2014; Witherspoon et al., 1980):

$$k_m = \frac{b^3}{12B} \tag{2.50}$$

where B is the spacing between each single crack.

According to Wittke (2014) the mean aperture cannot be determined with available laboratory testing protocols and must be therefore estimated, which results in a high uncertainty. Furthermore, Wittke (2014) demonstrates that using the cubic law (Equation 2.50) but changing the mean aperture from 0.2 mm to 1 mm the resulting permeability will vary from a permeability being typical for a fine sand (B=0.2 mm) to a value being representative of gravel (B=1 mm).

Another limiting factor of this simple cubic model is, that it can not consider rough walls or variable apertures, therefore the use of this model is not appropriate (Levasseur et al., 2010). However, it serves as a basis for more sophisticated models which include the stress state (e.g., normal or shear stress (Wittke, 2014; Levasseur et al., 2010; Pardoen, Levasseur and Collin, 2015)).

When considering tensile fractures (see Mode I in Figure 2.19) as the dominant failure mechanism, a volumetric strain-dependent permeability evolution can be considered.

Therefore the following relationship, based on a cubic law is considered:

$$k_{w,ij} = k_{w,ij,0}\,(1 + \beta_{per}\,\varepsilon_v^{p3}) \tag{2.51}$$

where ε_v^p is the plastic volumetric strain and β_{per} controls the permeability increase, similar to Equation 2.52.

Considering the fact that the EDZ is modeled using shear strain localization, and that one of two dominating failure mechanisms in the EDZ is shearing (see Section 2.4), a shear strain depended permeability evolution can be taken into account. According to Pardoen, Seyedi and Collin (2015), this can be formulated as:

$$k_{w,ij} = k_{w,ij,0} \left(1 + \beta_{per} \langle YI - YI^{thr} \rangle \hat{\varepsilon}_{eq}^3\right) \tag{2.52}$$

In the above equation, $\hat{\varepsilon}_{eq}$ represents the Von Mises' equivalent deviatoric total strain, β_{per} is a model parameter which controls the amount of permeability increase, YI is the yield index, YI^{thr} is the threshold yield index, and $\langle \cdot \rangle$ denotes the Macaulay brackets. The Yield Index indicates whether the material is in an elastic state ($YI < 1$) or has entered a plastic state ($YI = 1$). It should be noted that the formulation of the Yield Index depends on the corresponding yield surface of the employed material model. According to Pardoen, Seyedi and Collin (2015) the consideration of only the plastic zone will underestimate the permeability whereas considering both elastic and plastic zone will overestimate the permeability evolution. Therefore, Pardoen, Seyedi and Collin (2015) included the yield index YI, as well as a threshold value YI^{thr} below which changes in intrinsic permeability are not taken into account.

In the end, the choice of the permeability evolution strongly depends not only on the material behavior but also on the mechanism of shear band formation and the geometrical extension of the shear band within the domain. It must be selected in accordance with in situ observations and validated by comparing to numerical results. Therefore, it is strongly recommended to investigate the different permeability evolution approaches in a numerical model with clear boundary conditions (e.g. a biaxial compression test), which is further elaborated in Section 4.2.

3. Determination of material parameters

3.1. Introduction

After discussing the fundamentals of this research in the previous section, the focus now shifts to the actual material under investigation: Opalinus clay. Opalinus clay is considered a candidate for nuclear waste disposal host rock in Switzerland, consequently extensive research to characterize its mechanical and hydraulic properties has been done, allowing the direct derivation of constitutive model parameters from the existing literature.

However, due to the presence of inhomogeneities such as microfossils and pyrite, which significantly influence the reproduction of swelling tests, the limited sample size of intact Opalinus clay compared to the size of these inhomogeneities poses significant challenges. To mitigate this issue, reconstituted Opalinus powder is investigated by Christ et al. (2025), eliminating the influence of anisotropy, structure, and inhomogeneities, allowing for a more in-depth analysis of resulting swelling compared to intact material.

This chapter is structured as follows. Section 3.2 begins with a literature review to derive both mechanical and hydraulic constitutive parameters for intact Opalinus clay. Following this, Section 3.3.1 details the derivation and calibration of mechanical constitutive parameters for remolded Opalinus clay, based on an analysis of various oedometer tests and a series of triaxial tests. Section 3.3.2 then focuses on the determination of hydraulic parameters, utilizing soil water characteristic curves and permeability tests.

With these parameters established, Section 3.4 presents the numerical modeling of swelling tests for both intact and remolded Opalinus clay under various boundary conditions. This modeling facilitates the determination of suction-dependent model parameters and by comparing with laboratory results enables the validation of the model.

Finally, Section 3.5 introduces a biaxial test on remolded Opalinus clay, which is subsequently modeled to illustrate the impact and importance of shear strain localization. This section also demonstrates that the chosen constitutive model effectively captures this critical behavior.

3.2. Hydro-mechanical properties of intact Opalinus clay

As previously mentioned, Opalinus clay serves as a potential host rock for nuclear waste disposal in Switzerland. To ensure safe disposal over thousands of years, extensive testing and research have been conducted at the Mont Terri underground rock laboratory (URL), depicted in Figure 3.1.

Opalinus clay shale, a fine-grained sedimentary rock, was deposited around 180 million years ago. The overburden at the Mont Terri URL varies from 230 to 330 meters, but during the late Tertiary period, it is believed to have reached up to 1350 meters. These depth variations suggest that Opalinus clay may have experienced diverse stress conditions and diagenetic processes over its burial period. Consequently, its mechanical characteristics may differ between shallower and deeper depths (Giger et al., 2015; Favero et al., 2016). This research focuses primarily on shallow Opalinus clay, specifically the shaly facies from the Mont Terri URL at a depth of approximately 300 meters, which aligns with conditions in the New Belchen tunnel project used as the basis for the tunnel simulations described later (Bossart and Thury, 2008; Ziegler et al., 2022).

The determination of constitutive parameters for Opalinus clay has relied on a comprehensive review of existing literature. This review included Mont Terri Technical Reports,

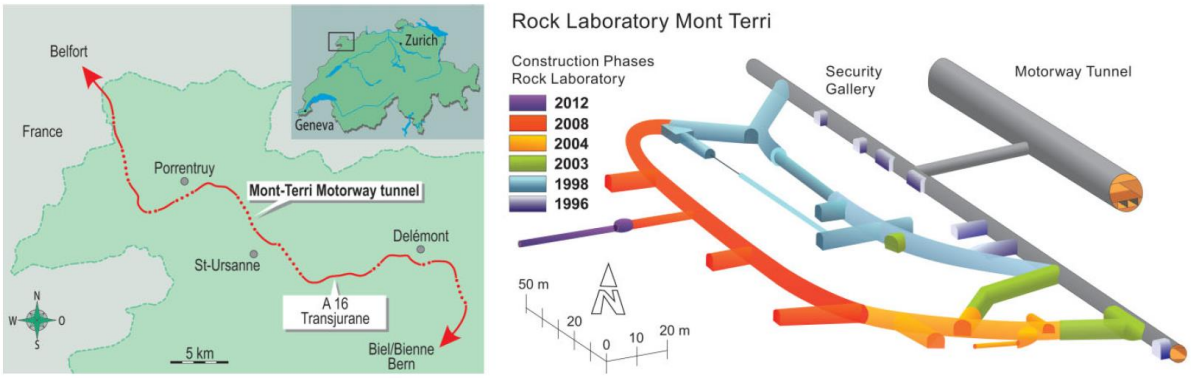

Figure 3.1.: Location and design of the URL at Mont Terri (Giger et al., 2015)

the GRS report by the Society for Plant and Reactor Safety (Gesellschaft für Anlagen- und Reaktorsicherheit) (Zhang et al., 2004), and various research articles.

The range of constitutive parameters for Opalinus clay has been established through various methods, including laboratory tests and field tests. Table 3.1 summarizes the range for these parameters. Due to the complexity of the experimental methodologies involved, a detailed discussion is outside the scope of this research. Interested readers are encouraged to explore the references listed in Table 3.1 for further insights into these methodologies.

Given the limited availability of suction-dependent laboratory tests, the calibration of the suction-dependent parameters of the Barcelona Basic Model relies on data from laboratory tests conducted at Ruhr University Bochum (RUB), which will be presented in Section 3.4.

Table 3.1.: Overview of constitutive parameter ranges for Opalinus clay from literature review

Property	Unit	Range	Method	Reference
Initial porosity (ϕ_0)	-	0.13 - 0.18	ISRM (1981)	(Bock, 2001, 2009; Bossart and Thury, 2011)
Grain density (ρ_s)	kg/m^3	2670 - 2720	ISRM (1981)	(Bock, 2001, 2009; Bossart and Thury, 2011)
Swelling index (κ)	-	0.004 - 0.011	Oedometer test	(Favero et al., 2016; Crisci et al., 2019)
Poisson's ratio (ν)	-	$\nu_{//} = 0.16$ - 0.34 $\nu_{\perp} = 0.30$ - 0.39	Uniaxial test	(Bock, 2001, 2009; Bossart and Thury, 2011)
Cohesion (saturated state) (c_0)	MPa	$c = 2.0$ - 4 ($\sigma_3 < 5$ MPa) $c = 4.5$ - 6 ($\sigma_3 > 5$ MPa)	Triaxial test Direct shear test	(Bock, 2001, 2009; Bossart and Thury, 2011)
Friction angle (φ)	degree	$\varphi = 25$ - 35 ($\sigma_3 < 5$ MPa) $\varphi = 18$ - 22 ($\sigma_3 > 5$ MPa)	Triaxial test Direct shear test	(Bock, 2001, 2009; Bossart and Thury, 2011)
Compression index (λ)	-	0.008 - 0.022	Oedometer test	(Favero et al., 2016; Crisci et al., 2019)
Preconsolidation pressure (p_0^*)	MPa	12 - 20	Oedometer test	(Zhang et al., 2004; Crisci et al., 2019)
Initial intrinsic permeability (k_0)	m^2	$k_{//} =$ 1E-19 - 1E-18 $k_{\perp} =$ 1E-21 - 1E-20	Borehole test Constant-head test	(Bock, 2001, 2009; Bossart et al., 2002)
Van Genuchten parameter (α)	MPa^{-1}	0.0190	Vapor equilibrium technique	(Christ and Lavasan, 2024)
Van Genuchten parameter (n)	-	2.132	Vapor equilibrium technique	(Christ and Lavasan, 2024)
Van Genuchten parameter (m)	-	0.452	Vapor equilibrium technique	(Christ and Lavasan, 2024)

// Parallel to bedding direction, $\perp$ Perpendicular to bedding direction

3.3. Parameter calibration of remolded Opalinus clay

In contrast to intact Opalinus clay shale, which has been extensively studied in the literature, laboratory testing on remolded Opalinus clay powder is very limited. Therefore, several laboratory tests (e.g., oedometer and triaxial tests) were conducted on remolded Opalinus powder at RUB to determine its hydro-mechanical properties.

In the following section, the mechanical and hydraulic constitutive parameters for remolded Opalinus clay are calibrated using these laboratory tests.

3.3.1. Mechanical parameters of remolded Opalinus clay

For the calibration of mechanical parameters for remolded Opalinus clay, oedometer and triaxial tests are performed. The oedometer tests provide insights into soil compressibility, while the triaxial tests determine the soil shear strength, both of which are crucial for accurately characterizing the soil and for calibrating the Barcelona Basic Model (BBM), already introduced in Section 2.2.3.2.

Oedometer tests

Oedometer tests are essential for determining the compressibility of remolded Opalinus clay, providing insights into its elastic and plastic behavior and enabling the calibration of the swell index κ, the compression index λ, and the preconsolidation pressure p_0. The parameters are calibrated using oedometer tests on remolded Opalinus powder conducted by Christ et al. (2025).

A high-pressure oedometer was utilized for these tests, as described in detail in Baille et al. (2010). Prior to commencing a test, the initially dry compacted sample ($\rho_d = 2.0\,\mathrm{g/cm^3}$, $w = 3.17\%$, $h = 2\,\mathrm{cm}$, $d = 5\,\mathrm{cm}$, compaction pressure $P_{comp} = 20\,\mathrm{MPa}$) was installed in the oedometer device. The dry density $\rho_d = 2.0\,\mathrm{g/cm^3}$ was chosen to match the inital dry density of the intact samples. It should be noted that preparing samples with higher densities was not feasible with the available equipment. A total of three oedometer tests were carried out: one in the unsaturated state with an initial suction $s_{init} = 68\,\mathrm{MPa}$, which corresponds to the initial water content of the remolded material according to the soil water characteristic curve (SWCC) and another where the sample was saturated with deionized (DI) water under constant volume conditions until the swelling process was complete. And lastly, one oedometer test where the sample was allowed to swell under a small load of around 10 kPa until the swelling process was complete, subsequently denoted

as free swollen sample. All three samples were loaded stepwise up to 24.95 MPa, followed by stepwise unloading and reloading.

For all three oedometer tests, the results are presented as void ratio e versus vertical stress σ_v, as shown in Figures 3.2 to 3.4.

Beginning with the oedometer test on the constant volume swollen sample, the initial void ratio e upon installation is 0.338, according to Christ et al. (2025). The first pressure increase up to around 1.17 MPa without a change in void ratio e is due to the saturation of the sample, thus hydro-mechanical swelling under constant volume conditions.

Before conducting a finite element test, the initial values of the compression index λ and swell index κ are estimated based on the slope of the corresponding path on the $\sigma_v - e$ diagram. For the initial value of the preconsolidation pressure p_0, the Casagrande method (Casagrande, 1936) is used. Assuming a true constant volume condition $\Delta\varepsilon_v = 0$ and solely elastic swelling pressure buildup, the slope of the reversible wetting-drying line κ_s can be analytically calculated as:

$$\kappa_s = \kappa \cdot \frac{ln(p_\mathrm{B}) - ln(p_\mathrm{A})}{ln\left(s_\mathrm{A} + p_a\right) - ln\left(s_\mathrm{B} + p_a\right)} \tag{3.1}$$

where index A represents the initial time and B the final time, respectively. Here, p denotes the net mean stress and s denotes the suction. For further details and the derivation, please refer to Appendix A.

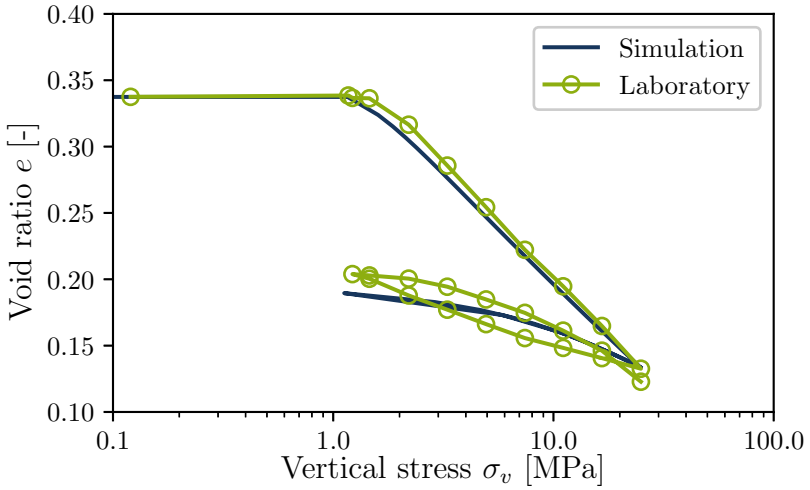

Figure 3.2.: Void ratio as a function of vertical stress of constant volume swollen oedometer test

In the BBM, the swell index κ, the compression index λ, and the preconsolidation pressure p_0 are defined in terms of the net mean stress p (see Section 2.2.3.2), rather than of the vertical stress σ_v measured during laboratory testing. As the horizontal stress during the test was not measured, and therefore p is not known from the laboratory, a parameter calibration is mandatory. Therefore, the initial estimated parameter values were manually varied until the best possible agreement between simulation and experiment was achieved. It should be noted that the initial parameter estimation and subsequent parameter calibration were performed separately for each oedometer test considered here.

The parameter calibration is conducted using a numerical element test, starting with the previously determined values for the swell index κ, the compression index λ, the preconsolidation pressure p_0 and the slope of the reversible wetting-drying line κ_s as the initial values. In the finite element model, only a single element was modeled, with the top nodes of the element fixed in vertical direction $u_y = 0$. For the modeling of the laboratory tests, the coupled finite element MWAT 2D (Collin, 2003) ia used. This element is an isoparametric element with eight nodes and four integration points. Each node possesses five degrees of freedom namely spatial coordinates, water pressure, gas pressure and temperature. As the temporal evolution of the void ratio e during swelling was not recorded, the initial suction of 68 MPa is linearly reduced until zero by controlling the pore water pressure p_w in all nodes in order to simulate the constant volume swelling process. Once the sample reached full saturation $s = 0$, the fixity on top of the element is released and replaced with a load condition, with an initial value equal to the swelling pressure. Throughout loading, the pore water pressure buildup is constrained to $\Delta p_w = 0$ to enforce drained behavior of the sample.

As previously stated, the horizontal stress σ_h during the test is unknown. Therefore, an assumption of the ratio of the horizontal and vertical stress, K_0, and an assumption of the Poisson's ratio ν are required. To align with the subsequent triaxial and the later described biaxial tests (see Section 3.5), the same Poisson's ratio $\nu = 0.17$, which could be derived directly from the triaxial and biaxial test data, is used here. The determination of the Poisson's ratio from the laboratory test data is elaborated in the corresponding section.

Looking at the resulting evolution of void ratio e with vertical stress σ_v, it becomes evident that the first two load steps after the sample is fully saturated result in only a small change in the void ratio. This suggests that the initial preconsolidation pressure p_0, arising from the compaction of the sample, is largely dissipated during the swelling

process. Consequently, the actual preconsolidation pressure p_0 should correspond to the resulting swelling pressure.

The comparison between laboratory results and the finite element simulation, shown in Figure 3.2, demonstrates a good agreement between the simulated and experimental outcomes. The normal consolidation line (NCL) was well represented using the Barcelona Basic Model (BBM). The unloading-reloading path from 24.95 MPa to 1.2 MPa in the experiments exhibits a steeper inclination in the $\sigma_v - e$ diagram compared to the inclination observed during the initial elastic loading from 1.2 MPa to 1.4 MPa, as illustrated in Figure 3.2. This stress-dependent variation in elastic stiffness cannot be accurately simulated using the BBM, which employs a constant swell index κ. Consequently, the hysteresis observed during unloading and reloading cannot be captured by this model.

To study the effect of the boundary conditions during swelling (e.g., free or constant volume) on the mechanical behavior of Opalinus clay, a second oedometer test was performed, where the sample was allowed to deform during the swelling. The outcome of this test also shows how much of the initial preconsolidation pressure p_0 due to sample compaction is degraded during swelling.

A sample with identical initial conditions was prepared for the test and installed in the oedometer. Unlike the previous test, the loading piston remained unfixed on the sample during hydration, resulting in a small constant vertical load of around 10 kPa, to allow the measurement of the vertical deformation after full saturation. After the sample was fully saturated $s = 0$, the load piston was attached to the load frame and the sample was gradually loaded up to the same maximum load of 24.95 MPa, as in the constant volume swollen oedometer test. In addition to the unloading and reloading at 24.95 MPa, a short unloading and reloading was applied at a load of 1.12 MPa. This has been done to estimate the swell index κ for smaller vertical loads, e.g., in the range of the equilibrium swelling pressure for constant volume conditions.

During the hydration process, the void ratio e of the sample increased from an initial value of 0.348 to 0.583 after swelling, as illustrated in Figure 3.3. In the first loading step, from a dead load of 10 kPa to 100 kPa, the void ratio e shows minimal change, suggesting that the sample remains within the elastic region. As the load increases to approximately 300 kPa, the sample transitions from the elastic to the plastic region, indicated by a straight line on the semi-logarithmic scale of the $\sigma_v - e$ diagram in the range from 300 kPa to about 5 MPa vertical load. This suggests that the preconsolidation pressure p_0 lies within this range. From 5 MPa to 11 MPa, a kink is observed in the $\sigma_v - e$ diagram, labeled as '1. kink' in Figure 3.3. A second kink, marked as '2. kink' in the same figure, appears between

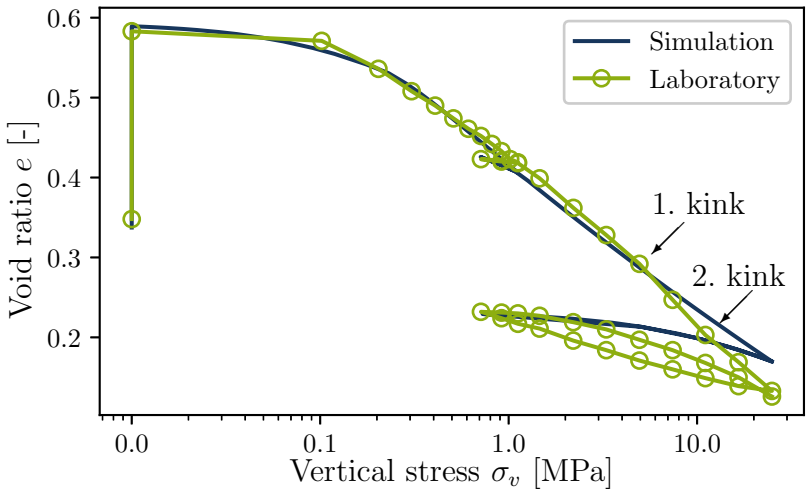

Figure 3.3.: Void ratio as a function of vertical stress of free swollen oedometer test

11 MPa and 24.95 MPa. Notably, after the second kink, the final load increment exhibits the same slope as observed in the range from 300 kPa to approximately 5 MPa, suggesting that both kinks together might represent a parallel shift in the stress-strain relationship.

This kink or parallel shift can be explained by two conclusive theories. The first theory suggests that a slight misalignment of the loading piston may have caused friction between the load piston and the oedometer ring, which was overcome in this specific stress region. However, no direct observations were made during the test to support this theory. The second theory posits that the particles within the sample's microstructure experienced reorientation, leading to the observed kink. This theory is supported by SEM investigations on free swollen and constant volume swollen Opalinus samples conducted by Christ (2025), which indicated different particle orientations after swelling. Assuming that, with increasing pressure, the particles will reorient similarly, this might explain the parallel shift. However, no SEM investigations were conducted after both tests to confirm this. Consequently, the extent to which this behavior is due to metrological or material factors cannot be conclusively determined. Regardless, the material model used, the Barcelona Basic Model (BBM), cannot replicate this kink, so the origin of the kink can be disregarded in the context of this thesis.

In contrast to constant volume swelling, the derivation of κ_s for free swelling under oedometric boundary conditions is not analytically feasible. This is because, although the vertical load σ_v is constant during the hydration, the net mean stress p is not constant due to the oedometric boundary conditions.

Therefore, the resulting swelling strain is affected not only by the slope of the reversible wetting-drying line κ_s, but also by the swell index κ. As already mentioned, the parallel shift as a consequence of either microstructure evolution or technical reasons can not be modeled using BBM, therefore a straight line in semi-logarithmic $\sigma_v - e$ diagram is assumed. The swell index κ and the slope of the reversible wetting-drying line κ_s are calibrated using a numerical element test. As in the previous calibration, initial values for the swell index κ, the compression index λ, the preconsolidation pressure p_0 and the slope of reversible wetting-drying line κ_s are determined using the $\sigma_v - e$ diagram.

By comparing the laboratory results and finite element simulations, illustrated in Figure 3.3, an almost perfect fit until a vertical load $\sigma_v = 5\,\text{MPa}$ could be achieved. The parallel shift although could not be simulated, as previously explained. All in all a satisfactory fit is achieved.

When comparing the two oedometer tests on the swollen Opalinus powder, several conclusions can be drawn. The swell index κ, for both the low-stress region (1 MPa) and the high-stress region (24 MPa), as well as the compression index λ, exhibit similar magnitudes in both tests, see Table 3.2. The observed difference in preconsolidation pressure p_0 can be attributed to the fact that, during constant volume swelling, the preconsolidation pressure is influenced by the resulting swelling pressure. Due to the kink or parallel shift in the oedometer test on the free-swollen material, the same final void ratio of $e = 0.13$ was reached in both tests. The difference in the slope of the reversible wetting-drying line κ_s can be explained by the modeling of truly constant volume boundary conditions, which are difficult to achieve in laboratory settings due to the necessity for the load cell to deform slightly in order to measure force. The significance of small deformations and their impact on the resulting swelling stress will be further explored in the modeling of the swelling tests in Section 3.4.

In addition to the two saturated oedometer tests, an oedometer test was conducted on dry compacted powder. The test procedure was identical to the previous tests, but without an initial swelling phase. Figure 3.4 presents the $\sigma_v - e$ diagram, indicating stiffer mechanical behavior compared to the saturated tests. Determining the preconsolidation pressure p_0, swell index κ, and compression index λ is challenging due to the difficulty in distinguishing the virgin loading and reloading paths clearly. Considering that the vertical compaction pressure during sample preparation was already $P_{\text{comp}} = 20\,\text{MPa}$, it can be assumed that only the final loading steps represent virgin loading. Additionally, the $\sigma_v - e$ relationship appears nearly linear in a non-logarithmic diagram, suggesting linear elasticity, whereas

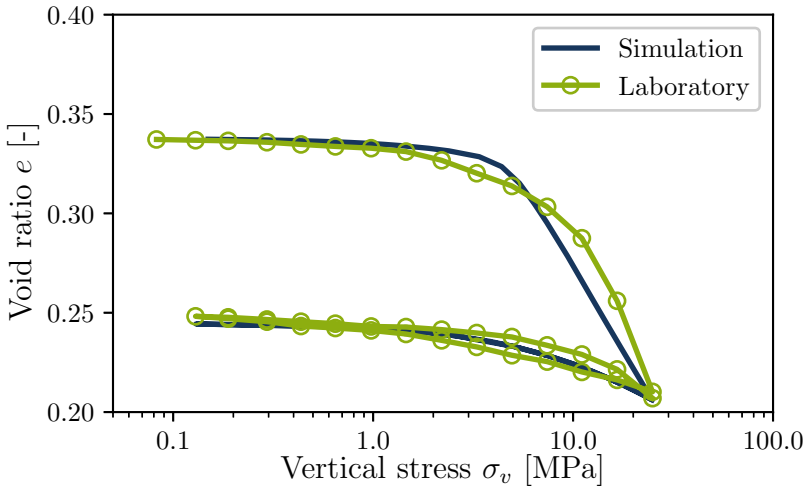

Figure 3.4.: Unsaturated oedometer test results in terms of void ratio as a function of vertical stress

the saturated tests exhibited linear behavior in semi-logarithmic diagram, indicating a non-linear elasticity.

To accommodate linear elasticity in the BBM, a minimum stress $p_{\min}$ can be defined beyond which the soil exhibits stress-independent stiffness.

The bulk modulus can then be expressed as:

$$K = \frac{1+e}{\kappa} \cdot p \quad \text{with} \quad p \geq p_{\min} \tag{3.2}$$

where $p \geq p_{\min}$ ensures linear elastic behavior until the stress exceeds $p_{\min}$.

For the finite element simulation, the same element test setup is employed as for the saturated oedometer tests. Despite the sample being unsaturated during the test, it is modeled as fully saturated. This simplification is adopted because the parameters dependent on suction are currently unknown, and furthermore, changes in suction are not expected during the test.

With this simplification and the assumption of a linear elastic zone ($p_{\min} = 7\,\text{MPa}$), the constitutive parameters for the dry Opalinus powder are calibrated. The results of the numerical simulation are compared with the laboratory results in Figure 3.4. Especially in the transition between the linear elastic zone and the plastic zone, fitting simulation and laboratory results is challenging. However, the overall agreement with the laboratory results is satisfactory.

The results of the parameter calibration for all three oedometer tests are summarized in Table 3.2. While the compression index λ and the swell index κ for constant volume

Table 3.2.: Summary of parameter calibration results for oedometer tests on remolded Opalinus clay powder

Parameter	Unit	Constant volume	Free swelling	Unsaturated
Compression index (λ)	-	0.079	0.079	0.080
Swell index (κ)	-	0.068	0.068	0.040
Preconsolidation Pressure (p_0)	MPa	1.2	0.1	5
Reversible wetting-drying (κ_s)	-	0.020	0.055	-

and free swelling conditions are the same, different preconsolidation pressures p_0 and κ_s values were found. These differences are caused by the variation in boundary conditions during saturation, as already explained. The unsaturated case, on the other hand, results in completely different values due to the increased mechanical stiffness caused by the suction.

Triaxial tests

The next section focuses on the calibration of shear strength parameters, specifically the friction angle φ and cohesion c, using triaxial tests. These tests are crucial for accurately characterizing the mechanical behavior of remolded Opalinus clay under various stress conditions.

A series of three drained triaxial tests was performed on compacted and saturated Opalinus clay powder to determine the friction angle φ and the cohesion c for the numerical model. Initially, the samples were compacted from both sides. The target dry density was set at $2.0\,\mathrm{g/cm^3}$, with sample dimensions of $d = 3.5\,\mathrm{cm}$ and $h = 7\,\mathrm{cm}$. The samples were then placed in the triaxial testing apparatus, where a support pressure of 0.3 bar and a backpressure of 0.2 bar was applied for the saturation process. After saturation, the support pressure was increased from 0.3 bar to 3 bar and the back pressure from 0.2 bar to 3 bar. After a successful B-test, which verifies the saturation of the sample, the samples were consolidated under the final effective confinement pressure σ_3'. For the test series, σ_3' values of 100, 300, and 500 kPa were selected. The axial deformations were recorded throughout the whole test whereas the volumetric deformations were recorded only during consolidation and shearing phases. The shear rate of 0.003 mm/min was used in the tests to prevent pore water pressure p_w buildup.

As there was neither a measurement of the radial deformations nor of the change in volume during saturation, isotropic volume increase during saturation was assumed to calculate

the volume after swelling. The values of the volume V_0 and porosity ϕ_0 after saturation for each test derived in this manner are presented in Table 3.3.

The resulting deviatoric stress q over axial strain ε_1 and the volumetric strain ε_v over axial strain ε_1 are illustrated in Figures 3.5 and 3.6, respectively. Figure 3.5 demonstrates continuous hardening across all three tests, and Figure 3.6 illustrates compaction during shearing.

The Poisson's ratio ν can be determined from the relationship between volumetric strain ε_v and axial strain ε_1 in the elastic region. Assuming triaxial test conditions and linear elasticity, the Poisson's ratio can be calculated using the following formula:

$$\nu_{\text{tri}} = \frac{\Delta\varepsilon_v - \Delta\varepsilon_1}{2\Delta\varepsilon_1} \tag{3.3}$$

where $\Delta\varepsilon_v$ and $\Delta\varepsilon_1$ are the volumetric and axial strain increments, respectively. Using Equation 3.3, a Poisson's ratio $\nu = 0.17$ was calculated for a strain increment $\Delta\varepsilon_1 = 0.014$, where all three tests exhibit a similar volumetric strain increment $\Delta\varepsilon_v$.

Table 3.3.: Initial porosity and volume values for triaxial test series on Opalinus powder

Parameter	Unit	$\sigma_3' = 100\,\text{kPa}$	$\sigma_3' = 300\,\text{kPa}$	$\sigma_3' = 500\,\text{kPa}$
Porosity (ϕ_0)	-	0.3061	0.2765	0.2608
Volume (V_0)	cm^3	82.020	80.154	78.474

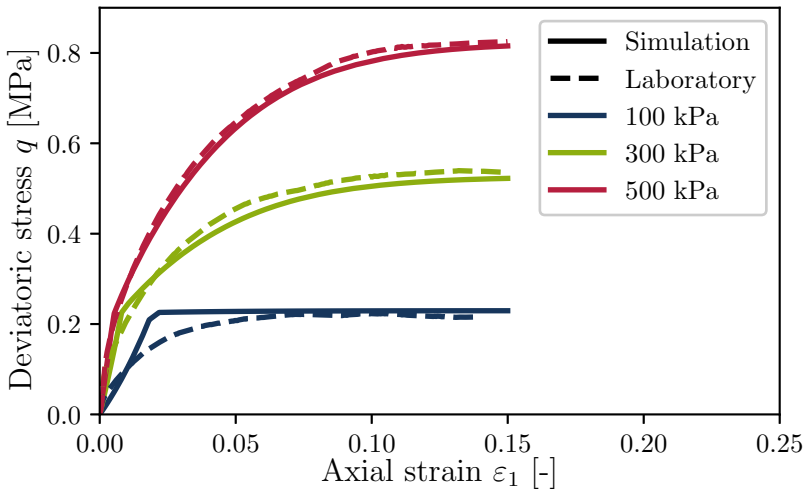

Figure 3.5.: Drained triaxial test results in terms of deviatoric stress over axial strain

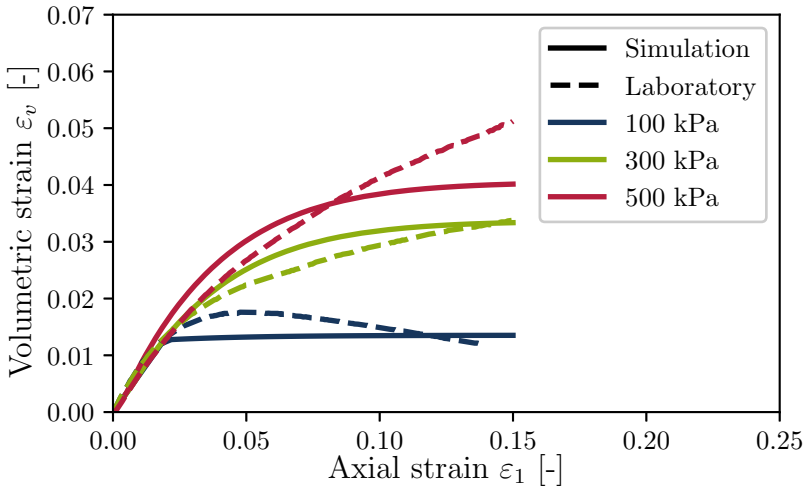

Figure 3.6.: Drained triaxial test results in terms of volumetric strain over axial strain

Figure 3.7 depicts the relationship between the deviatoric stress q and the net stress p. The residual values are connected by a line, the critical state line (CSL), which allows for the determination of the friction angle $\varphi = 25.2°$ and the cohesion $c = 25.7\,\text{kPa}$.

In order to validate the determined values of friction angle φ and cohesion c, numerical element tests are performed for final parameter calibration. The swelling and consolidation processes are not modeled, as the focus of this test is the determination of the shear strength parameters. Instead, the sample volume and void ratio after consolidation are considered for each test individually, see Table 3.3. Pore water pressure buildup is prevented by fixing pore water pressure evolution at $\Delta p_w = 0$.

One assumption made is that the swell index κ is considered constant and identical for all three tests. However, as observed in the previously discussed oedometer tests, the swell index κ decreases with decreasing stress (unloading-reloading path).

Due to the limited unloading in the small stress regime during oedometer testing, the swell index κ for low stresses remains unknown and needs to be calibrated as well. The preconsolidation pressure p_0 is assumed to differ for each test. Based on the free swelling oedometer tests, it is assumed that some part of the preloading resulting from the compaction pressure is preserved during saturation. A minimum preconsolidation pressure p_0 of either 300 kPa (support pressure) or effective confining pressure σ_3' can be assumed. This is further supported by the linear portion of the volumetric versus axial strain curve shown in Figure 3.6, indicating even higher preconsolidation pressure p_0 values.

As shown in Figure 3.5, the laboratory and simulation results for deviatoric stress q versus axial strain ε_1 are in good agreement.

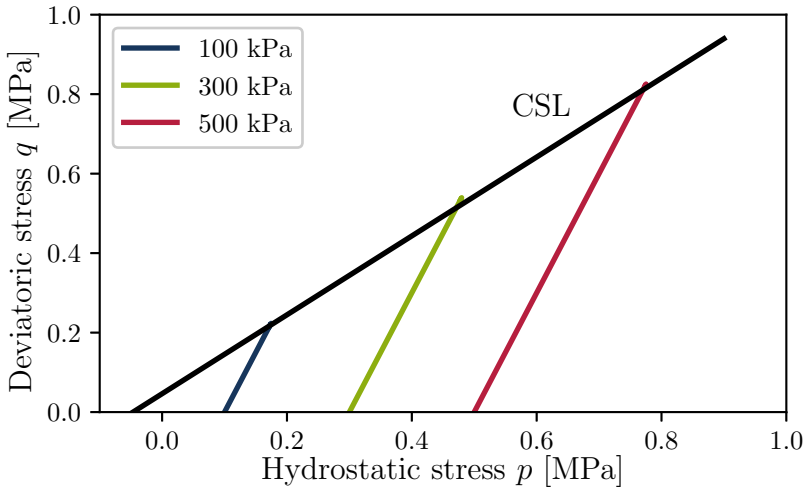

Figure 3.7.: Drained triaxial test results in terms of deviatoric over net stress

Considering that the amount of volumetric plastic strain, which contributes to hardening in this case, is controlled by the compression index λ and the swell index κ, accurately estimating these values is crucial for achieving a good match between laboratory and simulation results in terms of volumetric strain ε_v versus axial strain ε_1. As the oedometer tests indicate a consistent compression index $\lambda = 0.08$, calibration focuses purely on the swell index κ, which is not well-known for small stresses below 1 MPa.

The uncertainty in initial volume during laboratory testing, where only vertical displacements are measured during hydration and uniform swelling is assumed, an assumption that may not fully account for initial anisotropy during sample preparation, complicates parameter calibration. Consequently, the laboratory and simulation results in terms of volumetric strain ε_v versus axial strain ε_1, as shown in Figure 3.6, exhibit discrepancies.

Overall, the primary goal of determining the friction angle φ and cohesion c has been achieved, with the modeling demonstrating a good agreement with the experimental data. The parameters determined during the calibration process are summarized in Table 3.4.

Table 3.4.: Summary of parameter calibration for triaxial test series on Opalinus powder

Parameter	Unit	$\sigma_3' = 100\,\text{kPa}$	$\sigma_3' = 300\,\text{kPa}$	$\sigma_3' = 500\,\text{kPa}$
Friction angle (φ)	degree	25	25	25
Cohesion (c)	MPa	2	2	2
Swell index κ	-	0.033	0.033	0.033
Preconsolidation pressure (p_0)	kPa	400	500	650

3.3.2. Hydraulic parameters of remolded Opalinus clay

In the previous section, the mechanical parameters of remolded Opalinus clay were calibrated using oedometer and triaxial tests. Since the focus of this research is on the coupled hydro-mechanical behavior, it is also necessary to determine the hydraulic constitutive parameters. Therefore, in this section, the constitutive parameters for the soil water retention curve (SWCC) and hydraulic permeability are derived using laboratory test data from the literature.

3.3.2.1. Water retention behavior

For full hydro-mechanical coupling the relationship between the degree of saturation S_r and suction s, known as the soil water characteristic curve (SWCC), is crucial. For this thesis, tests on remolded Opalinus clay powder performed by Christ et al. (2025) for constant volume and free swelling boundary conditions are used. The samples with an initial dry density of 2.0 g/cm^3 exhibited an initial degree of saturation $S_r = 18\%$ at a suction s of around 68 MPa. The samples were then saturated or desaturated beginning from the initial state via the vapor phase in desiccators with different supersaturated salt solutions. In order to model the SWCC the Van Genuchten's equation (Van Genuchten, 1980) was used:

$$S_r = (1 + (\alpha \cdot s)^n)^{-m} \tag{3.4}$$

where S_r is the degree of saturation, s is the total suction and α, m and n are fitting parameters.

In the majority of finite element codes, the fitting parameters n and m are dependent, with m defined as $m = 1 - \frac{1}{n}$. This dependency results in a closed-form equation for Equation 3.4, as it eliminates the need for iterative or numerical methods to solve for m, thereby allowing for direct computation.

With the laboratory test data from Christ et al. (2025) and fitting with Equation 3.4 a relationship between the suction s and the degree of saturation S_r could be derived as illustrated in Figure 3.8. As shown, a good agreement for both boundary conditions, free and constant volume, with a single parameter set for the Van Genuchten fitting parameters ($\alpha = 0.220\,\text{MPa}^{-1}$, $n = 1.556$, and $m = 0.357$), could be found.

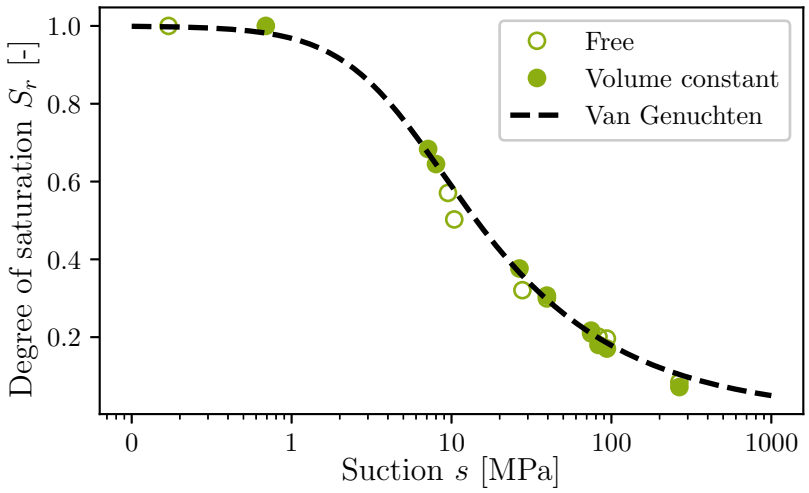

Figure 3.8.: Soil-water characteristic curves for free and constant volume swelling according to Christ et al. (2025) with Van Genuchten fitting ($\alpha = 0.220\,\mathrm{MPa}^{-1}$; $n = 1.556$)

3.3.2.2. Intrinsic hydraulic permeability

Another critical parameter influencing the coupled hydro-mechanical behavior is the hydraulic permeability k_f, as it directly impacts the temporal evolution of settlements and the buildup of pore water pressure. Given that hydraulic permeability is inherently dependent on soil density, it is essential to account for variations in this parameter across different initial dry densities. To this end, experimental tests were conducted by Christ et al. (2025) on remolded Opalinus clay powder with varying initial dry densities to systematically evaluate the impact of density on hydraulic permeability.

The determined values of hydraulic permeability k_f are shown as a function of the corresponding porosity ϕ in Figure 3.9. The relationship between permeability and porosity is clearly illustrated, providing insights into how variations in porosity influence the hydraulic permeability of the remolded Opalinus clay powder. For the sake of numerical modeling a modified Kozeny-Carman equation (Collin, 2003) is used:

$$k_f = k_{f,0} \frac{(1-\phi_0)^m}{\phi_0^n} \frac{\phi^n}{(1-\phi)^m} \tag{3.5}$$

where ϕ_0 is the initial porosity corresponding to the initial intrinsic permeability $k_{f,0}$, and the exponents n and m are fitting parameters. In this study, the initial porosity and permeability corresponding to a dry density of 2.0 g/cm^3, $\phi = 0.2526$ and $k_f = 6.15 \cdot 10^{-18}\,\mathrm{m}^2$, are selected. In the original Kozeny-Carman formulation, as shown in Equation 2.48, the exponents are set to $n = 3$ and $m = 2$. However, in this study,

exponents of $n = 5.5$ and $m = 1$ were determined to achieve better alignment with the laboratory results.

Figure 3.9 illustrates the laboratory results, the original Kozeny-Carman fit, as well as the modified Kozeny-Carman fit. As shown, the fit of the modified Kozeny-Carman equation aligns well with the experimental data, indicating that the adjusted parameters effectively capture the relationship between permeability and porosity for the Opalinus powder under the tested conditions. In contrast, the original Kozeny-Carman equation provides a reasonable fit for the two higher porosities but fails to accurately represent the smaller porosity.

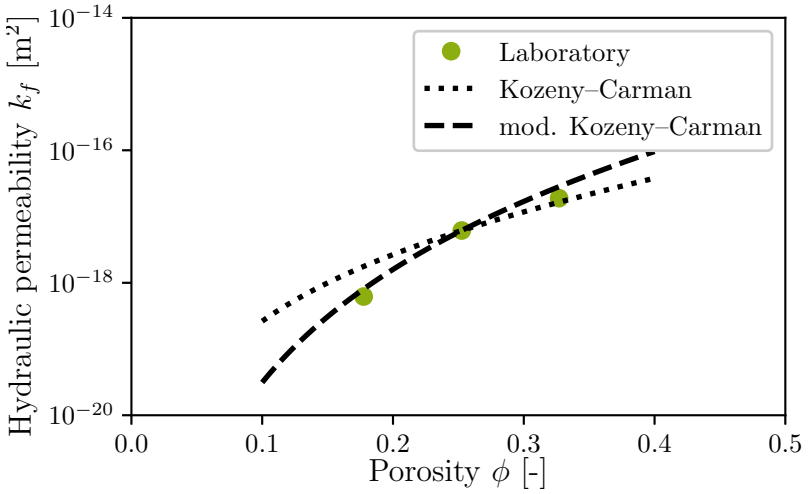

Figure 3.9.: Permeability over porosity for three different initial dry densities including Kozeny-Carman fit (Christ et al., 2025)

3.4. Numerical modeling of swelling tests

In the previous chapter, mechanical as well as hydraulic model parameters were either obtained by literature study (intact Opalinus) or calibrated using laboratory tests (remolded Opalinus). For the calibration of all constitutive parameters, including not yet determined suction-dependent parameters of the BBM, laboratory tests with controlled suction would be required. These are non-standard tests, and consequently, equipment and results are very rare. Nevertheless, to simulate the swelling phenomena, swelling tests with different boundary conditions were performed at RUB, allowing the calibration of the relevant constitutive parameters affecting swelling. Therefore, in this section, finite element models, that are capable of simulating the different swelling tests, and calibrated constitutive parameters are presented.

3.4.1. Intact Opalinus clay shale

The relationship between swelling pressure and swelling deformation is critical for applications in tunnel construction. To accurately model the swelling phenomenon, a series of swelling tests with varying boundary conditions were conducted on intact Opalinus clay shale samples by Christ (2025). Two types of tests were performed: constant volume swelling pressure tests, where both horizontal and vertical deformations were constrained, and free swelling tests, where the sample was confined laterally within an oedometer ring but allowed to deform vertically. These conditions are referred to as constant volume and free swelling, respectively. For each type of test, samples were prepared with orientations both perpendicular and parallel to the bedding plane. In the case of the sample cut perpendicular to the bedding, the bedding planes are oriented horizontally within the sample. Conversely, in the sample cut parallel to the bedding, the bedding planes are oriented vertically.

The boundary conditions of the axisymetric finite element models for both test types are illustrated in Figure 3.10. The finite element framework Lagamine, developed at the University of Liège (Charlier, 1987; Collin, 2003), was used with elements that allow coupled analyses. The model dimensions, with a diameter of 5 cm and height of 2 cm, are selected according to the laboratory swelling tests conducted by Christ (2025). In these tests, vertical displacements at the bottom of the sample, and horizontal displacements on the right side and along the symmetry axis of the sample are constrained. An initial pore water pressure p_w of -14.9 MPa is applied throughout the sample, based on an initial

suction s measurement of 15 MPa ($s = p_a - p_w$), as reported by Christ (2025). To simulate the hydration process, a pore water pressure $p_w = 15\,\text{MPa}$ is applied at the bottom of the sample. To mitigate oscillations during saturation, a finer mesh is employed in the lower section of the sample.

In the free swelling tests (Figure 3.10a), vertical movement of the sample is permitted, though a small load of 10 kPa is applied to the top of the sample as in the laboratory test. This load is necessary as the swelling strain and swelling pressure are highly sensitive to variations in pressure or deformation. Consequently, the boundary conditions are designed to closely replicate real-world conditions.

In the case of the constant volume swelling tests, a zero-thickness contact interface element (Cerfontaine et al., 2015) is implemented at the top of the model to record the contact forces, which are then used to calculate the swelling pressure, as illustrated in Figure 3.10b. The contact interface enforces the constraints using the penalty method. Since the contact problem only acts normal to the interface and no shear friction is anticipated, the primary parameter governing the interface behavior is the penalty coefficient K_N. This coefficient is set to $K_N = 2.4 \times 10^{10}\,\text{N/m}^3$, derived from observations of the deformation-controlled swelling test which will be described in Section 3.4.2.

For the constant volume swelling tests, two tests were conducted in each orientation. The results of the constant volume swelling tests are illustrated in Figure 3.11. As can be seen, the material response is both highly inhomogeneous and anisotropic. Perpendicular to the bedding plane, a swelling pressure ranging from 1000 to 2000 kPa develops, whereas parallel to the bedding plane, only a very low swelling pressure of about 100 kPa is observed.

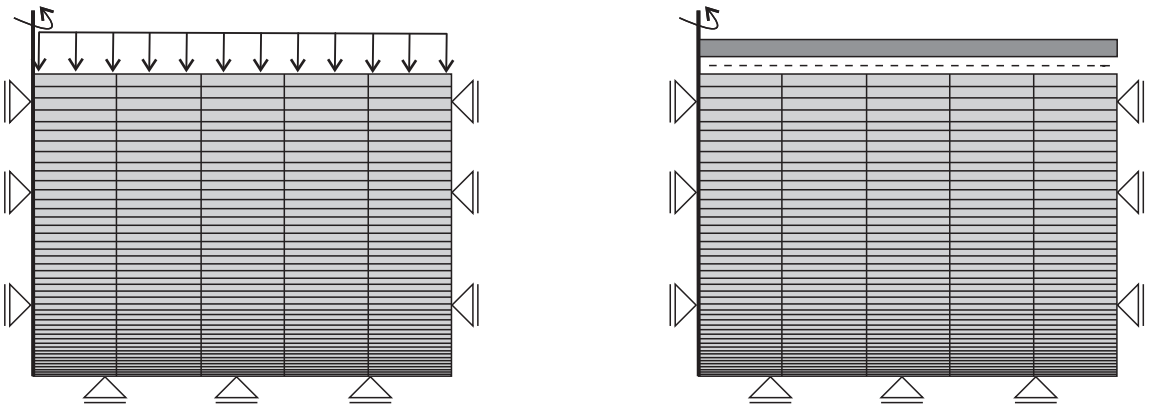

(a) Free swelling test (b) Constant volume swelling test

Figure 3.10.: Numerical models and boundary conditions of the two swelling tests

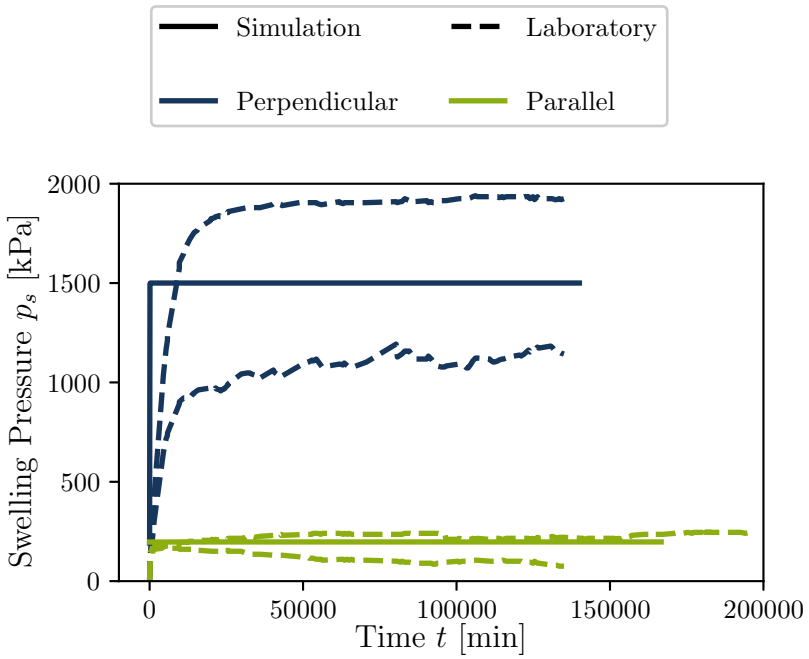

Figure 3.11.: Constant volume swelling test results in terms of swelling pressure over time

Even within the same direction, the results, particularly perpendicular to the bedding, vary significantly. Since Opalinus is a sediment rock, it is not homogeneous, meaning microfossils or pyrite can occur within the rock structure, which can lead to larger differences between tests on different intact samples (Christ, 2025).

For the modeling, a separate parameter set is calibrated for each orientation relative to the bedding plane (parallel and perpendicular). In the laboratory, two tests were conducted for each orientation, and the model calibration aimed to reproduce the mean swelling pressure observed for each orientation.

All suction-independent parameters are estimated using Table 3.1. The suction-dependent parameters, particularly the slope of the reversible wetting-drying line κ_s, which controls swelling magnitude, are calibrated using the results from the swelling tests. Since the objective of this calibration is to apply these parameters to a tunnel construction scenario, where only a single set of parameters can be utilized due to the lack of anisotropy in the BBM, parameters other than κ_s were kept consistent across both orientations.

When comparing simulated to measured swelling pressures, the target mean values of swelling pressure are achieved with good agreement (see Figure 3.11). The plateau of the swelling pressure in the perpendicular-to-bedding direction is reached more quickly than in the laboratory tests. This discrepancy may be attributed to the use of identical permeability for both orientations of the sample, whereas in reality, the permeability is

lower in the perpendicular-to-bedding direction, resulting in slower saturation and a more gradual increase in swelling pressure.

Moving towards the free swelling tests, the differences between the two orientations are not as pronounced. Figure 3.12 illustrates the temporal evolution of swelling strain. It is evident that both samples oriented either perpendicular or parallel to the bedding plane reach similar maximum strains, in the range of 12%. Consequently, only one parameter set is calibrated to accommodate both orientations.

As shown in Figure 3.12, the equilibrium swelling strains are modeled with good agreement. The reason for the quicker attainment of the plateau is, as before, the use of a single parameter set, resulting in the same permeability for both orientations.

The parameter values selected from the literature, along with the calibrated parameters derived from the previously discussed swelling tests, are compiled in Table 3.5. These parameters serve as the basis for the tunnel simulations presented in the subsequent chapters.

In summary, intact Opalinus clay shale exhibits inhomogeneous and anisotropic material behavior, although this anisotropy is observed less pronounced in free swelling tests. Additionally, the κ_s values determined showed significant discrepancies between different boundary conditions. To better understand these discrepancies, swelling tests with controlled deformation are necessary. However, given that such tests on intact Opalinus clay shale are time-consuming and subject to considerable uncertainty due to the material's inhomogeneities, it was decided to conduct these tests on remolded Opalinus clay. The results of these tests will be presented in the subsequent section.

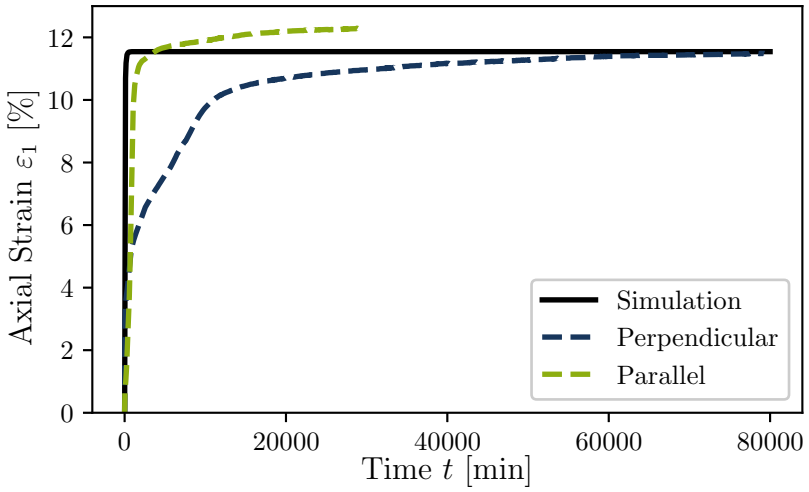

Figure 3.12.: Free swelling test results in terms of axial swelling strains over time

Table 3.5.: Summary of constitutive parameters of intact Opalinus clay

Parameter	Unit	Value
Initial porosity (ϕ_0)	-	0.14
Grain density (ρ_s)	kg/m^3	2675
Swelling index (κ)	-	0.004
Poisson's ratio (ν)	-	0.33
Cohesion (saturated state) ($c(0)$)	MPa	2
Evolution of cohesion with suction (k)	-	-
Friction angle (φ)	degree	25
Compression index (λ)	-	0.021
Preconsolidation pressure (p_0)	MPa	20
Reference pressure (p^c)	MPa	0.1
Maximum stiffness constant at infinite suction (r)	-	0.6
Rate of change of $\lambda(s)$ with suction (β)	MPa^{-1}	0.015
Plastic suction coefficient (λ_s)	-	0.008
Yield limit in terms of suction (SI curve) (s_0)	MPa	30
Slope of reversible drying-wetting line (κ_s)	-	$\kappa_{s,\perp,\mathrm{CV}} = 0.00290$ $\kappa_{s,//,\mathrm{CV}} = 0.00002$ $\kappa_{s,\mathrm{Free}} = 0.0380$
Initial intrinsic permeability (k_0)	m^2	$2 \cdot 10^{-18}$
Van Genuchten parameter (α)	MPa^{-1}	0.019
Van Genuchten parameter (n)	-	2.132

// Parallel to bedding direction, $\perp$ Perpendicular to bedding direction

3.4.2. Remolded Opalinus clay

As already discussed in the previous section, the applied boundary conditions within swelling tests are key to analyze the swelling and to model these tests, as small deformations have a major impact on the measured swelling pressures.

Beside the differences arising from varying bedding directions in intact Opalinus clay shale, it was not possible to calibrate a single parameter set that accurately models both boundary conditions, i.e. constant volume and free swelling tests. Specifically, when simulated swelling strains align well with observed values, the swelling pressure tends to be overestimated, and conversely, when swelling pressure is accurately represented, the swelling strains are underestimated. To better understand the phenomenological behav-

iors and fundamental coupled mechanisms, tests were conducted on remolded Opalinus powder by Christ et al. (2025). The homogeneity of the remolded sample reduces one potential source of uncertainty and facilitates faster laboratory testing.

In addition to the free swelling test, a constant volume swelling test with stepwise unloading, referred to as the deformation-controlled swelling test, was performed by Christ et al. (2025). This test was conducted to gain a clearer understanding of the relationship between swelling pressure and swelling strains.

For the free swelling test, the same finite element model as for the intact Opalinus clay shale is used, as described in the previous Section. For the deformation-controlled swelling test, the existing model for the constant volume test is extended. In this case, the deformations u applied in the laboratory to achieve the unloading of the sample are also incorporated into the finite element model at the interface. The boundary conditions of the deformation-controlled swelling test are illustrated in Figure 3.13.

As demonstrated during the modeling of the swelling test on intact Opalinus clay shale samples, the assumption of a constant κ_s is insufficient to represent the various boundary conditions (constant volume and free) with a single κ_s. During the modeling and analysis of the swelling tests performed on remolded Opalinus clay, it is observed that the primary differences between the two swelling tests, apart from variations in boundary conditions, are associated with the pressure regime. In the deformation-controlled swelling test, pressure is allowed to accumulate, whereas the free swelling test maintains relatively low pressure levels. Due to the swelling of the sample and the oedometeric boundary conditions, the net mean stress p is not constant but varies throughout the free swelling test.

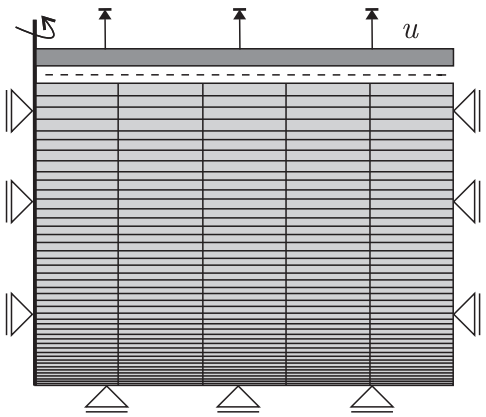

Figure 3.13.: Numerical model and boundary conditions of the deformation-controlled swelling tests

To account for the differences associated with the pressure regime, the Barcelona Basic Model for Expansive Soils (see Section 2.2.3.2) is employed, introducing a pressure-dependent κ_s. This model includes two new parameters, α_p and κ_{s0}, which govern the pressure dependency of κ_s. It should be noted that the calibration of a pressure-dependent $\kappa_s(p)$ was not feasible for the intact samples due to the lack of deformation-controlled swelling tests and the high variability in the laboratory data caused by the inhomogeneities of the intact Opalinus clay shale samples.

Notably, the suction dependency of κ_s is omitted to limit the number of unknown parameters requiring calibration. This decision is based on the lack of suction-controlled oedometer tests. The swelling tests were commenced from unsaturated conditions and transitioned to a saturated state during the testing process. The calibration of the oedometer tests revealed different values for κ in the unsaturated and saturated states, indicating a suction dependency of κ. However, a constant value for κ is used during the calibration process as a simplification, necessitated by the absence of suction-controlled oedometer tests for calibration. Additionally, it is noted that the penalty coefficient K_N influences the unloading behavior of the sample, making its calibration critical for the deformation-controlled swelling test. Consequently, K_N is included in the parameter calibration process. All other parameters were previously calibrated based on laboratory tests, as detailed in the preceding sections, and are utilized for the modeling of the swelling tests. Therefore, the parameter calibration is limited to κ, $\kappa_{s,0}$, α_p, and K_N.

Although the available laboratory tests do not permit the individual determination of all unknown parameters due to their interdependencies, a comprehensive calibration process is undertaken to establish reasonable parameter values. This calibration begins with several parameter studies to assess the isolated influence of each unknown parameter on the model's response, including swelling pressure, swelling strains, and the unloading process. After gaining insights into these effects, the unknown parameters are manually calibrated to reproduce the observed swelling behavior. This iterative process results in a single parameter set that reasonably predicts the behavior of both test conditions with a high degree of agreement.

The resulting temporal evolution of the free swelling strains as well as the temporal evolution of the swelling pressure during deformation controlled swelling test, are presented in Figures 3.14 and 3.15, respectively.

When comparing the swelling strain evolution during the free swelling test illustrated in Figure 3.14, it can be seen that both the laboratory and the simulated temporal evolution are almost coinciding until approximately 1100 s, indicating an almost perfect fit.

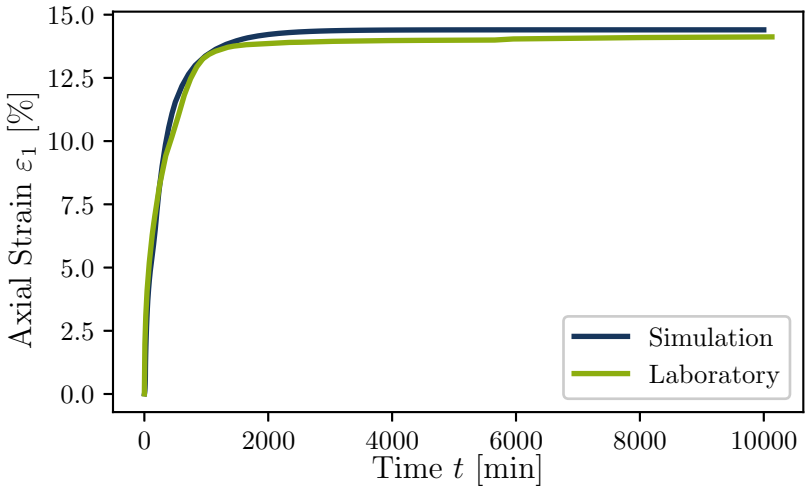

Figure 3.14.: Free swelling test results in terms of axial swelling strains over time

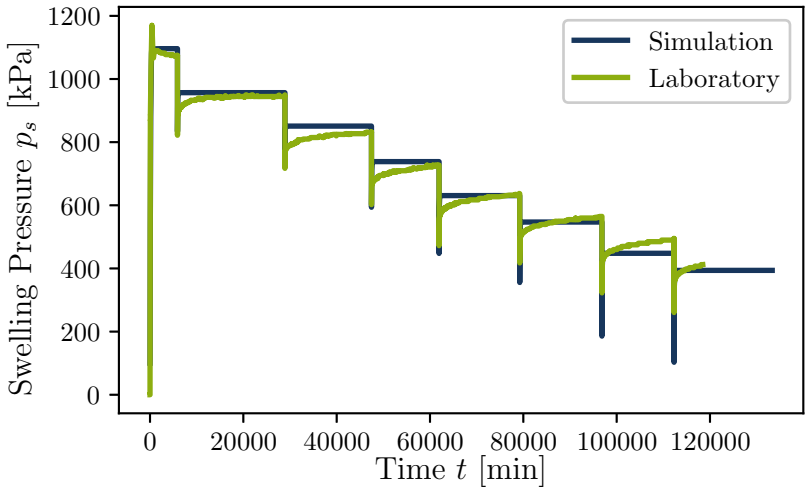

Figure 3.15.: Temporal evolution of the swelling pressure in deformation-controlled swelling test

Afterwards, the simulated swelling strain slightly overestimates the measured swelling strain. Given that the deviation is within the per mille range, it can be considered a negligible quantity.

In the deformation-controlled swelling test, the highest swelling pressure of approximately 1100 kPa is observed during saturation. With each unloading step, which is displacement-controlled, the swelling pressure decreases rapidly but then gradually increases again over time. However, the equilibrium swelling pressure reached after each unloading is lower than the pressure observed before the unloading step. During the first constant volume swelling phase, a peak in swelling pressure can be observed in the laboratory results (see

Figure 3.15). This phenomenon can be attributed to the reorientation of particles within the sample, which occurs as a result of swelling and the restriction of volumetric strains. This assumption is underlined by scanning electron microscope (SEM) images taken before and after swelling by Christ (2025). As this particle reorientation is on the microstructure level, it cannot be simulated with the used constitutive model. A comparison of the equilibrium swelling pressure for each unloading step reveals a close agreement between the simulated and measured results. In the laboratory the swelling pressure slowly evolves after each unloading step, whereas in the simulation the equilibrium swelling pressure is reached faster. For clarity, the equilibrium states are presented in a swelling pressure versus swelling strains diagram in Figure 3.16. As shown, the equilibrium states are simulated with good agreement.

In addition to the equilibrium states, the unloading process is also a relevant aspect. As illustrated in Figure 3.15, the first four unloading steps show good agreement between the laboratory tests and simulations in terms of the swelling pressure reached directly after unloading. However, the unloading for the subsequent three steps is overestimated. Christ et al. (2025) calculated an unloading stiffness using the same approach employed to estimate the swell index κ in oedometer tests. However, in this case, instead of the difference between two equilibrium states, the difference between the equilibrium state and the minimum swelling pressure during unloading was utilized for the calculation.

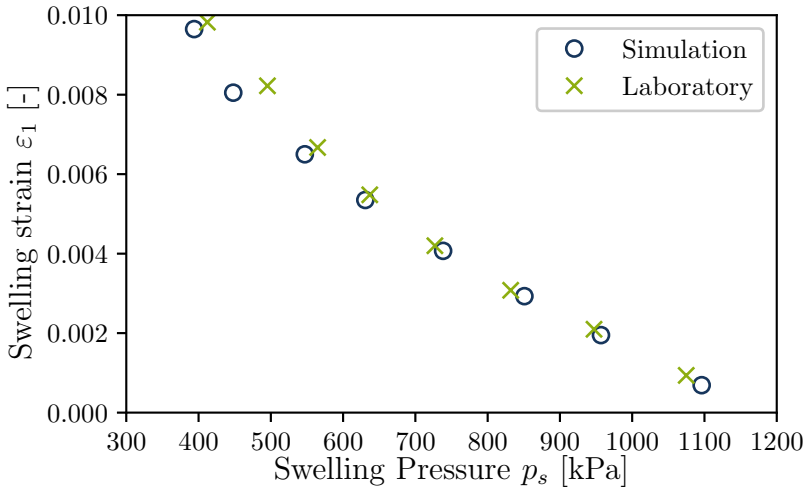

Figure 3.16.: Equilibrium swelling pressure as a function of swelling strains in deformation-controlled swelling test

In this study, the unloading stiffness is also determined from the simulation results and used to quantify the discrepancies between the laboratory and simulation outcomes. Given that the unloading process lasts only a few seconds in both the laboratory and simulations, and considering the very low permeability of remolded Opalinus clay, the conditions can be assumed to be approximately undrained. Therefore, the unloading stiffness is referred to as $\kappa_{\text{undrained}}$. It must be clarified at this point that $\kappa_{\text{undrained}}$ does not correspond to the swelling index κ or the slope of the reversible drying-wetting line κ_s.

The calculated $\kappa_{\text{undrained}}$ values from both the laboratory tests and simulations are plotted in Figure 3.17 as a function of swelling pressure. A pressure dependency of $\kappa_{\text{undrained}}$ is evident for both the laboratory experiment and the simulation, i.e., as the pressure decreases, the undrained unloading stiffness also decreases. However, certain discrepancies between the simulated and experimental undrained unloading stiffness values can be observed.

To explain the reason for these discrepancies, it is essential to understand how swelling is modeled in the Barcelona Basic Model (BBM) and which parameters of the model affect the unloading in the deformation-controlled swelling test. All processes that contribute to swelling at the microstructural level, as discussed in Section 2.2.1, are simplified in the Barcelona Basic Model (BBM), where the swelling process is solely triggered by a reduction in suction. Looking just on the mechanical aspects, the unloading of the sample leads to a volume increase and consequently to a pressure reduction in the sample, analogous to the unloading in an oedometer test that has previously been loaded.

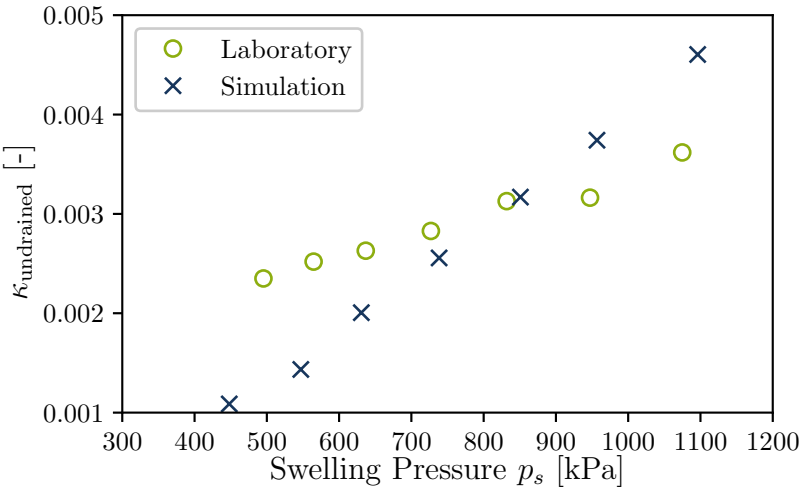

Figure 3.17.: Undrained unloading stiffness $\kappa_{\text{undrained}}$ as a function of swelling pressure in deformation-controlled swelling test

From a purely mechanical perspective, where generation of pore water pressure is not considered, the unloading is modeled exclusively with the swelling index κ in the BBM.

When dealing with a low-permeability material, such as the Opalinus clay studied here, and aiming to model not only equilibrium states (where a saturation degree of $S_r = 1$ or suction $s = 0$ is commonly assumed), but also the time-dependent behavior, the simulation must consider changes in pore water pressure and consequently should be performed hydro-mechanically coupled.

During unloading, the pore space expands, and due to the low permeability, water cannot flow into the material quickly enough to maintain fully saturated conditions. Analogous to consolidation theory, this results in the formation of negative pore water pressure or suction within the sample. The buildup of suction leads to a volume decrease, as described by Equation 2.9, which reduces the total volume increase induced by the unloading, leading to lower pressure. Over time, however, water gradually infiltrates the sample, which leads to a reduction in suction and causes the sample to swell. The constant volume boundary conditions prevent volumetric strains generated by the reduction of suction, which are instead transformed into swelling pressure, as previously explained during the modeling of constant volume swelling tests in the previous section.

In the BBM, the increase or decrease in suction results in volumetric strains, the magnitude of which is controlled by κ_s according to Equation 2.9. A change in the net mean stress p, in turn, also leads to volumetric strains, and the magnitude is controlled by κ according to Equation 2.8. When considering constant values for κ and κ_s and neglecting the relatively small changes in void ratio e during unloading compared to the subsequent constant volume swelling, the effect of κ_s on the equilibrium states is limited, as this process is essentially reversible. However, since a pressure-dependent κ_s is used in this simulation, κ_s differs during unloading (suction buildup) and resaturation (suction decrease), which consequently influences the equilibrium states. Consequently, both κ and κ_s influence the unloading process as well as the equilibrium state. It is worth noting that in the laboratory experiment, neither water inflow was measured nor pore water pressure sensors were used. Consequently, the suction and degree of saturation are unknown during the unloading phase and their distribution within the sample cannot be determined. However, at equilibrium states, it can be assumed that the sample is fully saturated.

After explaining how swelling is modeled in the BBM and which model parameters influence the unloading phase during the deformation-controlled swelling test, the discrepancies between the experimentally measured and simulated swelling pressure curves can now be addressed.

One reason for these discrepancies is the assumption of a constant value for κ, despite back-analysis of oedometer tests in Section 3.3.1 indicating its dependence on both suction and pressure. Another reason of the observed discrepancies between laboratory results and BBM simulations can be attributed to microstructural changes caused by constant volume swelling, which cannot be modeled by the BBM. Christ et al. (2025) demonstrated this issue by performing complete unloading at different times during constant volume swelling tests. When unloading was conducted before the swelling pressure peak, swelling strains of $\varepsilon_1 \approx 14\%$, comparable to those observed in the free-swelling test, were recorded. In contrast, unloading after the peak resulted in significantly reduced swelling strains of $\varepsilon_1 \approx 8.5\%$. According to Christ et al. (2025), these reductions were due to microstructural changes. To address this, the BBM parameters were calibrated to reproduce the target free-swelling strains of approximately 14%. Since $\kappa_s(p)$ increases at lower net mean stresses p according to Equation 2.19, this calibration leads to a progressive overestimation of the unloading process at lower stress levels.

In conclusion, both swelling tests on remolded Opalinus clay could be simulated with a single parameter set, resulting in a high level of agreement, leading to the conclusion that the BBMEx is capable of modeling the swell behavior for swellable clay shales.

All previously determined constitutive parameters of remolded Opalinus clay are summarized in Table 3.6.

Table 3.6.: Summary of calibrated parameters of remolded Opalinus clay

Parameter	Unit	Value
Initial porosity (ϕ_0)	-	0.2523
Grain density (ρ_s)	kg/m^3	2675
Swelling index (κ)	-	0.02
Poisson's ratio (ν)	-	0.18
Cohesion (saturated state) ($c(0)$)	kPa	25.768
Evolution of cohesion with suction (k)	-	-
Friction angle (φ)	degree	25.2
Compression index (λ)	-	0.079
Preconsolidation pressure (p_0)	MPa	12
Reference pressure (p^c)	MPa	0.1
Maximum stiffness constant at infinite suction (r)	-	0.6
Rate of change of $\lambda(s)$ with suction (β)	MPa^{-1}	0.015
Plastic suction coefficient (λ_s)	-	0.008
Yield limit in terms of suction (SI curve) (s_0)	MPa	100
Slope of reversible drying-wetting line (κ_s)	-	0.064
Pressure dependent fitting parameter (α_p)	-	$2.8 \cdot 10^{-6}$
Initial intrinsic permeability (k_0)	m^2	$2 \cdot 10^{-18}$
Van Genuchten parameter (α)	MPa^{-1}	0.220
Van Genuchten parameter (n)	-	1.556

3.5. Strain localization of Opalinus clay using biaxial test

In the previous section several laboratory tests were elaborated in order to investigate the mechanical compression behavior using oedometer testing, shear behavior by utilizing triaxial tests, and the swell phenomena using different swelling tests. As already discussed in Section 2.6 the most dominant failure mode in the excavation damaged zone is shear failure, therefore, the development of shear bands is very important to analyze. For that purpose, plane strain biaxial tests are studied, both in the laboratory and in finite element simulations.

In the laboratory, remolded Opalinus clay powder was compacted in a purpose built mold with a target dry density of 2.0 g/cm^3, consistent with the previous laboratory tests. The samples for the biaxial test measured 120 mm in height, 100 mm in width and 40 mm in depth, as illustrated in Figure 3.18. After the compaction, the sample was placed in the double wall biaxial test device (Alabdullah and Schanz, 2010) and covered by a membrane. The double wall biaxial device was filled with water and an isotropic cell pressure $\sigma_x = \sigma_y = 100\,\text{kPa}$ was applied. Then the sample was loaded vertically with a constant displacement rate of 0.002 mm/min until 5% of axial strain. During the test, the applied vertical displacements u_y, the resulting vertical force F_y, as well as the change in volume ΔV were recorded. The idealization of the previously elaborated boundary conditions, later used for the numerical modeling, are highlighted in Figure 3.18.

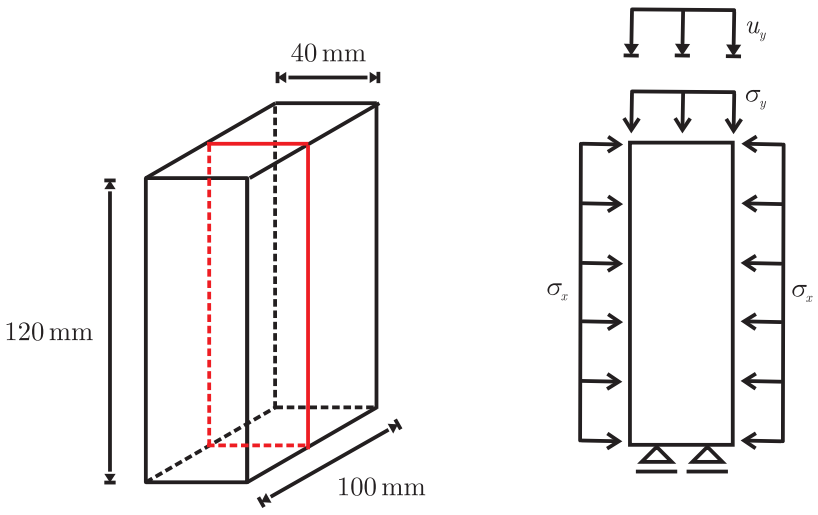

Figure 3.18.: Biaxial test sample geometry and idealization for plane strain modeling

In Figure 3.19 the deviatoric stress versus axial strain relationship and in Figure 3.20 the volumetric versus axial strains are illustrated.

As can be seen from Figure 3.19 up to a deviatoric stress $q = 1.8\,\text{MPa}$ the stress-strain relationship is linear, similar as in the odometer test on dry material (see Section 3.3.1). Exceeding 1.8 MPa deviatoric stress, a small phase with a non-linear stress-strain relationship can be observed. Starting from axial strain $\varepsilon_1 = 0.12$ the sample experienced softening, followed by a rapid fracture development, which could not be captured in detail with the installed monitoring system. Therefore, a lack of measurement points can be seen in both Figure 3.19 and 3.20.

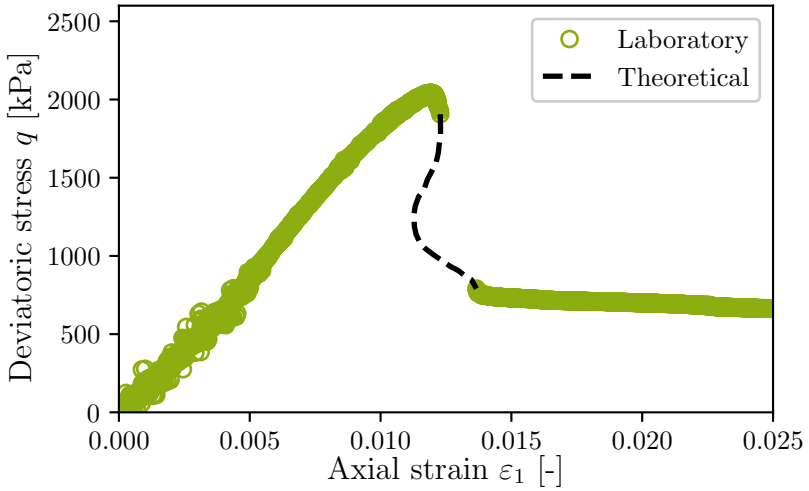

Figure 3.19.: Biaxial test results in terms of deviatoric stress versus axial strain

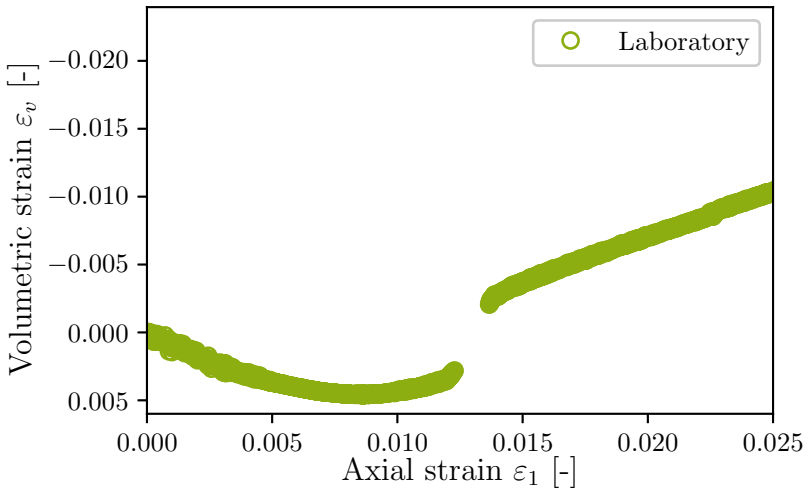

Figure 3.20.: Biaxial test results in terms of volumetric strain versus axial strain

This indicates a very brittle behavior, which results in both strong softening and very localized failure of the sample. One possible theoretical model response is also plotted in Figure 3.19 but will be elaborated later in this section.

As can be seen in Figure 3.20 the sample shows contractive behavior up to an axial strain $\varepsilon_1 = 0.009$, followed by a dilative response with increasing axial strain.

Using linear elasticity theory and the given boundary conditions of the biaxial test, the Poisson's ratio ν can be calculated using the following relationship:

$$\nu_{\text{bi}} = \frac{\Delta\varepsilon_v - \Delta\varepsilon_1}{\Delta\varepsilon_v - 2 \cdot \Delta\varepsilon_1} \tag{3.6}$$

Assuming linear elastic behavior for the range of axial strains between 0 and 0.010, the Poisson's ratio is derived as $\nu = 0.15$ from the biaxial test data, which is in a good agreement with the triaxial tests, which delivered a Poisson's ratio of $\nu = 0.17$. The derivation of the Poisson's ratio ν as well as the Young's modulus E is described more in detail in Appendix B.

The numerical modeling of laboratory tests is typically done using element tests, due to the clear boundary conditions and the fast calculation time. However, it will be shown that element tests are not able to capture a localized shear failure. Instead the test was modeled using a discretized model with the second gradient model as the regularization technique.

Due to the plane strain nature of biaxial tests, this test is modeled in 2D plane strain conditions. The bottom of the sample is fixed in vertical direction, while on both sides and on top, the cell pressure is modeled as a line load. Additionally, the central node at the bottom is constraint horizontally to prevent rigid body movement. During the test, the vertical displacements u_y of the top nodes of the sample are controlled to match the applied displacement rate of 0.002 mm/min. All boundary conditions of the biaxial test modeling are illustrated in Figure 3.18.

To model the mechanical behavior, the BBM is utilized again and the mechanical parameters obtained for the dry material are used.

In order to capture the linear instead of non-linear behavior of the sample up to a deviatoric stress of $q = 1.8$ MPa, a minimum stress p_{min} can be defined in the BBM in order to achieve a stress-independent stiffness, as already mentioned in Section 3.3.1.

To estimate the minimum stress, the bulk modulus K from the laboratory test, calculated using linear elasticity theory as:

$$K = \frac{E}{3(1-2\nu)} = \frac{\Delta\sigma}{\Delta\varepsilon} \cdot \frac{1-\nu^2}{3(1-2\nu)} \tag{3.7}$$

and the bulk modulus K in the BBM, calculated as:

$$K = \frac{1+e}{\kappa} \cdot p \tag{3.8}$$

are considered. By setting the two above terms equal and solving the resulting equation for p, the minimum stress $p_{\min}$ can be calculated as:

$$p_{\min} = \frac{K \cdot \kappa}{1+e} \tag{3.9}$$

Using Equation 3.9 and the laboratory results, a value of $p_{\min} = 7.9\,\text{MPa}$ is calculated and subsequently used for the following numerical modeling.

When using element tests, it is not possible to replicate a localized shear fracture as observed in the laboratory. Therefore, the only way to induce more softening in the model is by decreasing the compression index λ or increasing κ, as these parameters govern the plastic volumetric strains (refer to Equation 2.10).

As illustrated in Figure 3.21, the model's response using the calculated $p_{\min}$ shows good agreement with the laboratory results in terms of the elastic portion of the deviatoric stress q versus axial strain ε_1 relationship. Additionally, it can be observed that as the compression index λ decreases, the model's response becomes softer and aligns more closely with the measured behavior of the remolded Opalinus clay.

However, since the swell index κ and the compression index λ have already been determined from oedometer tests, further reduction of these parameters cannot be justified. Moreover, decreasing the compression index λ is constrained by the requirement that λ must remain larger than κ ($\lambda > \kappa$) to prevent unintended volume increase during softening.

To address the limitations mentioned, it is essential to model this test using multiple elements to allow for localized shear failure. To mitigate the mesh dependency discussed in Section 2.7.3, the local second gradient method (described in Section 2.7.4) is employed.

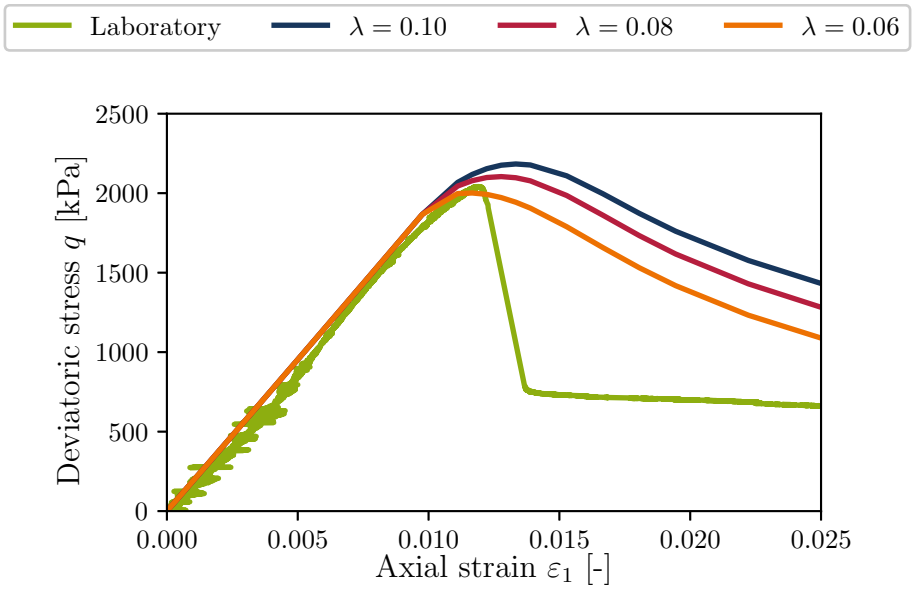

(a) Biaxial test results in terms of deviatoric stress over axial strain

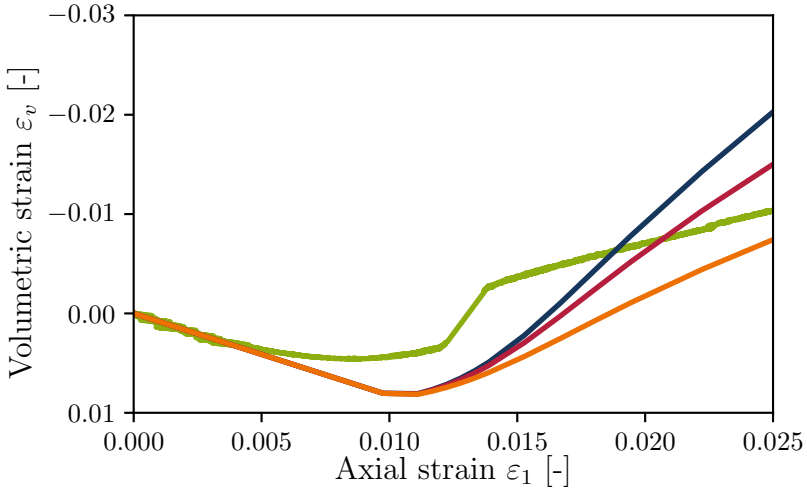

(b) Biaxial test results in terms of volumetric strain over axial strain

Figure 3.21.: Comparison of simulated biaxial test results for different values of λ with laboratory results

To make use of this model, the element type SGRT (Corman, 2024) was employed. This element is based on the previously introduced MWAT2 element and includes additional degrees of freedom required for the local second gradient model. It is a 2D isoparametric element with nine nodes. In the eight outer nodes, each node possesses five degrees of freedom, namely spatial coordinates, water pressure, gas pressure and temperature. In the four corner nodes, the element includes additional degrees of freedom for the microkinematic gradient field. The center node contains a degree of freedom for the Lagrange multiplier field.

To validate this approach, models with identical dimensions are created using three different mesh sizes, incorporating 184, 800, and 3200 elements. The corresponding element sizes are $5.2 \times 5\,\text{mm}$, $3 \times 2\,\text{mm}$, and $1.5 \times 1\,\text{mm}$, respectively. In all three models, the same elastic modulus of the microstructure, denoted as D, is used to act as an internal length scale. To achieve localized shear failure in this model, an imperfect element with reduced cohesion is placed in the lower left corner of the numerical model to initiate shear failure. The significance and effects of imperfections are discussed in more detail in the following chapters.

The results are presented in Figure 3.22. Only a minor difference between the models with different mesh sizes during the initial plastic phase is observed, which can be attributed to the different sizes of the imperfect elements that initiate shear failure. Nevertheless, all models ultimately yield the same response, demonstrating that the local second gradient model effectively allows for mesh-independent shear strain localization. To achieve numerical convergence in the simulation, it is necessary to increase the compression index λ from 0.08 to 0.18. This adjustment is supported by the model's nearly vertical drop in the deviatoric stress q versus axial strain ε_1 curve, as shown in Figure 3.22a for a compression index of $\lambda = 0.18$. If the compression index λ remain at the laboratory-determined value of $\lambda = 0.08$, the model would exhibit a snapback behavior, as illustrated by the dashed theoretical curve in Figure 3.19.

Conventional Newton-type iterative strategies, such as those used in the finite element framework Lagamine applied in this thesis, hold the load parameter constant while iterating to convergence. As a result, they often fail to capture structural or material instabilities like snapback behavior (Kotronis and Collin, 2005). To overcome this limitation, a path-following technique such as the Arc Length Method (Riks, 1979) is required. Unfortunately, at the time of writing of this thesis, this method has not yet been implemented in the Lagamine finite element code, and therefore the aforementioned limitations persist.

To illustrate the effect of a thinner shear band, or more localized failure, the model with 3200 elements and a compression index of $\lambda = 0.18$ is used with different values of the elastic stiffness of the microstructure D, which controls the shear band width. As shown in Figure 3.23, the elastic modulus of the microstructure D influences the model response. As D decreases, the shear band becomes thinner, resulting in a more localized or softer model response.

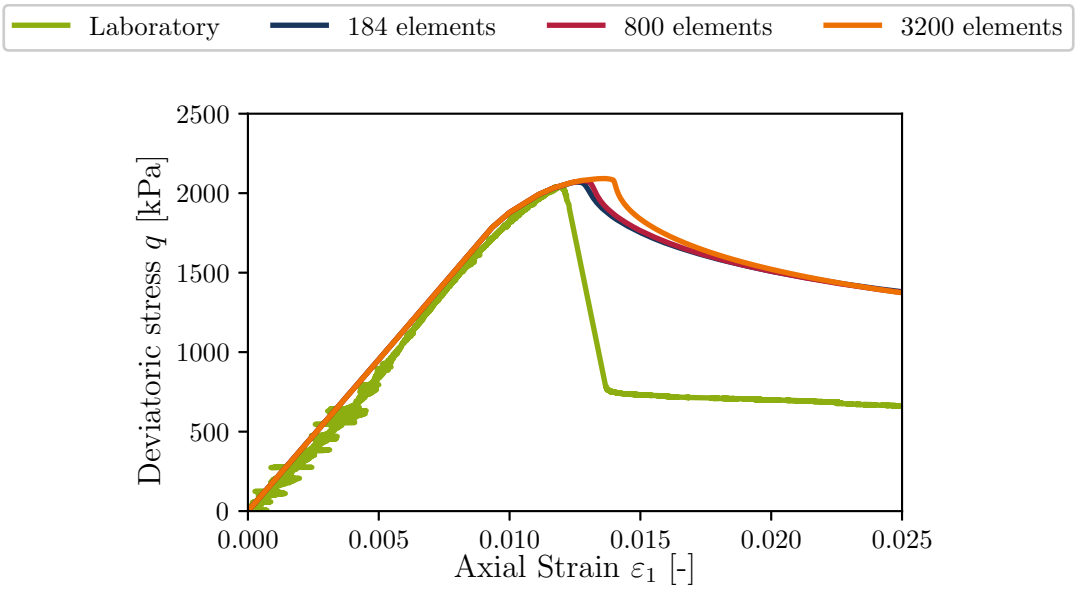

(a) Biaxial test results in terms of deviatoric stress over axial strain

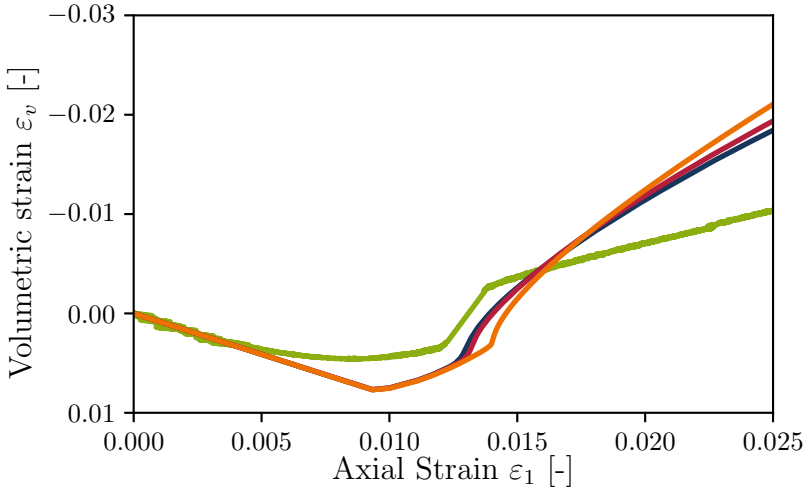

(b) Biaxial test results in terms of volumetric strain over axial strain

Figure 3.22.: Comparison of simulated biaxial test results for different mesh densities with laboratory results

Although the previously discussed limitations still prevent achieving an optimal fit, the impact of D on the model response is clearly demonstrated. This highlights the importance of the microstructure's elastic stiffness in controlling the degree of strain localization within the model.

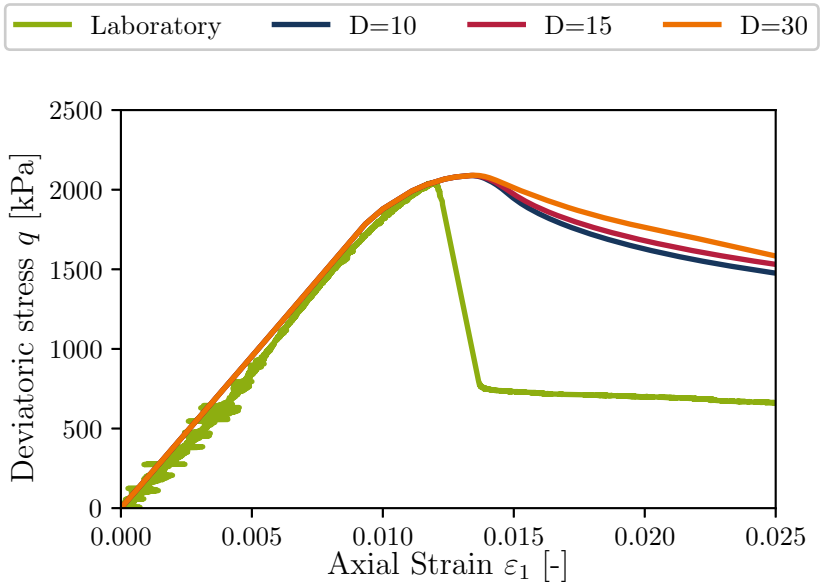

(a) Biaxial test results in terms of deviatoric stress over axial strain

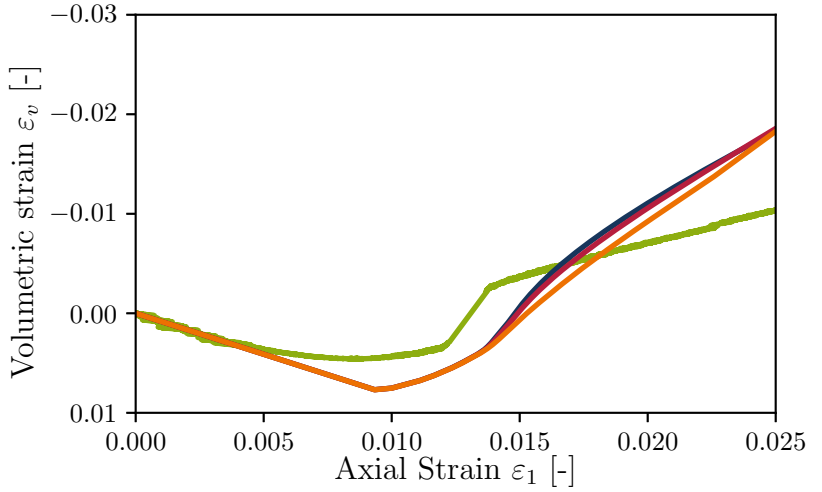

(b) Biaxial test results in terms of volumetric strain over axial strain

Figure 3.23.: Comparison of simulated biaxial test results for different values of the elastic stiffness of the microstructure D with laboratory results

In conclusion, element tests alone are insufficient to capture the brittle shear failure of Opalinus clay during biaxial testing. To address the issue of mesh dependency, the local second gradient model was successfully implemented, enabling the accurate representation of localized shear failure. However, to achieve a more precise fit, it is necessary to implement advanced solving algorithms in the finite element code, which would allow for the snapback behavior of the sample. It should be noted that the snapback behavior is only an assumption due to the lack of laboratory measurements during failure.

With the compression index λ and swell index κ initially determined from oedometer tests, the elastic modulus of the microstructure D was identified, providing the best possible agreement with the laboratory results. However, it is important to note that λ was adjusted to 0.18 to achieve numerical convergence, representing the best case achievable without implementing advanced solving algorithms. This approach demonstrates the importance of considering microstructural effects and advanced numerical techniques to accurately model the complex behavior of Opalinus clay under biaxial loading conditions.

4. Numerical modeling of shear strain localization

4.1. Introduction

In the previous chapter, constitutive parameters for both intact and remolded Opalinus clay were derived. For the remolded Opalinus clay, the significance of shear strain localization was already demonstrated through a biaxial test conducted in the laboratory. Before starting the tunnel modeling, it is essential to derive the parameters decisive for shear strain localization. Due to the inherent complexity, tunnel simulations are not well-suited for this purpose. Instead, a biaxial test is typically employed, owing to its well-defined boundary conditions and the reduced complexity of the model, which consequently leads to shorter computation time.

In this chapter, the numerical modeling of shear strain localization in intact Opalinus clay is examined through a parameter study based on biaxial tests. The parameters investigated include the element size and the second gradient elastic modulus D, both of which influence the formation of the shear band. Additionally, various approaches to modeling the increase in permeability within the shear band are examined. The fundamental idea is to utilize shear strain localization to simulate the development of cracks and the consequent increase in permeability within the damaged zone in the context of continuum mechanics. Two different scenarios are investigated: mechanical shear failure and wetting-induced failure, both of which are relevant for tunnel simulations. The insights gained from this study will subsequently be applied in the following chapter to simulate mechanized tunnel excavation.

The chapter starts with the introduction of the numerical model of the biaxial compression test in Section 4.2.1, with a focus on the geometry, boundary conditions, and the two different stress path scenarios. This is followed by a presentation of the parameter study in Section 4.2.2. In Section 4.3, the results of the parameter study are subsequently

presented and discussed. Finally, a conclusion is provided in Section 4.4, where the parameters and permeability approaches that proved suitable for the subsequent tunnel simulation are selected.

4.2. Simulation of biaxial compression test

This section first introduces the geometrical configuration, loading parameters, and boundary conditions of the biaxial compression test simulation. Subsequently, the parameters and variations examined in the parameter study are presented.

4.2.1. Geometry, loading and boundary conditions

In contrast to Section 3.5, where a biaxial test was modeled to validate the results using a laboratory experiment, here the model of a biaxial test is employed as a numerical tool with well-defined boundary conditions to gain a deeper understanding of shear strain localization, in particular the conditions and influences resulting from the choice of constitutive parameters and the followed stress path leading to shear strain localization. Therefore, a numerical 2D plane strain model of a biaxial test with a height of 1 m and a width of 0.5 m is simulated. For the model discretization, the SGRT elements are used again. The bottom of the model is constrained in the vertical direction and the central node is additionally constrained horizontally to prevent any rigid body movement. A load boundary condition is applied to the sides and top of the model, allowing for the establishment of an initial isotropic stress level. Additionally, a displacement boundary condition is imposed on the top of the sample to induce shearing. Temperature T and air pressure p_a changes are not considered, and the corresponding degrees of freedom in all nodes of the finite element model are similarly constrained to $T = 293$ K and $p_a = 0.1$ MPa, respectively. The dimensions and boundary conditions of the model are illustrated in Figure 4.1.

To determine the initial stress level and the magnitude of the displacement boundary condition, it is crucial to understand the conditions under which the mechanical constitutive model leads to shear strain localization. As explained in Section 2.7.1, shear bands form at failure when the soil exhibits a softening behavior. In clay shales, two mechanisms may lead to softening from a physical standpoint. First, softening occurs during shear failure in overconsolidated clays, which exhibit volumetric expansion or dilative soil behavior under increased deviatoric stress. Second, in partially saturated soils, softening

may arise during saturation. When suction decreases, these soils either collapse under high confining stress or expand under low confining stress.

When considering a Cam-clay type model, such as the applied Barcelona Basic Model (BBM) (introduced in Section 2.2.3.2), these observations can be modeled.

First, in highly overconsolidated clays, shear bands may form when an increase in deviatoric stress q causes the yield surface to be reached on the left side, also known as dry side, resulting in volumetric expansion or dilative soil behavior illustrated in Figure 4.1a, hereinafter referred to as shearing path. Second, specific to the BBM, softening may occur when partially saturated soils ($s > 0$) become fully saturated ($s = 0$), and the stress state before saturation is in the vicinity of the yield surface. In this case, the yield surface shrinks as suction decreases, leading to softening behavior as depicted in Figure 4.1b, hereinafter referred to as wetting path. The shearing path is particularly relevant for tunnel excavation in nearly fully saturated, highly overconsolidated clay shales, where the excavation process results in the unloading of the surrounding formation, leading to an increase in deviatoric stress q. Additionally, the wetting path may become relevant in cases where excavation occurs in partially saturated clay rock. Although the initial increase in deviatoric stress q might not cause the yield surface to be reached due to the larger yield surface under partially saturated conditions, saturation can occur, potentially leading to yield surface shrinkage and subsequent material softening and strain localization. Both scenarios are critical for modeling tunnel excavation in clay shales, making them essential aspects in setting up initial stress conditions and boundary displacements in the numerical model.

The boundary conditions for the shearing path model are illustrated in Figure 4.1a. To achieve initial fully saturated conditions, the pore water pressure p_w is initially set equal to the air pressure $p_a = 0.1\,\mathrm{MPa}$, resulting in an initial suction $s = 0$. The pore water pressure p_w is fixed only at the nodes located at the top and bottom of the model throughout the simulation, facilitating local drainage at these boundaries. To ensure that the stress path touches the yield surface on the left side, a low initial confining stress of $\sigma_x = \sigma_y = 0.9\,\mathrm{MPa}$ is applied. An increase in deviatoric stress q is simulated by incrementally increasing the vertical displacement u_y at the top of the sample, with a constant loading strain rate of $5 \times 10^{-7}\,\mathrm{s}^{-1}$ until a vertical displacement $u_y = 0.05\,\mathrm{m}$ is reached.

In the wetting path scenario, the sample is initially partially saturated with an initial suction $s = 20.1\,\mathrm{MPa}$, as illustrated in Figure 4.1b. To achieve this, the pore water pressure in all nodes is set to $p_w = -20\,\mathrm{MPa}$. The initial confining stress is selected as $0.6\,\mathrm{MPa}$. The displacement boundary condition at the top of the sample is applied with

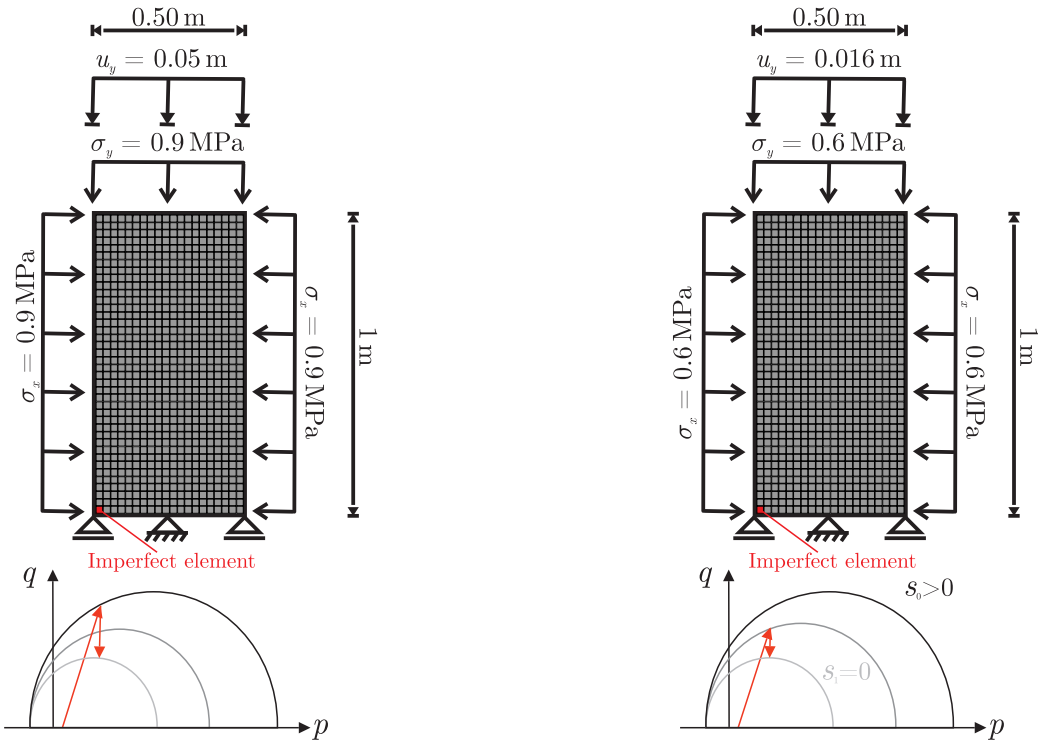

(a) Shearing path (b) Wetting path

Figure 4.1.: Numerical models of a plane-strain biaxial compression test

a strain rate of $1.6 \times 10^{-6}\,\mathrm{s}^{-1}$ until a vertical displacement $u_y = 0.016\,\mathrm{m}$ is reached. At this point, the current stress level is still within the elastic range but close to the yield surface. Following this, suction is reduced by linearly decreasing the pore water pressure in all nodes from $p_w = -20\,\mathrm{MPa}$ to $0.1\,\mathrm{MPa}$. This reduction in suction causes the yield surface to shrink, leading to softening of the material and causing the elements to enter plasticity.

Additionally, a material imperfection is incorporated into the numerical model to ensure robust shear strain localization. Since the element with material imperfection transitions into plasticity before other elements, it initializes the shear band. This imperfect element is introduced at the bottom left of the sample, as illustrated in Figures 4.1a and 4.1b. For the shearing path, the material imperfection is not strictly necessary due to the anisotropic stress conditions and the local drainage, resulting in a non-uniformed stress state within the model. However, it has been shown by Pardoen, Seyedi and Collin (2015) that the material imperfection is essential for models with uniform stress state, as in the investigated wetting path scenario, because all elements exhibit almost identical stress states leading to a diffuse failure without any localization. Therefore, an imperfect element

is included in both, the shearing and wetting path scenarios, to maintain consistency between them.

The material imperfection involves degrading the parameters of the constitutive model that influence the onset of plasticity. Within the framework of the BBM used in this study, possible parameters include the shear strength parameters φ and c, as well as the preconsolidation pressure P_0, all directly affecting the size of the yield surface. For this study, the cohesion is gradually reduced until a point is reached where robust shear strain localization is achieved. As a result, the cohesion is reduced from 2 MPa (see Table 3.5) to 1.5 MPa for the wetting path and to 1.75 MPa for the shearing path. The impact of the imperfection on the formation of shear bands will be analyzed in detail in the framework of the tunnel simulations presented in Chapter 5.

4.2.2. Parameter study of the biaxial compression test

A parameter study is a critical step for complex numerical models, enabling the systematic exploration of how variations in input parameters influence the model's outcomes. This approach is particularly essential when dealing with parameters that cannot be directly obtained from laboratory tests, such as material constants or boundary conditions. Since these parameters often rely on assumptions or estimations, a parameter study helps to identify their impact on simulation accuracy and reliability.

Since the mechanical and hydraulic constitutive parameters are already well-established through an extensive literature review (see Section 3.2), this parameter study focuses primarily on shear strain localization. Therefore, the constitutive model parameters from Table 3.5 are utilized. From the three determined values of the slope of the reversible drying-wetting line, κ_s, the value $\kappa_{s,\perp,\mathrm{CV}} = 0.0029$ (see Table 3.5) is selected. This choice is made because the constant volume condition more closely aligns with the boundary conditions in both the biaxial test and the mechanized tunnel excavation scenario. Moreover, since the direction perpendicular to the bedding plane generates more swelling than the direction parallel to the bedding, this parameter is chosen accordingly.

It should be noted that for the following simulations, exclusively the BBM with the parameters obtained for intact Opalinus clay shale is used. The calibration of the additional BBMEx parameters was not possible due to the lack of deformation-controlled swelling tests on intact Opalinus clay shale.

The local second gradient model, as discussed in Section 2.7.4, is employed for mesh-independent analysis of shear band localization. Consequently, the influence of the pri-

mary model parameter of the local second gradient model, the elastic modulus of the microstructure D, which directly influences the width of the shear band, is studied. Specifically, a smaller value of the elastic modulus of the microstructure D results in a thinner shear band. The values of the elastic modulus of the microstructure D that are investigated within this parameter study can be found in Table 4.1.

To ensure a clear localization, it is crucial that the shear band covers a sufficient number of elements. For instance, the shear band should ideally encompass at least three elements, according to Pardoen, Seyedi and Collin (2015), in the direction perpendicular to the shear band. This ensures a well-defined shear band that can be clearly differentiated from the surrounding material, allowing for a more precise analysis of the strain localization and the associated mechanical behavior. Therefore, three different element sizes ($0.042 \times 0.042\,\mathrm{m}$, $0.025 \times 0.025\,\mathrm{m}$ and $0.015 \times 0.015\,\mathrm{m}$) are investigated while keeping all other parameters constant. The three meshes including 288, 800 or 2312 elements are illustrated in Figure 4.2.

It is important to note that the study with mesh variation is conducted only for the shearing path scenario. Given that the use of the local second gradient model ensures mesh-independent simulations, as demonstrated in Section 3.5, the goal of this investigation is to determine the minimum element size that allows for a reliable and well-defined shear band localization while remaining computationally efficient. Once this optimal element size is identified, it is used for further parameter studies.

In the parameter study on the influence of the element size and the elastic modulus of the microstructure D, the evolution of permeability within the shear bands is not considered. This simplification is made to better analyze the influence of these two parameters in isolation.

Another parameter study, which focuses on changes in permeability within the shear band is conducted for both scenarios, namely the shearing path and the wetting path. This study examines two approaches introduced in Section 2.8: the volumetric strain-dependent method (see Equation 2.51) and the deviatoric strain-dependent method (see Equation 2.52). The variations in parameters for each method are presented in Table 4.2.

The variables highlighted in bold in Tables 4.1 and 4.2 represent the reference values for each parameter. During the analysis, only one parameter is varied at a time, while all other parameters are held constant at their reference values, in order to isolate the effect of the individual parameter on the results. The next section presents and discusses the outcomes of the performed parameter studies.

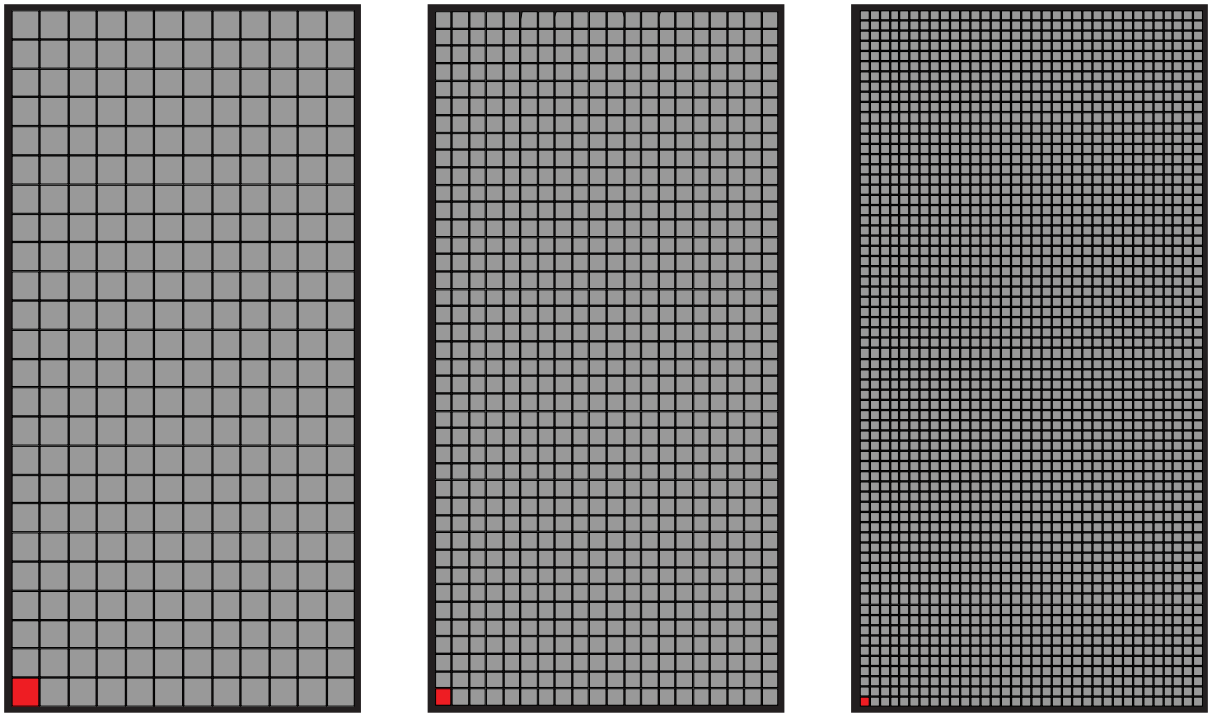

(a) coarse mesh
$0.042 \times 0.042\,\mathrm{m}$
288 elements

(b) medium mesh
$0.025 \times 0.025\,\mathrm{m}$
800 elements

(c) fine mesh
$0.015 \times 0.015\,\mathrm{m}$
2312 elements

Figure 4.2.: Comparison of different element sizes for the biaxial compression test

Table 4.1.: Sets of values in the parameter study on the influence of element size and second gradient elastic modulus for the numerical models of the biaxial compression test

Shearing Path	
Parameter	Set of Values
Element size (m × m)	0.015×0.015
	$\mathbf{0.025 \times 0.025}$
	0.042×0.042
Second gradient elastic modulus D (N)	**500**
	1000
	2000
	5000
Wetting Path	
Second gradient elastic modulus D (N)	500
	1000
	2000
	5000

Table 4.2.: Sets of values in the parameter study using different permeability evolution methods for the numerical models of the biaxial compression test

Shearing Path		
Method	Parameter	Set of Values
Volumetric strain-dependent	Permeability evolution parameter β_{per}	2×10^6
		2×10^7
		$\mathbf{2 \times 10^8}$
		2×10^9
Deviatoric strain-dependent	Permeability evolution parameter β_{per}	3×10^3
		$\mathbf{3 \times 10^4}$
		3×10^5
		3×10^6
	Threshold yield index YI^{thr}	0.80
		0.85
		0.90
		0.95
Wetting Path		
Volumetric strain-dependent	Permeability evolution parameter β_{per}	3×10^8
		3×10^9
		$\mathbf{3 \times 10^{10}}$
		3×10^{11}
Deviatoric strain-dependent	Permeability evolution parameter β_{per}	4.6×10^4
		4.6×10^5
		$\mathbf{4.6 \times 10^6}$
		4.6×10^7

4.3. Results and Discussion

In this section, the results of the previously elaborated parameter study are presented and discussed. First, the results of the mesh study are analyzed to determine a suitable mesh discretization for the subsequent parameter variations. Second, the influence of the elastic modulus of the microstructure D is examined. Furthermore, different permeability evolution methods are evaluated by studying the relevant model parameters.

4.3.1. Effect of element size

As described in Section 4.2.2, a mesh study is conducted for the shearing path scenario using three different element sizes (see Figure 4.2). For all three models, a constant value of the elastic modulus of microstructure is set at $D = 500\,\mathrm{N}$. The total deviatoric strains after $100,000\,\mathrm{s} \approx 28\,\mathrm{h}$ are evaluated, indicating the end of the loading. As a scalar measure the von Mises equivalent strain ε_{eq} is used to quantify the intensity and distribution of the deviatoric strain for the three biaxial models. The results are shown in Figure 4.3.

To avoid the influence of the chosen upper and lower limits of the contour plots (see Figure 4.3), the plastic points, which represent the integration points in plasticity, are additionally illustrated in Figure 4.4, allowing a clear distinction of the shear bands. Upon comparing the three different meshes, it can be observed that a shear band forms with a similar width ranging from 0.12 m (fine mesh) to 0.15 m (coarse mesh). This confirms that the local second gradient model allows for mesh-independent shear strain localization. The minor differences arise from the fact that the models are not perfectly identical, as the imperfect elements introduced by the respective meshes differ in size, as noted in Bésuelle et al. (2006). Additionally, as the element size increases, the resolution also diminishes, making it more difficult to clearly distinguish between the shear band and the surrounding zone.

However, additional insights can be drawn from the mesh study. For the subsequent application of the model, particularly for simulating the permeability increase within the shear band, it is advantageous if the shear band spans a sufficient number of elements in the direction normal to the shear band propagation. This ensures a clear distinction between the shear band and the surrounding elements.

A visual comparison of the three models regarding the deviatoric strains reveals no significant difference between the medium and the fine mesh. Both meshes also exhibit enough elements within the shear band to provide a distinct demarcation. Only for the plastic

points shown in Figure 4.4, differences can be observed in the lower boundary area of the specimen. However, no significant differences are present in the region of the shear band. Therefore, due to the reduced computational effort, the model with the medium mesh ($0.025 \times 0.025\,\mathrm{m}$) is selected for all subsequent simulations.

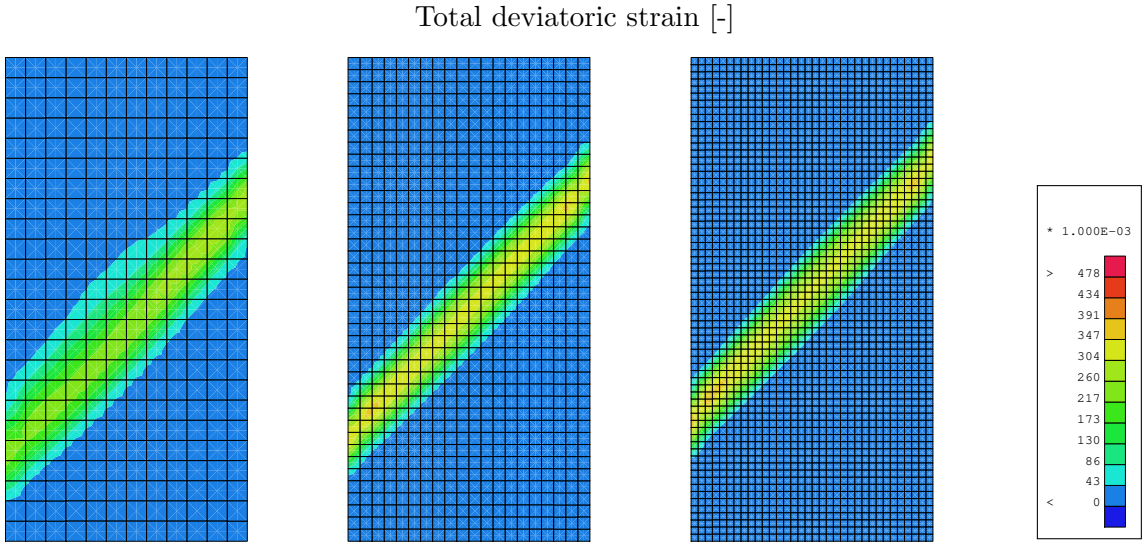

(a) coarse mesh (b) medium mesh (c) fine mesh

Figure 4.3.: Total deviatoric strain within the numerical biaxial model subjected to a shearing path for three different element sizes (time = 100,000 s, $D = 500\,\mathrm{N}$)

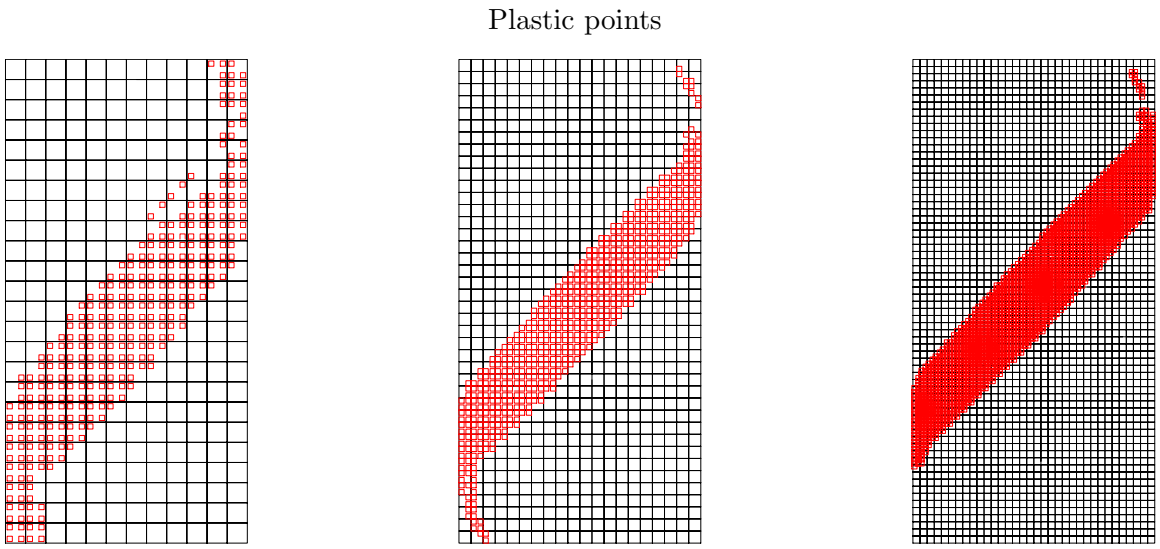

(a) coarse mesh (b) medium mesh (c) fine mesh

Figure 4.4.: Plastic points within the numerical biaxial model subjected to a shearing path for three different element sizes (time = 100,000 s, $D = 500\,\mathrm{N}$)

4.3.2. Effect of second gradient elastic modulus

This section investigates the influence of the second gradient elastic modulus D on shear band development, focusing on both the shearing path and wetting path scenarios. As outlined in Table 4.1, four different values for D are examined: 500 N, 1000 N, 2000 N, and 5000 N. Initially, the shearing path scenario is considered. For comparison purposes, Figures 4.5 and 4.6 illustrate the total deviatoric strains and plastic points, respectively, after 100,000 s for each investigated value of D.

As anticipated, D directly impacts the shear band width. Specifically, the higher the value of D, the wider the resulting shear band. For $D = 500\,\mathrm{N}$, the shear band spans approximately 3.5 to 4 elements in width, corresponding to a width of 0.14 m. In contrast, for $D = 5000\,N$, the shear band encompasses 6 elements, resulting in a shear band width of 0.25 m.

Although the imperfection is placed in the lower left corner of the model, the shear band initiates at this location but subsequently migrates upward during ongoing deformation. This upward movement can be attributed, among other factors, to the evolving stress path inhomogeneities caused by the local pore water pressure buildup. Such migration of shear bands during shear deformation has also been observed and discussed by Bésuelle et al. (2006).

It is evident in Figures 4.5 and 4.6 that as the shear band width decreases, the maximum value of the total deviatoric strain within the shear band increases. Specifically, in the case of $D = 5000\,\mathrm{N}$, the maximum deviatoric strain amounts $\varepsilon_{eq} \approx 0.15$, while for $D = 500\,\mathrm{N}$, it increases to $\varepsilon_{eq} \approx 0.30$, representing a doubling of the strain value. This observation can be explained, as with the same global deformation of the specimen, the failure becomes much more localized, occurring over half the area. Consequently, the deviatoric shear strains must be correspondingly higher.

Before presenting the results of the parameter study for the wetting path scenario, it is first necessary to address the different stress paths involved. In the shearing path scenario, axial deformations are continuously increased, and initially, all elements of the model follow a comparable stress path. The stress path is not uniform within the model due to pore water pressure buildup in the model center, which results from the hydraulic boundary conditions allowing drainage only at the top and bottom, combined with the low permeability of the material. By placing an imperfect element in the lower left corner of the model, this element reaches the plasticity limit first, aiding in the formation of the shear band. The elements along the shear band, as shown in Figure 4.7a, reach the yield

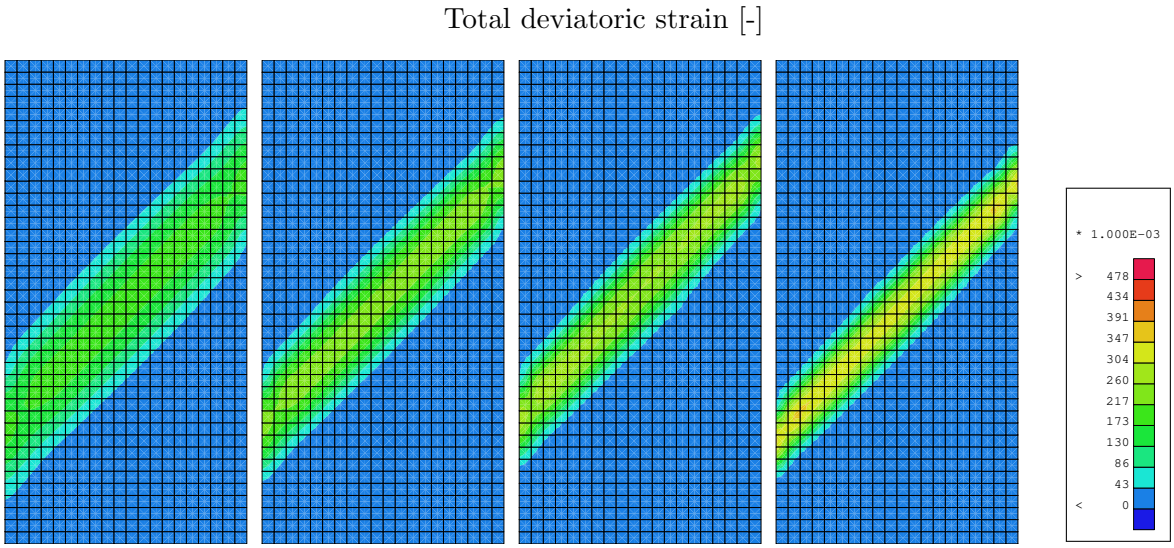

(a) $D = 5000\,\mathrm{N}$ (b) $D = 2000\,\mathrm{N}$ (c) $D = 1000\,\mathrm{N}$ (d) $D = 500\,\mathrm{N}$

Figure 4.5.: Total deviatoric strain within the numerical biaxial model subjected to a shearing path for different second gradient elastic moduli (time = 100,000 s)

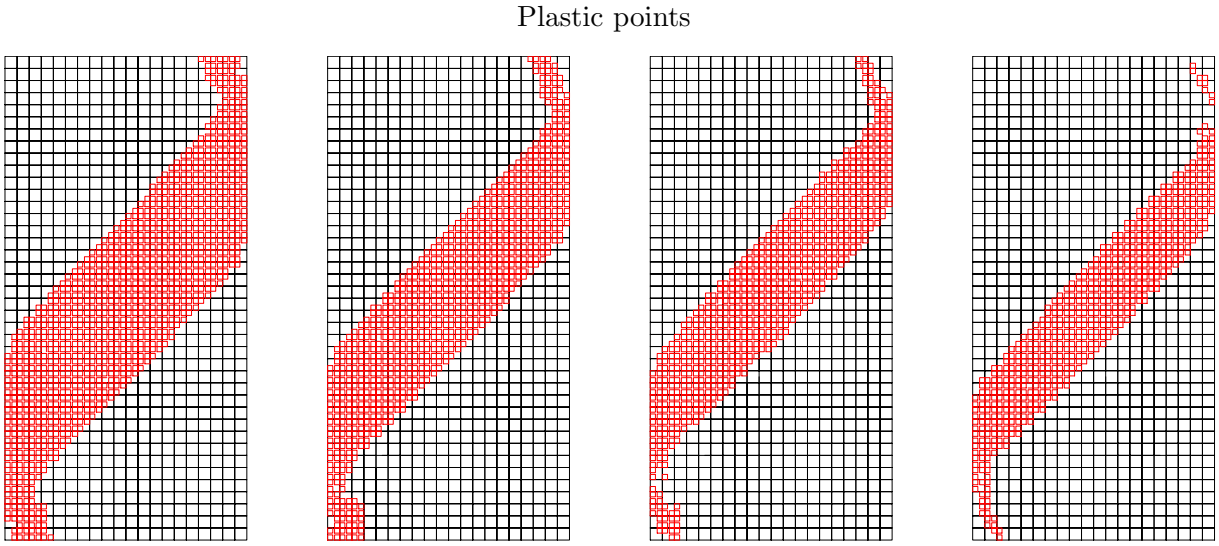

(a) $D = 5000\,\mathrm{N}$ (b) $D = 2000\,\mathrm{N}$ (c) $D = 1000\,\mathrm{N}$ (d) $D = 500\,\mathrm{N}$

Figure 4.6.: Plastic points within the numerical biaxial model subjected to a shearing path for different second gradient elastic moduli (time = 100,000 s)

surface on the dry side, leading to softening until the critical state line (CSL) is reached. Due to the localization and formation of the shear band, the surrounding elements are unloaded and deform fully elastically, as illustrated in Figure 4.7b, preventing them from reaching the yield surface.

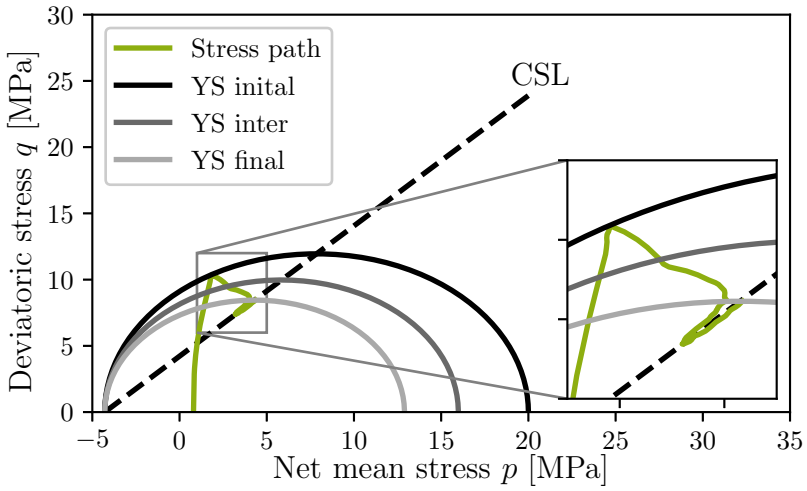

(a) Element on the shear band

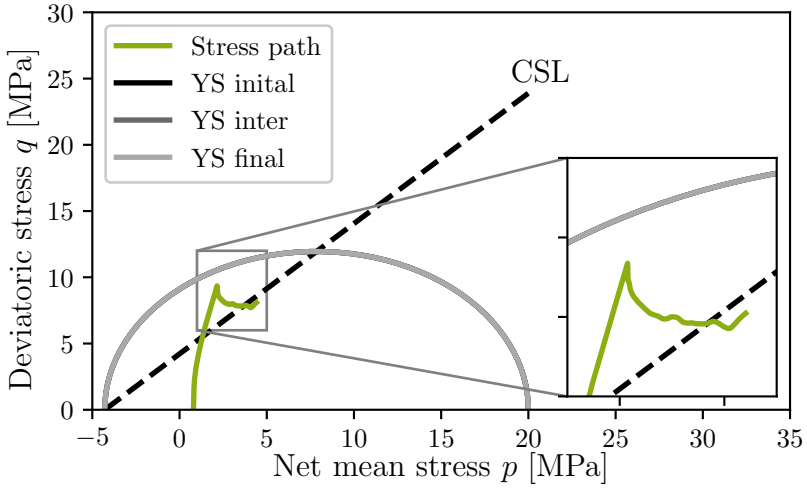

(b) Element outside of the shear band

Figure 4.7.: Stress path of biaxial test in the shearing path scenario

In contrast, the wetting path scenario presents a more complex behavior. Initially, axial deformations increase the deviatoric stress q, with all elements remaining in the elastic range, as depicted in Figure 4.8. During this phase, pore water pressure buildup is prevented, resulting in a uniform stress state across the model. Consequently, both the elements inside (see Figure 4.8a) and outside (see Figure 4.8b) the eventual shear band follow the same stress path. Once the top boundary is fixed against deformation and the pore water pressure is increased in every node, swelling pressure develops, which will be analyzed in detail afterwards, causing a further increase in deviatoric stress q, marked by a noticeable kink in the stress path due to the different inclination. As saturation increases, the stress path moves along the suction axis. When the stress path is plotted

in a $p-q$ space, it becomes evident that with decreasing suction the yield surface shrinks. This reduction in the size of the yield surface, when viewed solely within the $p-q$ space, corresponds to a form of softening.

The imperfect element reaches the yield surface before the rest of the model, initiating shear strain localization and resulting in elastic unloading outside the shear band. At this stage, two competing processes occur in the elements outside the shear band: unloading due to localization and an increase in deviatoric stress q alongside the shrinking yield surface due to swelling. Until 95,000 s, indicated by a red dot in Figure 4.8, a distinct shear band forms (see Figure 4.9a), but as saturation continues, the stress path of elements outside the shear band eventually touches the yield surface, transforming all elements into plasticity, as illustrated in Figure 4.9b.

For better understanding, the axial pressure derived from the y-reaction forces at the top of the sample over time is shown in Figure 4.10. Up to 10,000 s (I), the pressure increases due to the application of axial deformations. As the sample is gradually saturated while maintaining axial movement constraints, a swelling pressure of approximately 4 MPa develops, highlighted by the gray area in Figure 4.10 (II). Around 84,000 s, a shear band forms (III), leading to localized failure, which is reflected by a decrease in axial pressure. When all elements are in wetting-induced plasticity $t > 95,000\,\mathrm{s}$ an even softer model response is visible, indicated by a further kink in axial pressure in Figure 4.10.

Having analyzed the differences between the two scenarios, the influence of the second gradient elastic modulus D on shear band formation is examined for the wetting path scenario. Since the objective of this study is to model the permeability change at the shear band, only the final time step exhibiting localized deformation (95,000 s) is analyzed for the wetting path scenario. Similar as for the shearing path scenario the total deviatoric strain as well as the plastic points are evaluated, and these are depicted for various values of D in Figures 4.11 and 4.12, respectively. Similar to the shearing path scenario, the influence of the second gradient elastic modulus D on the shear band width and the maximum deviatoric strain within the shear band is evident. As D decreases, the shear band width narrows, reducing the area of the shear band, which in turn increases the maximum value of the deviatoric strains. For $D = 5000\,\mathrm{N}$, the shear band encompasses approximately four elements in the direction normal to the shear band, corresponding to a shear band width of 0.14 m. In contrast, for $D = 500\,\mathrm{N}$, the shear band encompasses only about two elements, resulting in a shear band width of approximately 0.07 m.

When examining the deviatoric strains, there is a clear trend: from $D = 5000\,\mathrm{N}$ with deviatoric strains $\varepsilon_{eq} \approx 0.03$ to $D = 500\,\mathrm{N}$ with deviatoric strains $\varepsilon_{eq} \approx 0.06$, showing

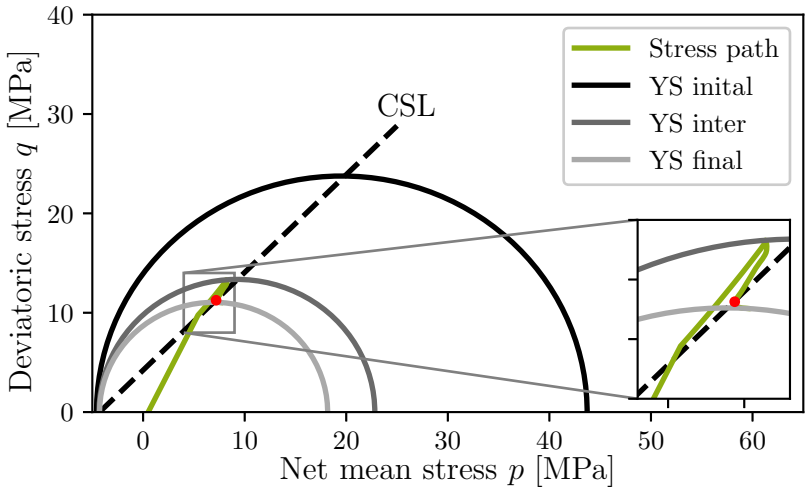

(a) Element on the shear band

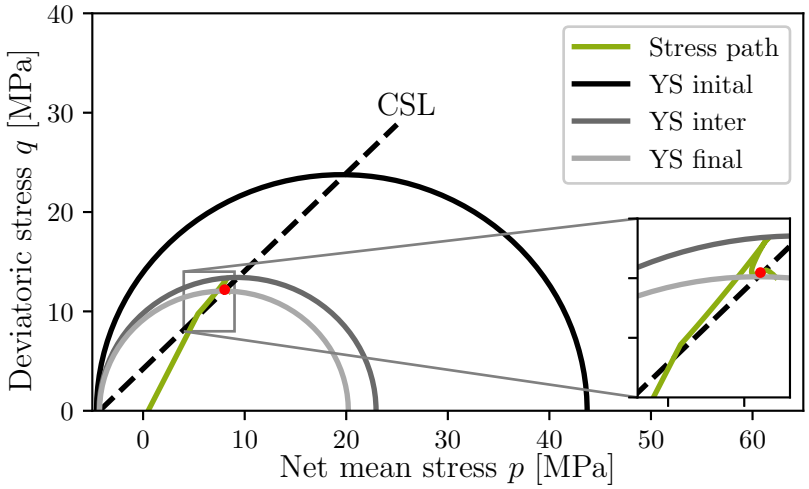

(b) Outside of the shear band

Figure 4.8.: Stress path of biaxial test in the wetting path scenario

a doubling of the deviatoric strains, similar to what was observed in the shearing path scenario and the same explanation can be applied here.

Comparing the shear bands for the same value of D between the shearing path and wetting path scenarios reveals significant differences in both shear band width and maximum deviatoric strain values and location. This difference can be explained by the distinct stress paths, which have already been discussed and illustrated for both scenarios. These stress paths are shown for an element on the shear band and one adjacent to the shear band in Figures 4.7 and 4.8, respectively. Due to the concurrent processes in the wetting path scenario, namely, the increase in deviatoric stress from swelling and the softening due to saturation, all elements of the model remain very close to the yield surface. Under these

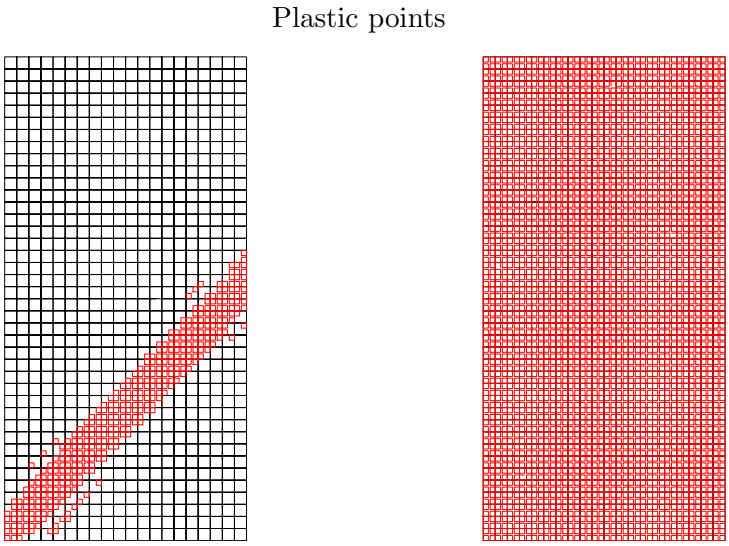

(a) $t = 95,000\,\mathrm{s}$ (b) $t = 100,000\,\mathrm{s}$

Figure 4.9.: Plastic points within the numerical biaxial model subjected to a wetting path for different time steps

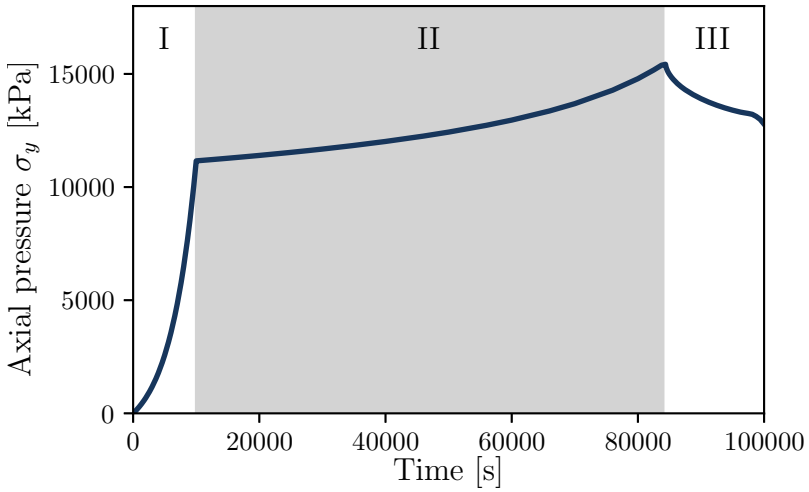

Figure 4.10.: Temporal evolution of the axial pressure in biaxial testing during wetting path scenario

conditions, localized failure can occur only if the unloading from shear strain localization exceeds the buildup of swelling pressure. This constraint provides a potential explanation for why the location of the shear band does not change over time compared to the shearing path scenario, where it moves upward. The distinctly different stress paths and the resulting variations in softening make a direct comparison of the shear band widths not reasonable.

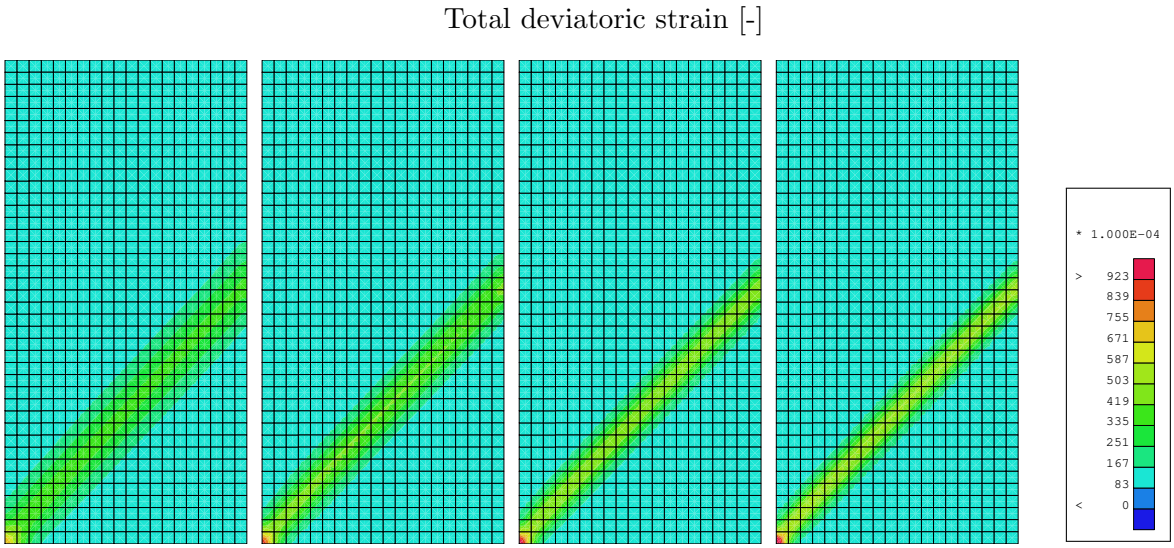

(a) $D = 5000\,\mathrm{N}$ (b) $D = 2000\,\mathrm{N}$ (c) $D = 1000\,\mathrm{N}$ (d) $D = 500\,\mathrm{N}$

Figure 4.11.: Total deviatoric strain within the numerical biaxial model subjected to a wetting path for different second gradient elastic moduli (time = 95,000 s)

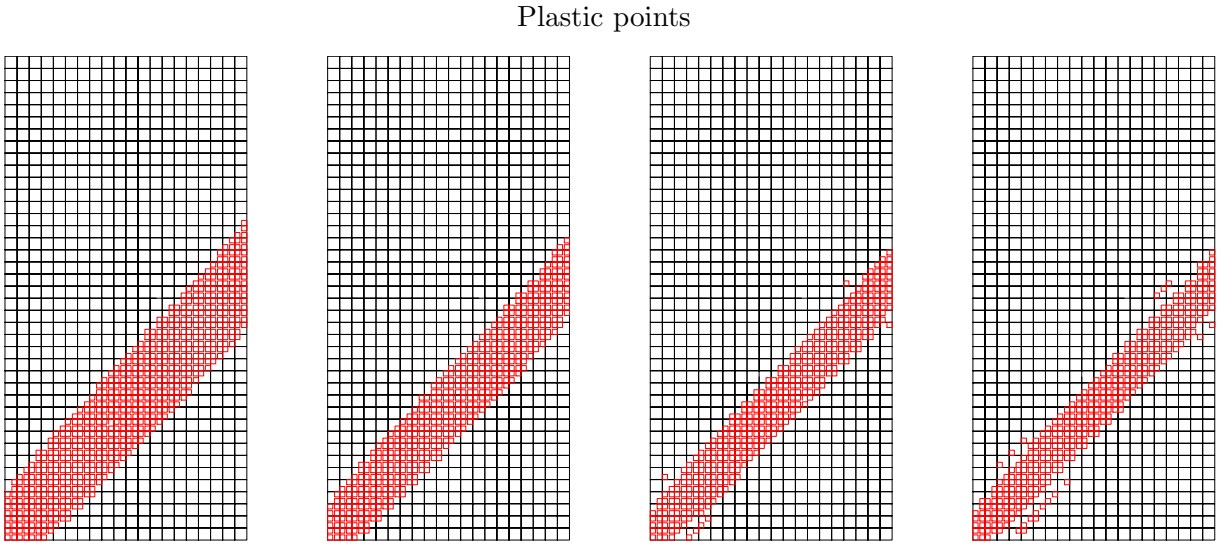

(a) $D = 5000\,\mathrm{N}$ (b) $D = 2000\,\mathrm{N}$ (c) $D = 1000\,\mathrm{N}$ (d) $D = 500\,\mathrm{N}$

Figure 4.12.: Plastic points within the numerical biaxial model subjected to a wetting path for different second gradient elastic moduli (time = 95,000 s)

In summary, the second gradient modulus D has a clear and significant impact on both the shear band width and the maximum value of the deviatoric strains within the shear band. As D decreases, the shear band width narrows, while the maximum value of the deviatoric strains increases, regardless of the scenario being examined (shearing path or

wetting path). Given that both the shear band width and the maximum deviatoric strain are critical parameters for the subsequent analysis of permeability within the shear band, it is essential to make informed assumptions regarding the second gradient elastic modulus D.

Ideally, this decision would be based on results from biaxial tests conducted in the laboratory, preferably with x-ray microtomography to visualize the shear band (see Section 2.6). However, in the absence of such data, the simulation will proceed with the value of D that produces a shear band width covering approximately three elements, ensuring a clear distinction between the shear band and the surrounding elements. For the shearing path scenario, this corresponds to $D = 500\,\mathrm{N}$, and for the wetting path scenario, to $D = 2000\,\mathrm{N}$.

It is important to note in this context that the chosen shear band width is likely broader than the actual fracture width expected in reality. However, literature suggests that permeability increases not only within the damaged area but also in its immediate vicinity, which justifies the selection of these values.

With a suitable element size and corresponding local second gradient elastic moduli D now established, the focus can shift to analyzing the permeability increase within the damaged zone, which in this study is modeled as shear bands.

4.3.3. Effect of different permeability evolution methods during shearing path

As discussed in Section 2.4, in-situ measurements have shown that permeability within the Excavation Damaged Zone (EDZ) significantly increases compared to the intact formation. The primary reason for this is the propagation of cracks and other forms of damage, which result in higher permeability compared to the intact material. To numerically model this phenomenon, various approaches have been proposed in literature, as explained in Section 2.8. Given the complexity and computational intensity of simulating a full tunnel excavation, it was decided, similar to the previous section's approach regarding element size and the second gradient elastic modulus D, to investigate different permeability models through a parametric study using biaxial tests, with the previously determined mesh and second gradient elastic modulus of $D = 500\,\mathrm{N}$.

In this study, three permeability models, namely the porosity-dependent (Equation 2.48), the deviatoric strain-dependent (Equation 2.52), and the volumetric strain-dependent method (Equation 2.51), are examined. To illustrate the fundamental differences among

these models, Figure 4.13 presents the input variables (porosity, volumetric strain, and deviatoric strain) in the top row as well as the resulting permeability evolution $\frac{k_{w,ij}}{k_{w,ij,0}}$ in the bottom row. Here, $\frac{k_{w,ij}}{k_{w,ij,0}}$ represents the change in permeability relative to the initial permeability $k_{w,ij,0}$. It should be noted that in Figure 4.13 (top row), various quantities are presented that, while related to the shear bands, are not directly comparable due to their nature as different quantities. Therefore, the term "band" is used in the following.

Figures 4.13a and 4.13d illustrate the variation in porosity and the corresponding permeability evolution, respectively, using the porosity-dependent Kozeny-Carman method (Equation 2.48). As observed in Figure 4.13a, a band forms where the porosity is slightly higher than in the rest of the model. When comparing the porosity within and outside this band, the changes are minimal, amounting approximately 0.01. Consequently, as shown in Figure 4.13d, the permeability increase within this band is also minor, with a maximum value of $\frac{k_{w,ij}}{k_{w,ij,0}} \approx 1.1$. Outside the band, however, permeability decreases compared to the initial value. This can be attributed to the initial compaction of the specimen caused by the applied vertical deformation, leading to a global reduction in porosity.

It is important to emphasize that the original Kozeny-Carman model, which underpins the porosity-dependent method, does not contain any fitting parameters. This inherent characteristic further limits its flexibility in accurately capturing significant permeability changes, particularly within localized shear bands. The absence of adjustable parameters means that the model is constrained by the direct relationship between porosity and permeability, which, as observed, leads to only minimal changes in permeability within the band. This is significantly different in case of the volumetric strain-dependent and deviatoric strain-dependent methods, where permeability increases by a factor of 100 compared to the initial value, whereas this method shows only an increase of 1.1 times the original permeability. These alternative methods will be described in detail in the following. Consequently, the Kozeny-Carman model is not suitable for effectively capturing significant permeability changes within the shear band when used in combination with the Barcelona Basic Model (BBM).

In Figures 4.13b and 4.13e, the plastic volumetric strains and the corresponding permeability changes are depicted. Similar to the previously discussed porosity-dependent method, a broad band forms, with concentrated maxima of volumetric strains at the ends of the band. Since plastic volumetric strains are the critical input parameter for the volumetric strain-dependent method (as per Equation 2.51), this behavior is directly reflected in the permeability increase (see Figure 4.13e).

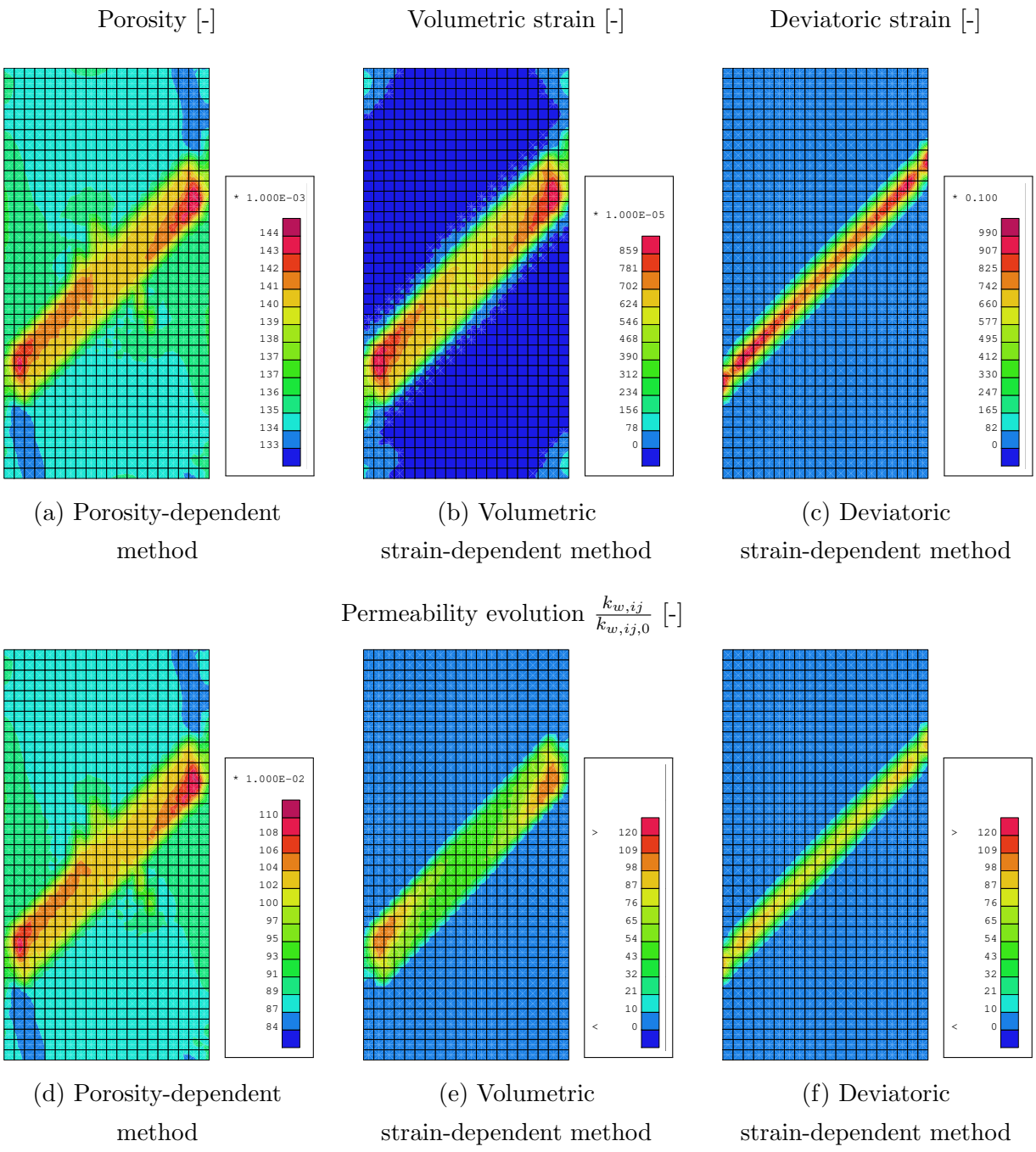

(a) Porosity-dependent method

(b) Volumetric strain-dependent method

(c) Deviatoric strain-dependent method

(d) Porosity-dependent method

(e) Volumetric strain-dependent method

(f) Deviatoric strain-dependent method

Figure 4.13.: Comparison of different methods of permeability evolution within the numerical biaxial model subjected to a shearing path (time = 100,000 s, $D = 500$ N)

By adjusting the evolution parameter β_{per}, the permeability increase can be calibrated to a desired level. In the present case, a value of $\beta_{per} = 2 \times 10^8$ is employed, resulting in an approximate permeability evolution ratio of $\frac{k_{w,ij}}{k_{w,ij,0}} = 50$ at the band's central region. The influence of β_{per} will be analyzed more thoroughly in Section 4.3.4, within the context

of an additional parameter study. This adjustment capability allows the model to better simulate the substantial permeability changes observed in damaged zones, making it more suitable for representing the conditions within shear bands.

When considering the deviatoric strain-dependent method, it can be observed in Figure 4.13c that a thinner band, compared to the two other methods, develops. This can also be observed in the permeability increase shown in Figure 4.13f. Unlike the other two methods, the permeability is more homogeneously distributed along the band and is not concentrated at the ends. The deviatoric strain method, in addition to the evolution parameter β_{per}, also uses the threshold yield index YI^{thr} as an input parameter (see Equation 2.52). In the present case, calculations are performed with $\beta_{\text{per}} = 2.3 \times 10^4$ and $YI^{\text{thr}} = 0.9$. The influence of these two parameters is also examined in an additional parameter study, see Section 4.3.5 and 4.3.6.

To ensure a more systematic evaluation and better comparability between the methods, the increase in permeability along a vertical cross section is considered. To find a suitable location, two possible cross sections, illustrated in Figure 4.14, are analyzed. The two sections are chosen once in the center of the model (w/2) and once close to the edge of the model (w/10) to examine the permeability distribution along the shear band. Since Figure 4.13 already indicates that the porosity-dependent method is unsuitable, it is no longer considered in further analyses.

Figure 4.15 illustrates the differences between the two strain-dependent permeability evolution methods along both cross sections. For the volumetric strain-dependent method, there is a clear difference in permeability evolution ratios $\left(\frac{k_{w,ij}}{k_{w,ij,0}}\right)$ between cross section w/10 and w/2. In this method, the ratio drops significantly from about 105 at cross section w/10 to around 50 at cross section w/2. In contrast, the deviatoric method shows a decrease from about 100 to 80 between both cross sections, resulting in a more uniform permeability distribution along the band. Since differences only emerged in the volumetric strain-dependent method, and these are due to a concentration of volumetric strains at the model boundaries, all subsequent results will be analyzed along the center of the model (cross section at w/2).

In the following sections, the input parameters of the volumetric strain-dependent and deviatoric strain-dependent models will be analyzed in more detail through a parameter study.

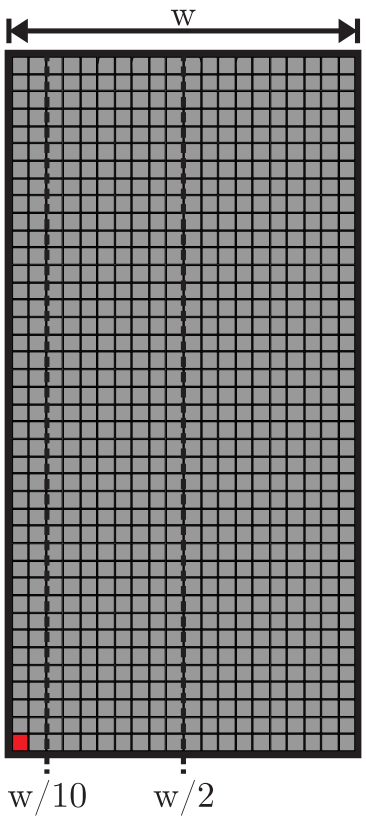

Figure 4.14.: Positions of analyzed cross sections of the numerical biaxial model

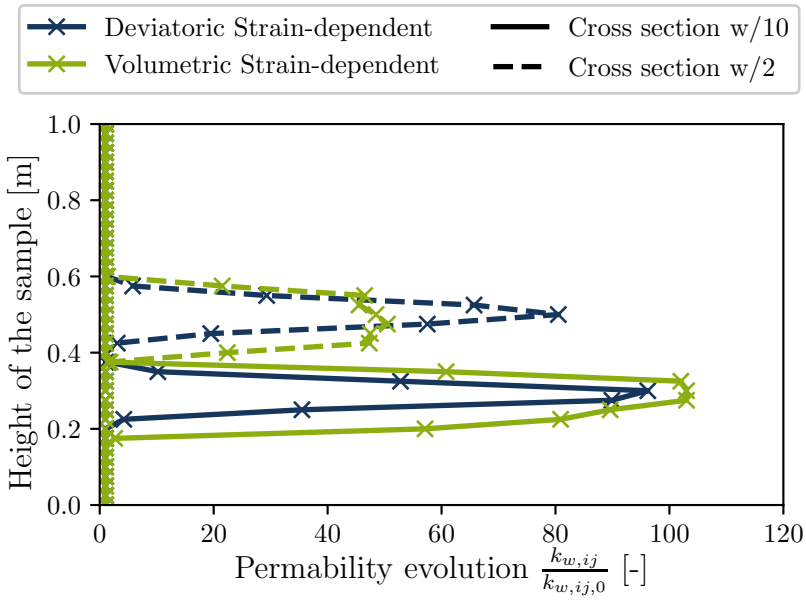

Figure 4.15.: Comparative analysis of strain-dependent permeability evolution methods along two vertical cross sections (see Figure 4.14) in the biaxial model subjected to a shearing path

4.3.4. Effect of the evolution parameter β_{per} on volumetric strain-dependent permeability evolution

In this subsection, the influence of the evolution parameter β_{per} in the volumetric strain-dependent permeability evolution method is analyzed. As shown in Equation 2.51, β_{per} is the sole fitting parameter. To systematically investigate the influence of β_{per} on the model, the relative change in permeability with respect to the initial permeability $\frac{k_{w,ij}}{k_{w,ij,0}}$ is examined at the end of the loading phase (after 100,000 s). Since the change in permeability also affects the pore water pressure development, which in turn influences the stress path due to hydro-mechanical coupling, the relative change in pore water pressure $\frac{p_{\mathrm{w}}}{p_{\mathrm{w},0}}$ is also analyzed. The permeability evolution is depicted in Figure 4.16b and the change in pore water pressure in Figure 4.16c.

As evident in Figure 4.16b, an increase in β_{per} results in a corresponding increase in permeability. As β_{per} increases from 2×10^6 to 2×10^9, the permeability evolution ratio shifts from 1.5 to 493, representing an increase of approximately 330 times. The width over which the permeability increases is only minimally affected by β_{per}, indicating that β_{per} primarily influences the magnitude of the permeability increase.

When examining the changes in pore water pressure, a significant influence is evident. Due to the low permeability of Opalinus clay, the applied vertical displacements lead to an increase in pore water pressure, particularly in the center of the sample, as this region has the longest drainage path. Once the shear band forms, dilative behavior occurs within the shear band, leading to a reduction in pore water pressure. Additionally, as permeability increases, the pore water pressure can dissipate more rapidly. This effect is also observable in Figure 4.16c, where, for the highest value of β_{per}, the relative pore water pressure is at its lowest. At the sample's mid-height, the relative pore water pressure decreases by about 21% as β_{per} is reduced from 2×10^6 to 2×10^9.

It is also noteworthy that for $\beta_{per} = 2 \times 10^7$ to 2×10^9, the maximum change in pore water pressure remains constant across the entire width of the band, whereas for $\beta_{per} = 2 \times 10^6$, a more pronounced peak is observed. This can be explained by the fact that in the latter case the permeability is similarly low both inside and outside the shear band.

In summary, it can be stated that β_{per} has a significant impact on the magnitude of permeability within the shear band. However, the width over which this change occurs is practically independent of β_{per}. The next section will focus on the deviatoric strain-dependent method.

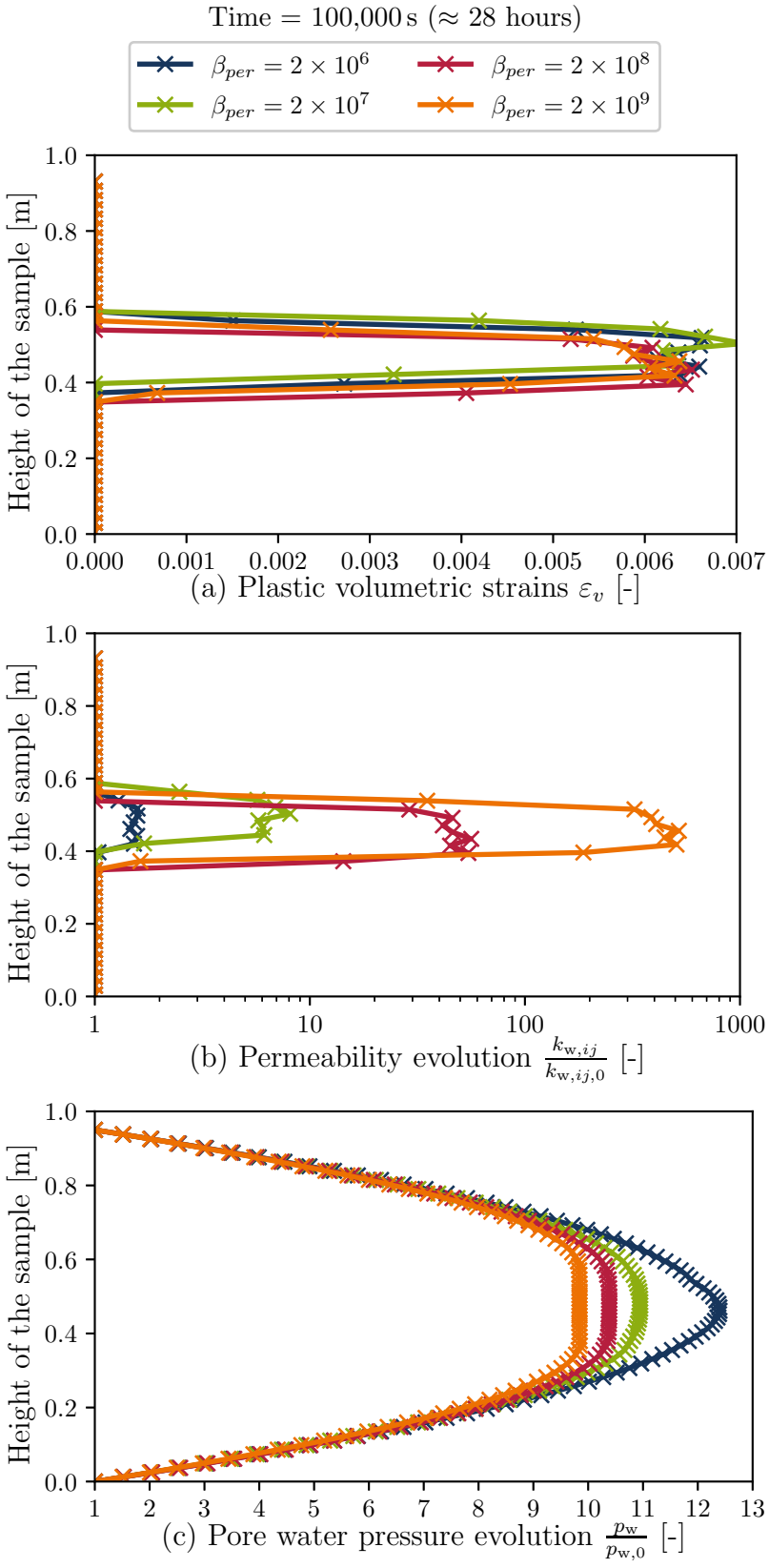

Figure 4.16.: Effect of β_{per} on volumetric strain-dependent permeability evolution method in the biaxial model subjected to a shearing path

4.3.5. Effect of the evolution parameter β_{per} on deviatoric strain-dependent permeability evolution

In this section, the influence of the evolution parameter β_{per} on the predictions with the deviatoric strain-dependent method is examined. Unlike the previous method, the deviatoric strain method has two key fitting parameters: the threshold yield index (YI^{thr}) and the evolution parameter β_{per}. To isolate the influence of β_{per}, YI^{thr} is fixed at 0.90 for this parameter study. Similar to the volumetric strain method, β_{per} in this context governs the evolution of permeability, but here it is dependent on deviatoric strains.

As in the previous section, the development of permeability and pore water pressure along the center of the model is analyzed, as shown in Figure 4.17. Furthermore, the current yield index YI and the deviatoric strains ε_{eq}, which are the model inputs determining the permeability evolution are depicted in Figures 4.17a and 4.17b, respectively. A clear trend emerges, indicating that β_{per} influences the magnitude of the buildup, as well as the dissipation of excess pore water pressure caused by vertical deformations (4.17d). Since the values of deviatoric strains and volumetric strains are not directly comparable, a direct comparison of the two methods using the same β_{per} value is not meaningful.

Unlike the volumetric strain-dependent method, the permeability evolution significantly varies across the height of the shear band. A peak is observed in the middle of the band because the highest deviatoric strains occur in the center of the shear band, as shown in Figures 4.13c and 4.17b. Furthermore, the permeability change is also influenced by the difference between the current yield index YI and the threshold yield index YI^{thr}, as described in Equation 2.52. In the center of the shear band the yield index equals one, meaning that the stress path is on the yield surface, while at the edges of the shear band, the values are below one as illustrated in Figure 4.17a. This also contributes to the observed peak formation. This aspect will be further explored in the next section, which examines the influence of the threshold yield index YI^{thr}.

The changes in pore water pressure (4.17d) lead to the same conclusions as in case of the volumetric strain-dependent method (see Section 4.3.4).

When comparing the zone where the yield index YI exceeds the threshold value of $YI^{\text{thr}} = 0.9$, highlighted by a gray region in Figure 4.17a, with the permeability evolution in Figure 4.17c, a broader area of increased permeability can be observed. An explanation can be derived from Figure 4.18, which illustrates a comparison of key model inputs and results, including the yield index (YI), deviatoric strain (ε_{eq}), pore water pressure (p_w), and permeability (k_w). These quantities are presented for two values of the deviatoric

strain-dependent permeability evolution parameter, $\beta_{per} = 3 \times 10^3$ and $\beta_{per} = 3 \times 10^6$, at a time before strain localization ($t = 45,000\,\mathrm{s}$). Even before localization occurs, a yield index YI greater than $YI^{\mathrm{thr}} = 0.9$ is found in the center of the model, as illustrated in Figures 4.18a and 4.18e.

This phenomenon can be analyzed by considering the stress path of an element located at the center of the model, as depicted in Figure 4.19. As axial deformation increases, deviatoric stress q rises. Due to the low permeability of Opalinus clay, an excess pore water pressure develops in the model's center, as illustrated in Figures 4.18c and 4.18g, reducing the effective stresses. At the time step of $t = 45,000\,\mathrm{s}$, the element is already close to the yield surface, as depicted by the red point in Figure 4.19. This explains why a yield index YI greater than 0.9, as well as deviatoric strains ε_{eq}, are present in the center of the model.

Depending on the chosen β_{per}, this leads to varying range of permeability increase, as illustrated in Figures 4.18d and 4.18h for $\beta_{per} = 3 \times 10^3$ and $\beta_{per} = 3 \times 10^6$, respectively. With $\beta_{per} = 3 \times 10^3$, the permeability increase in the model's center is minimal, whereas with $\beta_{per} = 3 \times 10^6$, a significant increase up to 10 times the initial permeability is observed. This early increase in permeability, before localization, is visible in Figure 4.17c. Therefore, the selection of a proper value for the threshold yield index YI^{thr} and the evolution parameter β_{per} is crucial for accurate modeling.

For a comprehensive understanding of this method, the following section will analyze the influence of the threshold yield index YI^{thr}.

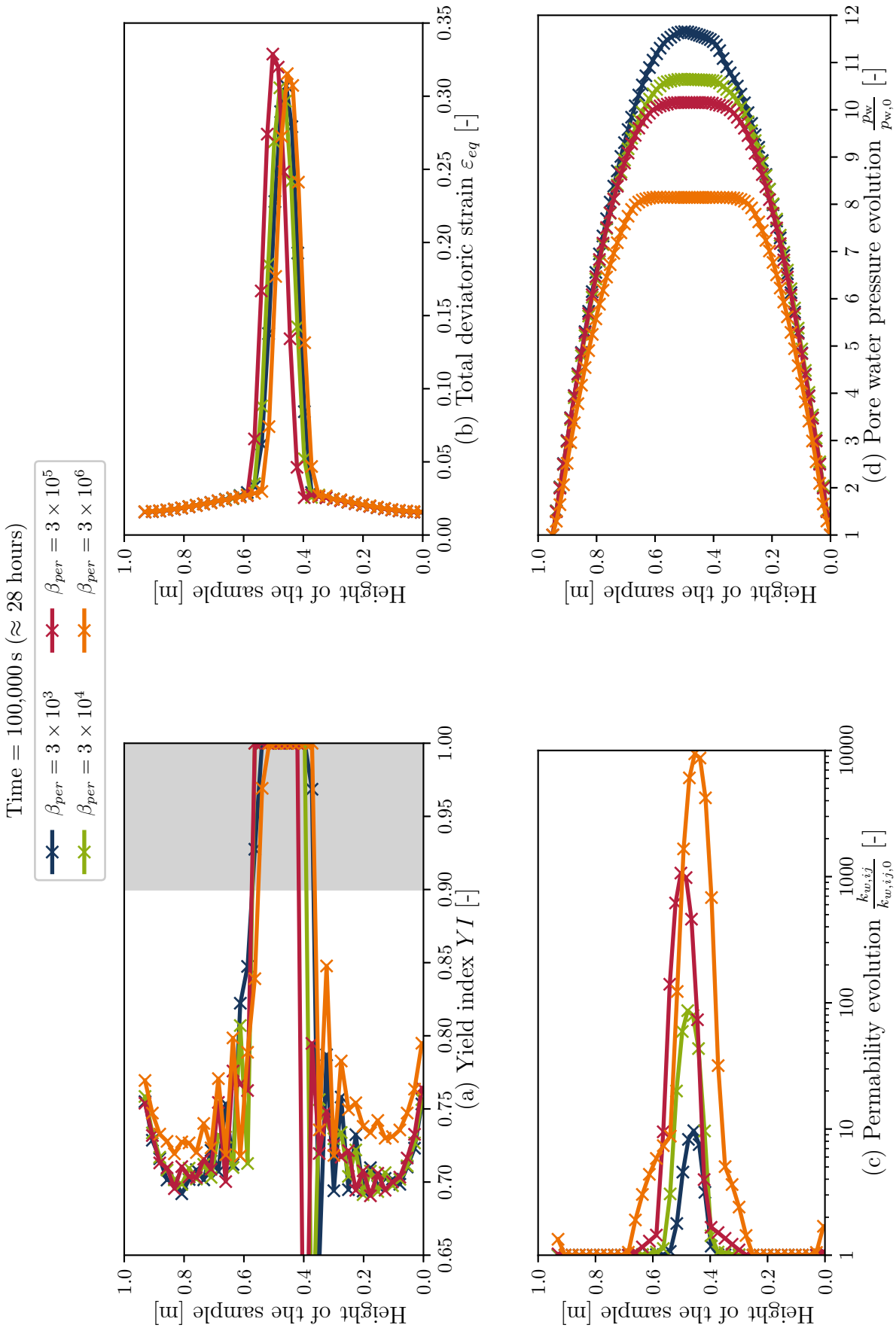

Figure 4.17.: Effect of β_{per} on deviatoric strain-dependent permeability evolution method along the central cross section of the biaxial model subjected to a shearing path

$\beta_{per} = 3 \times 10^3$

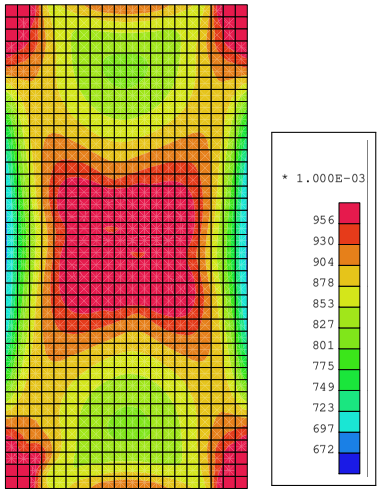

(a) Yield index YI

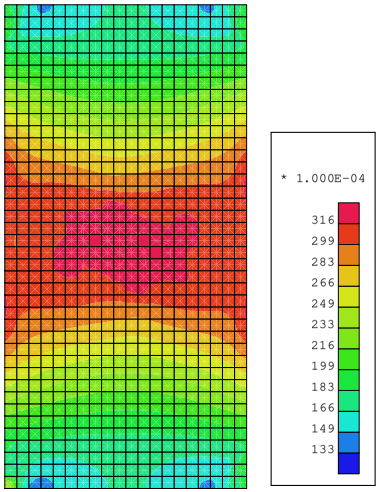

(b) Deviatoric strain ε_{eq}

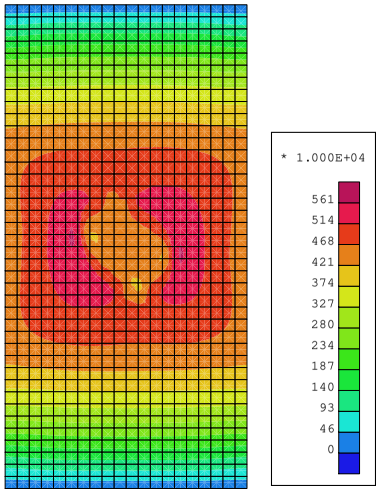

(c) Pore water pressure p_w

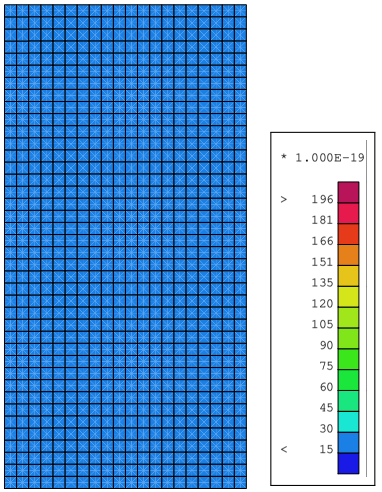

(d) Permeability k_w

$\beta_{per} = 3 \times 10^6$

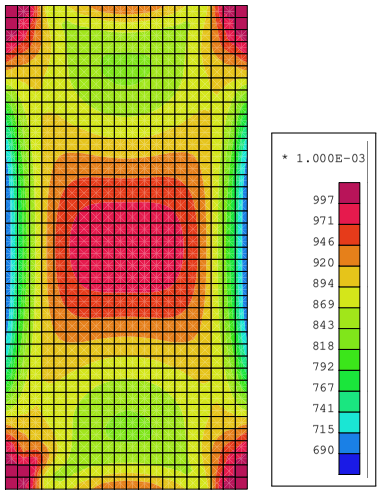

(e) Yield index YI

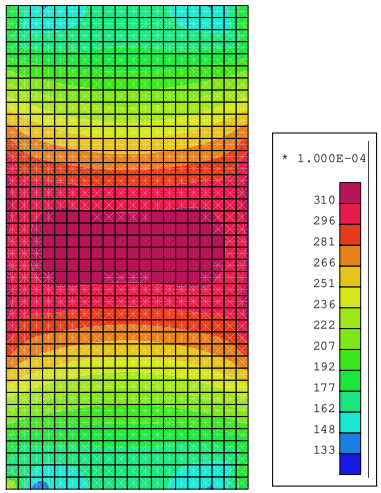

(f) Deviatoric strain ε_{eq}

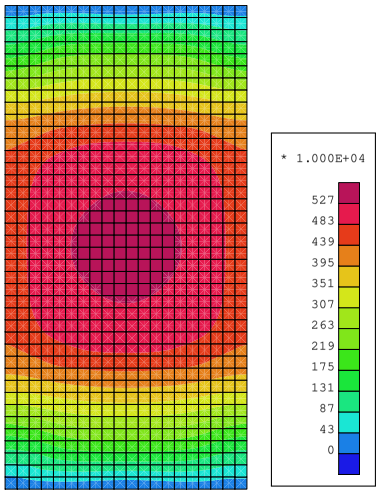

(g) Pore water pressure p_w

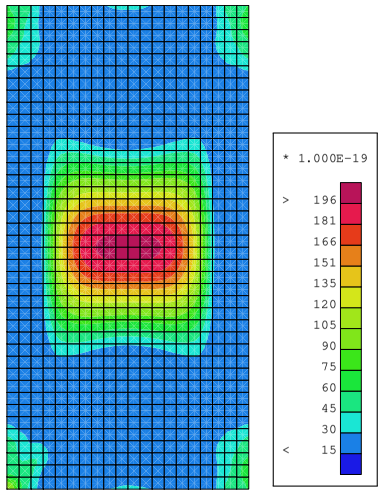

(h) Permeability k_w

Figure 4.18.: Comparison of $\beta_{per} = 3 \times 10^3$ and $\beta_{per} = 3 \times 10^6$ of deviatoric strain-dependent permeability evolution method before localization (time = 45,000 s)

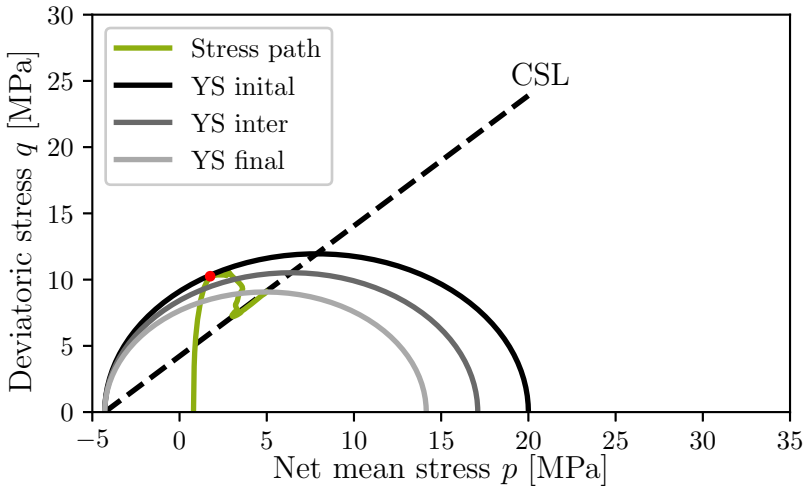

Figure 4.19.: Stress path of the central element of the biaxial model in the shearing path scenario with deviatoric strain-dependent permeability method

4.3.6. Effect of the threshold yield index YI^{thr} on deviatoric strain-dependent permeability evolution

As in the previous section, the two input variables, the yield index YI and deviatoric strain ε_{eq}, along with the output variables, the permeability evolution and the pore water pressure change, are examined along the center of the model and are shown in Figure 4.20. Four different threshold yield index values are analyzed, as outlined in Table 4.2. The evolution parameter is kept constant at $\beta_{\text{per}} = 3 \times 10^5$ for this study.

Apparently the yield index equals one on the shear band, while outside the shear band the yield index is 0.8 or lower, as can be seen in Figure 4.20a. This allows for a clear distinction between the inside and outside of the shear band. As for the resulting permeability change, only minor differences are observed. The width of the zone with increased permeability is similar, although it becomes slightly broader with lower YI^{thr} values. The maximum permeability increase on the shear band is higher for lower YI^{thr}, primarily because the calculation incorporates the difference between the current YI and the threshold, as described in Equation 2.52.

The change in pore water pressure correlates with the permeability change and can be explained, as previously, by the faster dissipation of pore water pressure due to increased permeability.

While the parameter study identifies minor differences in permeability changes when varying YI^{thr} between 0.80 and 0.95, the overall impact on permeability evolution remains rather small. Therefore, within this specific case, adjusting the threshold yield index has only a limited influence on the spatial extent of the material's permeability evolution.

However, as noted by Pardoen (2015), the threshold yield index plays a more significant role in modeling scenarios such as tunnel excavations, where it can be critical for capturing the extent of the increased permeability zone accurately.

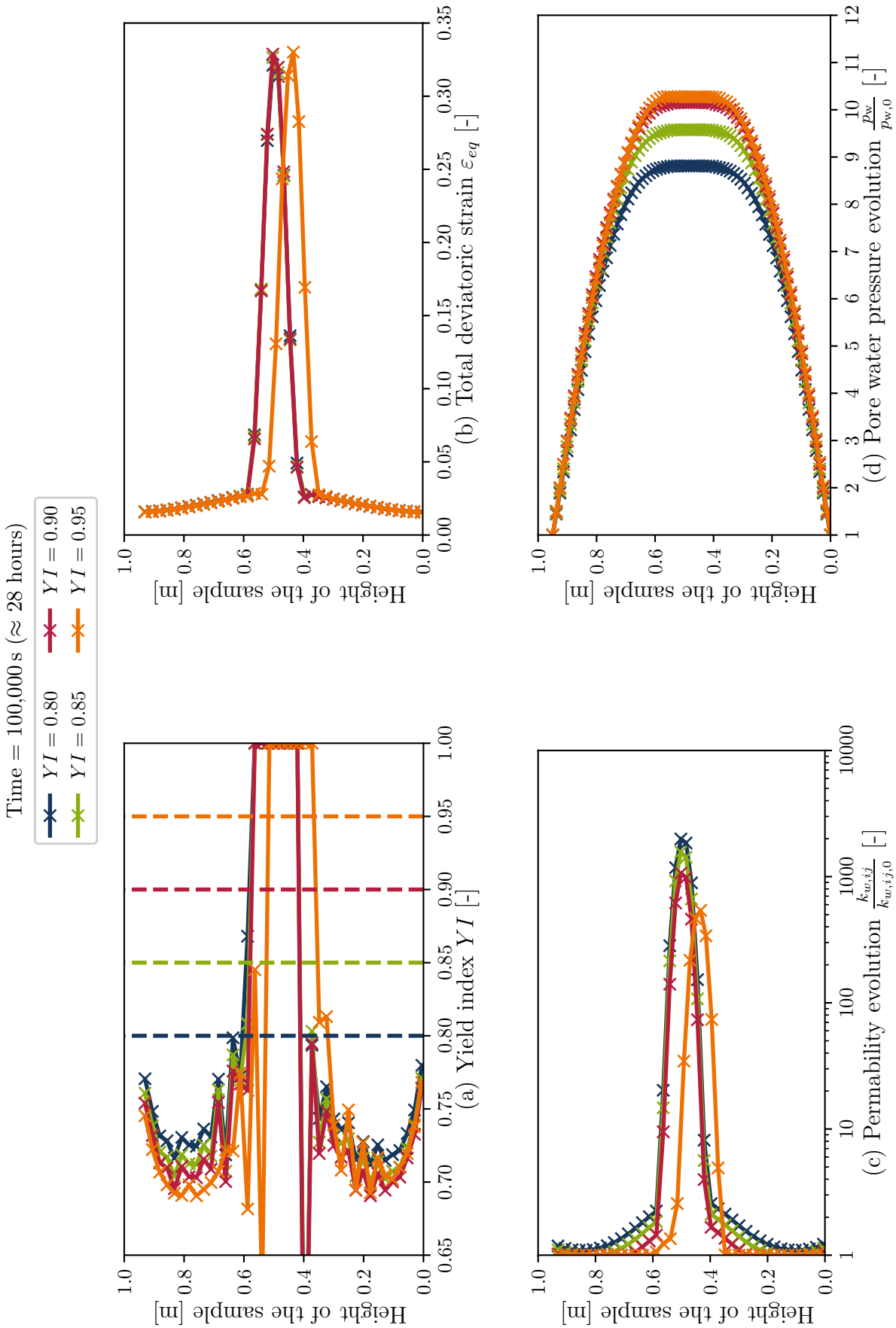

Figure 4.20.: Effect of YI^{thr} on deviatoric strain-dependent permeability evolution method along the central cross section of the biaxial model subjected to a shearing path (see Figure 4.14)

4.3.7. Effect of different permeability evolution methods during wetting path

In this section, the various permeability methods are investigated using the biaxial test model that follows the wetting path. The fundamental differences from the shearing path scenario were already discussed in Section 4.3.2. As an initial assessment, the input parameters of the two examined permeability models, volumetric strain and deviatoric strain, and their resulting permeabilities are shown in Figure 4.21. As highlighted in Section 4.3.3, the porosity-dependent Kozeny-Carman method is not suitable for achieving significant permeability increases in the shear band, and therefore it is not further considered in this section. The analysis focuses on the time up to the last stage of localized failure at 95,000 s. All models presented here are computed with a second gradient parameter of $D = 2000\,\mathrm{N}$.

As with the shearing path scenario, the resulting permeability change within the band in the case of the deviatoric strain-dependent method is more homogeneous than that of the volumetric strain-dependent method. However, unlike in the shearing path scenario, the band of increased permeability is similarly wide. This occurs because the wetting path scenario generally exhibits less softening, leading to lower volumetric strains. Furthermore, the movement of the shear band is restricted as all elements outside the initial shear band are very close to plasticity, with high yield indices, preventing shear band movement.

For a systematic evaluation, the two cross sections, w/10 and w/2 (see Figure 4.14), are analyzed, as presented in Figure 4.22. Similar to the shearing path, there is a concentration of volumetric strain at the model boundaries, which leads to an increased permeability in the volumetric strain-dependent method. Given the existence of a more homogeneous zone within the model center, cross section w/2 is selected for subsequent analysis.

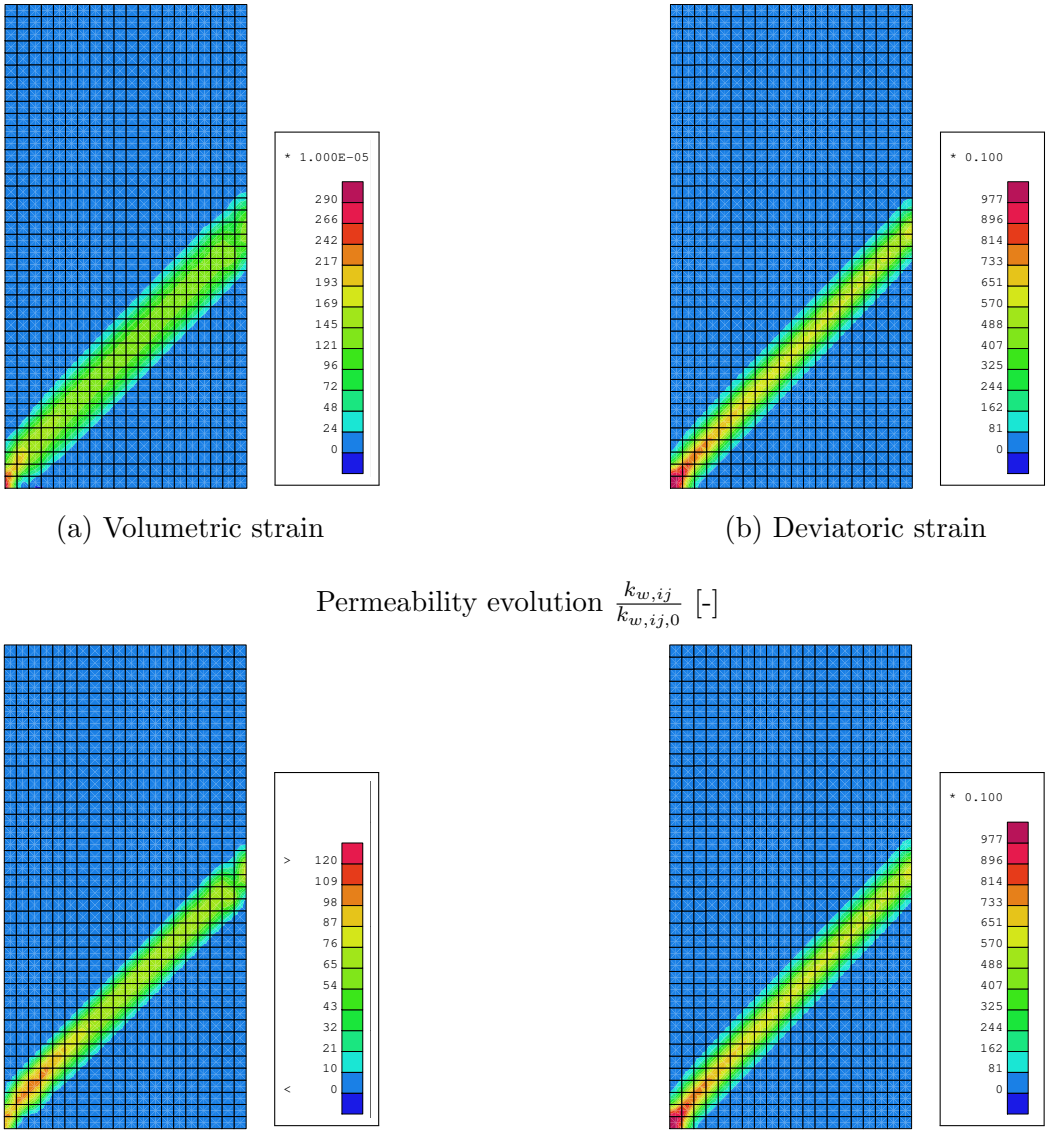

(a) Volumetric strain

(b) Deviatoric strain

(c) Volumetric strain-dependent method

(d) Deviatoric strain-dependent method

Figure 4.21.: Comparison of permeability evolution within the numerical biaxial model subjected to a wetting path. Left: volumetric strain-dependent method; Right: deviatoric strain-dependent method (time = 95,000 s, D = 2000 N)

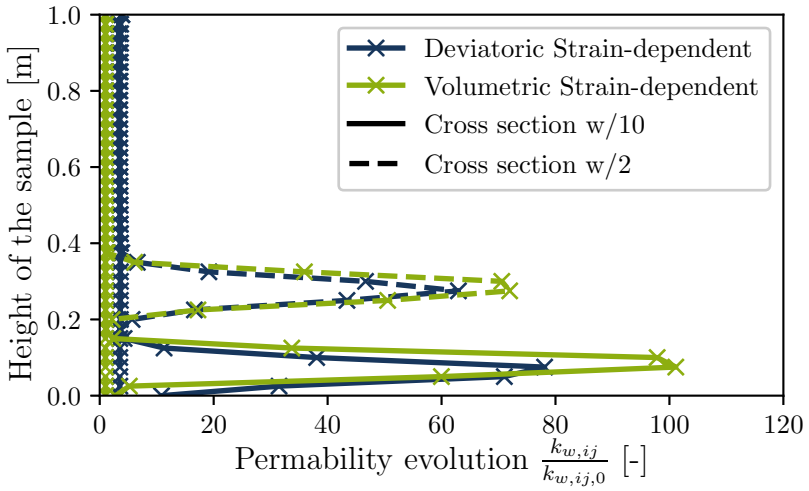

Figure 4.22.: Comparative analysis of strain-dependent permeability evolution methods along two cross sections in the biaxial model subjected to a wetting path

4.3.8. Effect of β_{per} on volumetric strain-dependent permeability evolution

This section investigates the influence of the evolution parameter β_{per} of the volumetric strain-dependent permeability evolution method (see Equation 2.51). The plastic volumetric strains, which are an input for this method, and the resulting permeability changes along the cross section w/2 are shown in Figure 4.23. Four simulations are conducted with $\beta_{\text{per}} = 3 \times 10^8$, 3×10^9, 3×10^{10}, and 3×10^{11}. Since in the wetting path scenario the pore water pressure is globally prescribed at all nodes to achieve saturation, it is not displayed here. Figure 4.23a illustrates that plastic volumetric strains of approximately 0.0015 develop, with an identical distribution over the height for all four values of β_{per}. This can be explained by the global prescription of pore water pressure, resulting in the same effective stresses during localization and, consequently, no variation in the resulting volumetric strains. When comparing the volumetric strains between the two scenarios, wetting path and shearing path, it becomes evident that significantly smaller volumetric strains occur in the wetting path scenario. This can be attributed to the lower softening in the wetting path scenario.

In Figure 4.23b, the influence of the evolution parameter β_{per} is clearly visible. As β_{per} increases, the permeability evolution also increases. However, it is evident that the width of the zone with increased permeability is not affected by β_{per} and remains consistent with the results from the shearing path scenario.

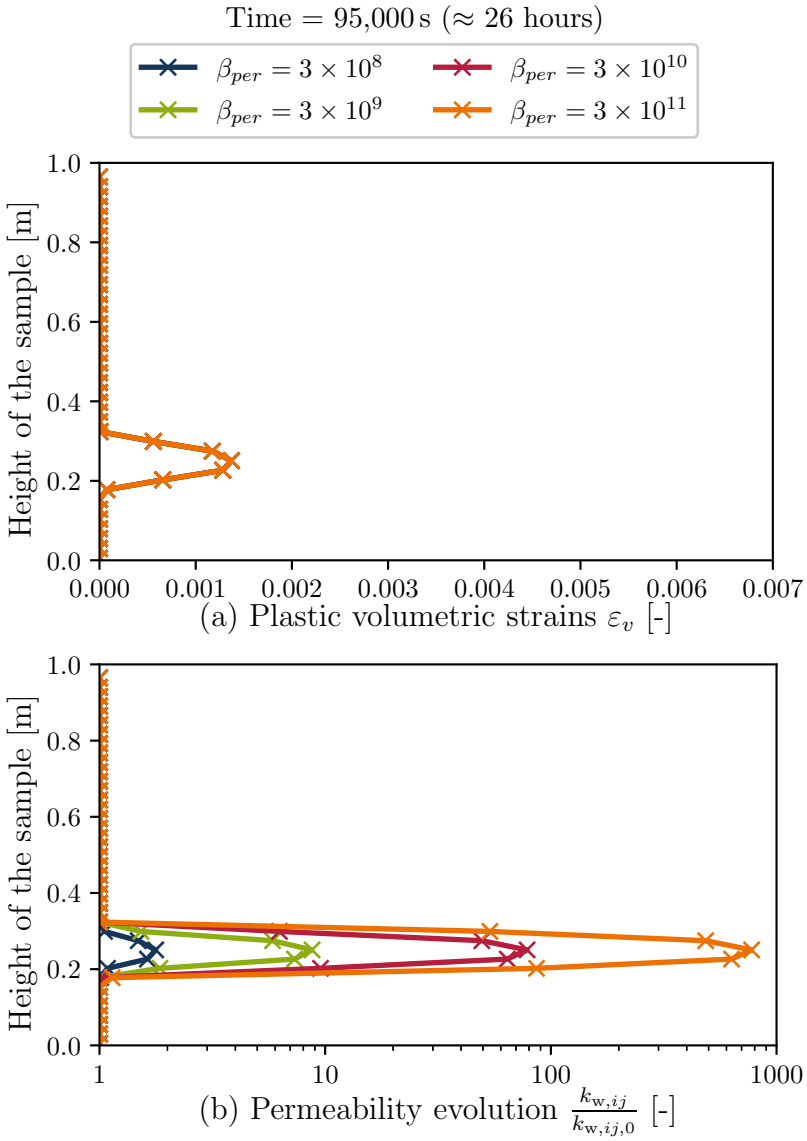

Figure 4.23.: Effect of β_{per} on volumetric strain-dependent permeability evolution method in the biaxial model subjected to a wetting path

4.3.9. Effect of β_{per} on deviatoric strain-dependent permeability evolution

In the previous section, the evolution parameter β_{per} was examined in the context of the volumetric strain-dependent permeability model. In the present section, a similar investigation is conducted with regard to its influence on the deviatoric strain-dependent method (see Equation 2.52). The input variables, yield index and deviatoric strain, as

well as the resulting permeability changes across the model height, are illustrated in Figure 4.24.

As shown in Figure 4.24a, an oscillation of the yield index can be observed. This originates from the method used to calculate the yield index, defined as the normalized distance from zero deviatoric strains to the yield surface in a $p - q$ plane, which represents a simplification for a three-dimensional yield surface such as that of the BBM. While the BBM incorporates not only the $p-q$ plane but also the s-axis, meaning the true distance must be calculated in 3D space, a more complex derivation of the yield index is beyond the scope of this thesis, particularly due to the limited benefit it would provide.

To ensure that permeability increases only within the shear band, it is essential to select a threshold yield index YI^{thr} that clearly distinguishes between the inside and outside of the shear band. As seen in Figure 4.24a, all points are close to plasticity ($YI = 1$), making the choice of this threshold particularly important in the wetting path scenario. A threshold yield index of $YI^{\text{thr}} = 0.99$ is selected, as shown by the gray-shaded area in Figure 4.24a. To assess the influence of β_{per}, four models are computed with different values of β_{per}.

As with the volumetric strains, the deviatoric strains across the model height are identical for all four models. This can be attributed to the globally prescribed pore water pressure, which results in no changes in the effective stress path, in a manner analogous to that observed with the volumetric strains. Additionally, the deviatoric strains are significantly lower compared to the shearing path scenario, which is due to the reduced softening in the wetting path scenario.

Regarding permeability changes, a clear influence of β_{per} is observed: as β_{per} increases, the permeability change becomes larger. The expansion of the zone with increased permeability as β_{per} increases can be explained by the fact that all nodes outside the shear band are close to plasticity ($YI = 1$), and depending on the time step, some of them are occasionally included in the permeability calculation.

Given that the majority of elements are situated close to the plasticity threshold, an investigation into the impact of the threshold yield index in the context of the wetting path scenario is not a viable avenue for research.

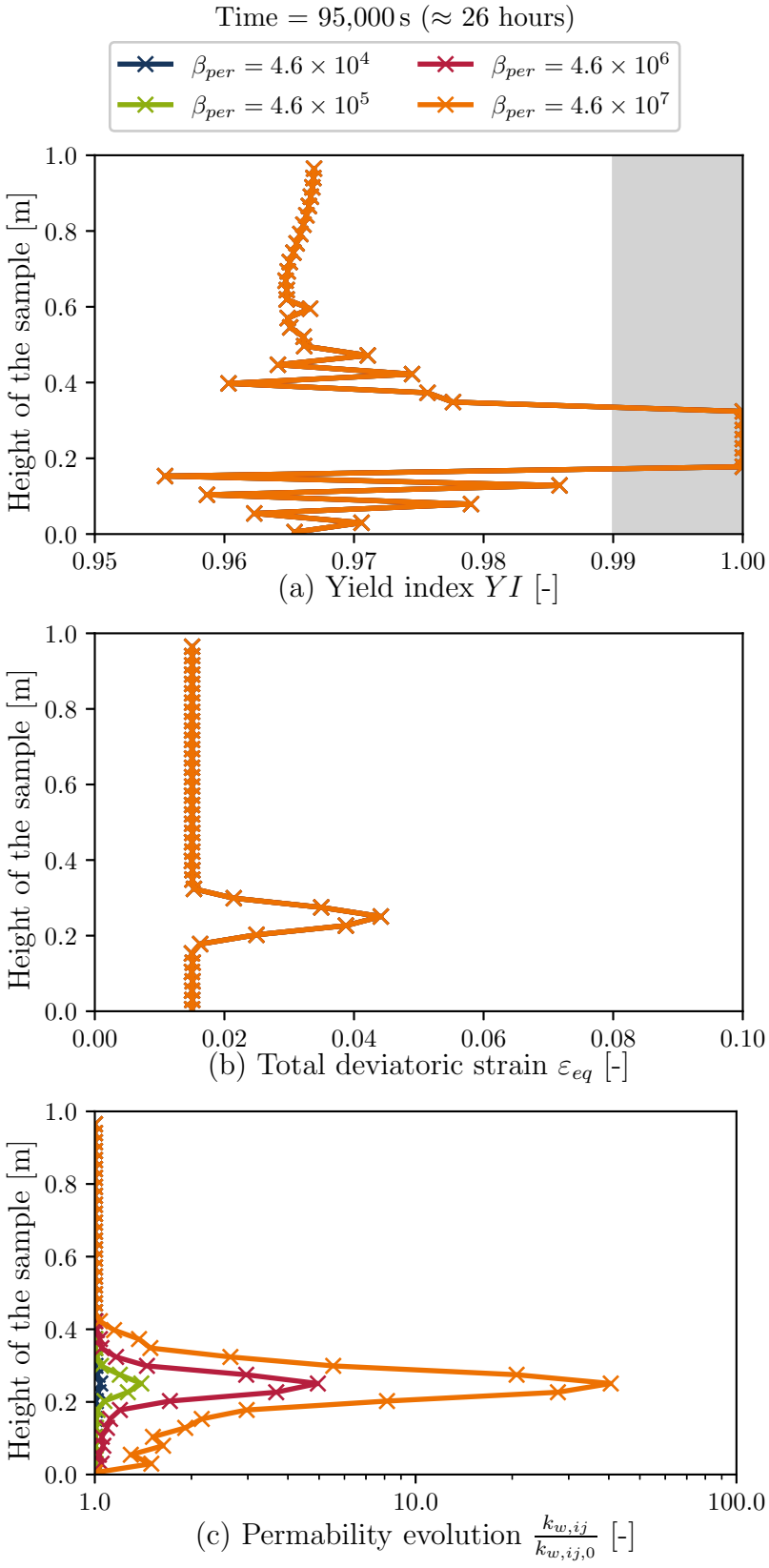

Figure 4.24.: Effects of β_{per} on deviatoric strain-dependent permeability evolution method in the biaxial model subjected to a wetting path

4.4. Conclusion

In the previous sections, both the influence of element size and the effect of the elastic modulus of the microstructure D on shear band localization were investigated. Two stress path scenarios, namely shearing and wetting path, were analyzed. Although these scenarios are quite different, they are both relevant to the upcoming tunnel excavation simulation presented in the next chapter. It was demonstrated that the local second gradient method enables mesh-independent shear band localization and that the elastic modulus of the microstructure D, serving as an internal length scale, directly influences the shear band width. After determining an appropriate mesh and an elastic modulus D that ensures a minimum of three elements across the shear band width, various approaches to increase the permeability within the shear band were explored. These approaches were rigorously evaluated through a parameter study, where each individual input parameter was changed at a time.

Notably, the deviatoric strain-dependent method yielded a more homogeneous permeability evolution within the shear band compared to the volumetric strain-dependent approach. Both methods feature an evolution parameter β_{per}, which allows control over the degree of permeability increase. Additionally, the inclusion of a threshold yield index in the deviatoric strain-dependent method offers more precise control over the zone affected by the permeability increase, which is particularly crucial for confining this effect to the shear band zone. As a result, the deviatoric strain-dependent method was chosen for the subsequent tunnel excavation simulations to effectively manage permeability increases in the Excavation Damaged Zone (EDZ). As demonstrated by the two different stress paths, the selection of the evolution parameter β_{per} and the threshold yield index YI^{thr} must be recalibrated for each individual stress path. Therefore, the values obtained here can only serve as an initial reference point for the subsequent tunnel excavation simulations.

5. Numerical modelling of mechanized tunnel excavation

5.1. Introduction

Following a detailed examination of strain localization through biaxial testing in the previous chapter, with a special focus on the conditions and stress paths under which the Barcelona Basic Model (BBM) exhibits localization and the various approaches linking permeability increase to shear band localization, the focus now shifts to tunneling and the simulation of the Excavation Damaged Zone (EDZ).

Tunnel excavation is a challenging three-dimensional problem that requires advanced constitutive models for components such as soil, tunnel lining, and grouting materials. Simulating the excavation process and tunnel lining construction with accuracy incurs significant computational costs and requires advanced tools. Moreover, modeling the EDZ necessitates enhanced knowledge of material behavior and complex interactions, making the modeling process not only computationally demanding but also inherently complex. To balance accuracy and computational efficiency, this study adopts a 2D plane strain analysis that incorporates sophisticated constitutive models and the second gradient method for mesh-independent strain localization.

To address the absence of the excavation direction, which is represented as the third dimension missing in a 2D plane strain model, the convergence-confinement method is applied. This method does not directly simulate the step-wise tunnel excavation but instead controls the tunnel convergence as a function of the tunnel boring machine (TBM) advancement, thereby mimicking the step-wise excavation process within the plane strain framework. By approximating the effects of excavation progression in the missing dimension, this approach allows for a more realistic simulation of the excavation process while maintaining computational effort affordable, avoiding the complexity and high computational cost of a full 3D model. As established in the previous chapter, certain model

parameters, such as mesh size as well as strength and number of material imperfections, require further examination to improve parameter estimates. Accordingly, in this chapter a parameter study is performed to refine these settings. The chapter also adopts the swelling phenomena studied in Chapter 3.1, analyzing various tunnel support strategies with a focus on resulting tunnel support deformations and internal forces of the tunnel lining. As a consequence, a modified convergence-confinement curve is developed using data extracted from an axisymmetric numerical model of tunnel excavation, enhancing the tunnel excavation simulation.

The chapter opens with a brief explanation of the case study (Section 5.2), which provides the model geometry and initial stress conditions. For material properties, values derived from the literature review in Section 3.2 are used, as they align well with the selected case study due to being for the same material, at the same depth, and within the same geological context, although from different locations. The next sections introduces the 2D plane strain numerical model of the tunnel excavation in detail, addressing boundary conditions, discretization, and tunnel excavation techniques. Subsequently, a systematic analysis of the EDZ is performed based on various results, followed by an investigation of the temporal evolution of the EDZ. A parameter study then evaluates the influence of various relevant parameters on the size and shape of the EDZ, with the goal of identifying key parameters impacting model outcomes, particularly the dimensions of the EDZ (Section 5.5).

The analysis proceeds to assess different tunnel support strategies, comparing unsupported tunnel excavation with two types of supported tunnel strategies, namely rigid support and deformable support, and examining their effects on the EDZ (Section 5.6). Finally, a modified convergence-confinement method is introduced, deriving critical information such as the longitudinal displacement profile from an axisymmetric numerical model (Section 5.7). After validating the internal force reduction method used in the axisymmetric model, which is essential for simulating the progressive tunnel excavation, a modified convergence-confinement curve is constructed and utilized in a new calculation of the plane strain model for the tunnel excavation. The results of this simulation are then analyzed in terms of the temporal evolution of the EDZ and compared with the linear convergence-confinement method used in the parameter study. The chapter concludes with a summary of findings in Section 5.8.

5.2. Case study: The new Belchen tunnel project

For modeling mechanized tunnel excavation in swellable clay shales, the simulation should be based on realistic boundary conditions, ideally on a real project. Consequently, the New Belchen Tunnel was selected as a case study for the subsequent tunnel simulations, and its key characteristics are briefly summarized in this section.

The New Belchen Tunnel, located between Basel and Lucerne in Switzerland, is a 3.2 km long tunnel. Over the course of their lifespan, the older tunnels have experienced damage caused by swelling anhydrite and Opalinus clay shale (Grob, 1972). As a result, a third tube was excavated in 2016 west of the existing ones (Ziegler and Loew, 2017). In contrast to the other two tubes, which were built in the 1960s using the NATM method, the new Belchen tunnel was excavated using the mechanized tunneling method.

The New Belchen Tunnel was constructed using a single-shield tunnel boring machine (TBM) with a cutter head diameter of almost 14 m and a 10 m long shield. Of the total tunnel length of 3.2 km, approximately 570 m are located in the Opalinus clay shale, as shown in Figure 5.1.

To prevent swelling induced damage like observed in the older tunnel tubes, a very robust tunnel support system was designed and built for the new tunnel. This includes a 35 cm thick segmental lining, a sealing membrane, and a 65 cm thick cast-in-place concrete layer (Ziegler et al., 2022). The overcut was approximately 22.5 cm and was filled with two-component grout material.

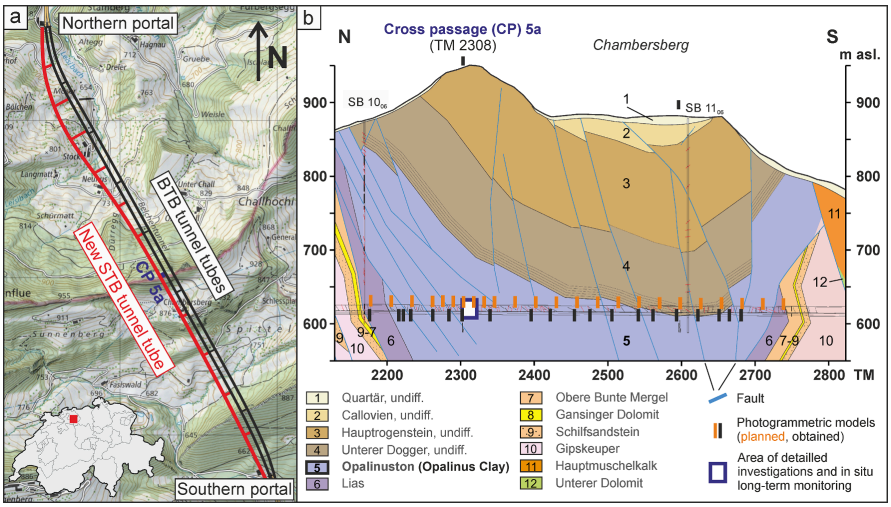

Figure 5.1.: (a) Topographic map (source: swisstopo) and (b) Geological profile of the New Belchen tunnel (Ziegler et al., 2022)

The tunnel passes through the Opalinus clay shale layer with varying overburden depths ranging from 200 m to 330 m. As Opalinus clay has gained considerable attention in recent years as a potential host rock for a repository for radioactive waste, its properties have been studied in great detail, as previously discussed in Section 3.2. The Opalinus clay shale in the Belchen region exhibits geological characteristics comparable to the shaly facies of Opalinus clay, which has been extensively examined at the Mont Terri Underground Research Laboratory. At tunnel meter (TM) 2300 - 2330 (see Figure 5.1), which is under an overburden of approximately 325 m, in situ measurements were conducted by the Swiss Federal Nuclear Safety Inspectorate (ENSI) (Martin and Lanyon, 2003; Ziegler and Loew, 2017; Renz et al., 2019; Ziegler et al., 2022). This cross-section was chosen as the reference for the subsequent simulations.

5.3. 2D plane strain model

Although tunnel excavation is inherently a three-dimensional problem, this thesis employs a 2D plane strain model to balance computational feasibility with the complexity of simulating both the excavation process and the Excavation Damaged Zone (EDZ). This section outlines the 2D plane strain model, beginning with a description of the geometry and boundary conditions. It then details the numerical simulation of the tunnel excavation process, followed by an exploration of the parameter study conducted to investigate the influence of model parameters on the EDZ.

5.3.1. Geometry and boundary conditions

The 2D plane strain tunnel model is based on the New Belchen Tunnel in Switzerland, as described in Section 5.2. The initial stresses at the Belchen tunnel depth are not explicitly available in the literature. However, measurements reported by Martin and Lanyon (2003) at the Mont Terri Underground Research Laboratory, located at a similar depth, indicate principal stresses of approximately 7 MPa. Assuming that vertical stresses are higher than horizontal stresses, the model assumes an initial vertical stress of 14 MPa and an initial horizontal stress of 7 MPa. While this assumption aligns with the data observed at Mont Terri, the exact values for Belchen remain uncertain. Additionally, a pore water pressure of 2 MPa is incorporated into the model, based on observations from the Mont Terri rock laboratory for Opalinus clay shale at a comparable depth (Amann et al., 2017).

To optimize computational efficiency, only a quarter of the tunnel is simulated by taking advantage of system symmetry. For the model discretization, the SGRT elements are used again. The model boundary conditions on the symmetry axes are chosen such that no water flow or deformation normal to the symmetry axis is possible. Additionally, due to the presence of gradient terms in the equilibrium equations of the second gradient model, a higher-order kinematic boundary condition must be imposed to maintain symmetry, according to Zervos et al. (2001) and Pardoen et al. (2016). This condition complements the classical boundary condition on normal displacements and ensures that the normal derivative of the radial displacement, with respect to the tangential direction along the symmetry axes is zero (Pardoen et al., 2016). To prevent the influence of boundary effects on the tunnel excavation, the model is sufficiently large, with dimensions of 200 m by 200 m. In the immediate vicinity of the tunnel, the mesh of the finite element model is refined, as illustrated in Figure 5.2a, resulting in 9827 nodes and 7365 elements.

As in the previous chapter, the Barcelona Basic Model (BBM) in conjunction with the local second gradient model is used for modeling. Additionally, based on the previous chapter, the deviatoric strain-dependent permeability approach is employed for the subsequent simulations.

For stress initialization, boundary stresses of 14 MPa in the vertical (y) direction and 7 MPa in the horizontal (x) direction are applied both at the model boundaries and within the tunnel. Throughout all nodes of the finite element model, an initial pore water pressure of 2 MPa was applied, resulting in net stresses of $\sigma'_y = 12\,\text{MPa}$ and $\sigma'_x = 5\,\text{MPa}$, yielding an earth pressure coefficient at rest $k_0 = 0.416$. Since the model boundaries represent the intact clay shale, both the pore water pressure of 2 MPa and the horizontal and vertical stresses are held constant at the boundaries.

Although temperature significantly influences the stiffness and swelling pressure of clay shales, it is assumed to remain constant at 20°C in this model to limit its complexity, which is already increased by the use of the second gradient formulation. This assumption aligns with the conditions under which all laboratory tests and parameter calibrations were conducted. At the Belchen site, the mean of the measured temperatures within the clay shale is approximately 15°C, based on in situ measurements (Ziegler et al., 2022). However, fluctuations due to concrete hydration during construction and seasonal variations have been observed by Ziegler et al. (2022). These temperature changes are not accounted for in the model to avoid adding further complexity, and the corresponding degree of freedom is fixed.

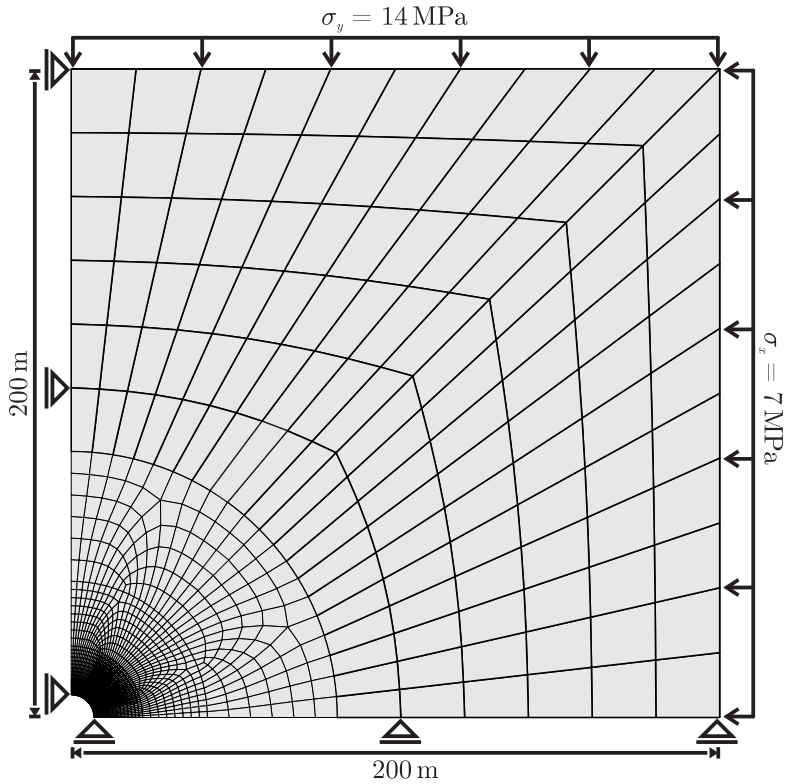

(a) Complete overview of mesh and boundary conditions

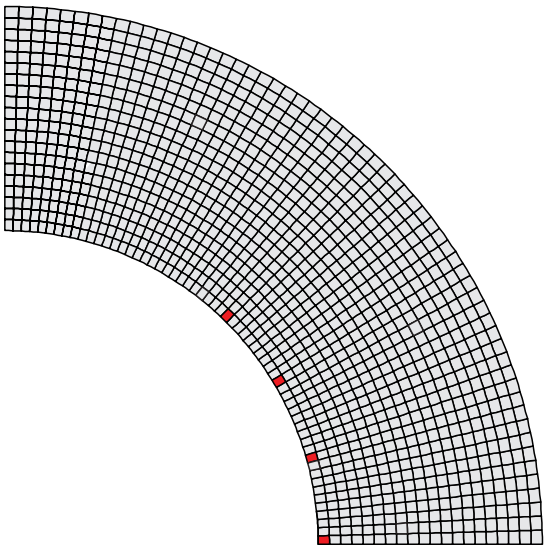

(b) Magnified area near tunnel excavation without support

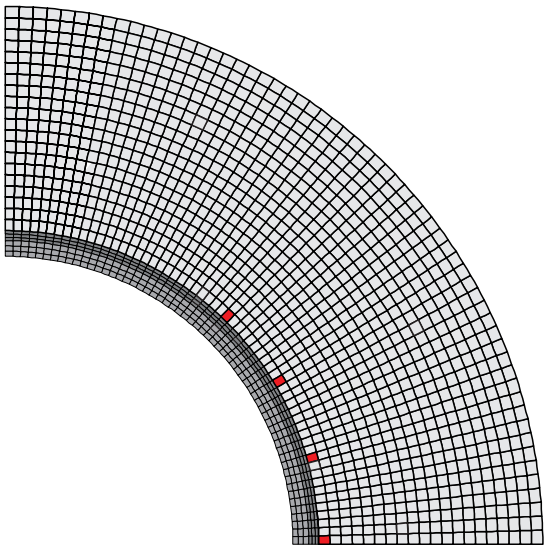

(c) Magnified area near tunnel excavation with support

Figure 5.2.: Schematic illustration of the 2D plane strain model employed in simulating the tunnel excavation of the Belchen tunnel

To ensure robust localization, elements with material imperfections, highlighted in red in Figures 5.2b and 5.2c, are incorporated into the model. The relevance of material imperfections has been detailed in the previous chapter. In the subsequent simulations, the material imperfection is introduced by reducing cohesion in certain elements, causing them to reach the plastic state earlier. Since the number, position, and strength of these material imperfections cannot be reliably determined in situ, they are highly uncertain and will consequently be addressed in the subsequent parameter study.

In addition to an unsupported tunnel, two different support strategies, namely rigid and deformable support, are investigated. Both strategies consist of a tunnel lining and a grout layer. The lining is modeled as a 35 cm thick layer, while the grout layer fills the void created by the 22.5 cm overcut between the outer diameter of the Tunnel Boring Machine (TBM) cutter head and the outer diameter of the tunnel lining (Ziegler et al., 2022). Consequently, the grout layer is assumed to have the same thickness of 22.5 cm as the overcut. The grout and lining are discretized with 180 elements, as shown in Figure 5.2c. A simplification applied in the model is that pore water pressure in all elements of the tunnel support is fixed at atmospheric pressure to prevent any fluid flow within these elements. Furthermore, the degrees of freedom related to the local second gradient model are restricted, as strain localization is not expected in the tunnel support system. The detailed modeling of the supported tunnel is presented in Section 5.3.4.

5.3.2. Simulation of the tunnel excavation process

To simulate the tunnel excavation, the convergence-confinement method described in Section 2.3.2.1 is employed. At the beginning of the simulation, when the tunnel has not yet been excavated, the radial pressure is applied to the tunnel wall, which is in equilibrium with the initial stresses. Due to the hydro-mechanical nature of the problem, the reduction of pore water pressure during excavation must also be considered.

Similar to the radial stress, the pore pressure acting on the tunnel wall is assumed to be a function of the deconfinement ratio λ_w.

$$p_w^{\Gamma} = (1 - \lambda_w)\, p_{w,0} \tag{5.1}$$

Where p_w^{Γ} represents the pore water pressure at the tunnel wall during excavation, and $p_{w,0}$ indicates the initial pore water pressure on the tunnel wall, which corresponds to the initial pore water pressure within the geological formation.

Since no additional measurements during the excavation, such as surface settlement measurements, are available, the reduction of radial stress to zero and that of pore water pressure to atmospheric pressure are assumed to occur linearly over the estimated mean excavation time of 4.5 h for each ring segment in the Belchen project, depicted in Figure 5.3.

Given the low permeability of the Opalinus clay used in this research, the Excavation Damaged Zone (EDZ) is investigated over a long period of 1000 days to assess the effects of swelling and other hydro-mechanical coupled interactions which might influence the EDZ. Therefore, the radial stress and pore water pressure, reduced during tunnel excavation, remain constant until 1000 days are reached. The details for the supported tunnel are explained in the subsequent section.

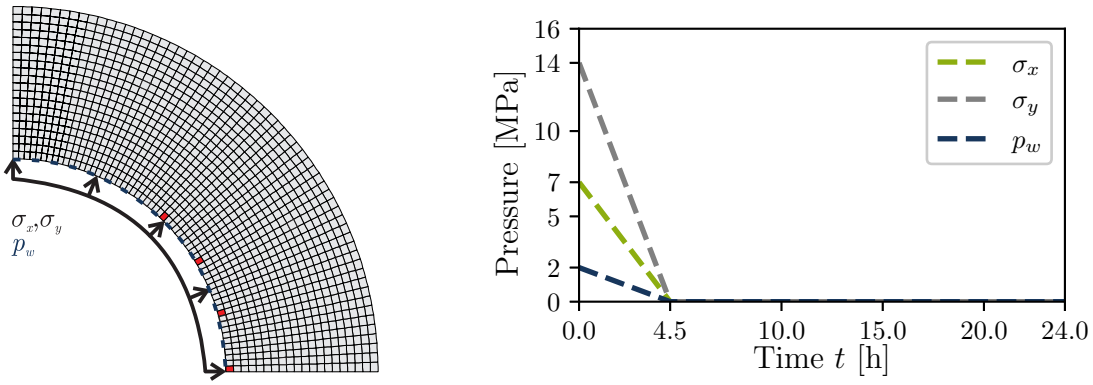

Figure 5.3.: Applied total stresses and pore water pressure at the tunnel wall

5.3.3. Constitutive parameters of tunnel support materials

Following the previous section's description of the modeling approach for tunnel excavation, the focus now shifts to the modeling of tunnel supports. Two scenarios, rigid and deformable support, are examined for the tunnel with support. Both, are based on the tunnel support system described for the Belchen Tunnel in Section 5.2, consisting of a tunnel lining and an annular gap grout. The difference between the two support systems lies in their approach to handling swelling pressures.

In the rigid support scenario, the tunnel support is designed to resist swelling pressures with little or no deformation. In contrast, the deformable support scenario allows the tunnel support to deform under the swelling pressure, which helps to reduce the magnitude of the pressure, similar to the behavior observed in the deformation-controlled swelling tests conducted on remolded Opalinus clay described in Section 3.4.2.

Both scenarios use the same tunnel lining, but differ in the grout composition of the annular gap. The grout in the deformable support is designed to allow for deformation, while the grout in the rigid support is meant to remain stiff and resist deformation.

5.3.3.1. Tunnel lining parameters

As described in Section 5.2, the tunnel support system consists of a segmental lining and a cast-in-place steel reinforced concrete layer, with a combined thickness of 100 cm as illustrated in Figure 5.4a. To reduce the complexity of the numerical model, both layers are treated as a single layer with a thickness of 35 cm and an increased equivalent stiffness, depicted in Figure 5.4b. Since no failure or plastic deformations of the tunnel lining are assumed, the tunnel lining is simplified and calculated using a linear elastic constitutive model. For this, a Young's modulus E and a Poisson's ratio ν are required.

To ensure realistic modeling of lining deformations, an equivalent stiffness, ensuring the same axial stiffness (EA), is determined using Equation 5.2. In this equation, the indices 35 and 100 denote the thicknesses of the simplified single-layer approach and the in situ dual-layer linings, respectively. The equivalent stiffness $E_{eq,35}$ is calculated based on the ratio of the areas A_{100} and A_{35}.

$$E_{eq,35} = \frac{\mathrm{A}_{100}}{\mathrm{A}_{35}} E_{100} \tag{5.2}$$

Although this model does not account for the stepwise construction of the tunnel support, first installing the segmental lining, followed by the cast-in-place concrete layer, this approach allows for future studies to incorporate such phasing by adjusting the stiffness during the simulation, starting with E_{35} during the segmental lining installation and changing to E_{100} when the cast-in-place concrete layer is installed, which is not in the scope of this research.

The specific concrete class used in the New Belchen Tunnel is not known to the author. However, a concrete class of C55/67, which corresponds to a Young's modulus of 38.2 GPa according to DIN EN 1992-1-1:2011, is assumed within this study. This leads to a calculated equivalent Young's modulus of around 100 GPa. The Poisson's ratio for the concrete lining, determined to be $\nu = 0.2$, is based on values cited in Ziegler et al. (2022).

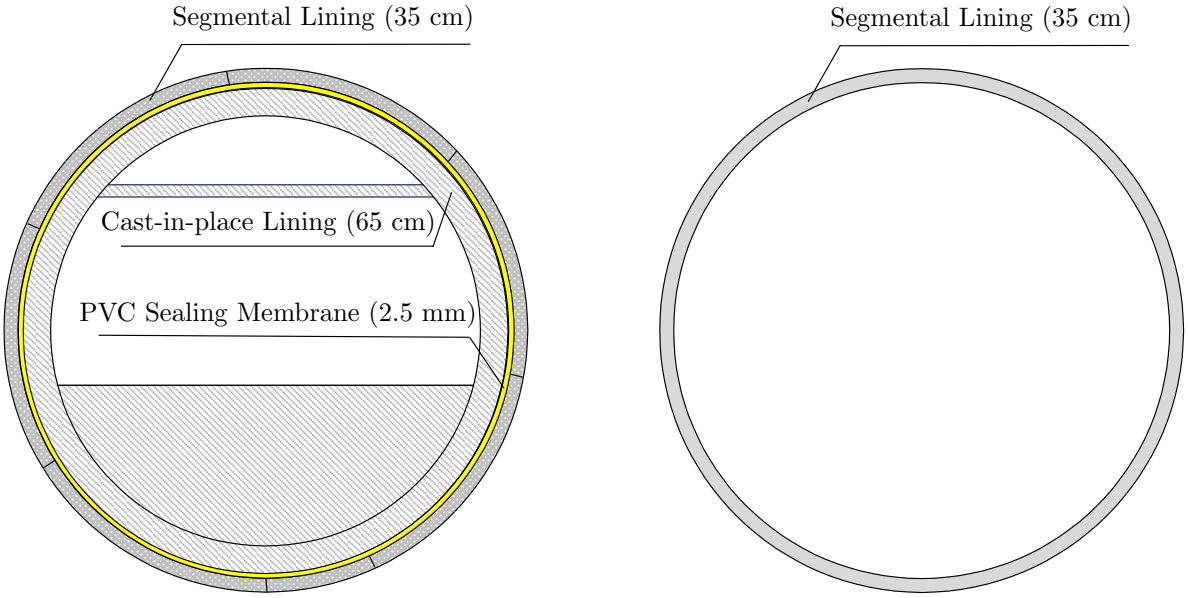

(a) In-situ: dual-layer lining (35 cm outer, 65 cm inner layer)

(b) Numerical model: simplified single-layer lining (35 cm)

Figure 5.4.: Comparison of schematic representations of tunnel lining: in-situ dual-layer (Ziegler et al., 2022) versus numerical model's simplified single-layer

5.3.3.2. Rigid grout parameters

In mechanized tunneling, the annular gap is filled with grout material. During the injection of this grout, it is in a liquid state and hardens over time. The time-dependent stiffness development of the grouting material has been studied in the literature by Shah et al. (2018); Lavasan and Schanz (2017); Marwan (2019).

For this research, the approach proposed by Marwan (2019) is utilized in a modified form. As seen in Figure 5.5, in the first six hours after injection, the stiffness of the grouting material increases from 10% to 75% of its final stiffness, which is achieved after a few days.

Instead of modeling the stiffness as a continuous time-dependent function, two distinct time periods are defined: one in which the grouting material remains liquid or soft, referred to as the soft phase, and another where the material has fully hardened, referred to as the hard phase (see Section 5.3.4).

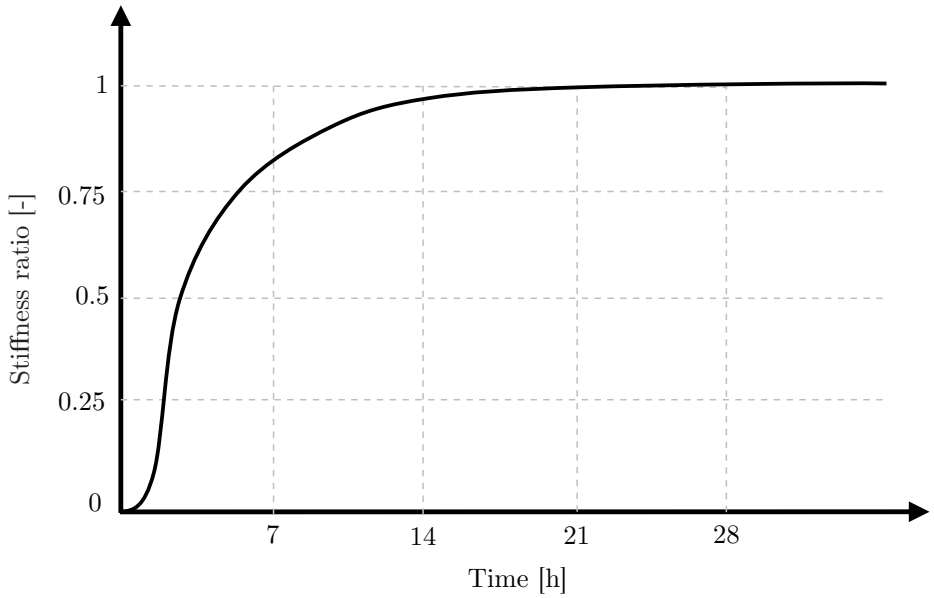

Figure 5.5.: Development of grouting stiffness with time after Marwan (2019)

For the modeling of the rigid grout, a linear elastic constitutive model is again employed, as no significant plastic deformations are expected. In the context of the New Belchen project, Uniaxial Compressional Strength (UCS) tests were conducted on hardened grout samples taken from the New Belchen Tunnel by Antonioli (2018), and the results are utilized for the constitutive parameters of the hard phase ($E_{\text{hard}} = 1.5\,\text{GPa}$ and $\nu = 0.3$), as detailed in Table 5.1. For the liquid phase, a stiffness ratio near the beginning of the curve depicted in Figure 5.5 is chosen. Accordingly, a value of $E_{\text{soft}} = 0.17 \times E_{\text{hard}} = 0.25\,\text{GPa}$ is selected to ensure a smooth numerical value.

5.3.3.3. Deformable grout parameters

In the scenario dealing with the deformable tunnel support, the grout material is allowed to deform under the influence of pressure, thereby reducing the pressure transfer to the tunnel support system. The behavior of these deformable grout materials, achieved by adding expanded glass or EPS, was investigated by Plückelmann and Breitenbücher (2020) through compression tests performed under oedometric boundary conditions. The resulting stress-strain curve is schematically illustrated in Figure 5.6.

As seen in Figure 5.6, initially, a linear elastic response (Stage I) is observed when increasing the axial strain ($\varepsilon_{\text{I–II}}$). Once a yield stress σ_{pl} is reached, a plastic behavior (Stage II) becomes evident, characterized by large plastic deformations ($\varepsilon_{\text{II–III}}$) at constant stress.

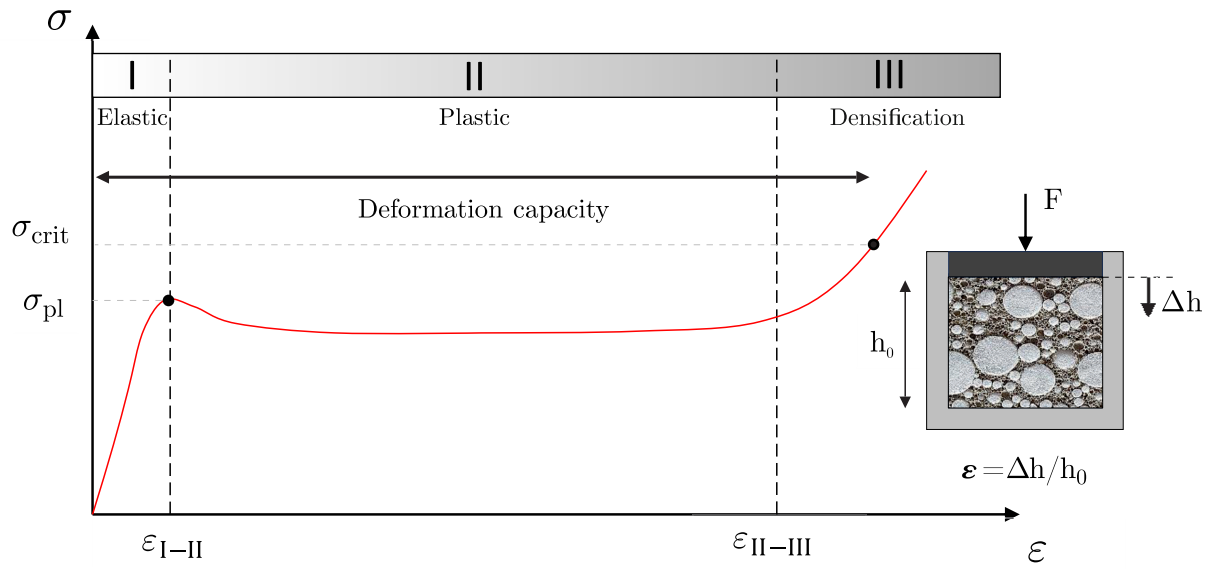

Figure 5.6.: Stress-strain behavior of deformable grout under oedometric boundary conditions after Plückelmann and Breitenbücher (2020)

In this stage, the voids created by foam and the addition of highly porous additives collapse. As the axial strains continue to increase, the material undergoes further densification, leading to a sharp increase in stress.

In the research conducted by Plückelmann and Breitenbücher (2020), various compositions of deformable grouting materials were investigated. For the deformable tunnel support examined in this research, the M4 material from Plückelmann and Breitenbücher (2020) is selected as the stresses developed in this material during axial loading are closest to the expected swelling stresses of Opalinus clay shale. Within the extensive testing program detailed by Plückelmann and Breitenbücher (2020), cylindrical samples were subjected to loading under oedometric boundary conditions. These tests are simulated to calibrate the corresponding model parameters, and the modeling approach is illustrated in Figure 5.7.

For the stress-strain behavior described in Figure 5.6, the previously used linear elastic constitutive model is inadequate, as it does not allow for plastic deformations. Therefore, the Modified Cam-Clay (MCC) model described in Section 2.2.3.2 is employed to model the hard phase of the deformable grout. It should be noted that the finite element framework Lagamine does not include a material model specifically tailored for deformable grout material. Although the MCC model was not originally developed for modeling grout material, it is capable of adequately reproducing the behavior observed in Figure 5.6.

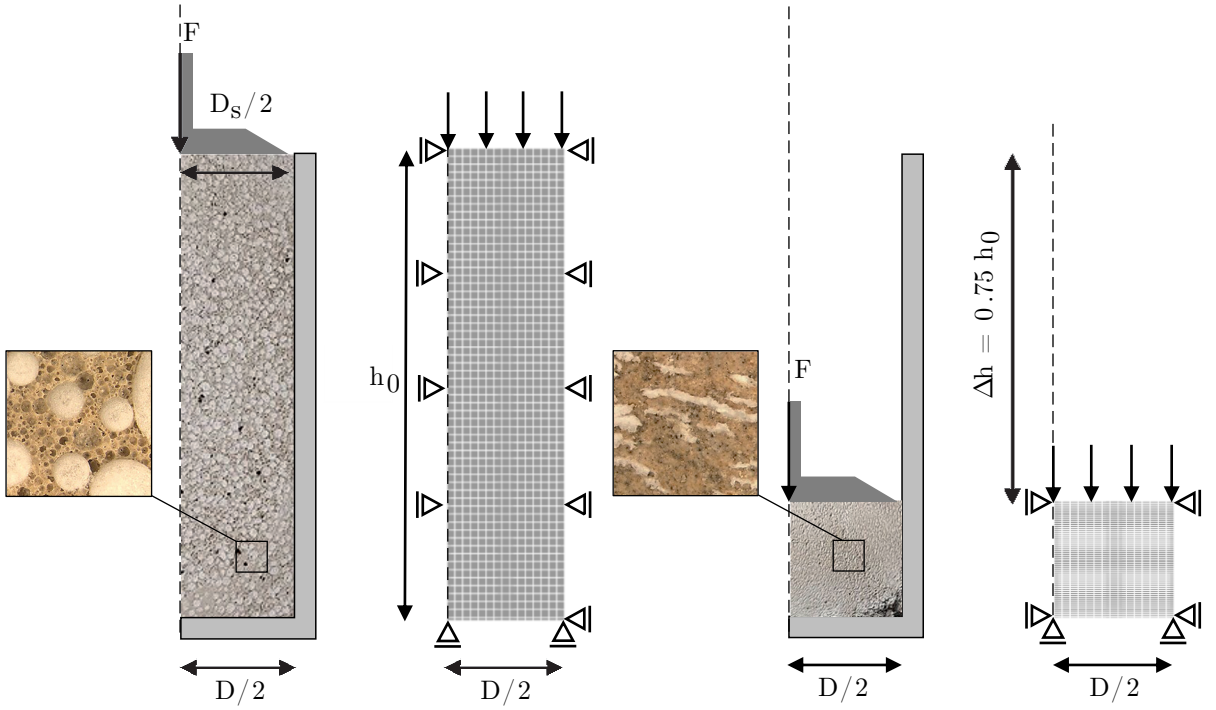

(a) before compression: (compression = 0 %) (b) after compression: (compression = 75 %)

Figure 5.7.: Comparison of the uncompressed and compressed states of the M4 specimen from experiments (Plückelmann and Breitenbücher, 2020) and numerical simulations, with annotations by the author

The results of the parameter calibration concerning the stress-strain curve are presented in Figure 5.8, and the determined constitutive model parameters can be found in Table 5.1. As shown in Figure 5.8, the experimental stress-strain behavior is well simulated using the Modified Cam-Clay model. The only aspect that could not be accurately represented is the stress response beyond $\varepsilon = 0.6$, which is, however, significantly outside the expected swelling strain range of Opalinus clay shale, estimated to be between $\varepsilon = 0.1$ and $\varepsilon = 0.12$ (see Section 3.4.1). Therefore, the underestimation of the measured stresses in that strain range can be accepted.

Similar to the rigid grout, a soft phase is also considered for the deformable grout. Since Marwan's investigation focused on non-highly deformable grouting materials, a ratio between final stiffness and soft phase stiffness of 0.4 is chosen instead of 0.17, as used for the rigid grout. This adjustment is made to avoid yielding excessively low stiffness values, which could lead to convergence issues in the finite element simulation.

All determined constitutive model parameters for the entire tunnel support are summarized in Table 5.1.

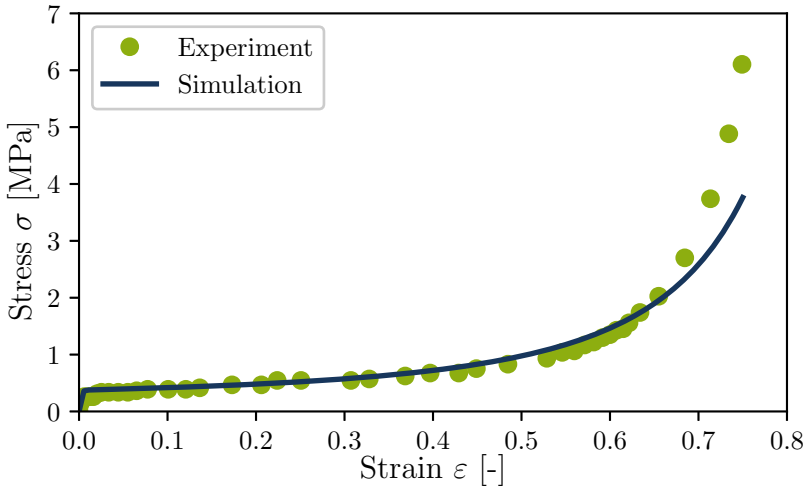

Figure 5.8.: Numerical and experimental (Plückelmann and Breitenbücher, 2020) stress-strain curves for deformable grout material M4

Table 5.1.: Mechanical parameters of tunnel support materials used in the numerical models of the supported tunnel

Rigid grout				
	Parameter	Symbol	Value	Unit
Soft state	Young's elastic modulus	E	0.25	GPa
	Poisson's ratio	ν	0.3	-
Hard state	Young's elastic modulus	E	1.50	GPa
	Poisson's ratio	ν	0.3	-
Deformable grout				
Soft state	Young's elastic modulus	E	0.08	GPa
	Poisson's ratio	ν	0.2	-
Hard state	Young's elastic modulus	E	0.20	GPa
	Poisson's ratio	ν	0.2	-
	Volumetric strain hardening parameter	H	0.9	-
	Preconsolidation pressure	p_0	0.15	MPa
	Friction angle for compressive paths	φ_C	25	°
	Friction angle for extensive paths	φ_E	25	°
	Cohesion	c	1	MPa
Tunnel lining				
	Equivalent Young's elastic modulus	$E_{eq,35}$	100	GPa
	Poisson's ratio	ν	0.2	-

5.3.4. Staged construction process of supported tunnel

As previously mentioned, not only an unsupported tunnel but also a tunnel with support will be investigated. As described in Section 5.3.1, the tunnel support consists of a tunnel lining and a layer of grouting material. Due to the tunnel excavation, the surrounding soil deforms. Once the soil is fully excavated, the tunnel lining is constructed with a predefined diameter within the tunnel boring machine, and the gap between the lining and the formation is filled with injected grouting material at the end of the shield tail.

Unfortunately, the exact width of the gap where the grout material is injected is not known prior to the simulation, as it depends on the ground deformation during excavation. To address this, the tunnel lining is activated from the beginning of the excavation, and a dummy layer with very low stiffness (elastic modulus of 0.05 MPa and Poisson's ratio of 0.01) is introduced between the tunnel lining and the Opalinus clay shale. The sole purpose of the dummy layer is to deform in conjunction with the ground.

As the grout material is liquid during injection and hardens over time, a soft grout layer is assumed between 4.5 h and 3 days. Therefore the dummy layer is deactivated and a soft grout layer is activated after 4.5 h. In order to consider the pressure at which the grout material is injected into the gap, an initial stress of $p_{\text{inject}} = 200\,\text{kPa}$ is applied in the grout elements. After 3 days, it is assumed that the grout material has hardened. Consequently, the previous soft grout layer is deactivated, and the stiff grout layer is activated until the end of the modeling period (1000 days). It should be noted that the dummy layer, the soft grout layer, and the stiff grout layer all share the same nodes, but only one layer is active at a given time.

5.4. Temporal evolution of the EDZ for unsupported tunnel excavation

Prior to examining the results of the parameter study, it is essential to establish a systematic approach for evaluating the size of the EDZ and to identify the appropriate time steps for evaluating the parameter study. Potential metrics for quantifying the EDZ area include deviatoric strain, plastic points, and bifurcation criteria. To illustrate these metrics, a reference model utilizing the bold values from Table 5.2 has been analyzed across eight selected time steps: two during excavation at $t = 3.3\,\mathrm{h}$ and $t = 4\,\mathrm{h}$, one at the end of excavation ($t = 4.5\,\mathrm{h}$), and five after excavation is completed ($t = 1$ day, $t = 10$ days, $t = 100$ days, $t = 500$ days, and $t = 1000$ days).

5.4.1. Temporal evolution of deviatoric strains

Considering that the approach utilized in this research involves examining the EDZ through shear strain localization, it might be logical to use deviatoric strains for a quantitative assessment of the EDZ size. Therefore, the temporal evolution of the field of deviatoric strains is initially presented in Figure 5.9.

As observed, the shear bands emerge and grow significantly until the end of the excavation. However, after excavation, the increase in size is not clearly discernible.

The main issue lies in the fact that the visual representation of the EDZ can vary depending on the choice of upper and lower limits in the contour plots, leading to inconsistencies in the perceived size of the EDZ. To utilize deviatoric strains as a measure for a quantitative evaluation of the EDZ, it would be necessary to establish thresholds to distinguish the EDZ from the surrounding intact zones. However, since this also depends on the stress path, as illustrated by comparisons between shearing and wetting paths in the biaxial test in Section 4.3.2, it is unlikely that a common threshold value can be determined for both stress paths.

Furthermore, shear strains around a tunnel excavation cannot be determined, and therefore, other quantities are subsequently investigated, which either do not require a threshold value or are quantities that can be better estimated on site.

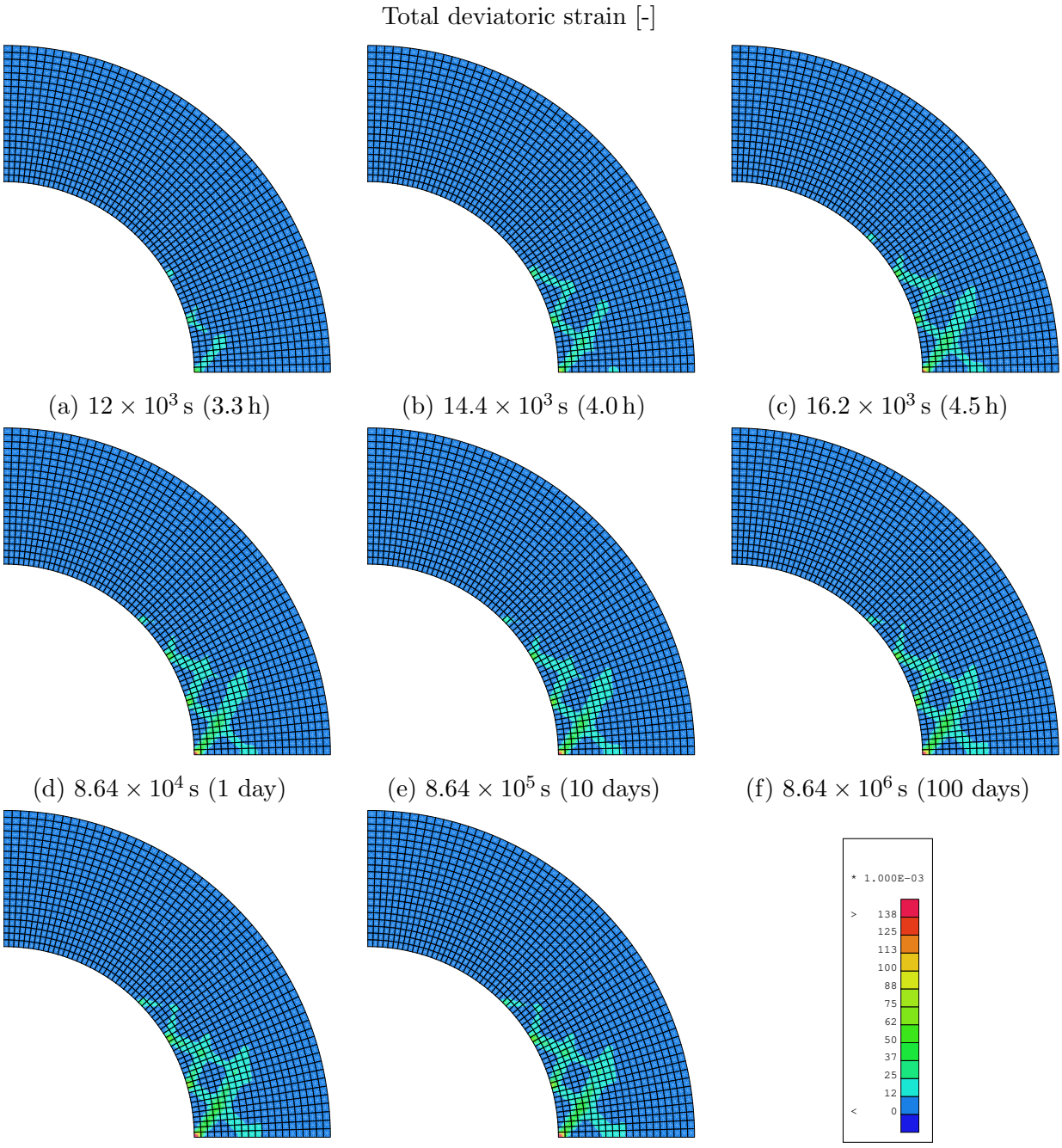

(a) 12×10^3 s (3.3 h) (b) 14.4×10^3 s (4.0 h) (c) 16.2×10^3 s (4.5 h)

(d) 8.64×10^4 s (1 day) (e) 8.64×10^5 s (10 days) (f) 8.64×10^6 s (100 days)

(g) 4.32×10^7 s (500 days) (h) 8.64×10^7 s (1000 days)

Figure 5.9.: Development of total deviatoric strain within the reference numerical model of unsupported tunnel during and after tunnel excavation (end of excavation: 16.2×10^3 s = 4.5 h)

5.4.2. Temporal evolution of plastic points around the tunnel

The EDZ is characterized by the presence of fractures and damage in the surrounding rock mass. While fractures cannot be directly modeled in finite element simulations, plastic deformations can serve as indicators of potential fracturing. To explore this approach, integration points exhibiting plasticity, referred to hereafter as plastic points, are analyzed to assess the size of the EDZ. The zone containing these plastic points is referred to as the plastic zone in the following.

The temporal evolution of these plastic points is presented in Figure 5.10, following an approach similar to the analysis conducted for deviatoric strains. At $t = 3.3\,\mathrm{h}$, a plastic zone begins to form around the excavation area. As the excavation progresses, this zone gradually expands, reaching its maximum extent by $t = 4.5\,\mathrm{h}$, when the excavation is completed. Within the first day, parts of the initial plastic zone undergo unloading and transition into an elastic state, as depicted in Figure 5.10d. Over time, this area reverts to plasticity and expands further until reaching 1000 days.

By comparing the evolution of deviatoric strain in Figure 5.9 with the development of plastic points in Figure 5.10, it becomes evident that the plastic zone extends beyond the region of shear strain localization, with the two zones only partially overlapping.

As shown in Figure 5.11 (middle), some plastic points coincide with the locations of the previously identified shear bands, indicating that the localized plastic deformation is associated with the development of these bands. However, a larger area of plastic points is observed to the right of the shear bands, which is not directly related to shear band formation. This additional plasticity is attributed to the elevated pore water pressure in this region, as depicted in Figure 5.11 (right). Consequently, the plastic points can be categorized into two types: shear-induced and pore water pressure-induced.

To explain the development of the plastic zone in detail, it is essential to examine both the temporal evolution of pore water pressure and the tunnel deformation mechanism over time. This will provide a clearer understanding of the interplay between shear-induced plasticity and the effects of pore water pressure on the overall deformation.

First, the temporal evolution of pore water pressure is examined. For this purpose, the pore water pressure distribution around the tunnel at various times during and after the tunnel excavation is shown in Figure 5.12. Due to the low permeability of Opalinus clay shale and the unloading due to the tunnel excavation, a negative pore water pressure or suction $s = 1.18\,\mathrm{MPa}$ develops in the crown of the tunnel, while an increase of pore water pressure occurs at the sides of the tunnel, with a peak value of $p_{w,\mathrm{peak}} = 6.22\,\mathrm{MPa}$.

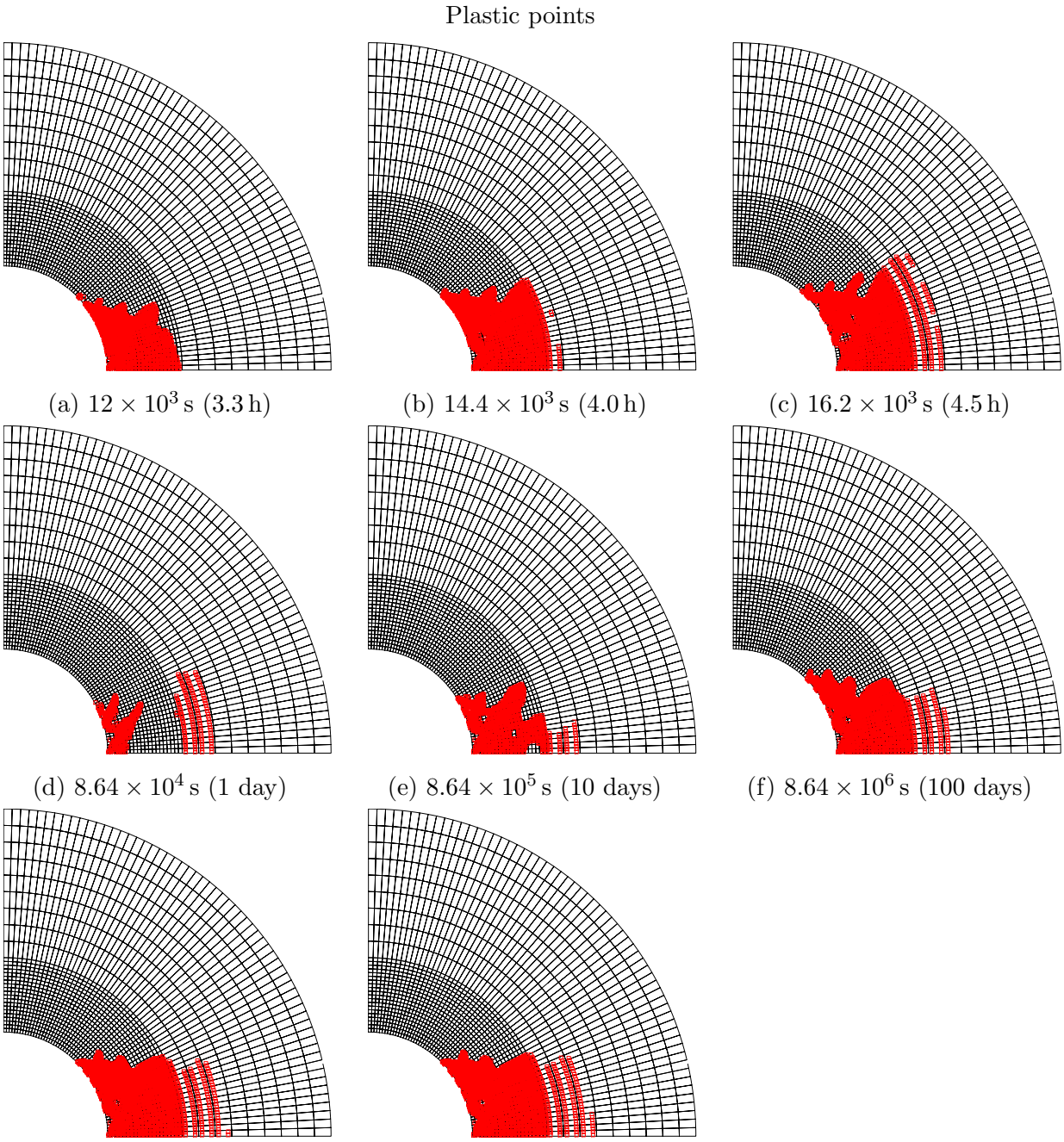

(a) 12×10^3 s (3.3 h) (b) 14.4×10^3 s (4.0 h) (c) 16.2×10^3 s (4.5 h)

(d) 8.64×10^4 s (1 day) (e) 8.64×10^5 s (10 days) (f) 8.64×10^6 s (100 days)

(g) 4.32×10^7 s (500 days) (h) 8.64×10^7 s (1000 days)

Figure 5.10.: Development of plastic points within the reference numerical model of unsupported tunnel during and after tunnel excavation (end of excavation: 16.2×10^3 s = 4.5 h)

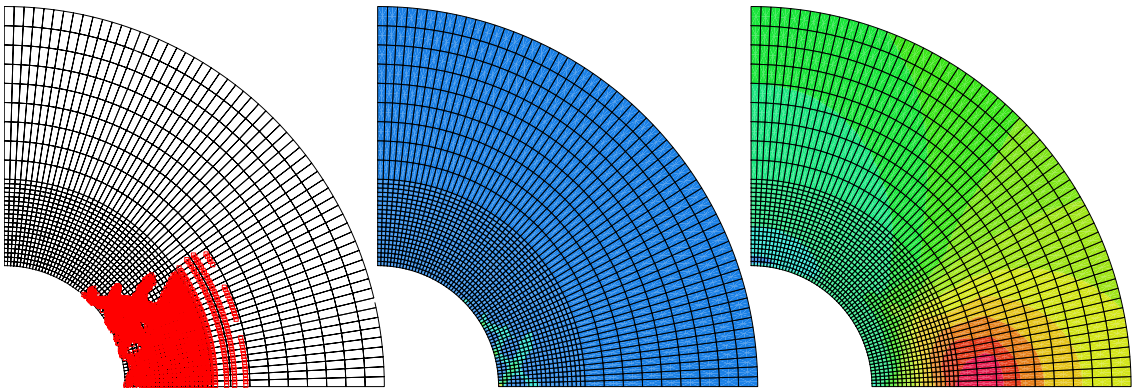

Figure 5.11.: Comparison of plastic points (left) with the deviatoric strain (middle) and pore water pressure (right) after excavation ($t = 4.5\,\mathrm{h}$)

This can be explained by the ovalization of the tunnel resulting from the anisotropic stress state, depicted in Figure 5.13a, which is explained in detail in the following.

Over time, the maximum value of the pore water pressure shifts along the horizontal axis, as depicted in Figures 5.12a to 5.12c. After the excavation is completed, the excess pore water pressure gradually dissipates over time, due to the hydraulic boundary conditions at the tunnel wall (local drainage) and is no longer visible after 100 days, as illustrated in Figure 5.12f.

Next, the temporal evolution of the tunnel wall deformations, illustrated in Figure 5.13, where the radial deformations are plotted in radial coordinates, are analyzed. Due to the anisotropic stress state, ovalization of the tunnel occurs during excavation, with the tunnel crown deforming more than the tunnel sides. After excavation is completed ($t = 4.5\,\mathrm{h}$), the tunnel wall deforms by about 4.5 cm to 5 cm at the sides, while the tunnel crown deforms by over 6.6 cm.

It should be noted that a negative sign here indicates a deformation towards the tunnel center. After the tunnel excavation is completed, additional deformation is observed at the tunnel crown and minor at the tunnel side. This can be explained by the sketch in Figure 5.13b, which illustrates the volume increase due to mechanical swelling and resulting tunnel wall deformations. After the excavation is completed, a negative pore pressure (blue area) develops at the tunnel crown due to the low permeability of the Opalinus clay shale. Over time, this negative pore pressure, or suction, decreases, leading to a volume increase (swelling). This leads to additional deformations at the tunnel crown and more ovalization of the tunnel.

It should be clearly stated at this point that the swelling discussed here refers to the pure mechanical swelling already explained in Section 2.2.1.1. This phenomenon arises due to

the initial saturation of the geological formation, which subsequently creates a suction as a consequence of the unloading induced by the tunnel excavation and the low permeability of the Opalinus clay shale.

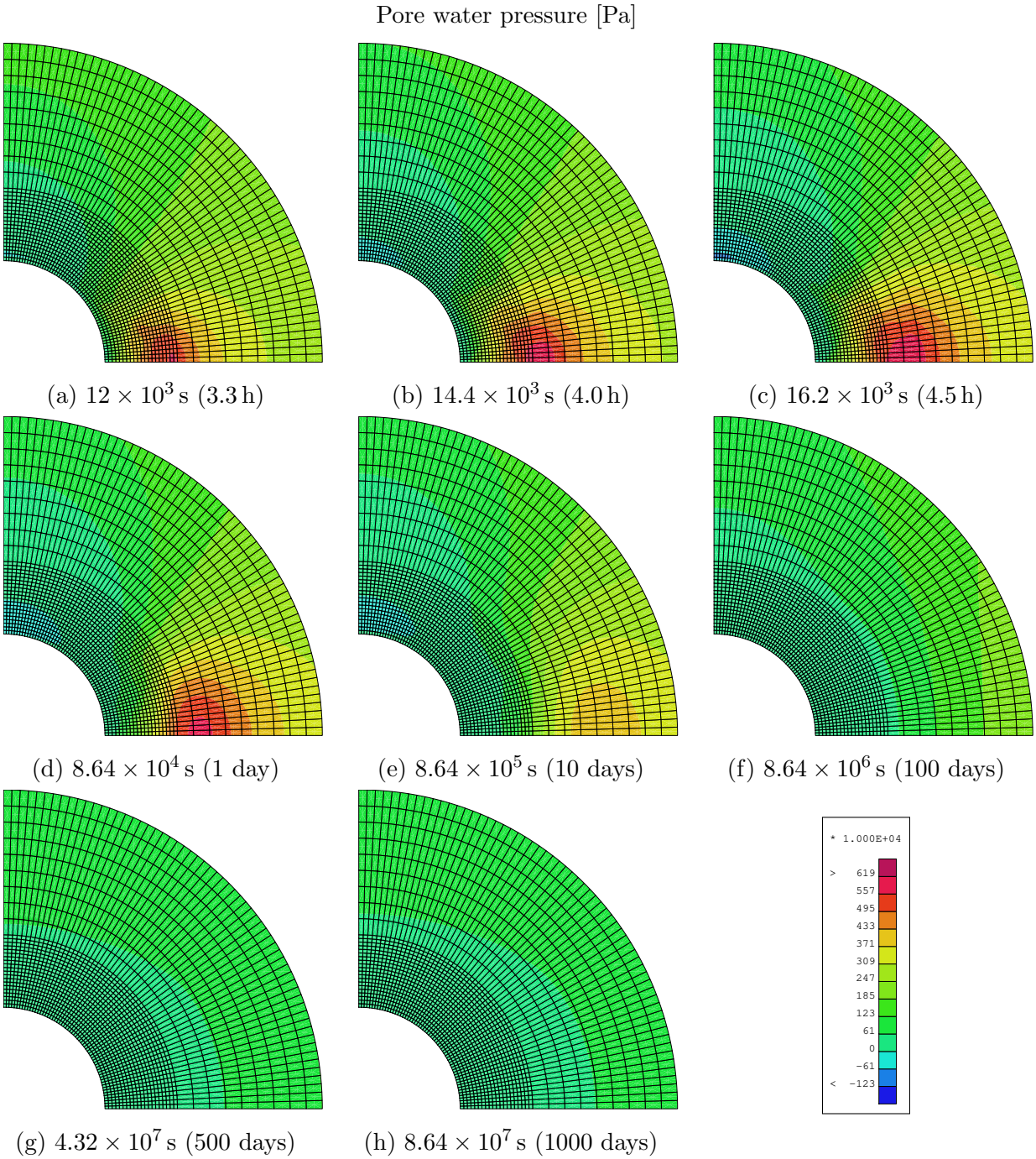

(a) 12×10^3 s (3.3 h) (b) 14.4×10^3 s (4.0 h) (c) 16.2×10^3 s (4.5 h)

(d) 8.64×10^4 s (1 day) (e) 8.64×10^5 s (10 days) (f) 8.64×10^6 s (100 days)

(g) 4.32×10^7 s (500 days) (h) 8.64×10^7 s (1000 days)

Figure 5.12.: Development of pore water pressure distribution within the reference numerical model of unsupported tunnel during and after tunnel excavation (end of excavation: 16.2×10^3 s = 4.5 h)

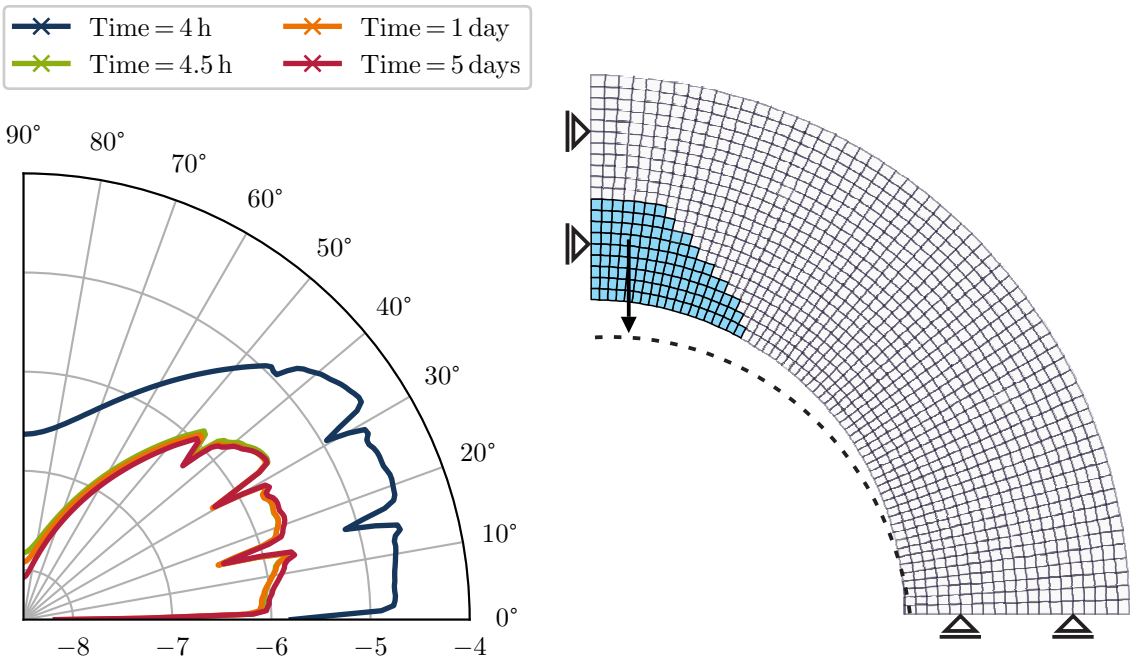

(a) Radial displacement u_r [cm] (b) Sketch of tunnel wall deformations

Figure 5.13.: Effects and resulting tunnel wall displacements for the reference numerical model of unsupported tunnel

In the radial displacements shown in Figure 5.13a, four distinct jumps are observed at the locations of the imperfect elements or shear bands. This can be attributed to the initiation of shear bands at these material imperfections. Within a shear band, deformations are concentrated in an extremely thin zone, leading to steep strain gradients. Depending on the underlying constitutive model, this concentration of deformation may result in a stress concentration, as depicted in Figure 5.14, which shows the stress distribution in a Cartesian coordinate system.

The radial stresses vary along the tunnel wall, consisting of different contributions from the Cartesian stress components $(\sigma_{xx}, \sigma_{yy}, \sigma_{xy})$ varying depending on the position along the tunnel wall. Notably, at the tunnel side, where the radial stresses are primarily resulting from the stresses in the horizontal direction (σ_{xx}), there is a region between the two shear bands where the stresses are lower than within the shear bands. This is clearly visible as the red triangular area in Figure 5.14a. These stress and strain concentrations give rise to the distinct jumps observed in Figure 5.13a. Another potential cause of the stress concentration is the increased permeability within the shear bands, leading to a faster dissipation of pore water pressure, which results in an increase in net stress p and further contributes to the observed stress concentration.

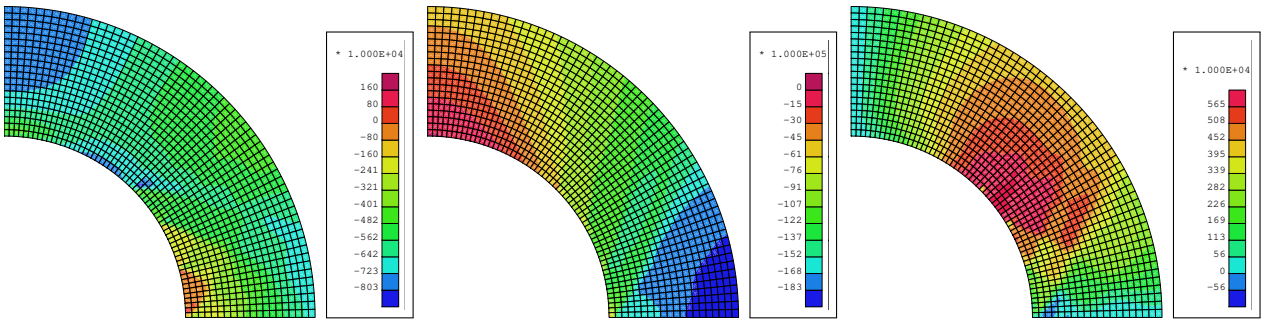

(a) σ_{xx} (b) σ_{yy} (c) σ_{xy}

Figure 5.14.: Stress distribution in the surrounding ground at the end of simulation ($t =$ 1000 days)

Although the temporal evolution of the pore water pressure as well as the temporal evolution of the tunnel wall deformation provide valuable insights, needed for the understanding of the plastic point evolution (see Figure 5.10), the reasons for the elastic unloading shown in Figure 5.10d are still not fully understood. Therefore, a detailed examination of the stress paths of selected elements along the x-axis, highlighted in red in Figure 5.15, is carried out and the resulting stress paths are illustrated in Figures 5.16 to 5.18.

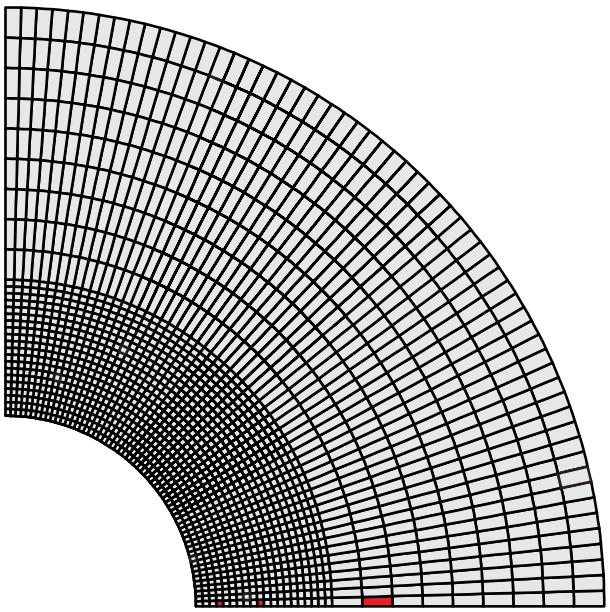

Figure 5.15.: Position of elements for which the stress path is investigated

First, the stress path of the element closest to the tunnel wall, located 0.75 m ($\approx 0.1r$) from the tunnel wall, is analyzed, as shown in Figure 5.16. The yield surfaces depicted in Figure 5.16 correspond to the initial yield surface (YS initial) at t=0 h, the final yield surface (YS final) at t=1000 days, and an intermediate yield surface (YS inter), which in this case corresponds to t=4.5 h. As illustrated in Figure 5.16, the element remains in plasticity at all selected time steps. The deviatoric stress increases from the initial anisotropic stress state (black mark) as a result of the tunnel excavation. Additionally, a leftward shift in the stress path is observed as excavation progresses, driven by pore water pressure buildup that reduces the net stress.

After $t = 1.7$ h, the stress path touches the yield surface on the dry side of the yield surface (blue mark). Since excavation is not yet complete, any additional unloading induces softening, visible in the magnified view in Figure 5.16.

After $t = 2.5$ h, net stress begins to increase with minimal softening, signifying a decrease in pore water pressure. When tunnel excavation is complete (red mark), the stress path has shifted to the wet side of the yield surface. Over time, pore water pressure continues to decrease, leading to an increase in net stress and resulting in hardening.

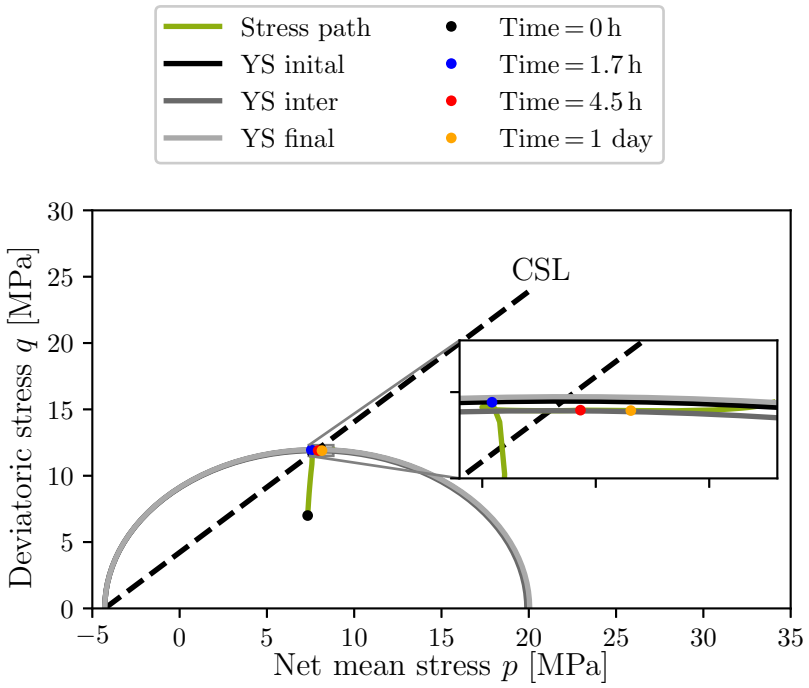

Figure 5.16.: Stress path for an element in 0.75 m ($\approx 0.1r$) distance to tunnel wall

A similar trend is observed in the stress path of an element located 2.25 m ($\approx 0.3r$) from the tunnel wall, depicted in Figure 5.17. A notable difference, however, is that the yield surface is reached later compared to the element closer to the tunnel wall. This delay can be attributed to the progressive pore water pressure buildup, which reduces the net stress, starting near the tunnel wall and moving along the x-axis over time, as illustrated in Figure 5.12.

Consequently, the stress path reaches the yield surface at $t = 2\,\text{h}$ on the dry side (blue mark), but closer to the critical state line (CSL). Between $t = 2\,\text{h}$ and $t = 3.33\,\text{h}$, the element undergoes softening due to increased deviatoric stress induced by tunnel excavation. When excavation is completed after 4.5 h, the stress path is on the wet side (red mark).

Following excavation, an elastic unloading phase occurs up to $t = 1$ day (orange mark), while the element stays in elasticity until $t = 5$ days. This unloading can be explained by changes in pore water pressure at two different locations. First, the dissipation of excess pore water pressure on the tunnel side leads to increased net stresses. Second, the decrease of excavation-induced suction at the tunnel crown causes local volume expansion or swelling. This local swelling leads to increasing tunnel ovalization, as illustrated Figure 5.13b.

Between $t = 4.5\,\text{h}$ and $t = 5$ days, the radial displacements at the tunnel side slightly decrease, consequently reducing the deviatoric stresses, leading to the observed elastic unloading. Due to the limited extent of the suction-induced area, the increase in ovalization and the resulting reduction in deviatoric stress is also limited. Since the element is located further from the tunnel wall and not within a zone with increased permeability (due to minimal deviatoric strains), pore water pressure dissipation continues, indicated by a further increase in net stress without further decrease in deviatoric stress.

After five days, the net stress increase is sufficient for the stress path to touch the yield surface on the wet side, leading to limited hardening through to the end of the simulation. This sequence explains why some elements in Figure 5.10 experience elastic unloading initially and subsequently return to plasticity over time.

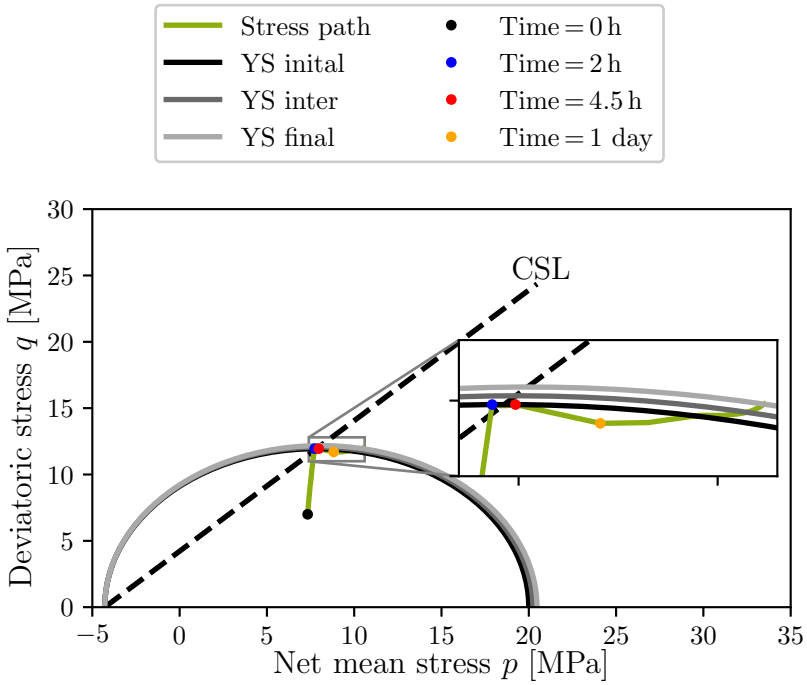

Figure 5.17.: Stress path for an element in 2.25 m ($\approx 0.3r$) distance to tunnel wall

Additionally, an element located 6.11 m ($\approx 0.9r$) horizontally from the tunnel wall is examined. This element exhibits a distinct stress path compared to the previously inspected elements as illustrated in Figure 5.18. Due to its relatively greater distance from the tunnel wall, it is less affected by tunnel excavation, causing its stress path to reach the yield surface on the wet side instead of the dry side as seen for the other two elements which are closer to the tunnel wall.

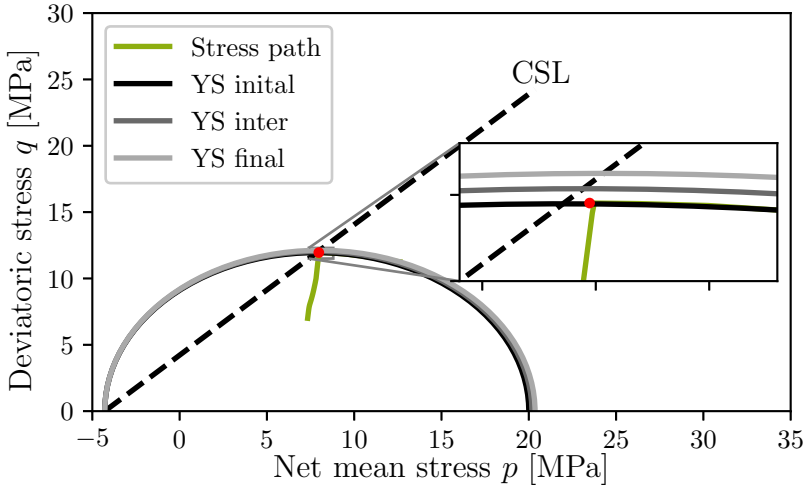

Figure 5.18.: Stress path for an element in 6.11 m ($\approx 0.9r$) distance to tunnel wall

As shown in Figure 5.18, after excavation (red mark), the stress path has just entered plasticity. Over time, hardening is observed, which, as with the other two elements, can be attributed to the gradual reduction of pore water pressure. Since the stress path shows no softening, it is logical that no localized shear failure occurs at this relatively large distance to the tunnel wall ($\approx 0.9r$).

Although the temporal evolution of plastic points has been previously discussed, their suitability for systematically determining the EDZ size has not been evaluated. This aspect will be examined in greater detail in the following section.

5.4.3. Computation and temporal evolution of the plastic zone in terms of size and permeability

In the literature, for example in Bossart et al. (2002), the EDZ is described as a zone where plastic deformations occur due to excavation processes. These plastic deformations can manifest as fractures, depending on the ground conditions. These fractures increase the permeability of the EDZ to several orders of magnitude greater than the permeability of intact ground.

It has already been demonstrated in the previous section that plasticity does not necessarily imply the presence of shear bands, as observed in the EDZ, since it can also be induced by other phenomena such as pore water pressure built-up. Nevertheless, it is worth investigating whether the zone in which the plastic points are located, hereafter referred to as the plastic zone, captures the unique features of the EDZ, such as the significant increase in permeability. To investigate this, in addition to the area of the plastic zone, the permeability of the plastic zone must also be examined.

To enable a systematic evaluation of the plastic zone at various times during and after the excavation, a python script is developed. The script loops radially through the elements, moving from the outer to the inner areas. Once an element in plasticity is identified, the corresponding element is stored and selected as the boundary of the plastic zone. The area of the plastic zone is then calculated by summing the areas of all elements within the detected boundary of the plastic zone.

To quantify the permeability of the plastic zone, the mean permeability $\bar{k}_{w,\text{plastic}}$ is determined by summing the permeability k_i of each individual element within the plastic zone, multiplied by its corresponding element size A_i, and subsequently dividing by the total plastic zone area $\sum_{i=1}^{n} A_i$.

$$\bar{k}_{w,\text{plastic}} = \frac{\sum_{i=1}^{n} k_i \mathrm{A}_i}{\sum_{i=1}^{n} \mathrm{A}_i} \tag{5.3}$$

Using the developed python script, the temporal evolution of the plastic zone, as well as the permeability within this zone, is calculated and illustrated in Figures 5.19 to 5.21. The permeability is expressed both as the mean permeability $\bar{k}_{w,\text{plastic}}$ and as the mean permeability ratio between $\bar{k}_{w,\text{plastic}}$ and the initial permeability $k_{w,0}$, denoted as $\Delta\bar{k}_{w,\text{plastic}}$. The latter expression facilitates a clearer understanding of how many orders of magnitude the permeability is increased in this zone compared to the initial permeability of the intact ground.

As shown in Figure 5.19, the plastic zone increases during excavation, reaching its peak at the end of excavation with an area $A_{\text{plastic}} \approx 50\,\text{m}^2$. After excavation is completed ($t = 4.5\,\text{h}$), the plastic zone decreases to $A_{\text{plastic}} \approx 18\,\text{m}^2$. The reasons for this decrease have already been explained based on the corresponding stress paths (see Figure 5.16). After $t = 5$ days, the plastic zone begins to increase again due to the reduction in excess pore water pressure, leading to an increase in net stress, as already explained during the analysis of the stress paths. By the end of the simulation, a steady plastic zone of $A_{\text{plastic}} \approx 48\,\text{m}^2$ is reached.

Although the plastic zone shows an increase during excavation, which initially aligns with the formation of the EDZ, the drastic reduction of the EDZ shortly after the end of excavation, followed by a re-expansion of the EDZ as suggested by the observed development of the plastic zone, cannot be physically justified.

The temporal evolution of the mean permeability within the plastic zone follows a different trend compared to the plastic zone area. From the start to the end of excavation, the mean permeability increases up to 2E-17 m^2, but after excavation is completed ($t = 4.5\,\text{h}$), it continues to increase up to 4.38E-17 m^2, even though the total size of the plastic zone decreases.

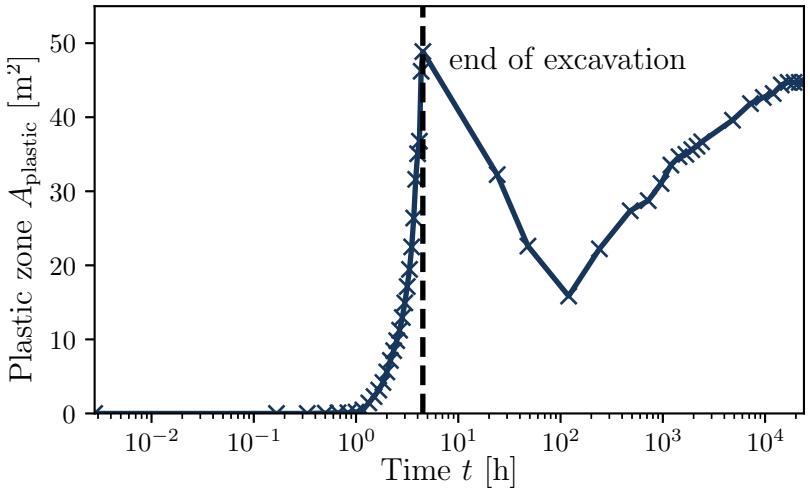

Figure 5.19.: Temporal evolution of the plastic zone for the reference numerical model of unsupported tunnel

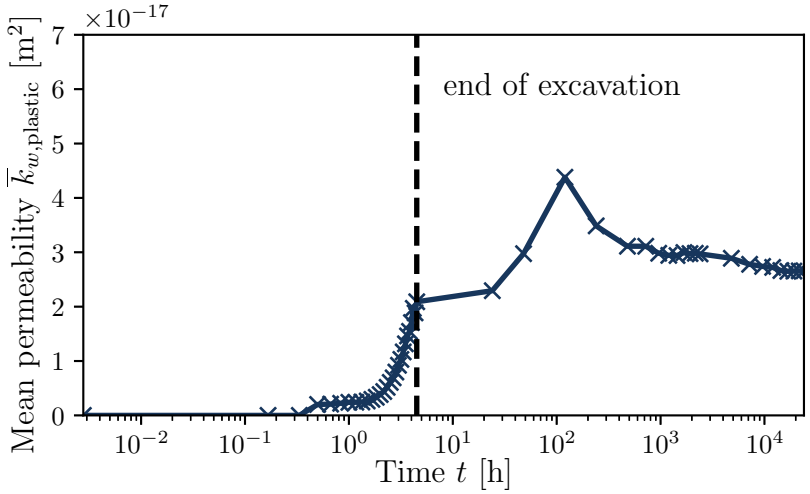

Figure 5.20.: Temporal evolution of the mean permeability within the plastic zone for the reference numerical model of unsupported tunnel

This phenomenon can be attributed to the observation that the primary increase in permeability occurs in the region where shear bands develop, as this increase is associated with the equivalent strains. Since this region remains in plasticity after excavation and the plastic zone created by the pore water pressure increase does not experience significant permeability changes, the mean permeability continues to rise.

When the plastic zone begins to expand again at $t = 5$ days, the mean permeability decreases, as zones with unaltered or only slightly increased permeability are now included

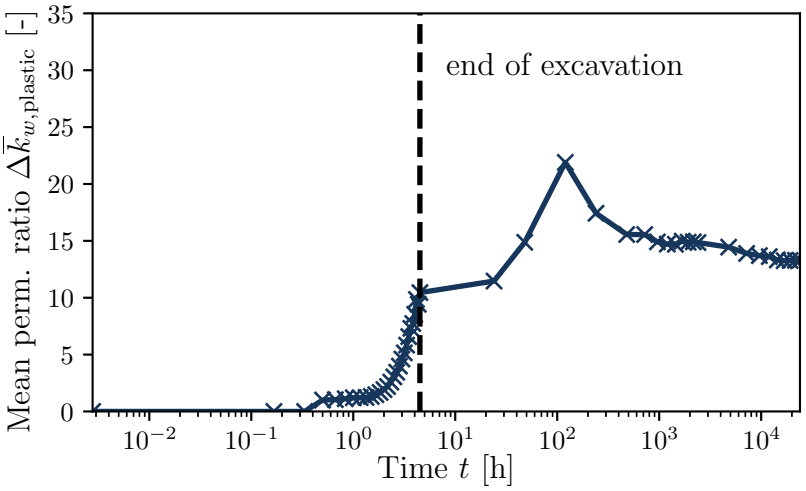

Figure 5.21.: Temporal evolution of the permeability ratio within the plastic zone for the reference numerical model of unsupported tunnel

in the calculation. A similar trend and conclusion can be drawn from Figure 5.21, where the mean permeability ratio is shown.

Although the evolution of permeability in the plastic zone shows an increase up to a maximum value followed by a decrease, which is also expected for the EDZ, it is clear that these changes are primarily due to the changing size of the plastic zone.

The resulting development of both the area and permeability of the plastic zone highlights the fact, already established in the previous section, that plasticity in the current model encompasses not only the region with shear bands and increased permeability but also an additional zone that experiences plasticity due to pore water pressure changes, which, however, does not lead to a significant change in permeability as expected in the EDZ.

Although the plastic zone is an important result, it does not fully capture the unique features of the EDZ, such as the significant increased permeability. Therefore, an alternative systematic method needs to be developed to better characterize the EDZ, limiting its size to the zones where shear bands appear, similar to previous studies focusing on deviatoric strains or the bifurcation criterion, which will be the subject of the next section.

5.4.4. Temporal evolution of the bifurcation criterion around the tunnel

The bifurcation, or Rice criterion, is a theoretical concept that indicates, based on the stress and strain states and the tangent tensors of the material model, whether an element satisfies the conditions for shear strain localization, as discussed in Section 2.7.2. Furthermore, it provides insight into the two possible directions of the shear band. Unlike the deviatoric strains, it does not necessitate the introduction of a threshold value, which makes it a useful indicator for the appearance of the EDZ. In this section, the temporal evolution of the bifurcation criterion is examined, and its potential for systematically characterizing the EDZ in terms of size and permeability is evaluated.

In Figure 5.22, the temporal evolution of the bifurcation directions is illustrated, indicated by green and red arrows. It should be noted that, from a theoretical perspective, both the green and red arrows indicate conjugated directions of the shear bands.

A comparison of the elements where the criterion is satisfied, along with the resulting bifurcation directions, reveals alignment with the shear bands shown in Figure 5.9. However, it is also evident that the Rice criterion is not fulfilled along the entire length of the shear bands. Consequently, using only this criterion to determine the size of the EDZ would lead, in this case, to an underestimation or, as will be shown in Section 5.5.2, an overestimation of the EDZ area. This finding indicates that the bifurcation criterion may not be adequate for a systematic evaluation of the EDZ. Nevertheless, it is crucial to acknowledge that the bifurcation criterion continues to serve as a valuable instrument for investigating shear strain localization in depth.

A rigorous examination of the most promising metrics (deviatoric strain, plastic points, and the bifurcation criterion) has been undertaken so far. However, it must be noted that each of these metrics has its limitations or is not suitable for the systematic evaluation of the EDZ. Therefore, in the following section, another important parameter that characterizes the EDZ, the permeability, is under investigation.

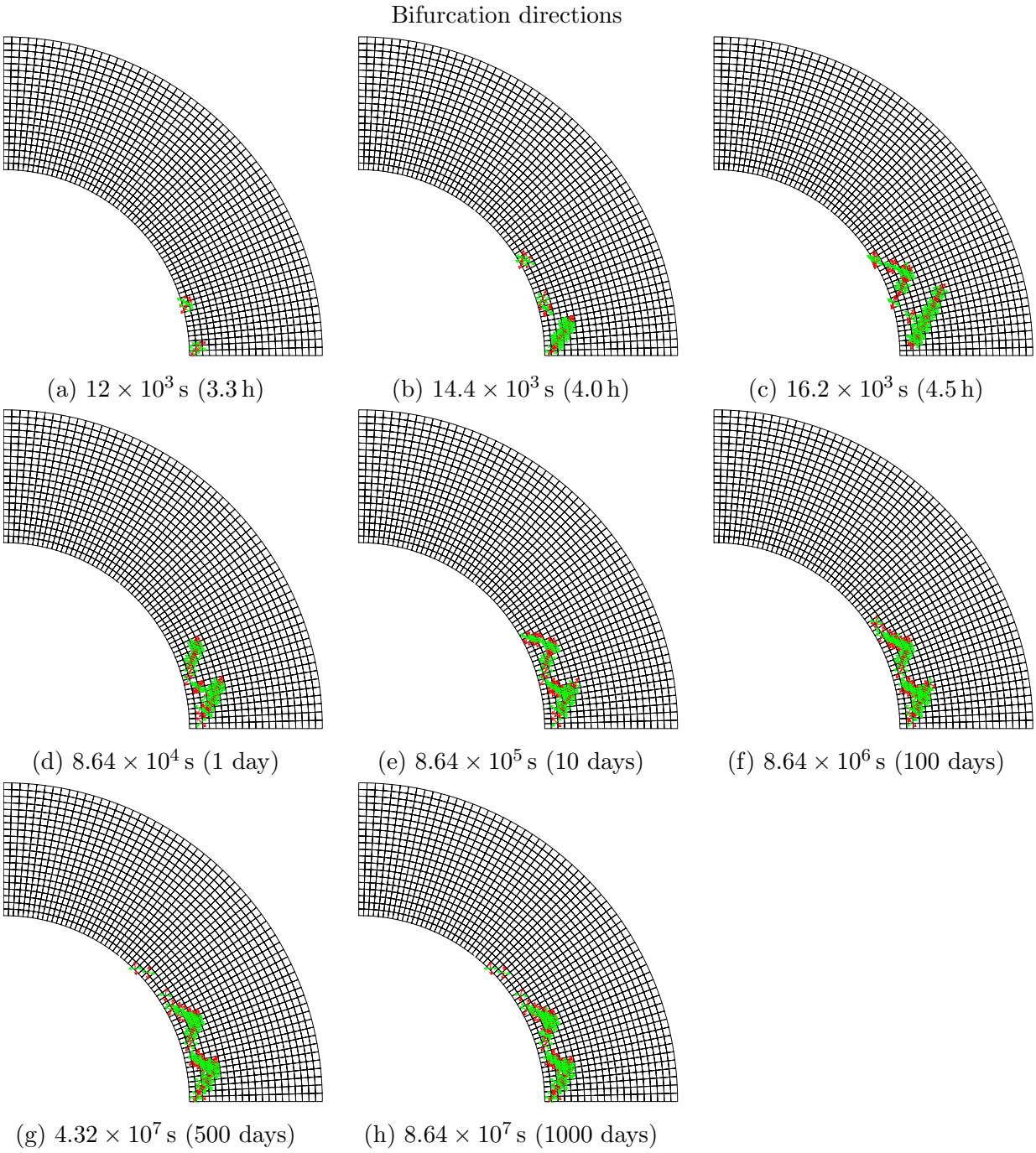

(a) 12×10^3 s (3.3 h) (b) 14.4×10^3 s (4.0 h) (c) 16.2×10^3 s (4.5 h)

(d) 8.64×10^4 s (1 day) (e) 8.64×10^5 s (10 days) (f) 8.64×10^6 s (100 days)

(g) 4.32×10^7 s (500 days) (h) 8.64×10^7 s (1000 days)

Figure 5.22.: Development of bifurcation directions within the reference numerical model of unsupported tunnel during and after tunnel excavation (end of excavation: 16.2×10^3 s = 4.5 h)

5.4.5. Temporal evolution of permeability around the tunnel

As described in Section 2.4, the EDZ is characterized not only by a reduction in stiffness due to damage but also by a significant increase in permeability compared to the intact clay shale. Therefore, in addition to the previously examined metrics, the evolution of permeability, expressed as the ratio between the current and the inital permeability $\Delta k_w = \frac{k_w}{k_{w,0}}$ is also investigated for the systematic assessment of the EDZ. To this end, the temporal evolution of permeability ratio is presented in Figure 5.23, following the same approach as in case of the previously discussed metrics.

Similar to the deviatoric strains, the increase in permeability develops up to $t = 3.3\,\mathrm{h}$ and progressively rises until $t = 4.5\,\mathrm{h}$ (the end of the excavation). The permeability along the shear band increases to a value being approximately 100 times greater than that of the intact formation. After the end of the tunnel excavation, until $t = 1000$ days, no significant changes in the permeability ratio are observed in Figure 5.23.

Although the distinction between intact clay shale and shear bands appears clearer in case of the permeability ratio compared to deviatoric strains, since the difference between intact clay shale ($\Delta k_w = 1$) and shear bands ($\Delta k_w \gg 1$) is more pronounced, a threshold is still required for a systematic evaluation of the EDZ area.

As shown in the previous sections, the plastic points and the bifurcation criterion are not suitable for the systematic evaluation of the EDZ. It was demonstrated that shear bands are the main contributors to the size of the EDZ, particularly the increase in permeability. Since permeability depends on deviatoric strains, both are capable of characterizing the EDZ.
However, both require a threshold value to distinguish between the inside and outside of the EDZ. Unlike deviatoric strains, permeability is measurable in situ, and there are documented observations in the literature regarding this parameter. Ultimately, the permeability ratio is selected for calculating the size of the EDZ. The following section presents the approach for calculating the EDZ size and determining a reasonable threshold value for the permeability ratio.

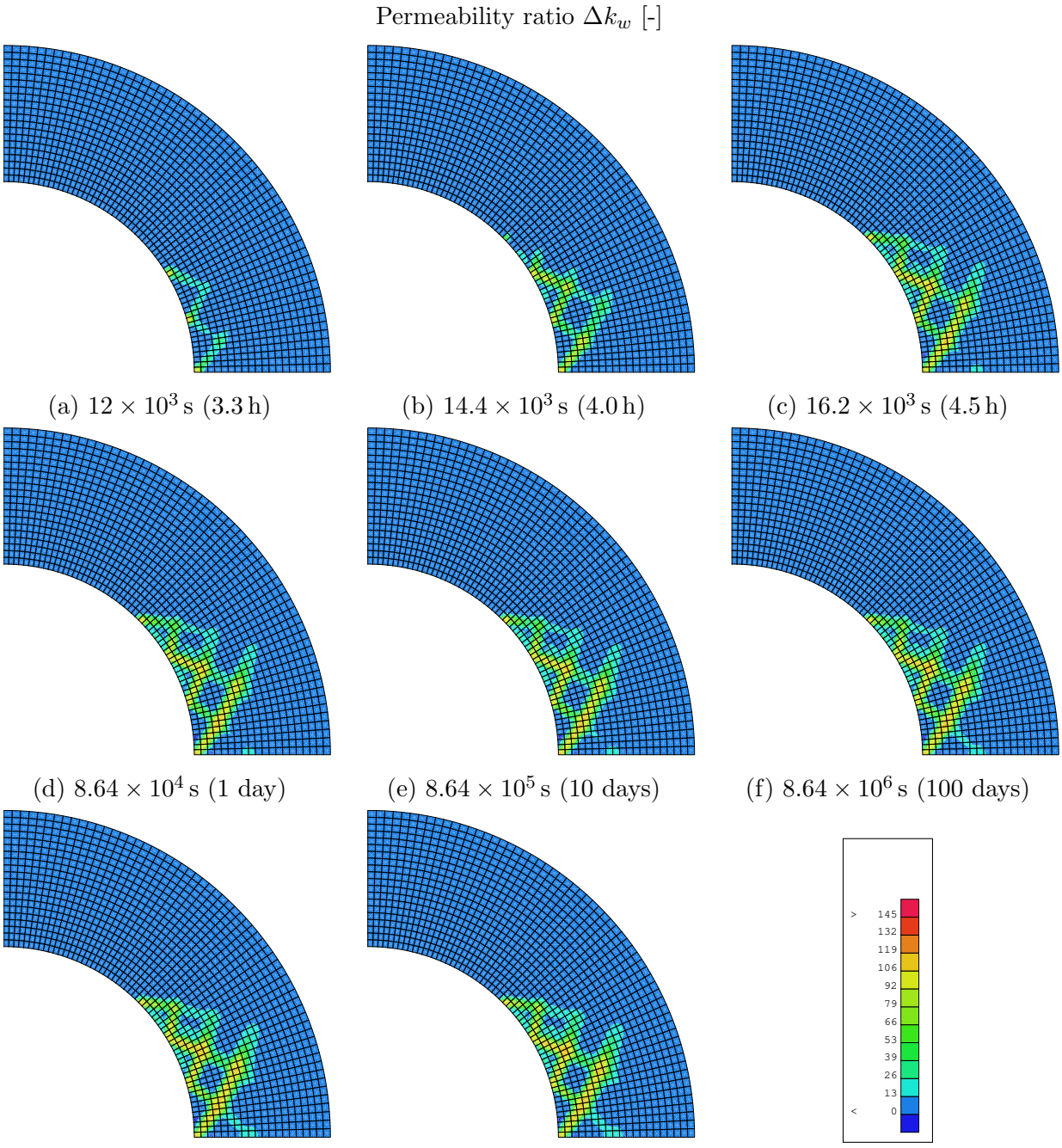

(a) 12×10^3 s (3.3 h) (b) 14.4×10^3 s (4.0 h) (c) 16.2×10^3 s (4.5 h)

(d) 8.64×10^4 s (1 day) (e) 8.64×10^5 s (10 days) (f) 8.64×10^6 s (100 days)

(g) 4.32×10^7 s (500 days) (h) 8.64×10^7 s (1000 days)

Figure 5.23.: Development of permeability ratio within the reference numerical model of unsupported tunnel during and after tunnel excavation (end of excavation: 16.2×10^3 s = 4.5 h)

5.4.6. Calculation of EDZ area based on permeability ratio and determination of the threshold value

Unlike the plastic points, where only two states are present, either plastic or elastic, the permeability ratio is a scalar quantity. Therefore, when using the permeability ratio to calculate the EDZ area, a threshold value is needed, as otherwise no distinction can be made between the inside and outside of the EDZ.

To address this, and similar to the plastic zone calculation, a python script is created that loops radially through the elements in the refined zone around the tunnel, moving from the outer to the inner areas. Once the criteria for identifying the EDZ, in this case $\Delta k_w > \Delta k_{w,\mathrm{thr}}$, is met, the corresponding element is stored and selected as the boundary of the EDZ. The area of the EDZ and the mean permeability within the EDZ is then calculated using the same approach as for the plastic zone (see Equation 5.3).

To establish a reasonable threshold value $\Delta k_{w,\mathrm{thr}}$, the EDZ area A_{EDZ} and mean permeability $\bar{k}_{w,\mathrm{EDZ}}$, along with the resulting mean permeability ratio $\Delta\bar{k}_{w,\mathrm{EDZ}}$ within the EDZ, are calculated across a range from $\Delta k_{w,\mathrm{thr}} = 1$ to 100 at the end of the simulation (1000 days). The resulting area and permeability are illustrated as functions of the threshold value in Figures 5.24 to 5.26.

As illustrated in Figures 5.24, as the threshold increases, the size of the EDZ decreases, while permeability increases as seen in Figures 5.25 and 5.26.

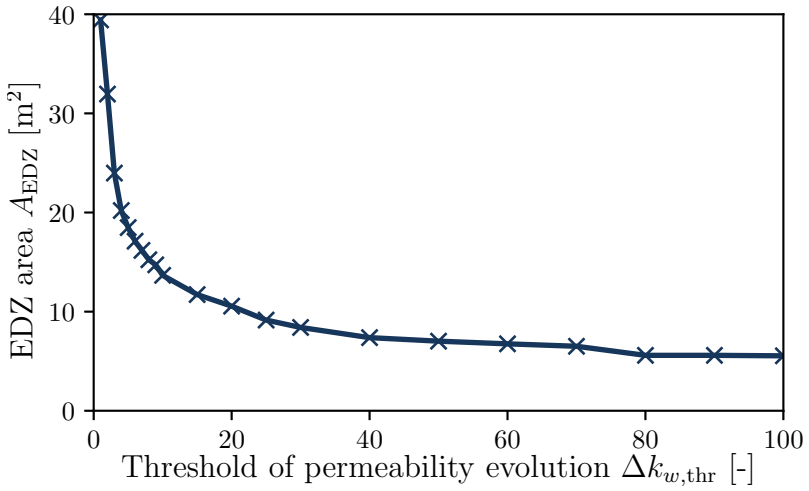

Figure 5.24.: Variation in the Excavation Damaged Zone (EDZ) area as a function of the permeability threshold after 1000 days

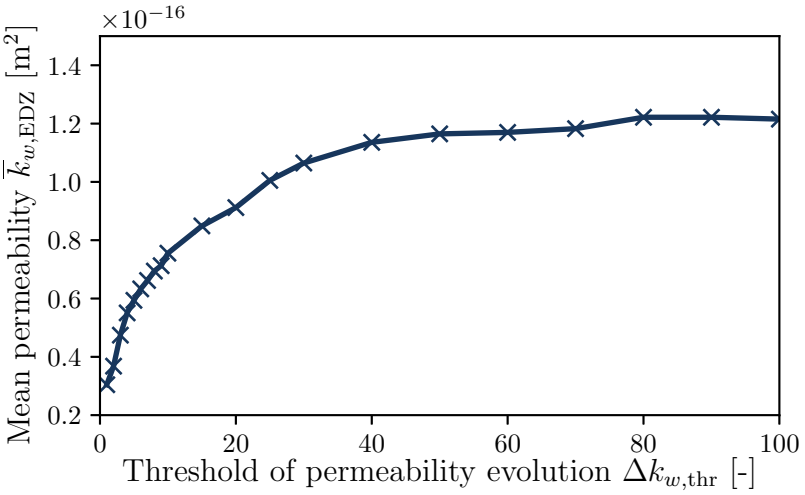

Figure 5.25.: Mean permeability of the Excavation Damaged Zone (EDZ) as a function of the permeability threshold after 1000 days

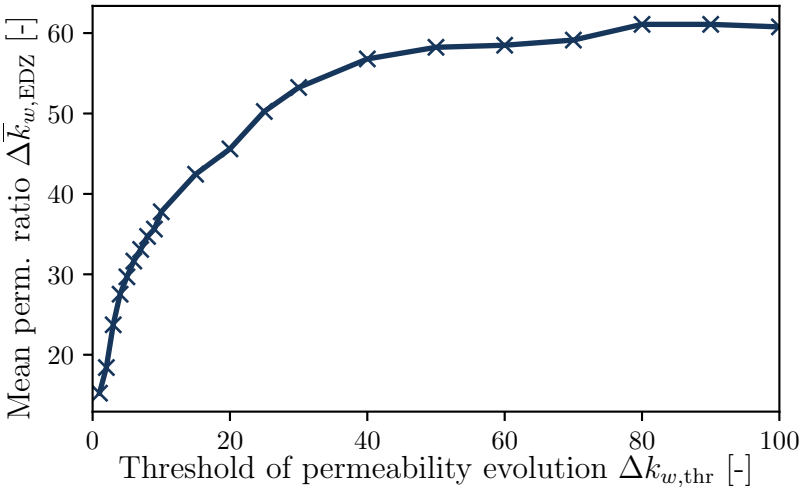

Figure 5.26.: Permeability ratio in the Excavation Damaged Zone (EDZ) as a function of the permeability threshold after 1000 days

The reduction of the EDZ area is non-linear and can be divided into four distinct phases. The most significant EDZ area reduction occurs between thresholds $\Delta k_{w,\mathrm{thr}} = 1$ to 10. While the decrease continuous, it is less pronounced between $\Delta k_{w,\mathrm{thr}} = 10$ and 20. From $\Delta k_{w,\mathrm{thr}} = 20$ to 40, the decrease is again more substantial, indicating a plateau between $\Delta k_{w,\mathrm{thr}} = 10$ to 20. Beyond a threshold value of 40, no further significant reduction in the EDZ area is observed. Similar observations can be made for permeability, with the key difference being that, unlike the EDZ area, permeability increases as depicted in Figures 5.25 and 5.26.

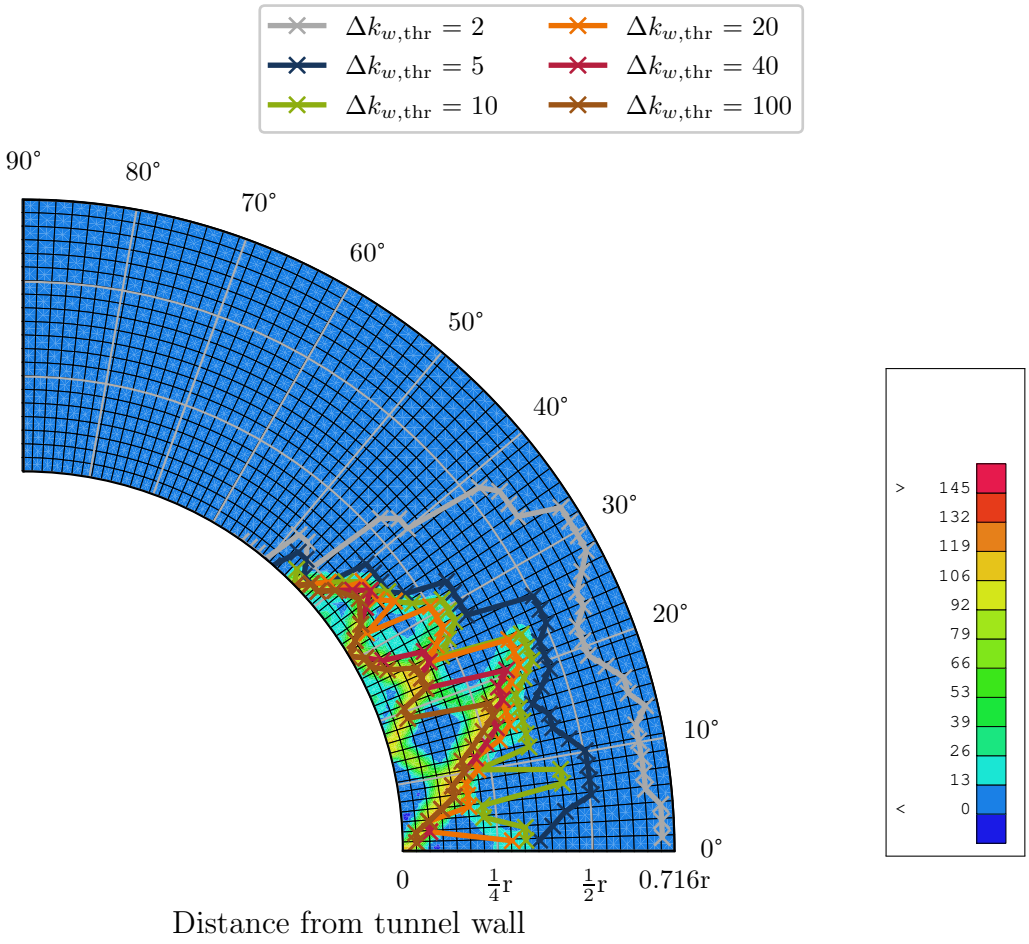

Figure 5.27.: Superposition of different outer boundaries of the Excavation Damaged Zone (EDZ) as a function of the selected thresholds for permeability ratio after 1000 days

To visually interpret this, six threshold values (2, 5, 10, 20, 40, and 100) are selected, and the corresponding EDZ outer boundaries are plotted on top of the permeability ratio in Figure 5.27. The permeability ratio threshold $\Delta k_{w,\mathrm{thr}} = 2$ overestimates the EDZ, as it includes zones where the permeability is only slightly increased, most likely due to deviatoric strains occurring prior to the localization, as also found in biaxial testing in Section 4.3.5. The threshold values between $\Delta k_{w,\mathrm{thr}} = 5$ and 20 appear to be reasonable choices. Conversely, thresholds $\Delta k_{w,\mathrm{thr}} = 40$ to 100 underestimate the EDZ.

When comparing the EDZ size to literature references, such as Bossart et al. (2002), an EDZ extension of approximately $0.5r$ is observed. Therefore, a threshold value of 5 is selected for all subsequent calculations, which is in good agreement with the EDZ extension reported by Bossart et al. (2002).

5.4.7. Temporal evolution of the EDZ area and permeability within EDZ

With a robust method established for determining the size of the EDZ and its mean permeability, the next step is to identify a representative time instance for conducting the parameter study. This time will serve as the basis for further analysis, where the relevant parameters are evaluated and their effects on the EDZ and its permeability are explored.

Therefore, the temporal evolution of the EDZ area as well as the mean permability ratio is depicted in Figures 5.28 and 5.29. As can be observed, the EDZ develops quite rapidly during the tunnel excavation reaching an EDZ area $A_{\mathrm{EDZ}} = 17\,\mathrm{m}^2$ and a mean permeability ratio $\Delta\bar{k}_{w,\mathrm{EDZ}} = 26$.

Once the tunnel is excavated ($t = 4.5\,\mathrm{h}$), the EDZ continues to increase, which is associated with the hydraulic changes within the EDZ due to the rise in permeability in the fractured zone and the reduction of excess pore water pressures (both positive and negative) with time. However, the further increase after excavation is relatively modest, with a final EDZ area $A_{\mathrm{EDZ}} = 19\,\mathrm{m}^2$ and a corresponding mean permeability ratio $\Delta\bar{k}_{w,\mathrm{EDZ}} = 30$, compared to the changes observed during the tunnel excavation. Consequently, both the time immediately at the end of excavation and the long-term scenario (up to 1000 days) are valid choices for investigation. Given that the long-term evolution appears to be the most critical, as here the EDZ area is highest, it is selected for the following conducted parameter study.

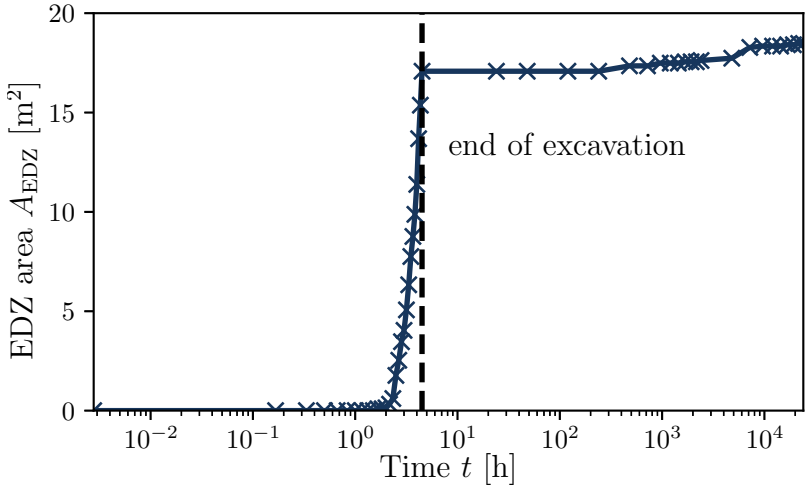

Figure 5.28.: Temporal evolution of the EDZ area for the reference numerical model of unsupported tunnel with $\Delta k_{w,\mathrm{thr}} = 5$

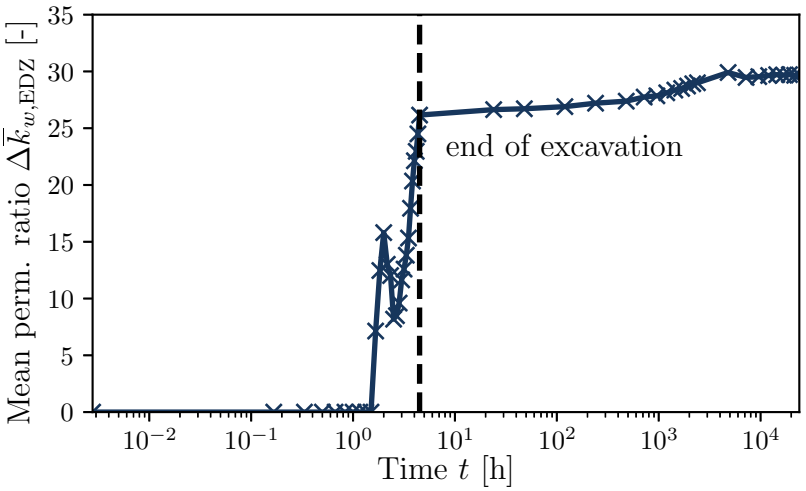

Figure 5.29.: Temporal evolution of the mean permeability ratio within the EDZ for the reference numerical model of unsupported tunnel with $\Delta k_{w,\mathrm{thr}} = 5$

In the evolution of permeability depicted in Figure 5.29, an initial increase is observed, followed by a decrease and a subsequent rise during the tunnel excavation. This phenomenon can be attributed to the fact that, at the beginning, only a few elements characterized by high permeability (see Figure 5.23), which are the imperfect elements that first enter plasticity, are considered in the EDZ calculation.

At this stage, no shear bands have formed, so the EDZ consists only of isolated, unconnected elements. In this context, it must be noted that the EDZ is just beginning to develop. As time progresses, the EDZ expands, incorporating elements with lower permeability, such as those situated between two or more shear bands. Consequently, despite the increase in area, the averaged permeability initially decreases.

By the end of the tunnel excavation, the mean permeability increases again, as the permeability in the shear bands becomes significantly higher, as shown in Figure 5.23. To visually illustrate this growth over time, the calculated outer boundary of the EDZ at various time instances is presented in Figure 5.30. As previously observed, the EDZ experiences significant growth during the tunnel excavation, while thereafter its change becomes minimal and locally limited to the 5° to 15° region, as shown in Figure 5.30.

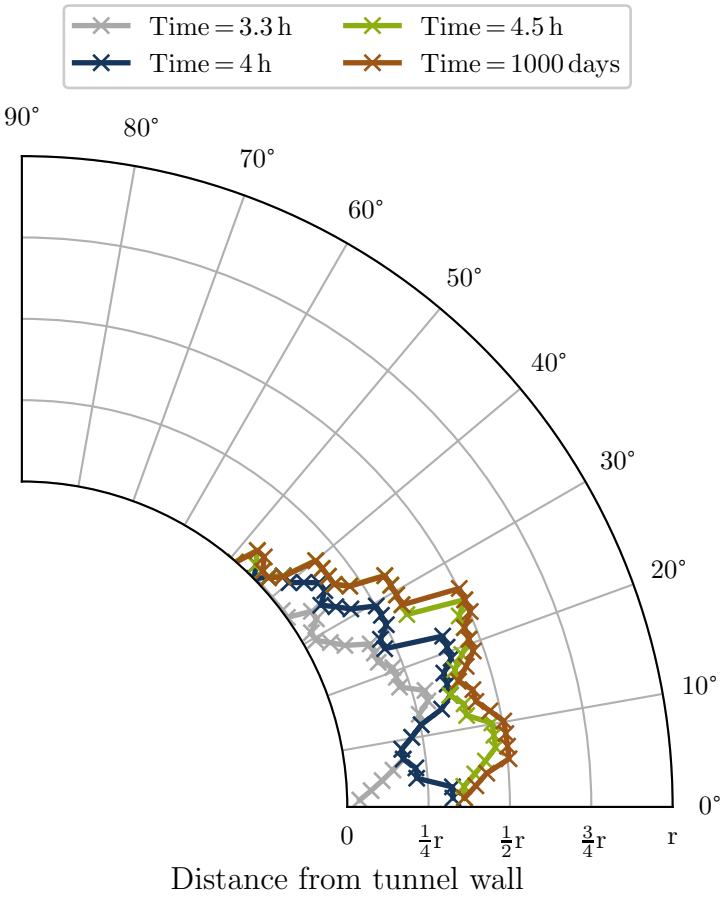

Figure 5.30.: Temporal evolution of the EDZ extension based on $\Delta k_{w,\mathrm{thr}} = 5$ for the reference numerical model of unsupported tunnel (end of excavation: 4.5 h)

In conclusion, it can be stated that among all examined metrics, the change in permeability was selected for the systematic evaluation of the EDZ size. Through the systematic investigation of various threshold values, an optimal threshold was determined.

Finally, the temporal evolution of the EDZ was analyzed, revealing that while the majority of the EDZ forms during tunnel excavation, the size still increased with time. Consequently, the simulation end (1000 days) was chosen as considered time instance for the subsequent parameter study presented in the following section.

5.5. Parameter study of unsupported tunnel

After introducing the numerical model, boundary conditions, and techniques for modeling tunnel excavation and support in the previous sections, a systematic approach was developed to determine the EDZ size, permeability, and the appropriate time for its assessment. Building on these insights, this section presents a parameter study to systematically investigate the influence of selected model parameters on the Excavation Damaged Zone (EDZ).

The study examines various factors, including mechanical law parameters, model geometry, and regularization methods, to understand their impact on the numerically determined EDZ size and permeability evolution within the EDZ. Consistent with the approach in Chapter 4, only one parameter is varied at a time, while all others remain constant.

The section begins by introducing the investigated parameters and their variations. This is followed by a presentation and discussion of the parameter study results, concluding with a summary of the findings.

5.5.1. Presentation of the investigated parameters

In the parameter study conducted in Section 4.3 on the biaxial test, the element size and the second gradient elastic modulus D demonstrated an influence on shear strain localization. Consequently, these parameters are also investigated in the current parameter study on the tunnel model. Additionally, the number, location, and strength of the material imperfections, which facilitate more robust localization, are examined. These factors are highly uncertain, as they cannot be determined in situ, making their investigation an essential part of this study. Furthermore, a geometric parameter, the tunnel diameter, is also investigated within this study, to analyze if the EDZ size can be expressed by the tunnel diameter.

Since the EDZ primarily develops during tunnel excavation and an unsupported tunnel allows for further expansion of the EDZ compared to a supported tunnel, as will be shown in Section 5.6, the present study is conducted exclusively for unsupported tunnels. The insights gained from the parameter study will then be used for the simulation of the supported tunnel.

As already mentioned, the parameter study of the biaxial test revealed hat a certain element size should not be exceeded in order to allow for clear localization.

Therefore, within this study, a total of five different element sizes are investigated: 0.20 m × 0.20 m, 0.25 m × 0.25 m, 0.28 m × 0.28 m, 0.42 m × 0.42 m, and 0.82 m × 0.82 m, as shown in Figure 5.31. This mesh study is limited to the near-tunnel area, since the EDZ only forms in this region. Outside the near-tunnel area, the mesh is the same for all investigated models. The red-marked elements in Figure 5.31 represent the imperfect elements.

At the start of the parameter study, the influence of the imperfect elements is still unclear, therefore they are placed only in the lower half of the modeled tunnel quarter. This decision is based on the expectation that, due to stress anisotropy, the EDZ forms primarily in the horizontal rather than the vertical direction.

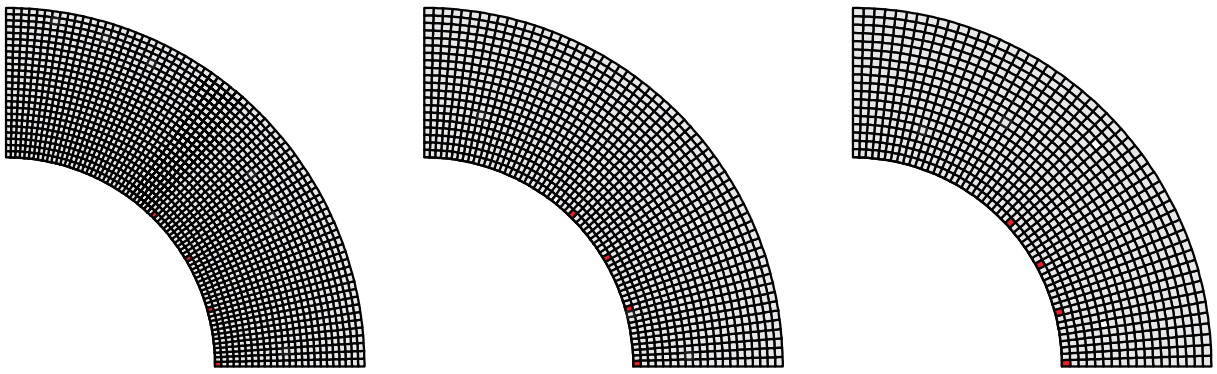

(a) 0.20 × 0.20 m
3722 elements

(b) 0.25 × 0.25 m
2412 elements

(c) 0.28 × 0.28 m
1938 elements

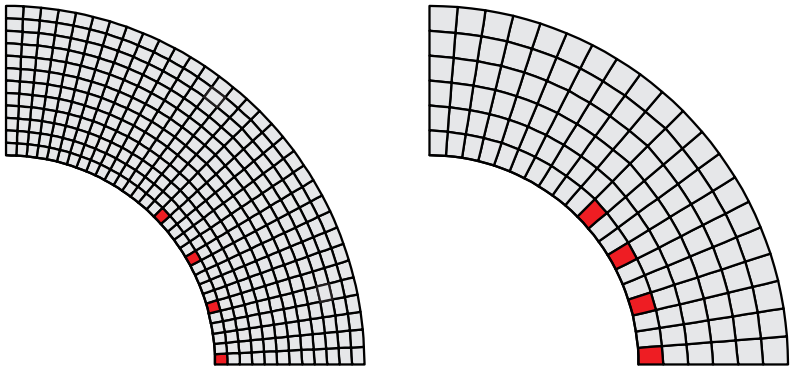

(d) 0.42 × 0.42 m
906 elements

(e) 0.82 × 0.82 m
472 elements

Figure 5.31.: Comparison of different element sizes for the unsupported tunnel model

In addition to the element size, it was also observed that the second gradient elastic modulus D influences the shear band width (see Chapter 4). Although reasonable values for the second gradient elastic modulus D were already determined for the biaxial test in Section 4.3.2, the tunnel model is significantly larger than the biaxial model. Due to the size differences between the model domains, larger elements are used for the tunnel model in order to keep the computational cost within a realistic range. Therefore, D is re-examined as part of this parameter study. The chosen values for D can be found in Table 5.2.

The necessity of incorporating imperfect elements was thoroughly discussed in the previous chapter, particularly in scenarios with highly homogeneous stress paths, such as the wetting scenario in the biaxial test, where all elements follow a similar stress path during saturation. While imperfect elements are mandatory in such cases to initiate localization, it is not initially clear whether, or to what extent, they are required in the tunnel model. However, according to Pardoen (2015), material imperfections are expected to facilitate strain localization. Therefore, their role and influence are investigated as part of this parameter study.

Similar to the approach in the biaxial test, this parameter study investigates four different reductions in cohesion aimed at creating material imperfections. As a result, the yield surface of the Barcelona Basic Model (BBM) becomes smaller, causing the imperfect elements to reach plasticity earlier under the same stress path. This, in turn, triggers the formation of shear bands. The reduced cohesion c, relative to the cohesion of the intact elements c_0, is expressed as $\frac{c}{c_0}$ and took the values 0.01, 0.1, 0.5, and 0.75.

In addition to the strength of the material imperfections, the influence of the number of imperfect elements is also investigated. A total of five different quantities, ranging from 4 to 8 imperfect elements, are examined. These imperfect elements are evenly distributed across the lower half of the modeled tunnel quarter, as shown in Figure 5.32. The aim is to determine whether the size of the EDZ is influenced by the number of imperfect elements and to identify a reasonable number of imperfect elements for subsequent simulations.

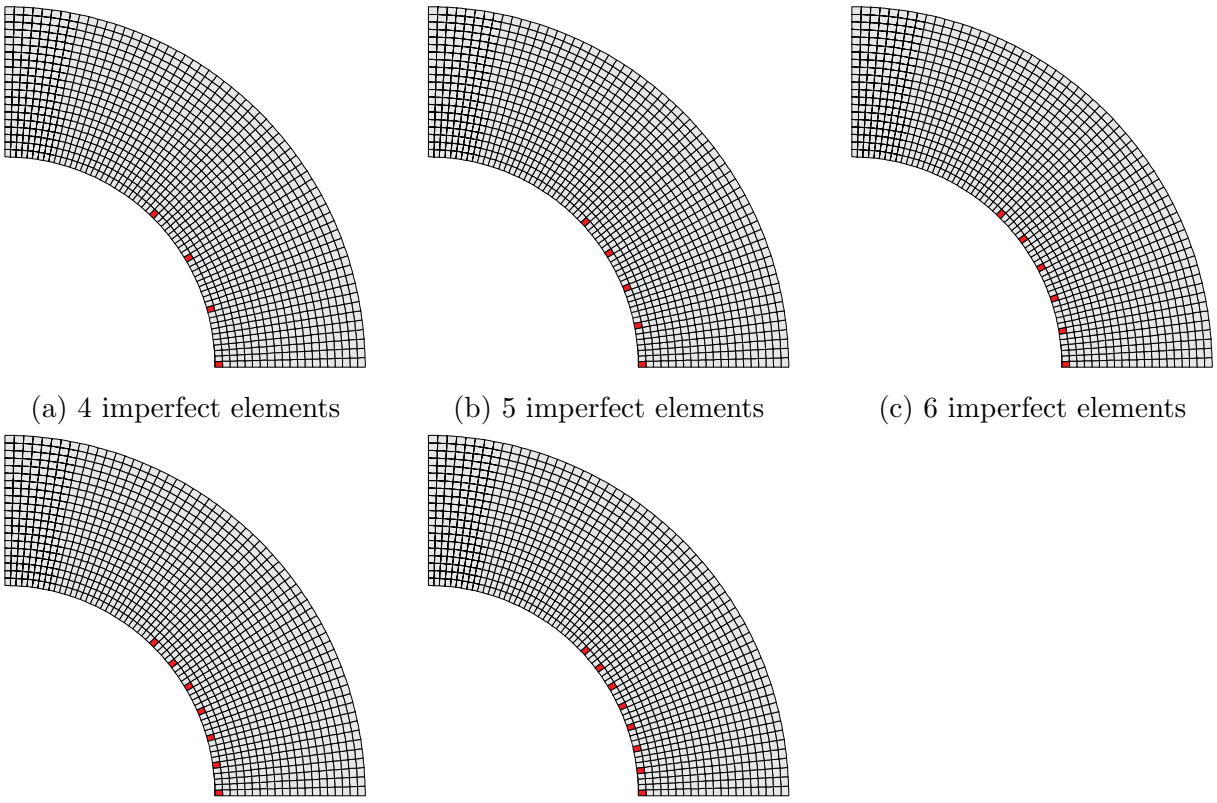

(a) 4 imperfect elements (b) 5 imperfect elements (c) 6 imperfect elements

(d) 7 imperfect elements (e) 8 imperfect elements

Figure 5.32.: Comparison of different numbers of imperfect elements at the excavation face of the unsupported tunnel model

Lastly, the tunnel diameter is investigated. To isolate the influence of the tunnel diameter, the following model discretization is employed. Based on the assumption that the EDZ extends approximately half of the tunnel radius ($0.5r$) in the horizontal direction, the near-tunnel area is set to 0.716r, based on models with a 14 m diameter, as shown in Figure 5.33. To avoid any effects from scaling and the associated changes in element size, an approximately identical element size within this zone is used for each examined diameter, to ensure that only the influence of the diameter is studied. A total of three tunnel diameters, 6 m, 10 m, and 14 m, are investigated.

Table 5.2 provides an overview of all the investigated parameters along with the considered values. The bold values in the table represent the selected values which are kept constant for the other scenarios.

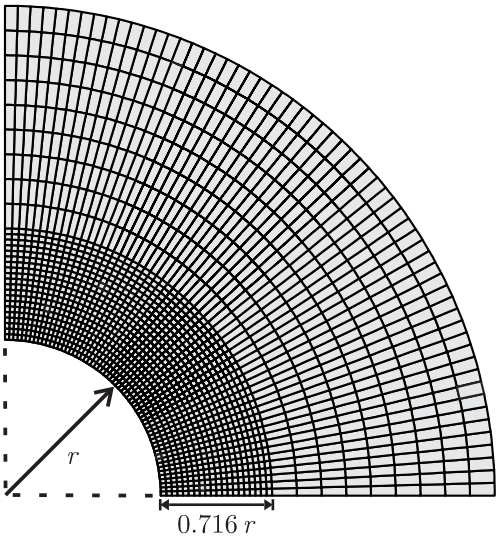

Figure 5.33.: Mesh strategy for unsupported tunnel model with different diameters

Table 5.2.: Sets of values in the parameter study for the unsupported tunnel model

Parameter	Set of Values
Flow rule of mechanical law	**Associated**
	Non-associated
Number of imperfect elements	**4**
	5
	6
	7
	8
Average element size within EDZ (m × m)	0.20×0.20
	$\mathbf{0.25 \times 0.25}$
	0.28×0.28
	0.42×0.42
	0.82×0.82
Reduced cohesion of material imperfection $\frac{c}{c_0}$	0.01
	0.1
	0.5
	0.75
Second gradient elastic modulus D (N)	5×10^1
	$\mathbf{5 \times 10^2}$
	5×10^3
	5×10^4
Tunnel diameter d (m)	6
	10
	14

5.5.2. Effect of flow rules of the mechanical law on the EDZ

The flow rule in an elastoplastic constitutive model governs the direction and magnitude of plastic strain increments under applied stress, encompassing both deviatoric and volumetric strain components. This rule defines the relationship between the plastic potential surface, which determines the strain direction, and the yield surface, which delineates the onset of plasticity. The flow rule dictates the proportion of plastic volumetric and deviatoric strains during the deformation process. Therefore, it can be expected that the flow rule may also influence shear strain localization in terms of size, magnitude and orientation. In the original formulation of the BBM, a non-associated flow rule (see Equations 2.16 and 2.17) was implemented, based on the assumption that zero lateral strains occur for stress states corresponding to Jaky's K_0 values. This section examines to what extent this assumption, compared to an associated flow rule ($\alpha = 1$ in Equation 2.16), affects shear strain localization.

For comparison, the deviatoric strains and the resulting permeability ratios after $t = 1000$ days are shown in Figures 5.34 and 5.35. When comparing the associated and non-associated flow rules in terms of deviatoric strain as well as permeability ratio, only marginal differences can be observed.

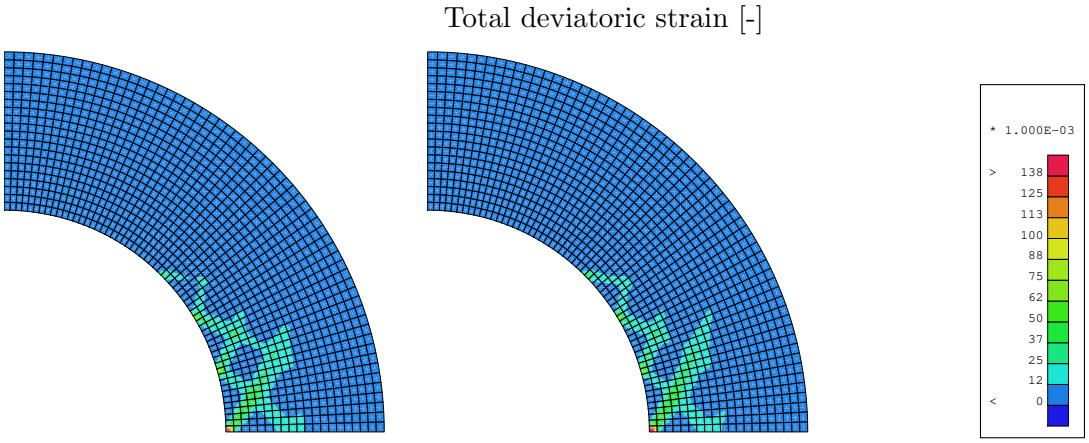

(a) Associated flow rule (b) Non-associated flow rule

Figure 5.34.: Comparison of total deviatoric strain within the unsupported tunnel model for different flow rules ($t = 1000$ days)

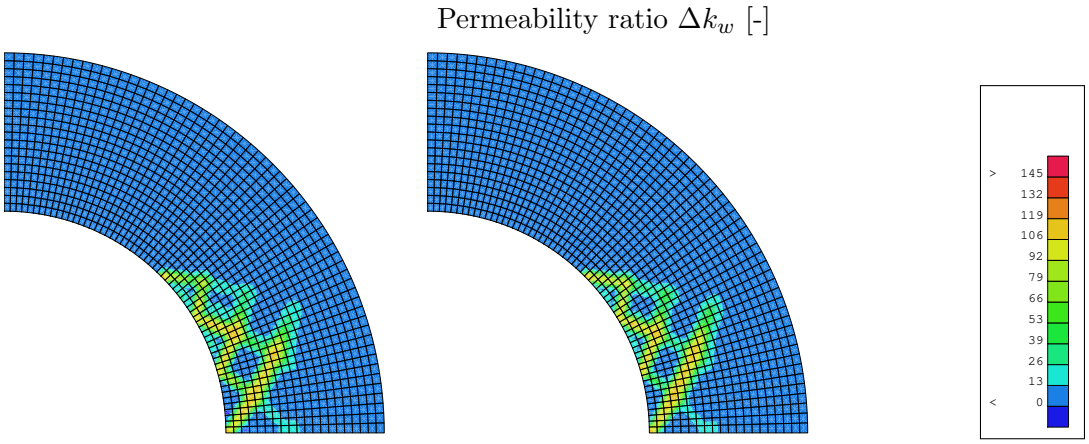

(a) Associated flow rule (b) Non-associated flow rule

Figure 5.35.: Comparison of permeability ratio within the unsupported tunnel model for different flow rules ($t = 1000$ days)

Therefore, the plastic points and the bifurcation directions are also depicted in Figures 5.36 and 5.37, respectively. The plastic points indicate that the shear bands can be more distinctly separated from the zones between them when using a non-associated flow rule compared to an associated flow rule. This improved separation arises because the regions between the shear bands remain predominantly in an elastic state under the non-associated flow rule, creating a clearer contrast with the localized areas of plasticity within the shear bands.

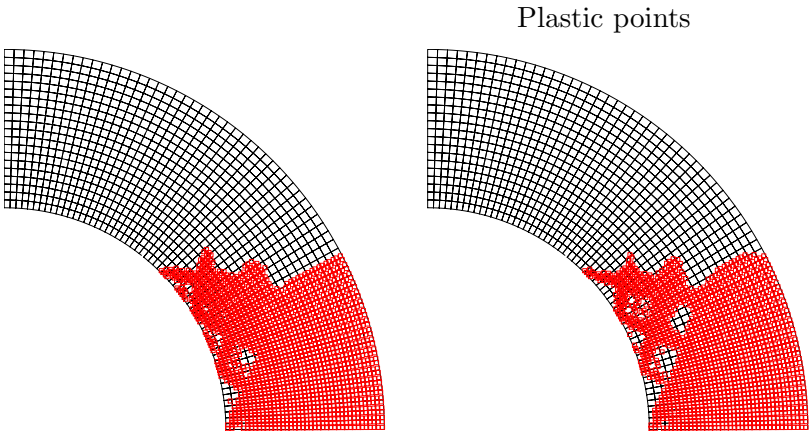

(a) Associated flow rule (b) Non-associated flow rule

Figure 5.36.: Comparison of plastic points within the unsupported tunnel model for different flow rules ($t = 1000$ days)

The bifurcation direction exhibits more pronounced differences between the associated and the non-associated flow rule. With the associated flow rule, only elements within the shear band meet the criterion, whereas using the non-associated flow rule, elements adjacent to the shear bands also fulfill the criterion. This suggests that, with a non-associated flow rule, more elements are prone to localization.

Subsequently, the EDZ area A_{EDZ}, the mean permeability $\bar{k}_{w,\mathrm{EDZ}}$, and the outer contour of the EDZ are presented in Figure 5.38, with the two former values given in the legend. As shown, the resulting EDZ area is $0.38\,\mathrm{m}^2$ smaller with the non-associated flow rule than with the associated one, while the resulting mean permeability differs only slightly.

The differences in the EDZ area, despite similar mean permeability, arise because the non-associated flow rule leads to greater unloading in the regions between shear bands due to localization. Consequently, these regions remain in the elastic range, leading to correspondingly lower permeability. As a result, in the outer boundary regions, some elements are considered in the EDZ area calculation for the associated flow rule that are not considered for the non-associated one. This is clearly visible in the region between 5° and 10° in Figure 5.38. Since these boundary areas with lower permeability, which are close to the threshold permeability ratio of $\Delta k_{w,\mathrm{thr}} = 5$, are excluded, yet the areas within the EDZ between the shear bands exhibit lower permeability compared to the associated flow rule, these two factors cancel each other out, leading to an almost identical mean permeability between the two flow rules.

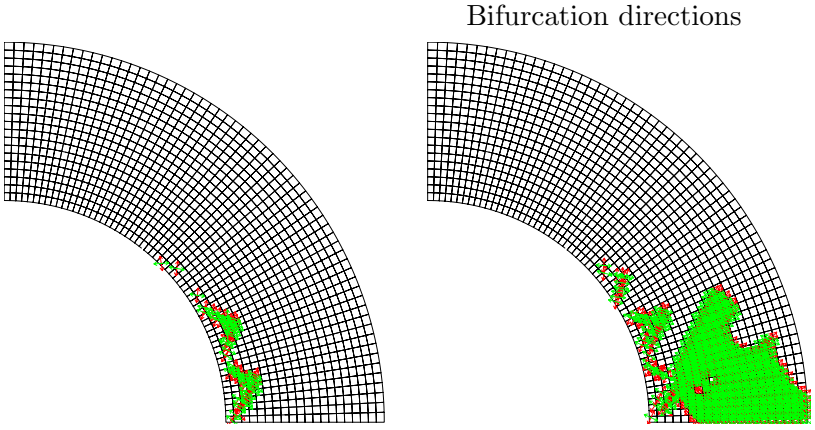

(a) Associated flow rule (b) Non-associated flow rule

Figure 5.37.: Comparison of bifurcation directions within the unsupported tunnel model for different flow rules ($t = 1000$ days)

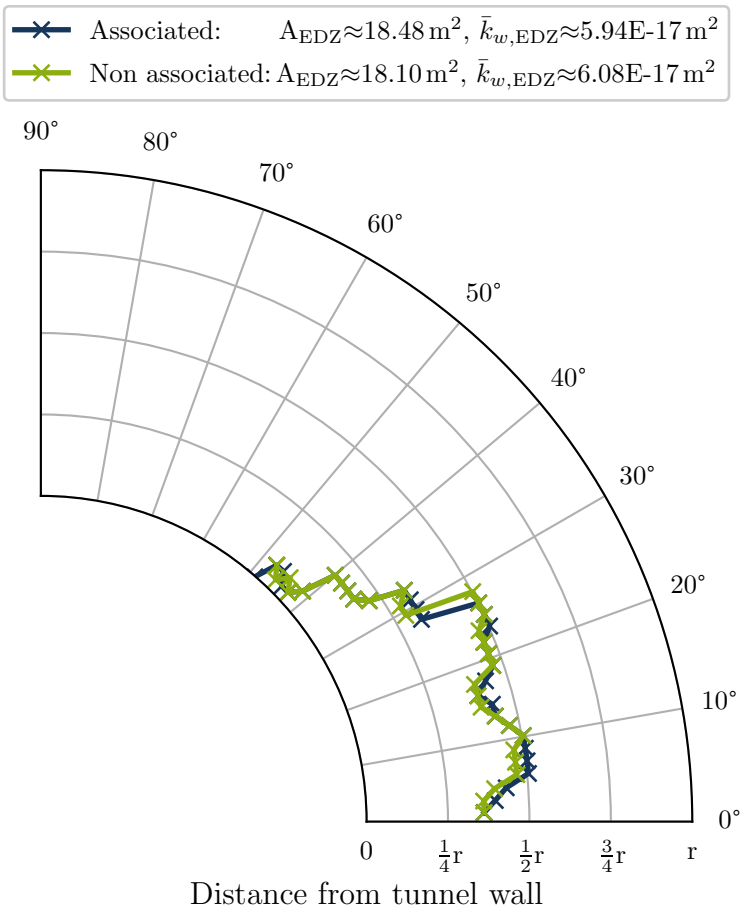

Figure 5.38.: Extension of the EDZ based on $\Delta k_{w,\mathrm{thr}} = 5$ for different flow rules ($t = 1000$ days)

It can be concluded that while the non-associated flow rule results in a more distinct differentiation of the shear bands from the surrounding areas, the EDZ area is slightly larger for the associated flow rule. Although the differences are relatively minor, the associated flow rule is selected for all subsequent simulations due to the larger generated EDZ size compared to the non-associated flow rule, thus representing the worst case scenario.

5.5.3. Effect of number of imperfect elements

As previously demonstrated, material imperfections are necessary for shear strain localization under certain stress paths, such as the wetting path in the biaxial test in Section 4.3.2, and generally enable more robust localization. While material imperfections cannot be directly determined through in situ investigations, their importance was examined, among others, by Desrues and Viggiani (2004) in laboratory tests. That study concluded that material imperfections did not affect the global stress-strain response of the specimen during biaxial testing but influenced the position of the shear band, as it acts as a strain localization attractor. This section aims to investigate the influence of the number of imperfect elements on the EDZ size and mean permeability. A total of five different numbers of imperfect elements are analyzed. As before, the deviatoric strains and the resulting permeability changes are first examined, as shown in Figures 5.39 and 5.40.

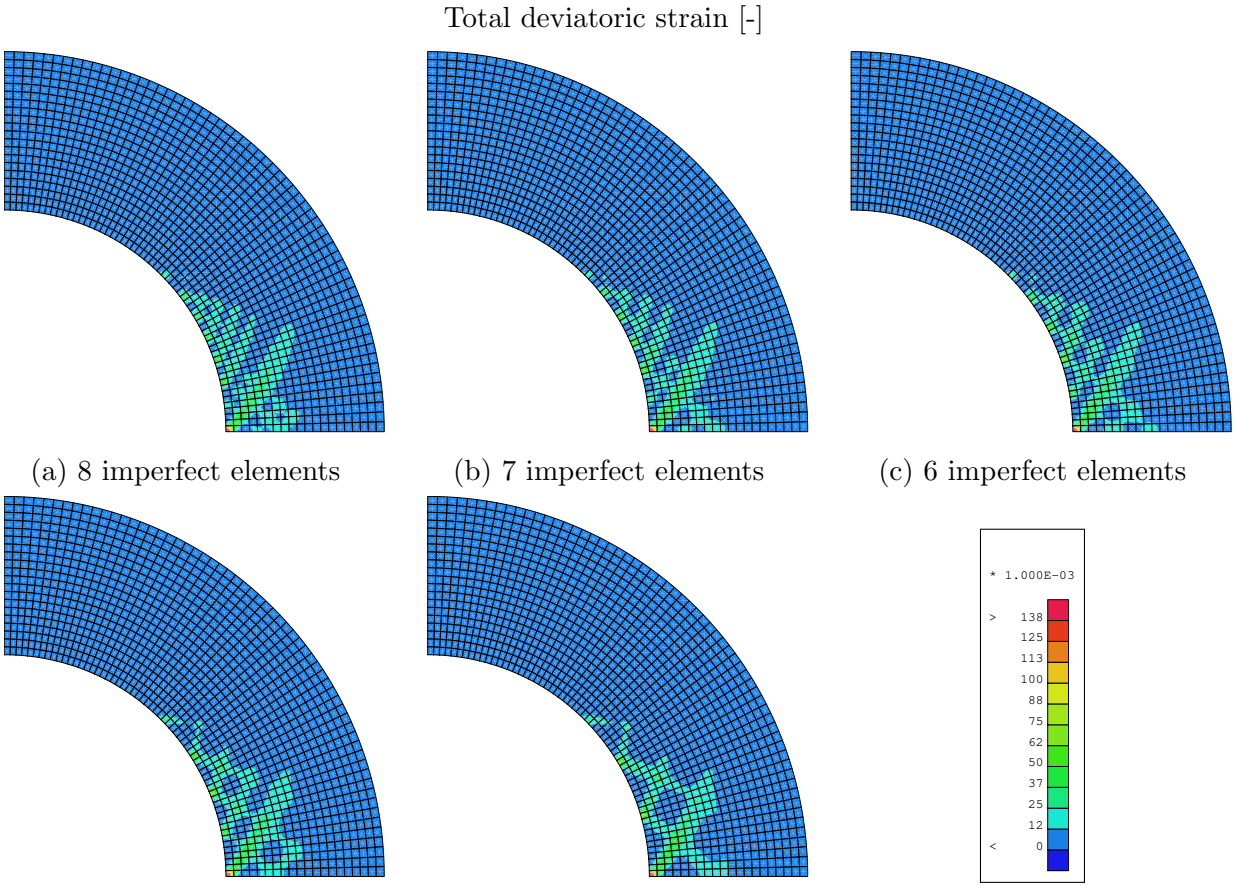

(a) 8 imperfect elements (b) 7 imperfect elements (c) 6 imperfect elements

(d) 5 imperfect elements (e) 4 imperfect elements

Figure 5.39.: Comparison of total deviatoric strain within the unsupported tunnel model for different numbers of imperfect elements ($t = 1000$ days)

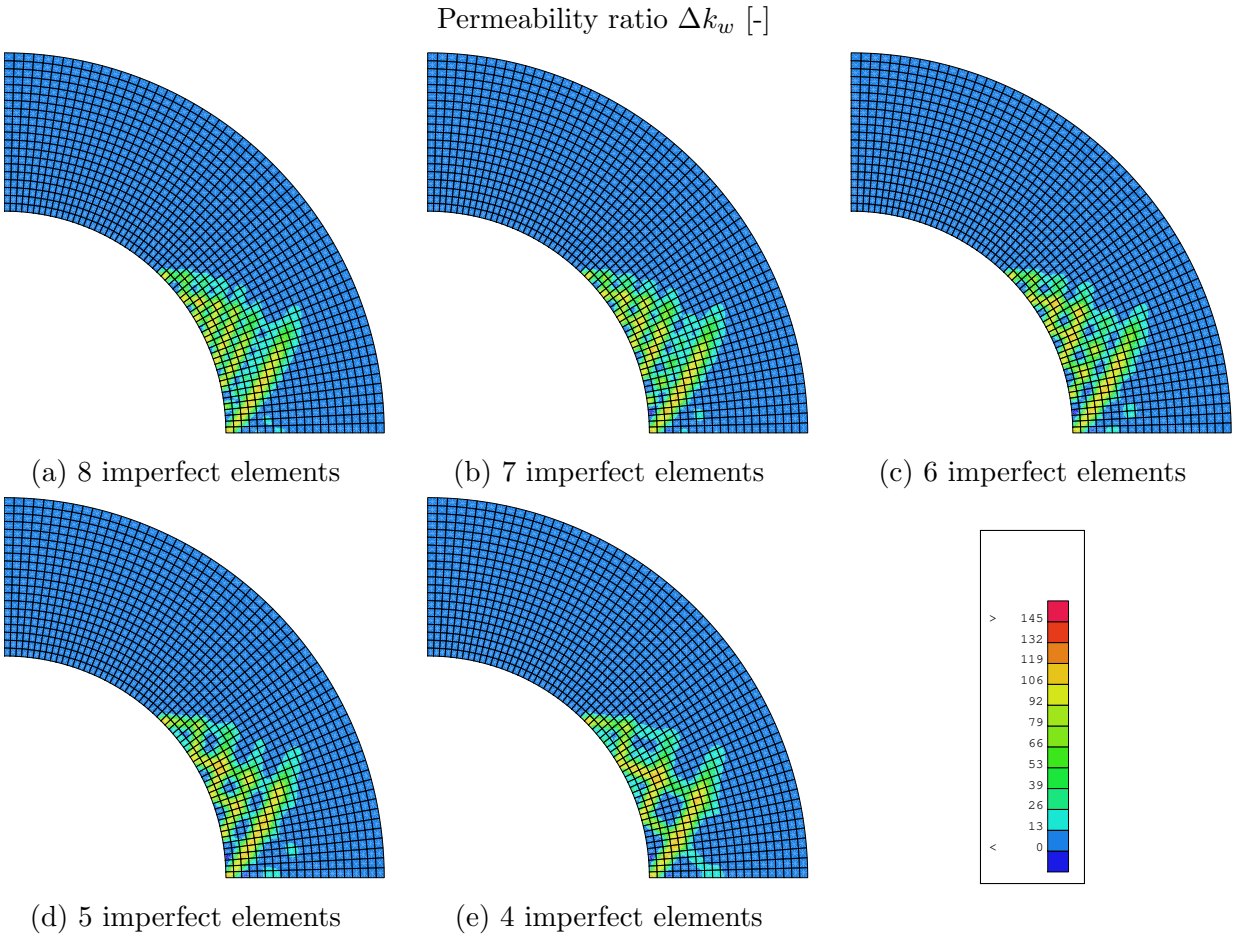

(a) 8 imperfect elements (b) 7 imperfect elements (c) 6 imperfect elements

(d) 5 imperfect elements (e) 4 imperfect elements

Figure 5.40.: Comparison of permeability ratio within the unsupported tunnel model for different numbers of imperfect elements ($t = 1000$ days)

In Figures 5.39 and 5.40 it can be seen that the more imperfect elements are present, the more shear bands develop. This can be explained by the role of the imperfect elements, which are introduced in the model to trigger shear strain localization. Beyond a certain number of shear bands, it becomes impossible to distinguish the individual shear bands from the areas outside of them, as seen e.g. in Figure 5.39a. This can be explained by the fact that, due to the uniform distribution of the imperfect elements on the tunnel excavation wall, the imperfect elements are positioned closer together, and thus the shear bands. When looking solely at the extent of the EDZ, Figures 5.39 and 5.40 reveal minimal differences between the investigated models. To quantify this, the EDZ size and mean permeability ratio as a function of the number of imperfect elements are shown in Figures 5.41 and 5.42.

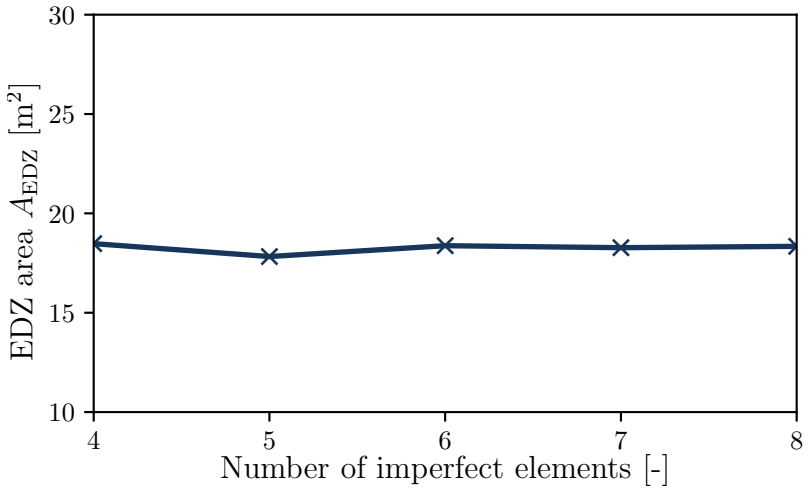

Figure 5.41.: EDZ area for different numbers of imperfect elements

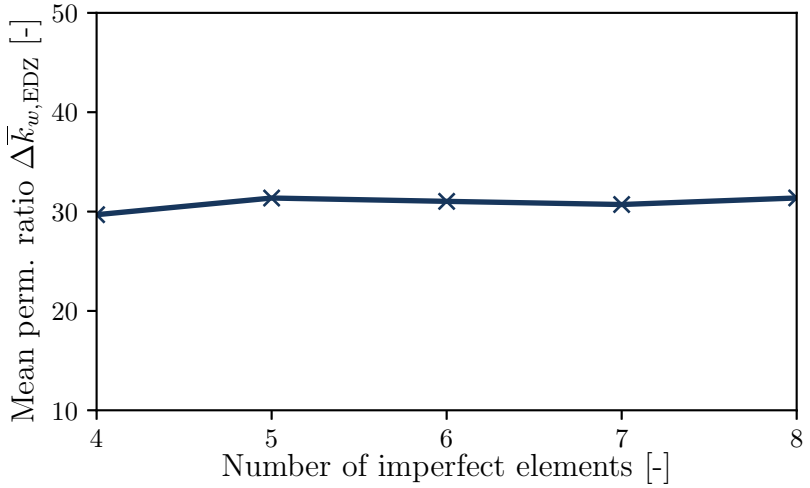

Figure 5.42.: Mean permeability ratio within the EDZ for different numbers of imperfect elements

The calculated EDZ area and mean permeability show only minimal fluctuations between the models analyzed. The EDZ area remains in the range of 18.4 m^2, and the mean permeability ratio around 30. For three selected cases (4, 6, and 8 imperfect elements), the calculated outer boundaries of the EDZ are shown in Figure 5.43. Again, very little variation is observed between the models analyzed.

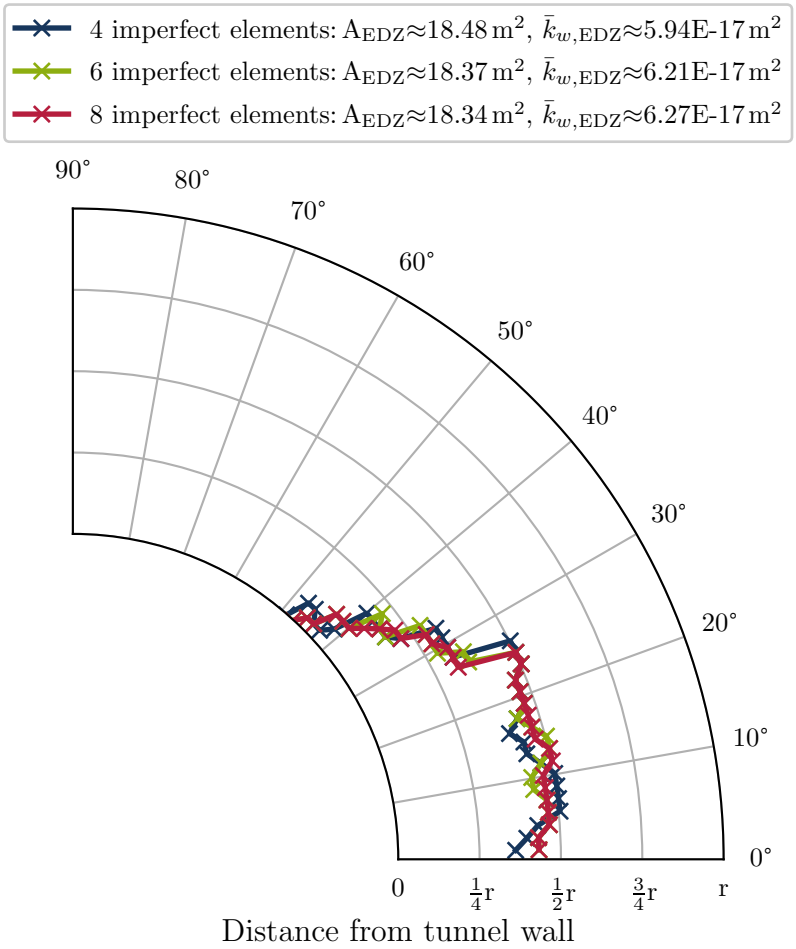

Figure 5.43.: Extension of the EDZ based on $\Delta k_{w,\mathrm{thr}} = 5$ for different numbers of imperfect elements ($t = 1000$ days)

This leads to the conclusion that while the amount of imperfections affects the number and position of shear bands, it has no significant impact on the size of the EDZ or on the mean permeability. Since no particular studies on the spacing of fractures in Opalinus clay shale during tunnel excavation are available to validate a specific choice, it is decided to proceed with the smallest number of imperfections, in this case four imperfections, to minimize their potential influence on other model parameters and results, and because they allow for a clear shear strain localization.

5.5.4. Effect of element size

In this section, the influence of different element sizes on the EDZ is investigated. Although the local second gradient model ensures mesh-independent shear strain localization, as demonstrated in Section 4.3.1, the underlying finite element method, particularly the shape functions used, requires a sufficiently fine mesh. This is especially important when modeling shear bands, where sharp deformation gradients are present, to clearly distinguish between the band and the area outside of it. This is visibly evident in Figures 5.44 and 5.45. For element sizes of $0.82 \times 0.82\,\mathrm{m}$ and $0.42 \times 0.42\,\mathrm{m}$, the individual shear bands consist of only one element in width, making it impossible to differentiate between areas within the shear band and outside of the shear band. As the element size decreases, the shear bands become more distinct. When comparing the three smallest element sizes ($0.28 \times 0.28\,\mathrm{m}$, $0.25 \times 0.25\,\mathrm{m}$, and $0.20 \times 0.20\,\mathrm{m}$), no differences in shear band width can be visually observed in Figures 5.44 and 5.45.

When calculating the EDZ area and permeability ratio within the EDZ, it becomes clear that the decrease in element size leads to a decrease in the EDZ area and the mean permeability, as depicted in Figures 5.46, 5.47 and 5.48. However, beyond a certain level of mesh refinement, this trend reaches a limit, which is in this case for element sizes below $0.25 \times 0.25\,\mathrm{m}$. This can be explained by the fact that with smaller elements, the shear bands can be better distinguished by the model, resulting in a smaller EDZ area. Once a certain element size is reached, further resolution or accuracy gain does not lead to any additional changes in the obtained values.

In conclusion, as in the biaxial test, a certain element size is necessary to achieve distinct shear bands. Once this element size is reached, further mesh refinement has no impact on the resulting EDZ size. Therefore, for all subsequent calculations, an element size of $0.25 \times 0.25\,\mathrm{m}$ is used in the vicinity of the tunnel to keep the computational cost of the simulations as low as possible.

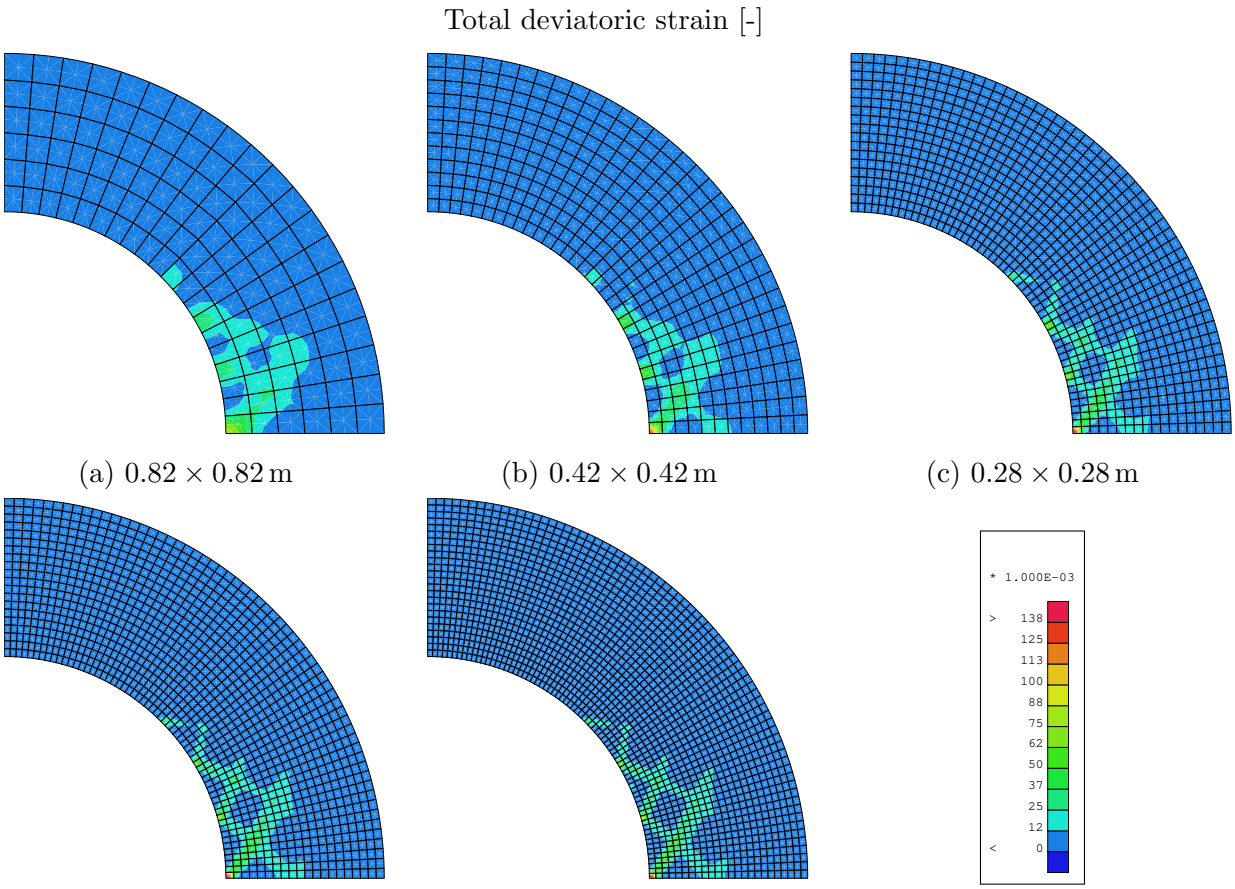

(a) $0.82 \times 0.82\,\mathrm{m}$ (b) $0.42 \times 0.42\,\mathrm{m}$ (c) $0.28 \times 0.28\,\mathrm{m}$

(d) $0.25 \times 0.25\,\mathrm{m}$ (e) $0.20 \times 0.20\,\mathrm{m}$

Figure 5.44.: Comparison of total deviatoric strain within the unsupported tunnel model for different element sizes ($t = 1000$ days)

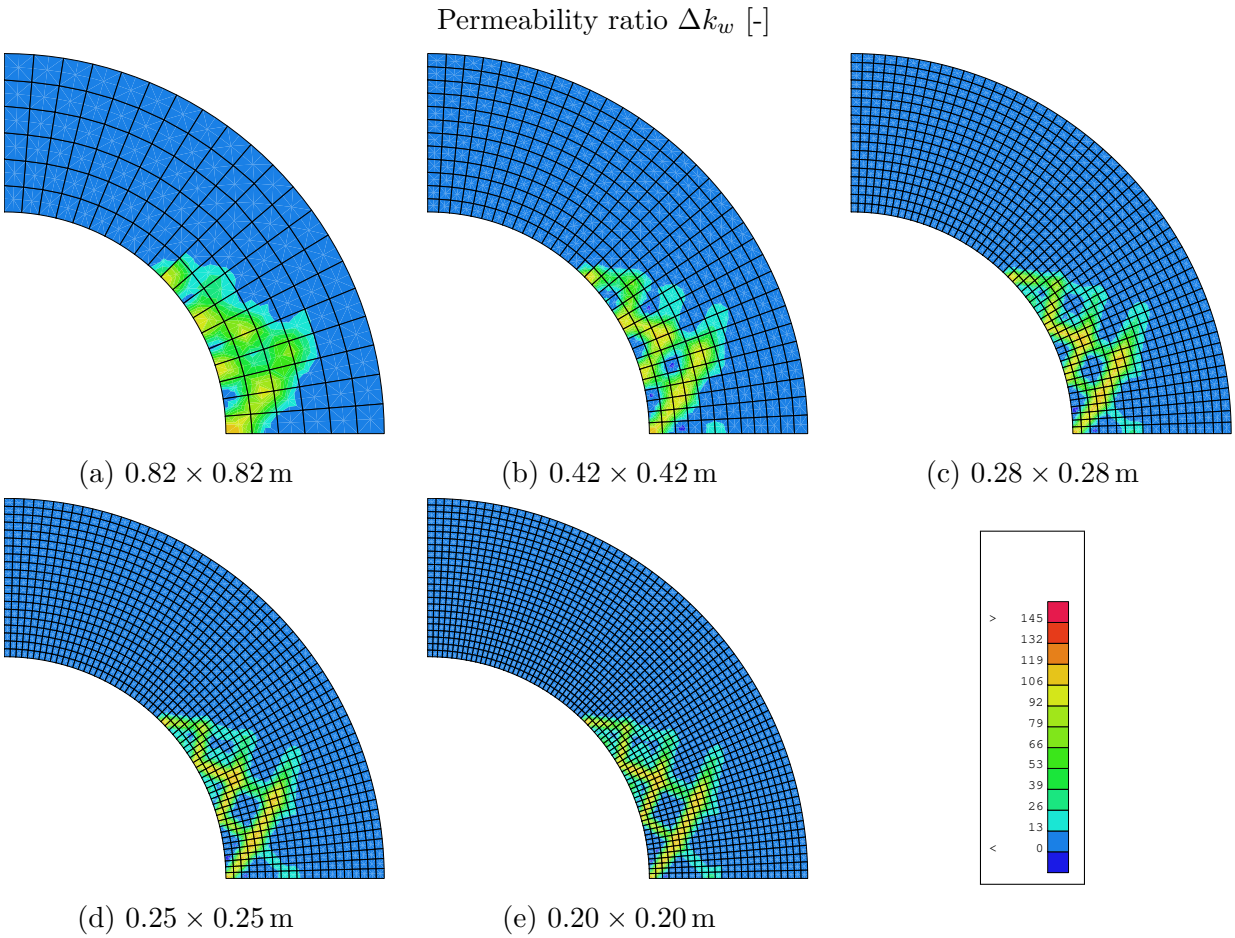

(a) $0.82 \times 0.82\,\mathrm{m}$ (b) $0.42 \times 0.42\,\mathrm{m}$ (c) $0.28 \times 0.28\,\mathrm{m}$

(d) $0.25 \times 0.25\,\mathrm{m}$ (e) $0.20 \times 0.20\,\mathrm{m}$

Figure 5.45.: Comparison of permeability ratio within the unsupported tunnel model for different element sizes ($t = 1000$ days)

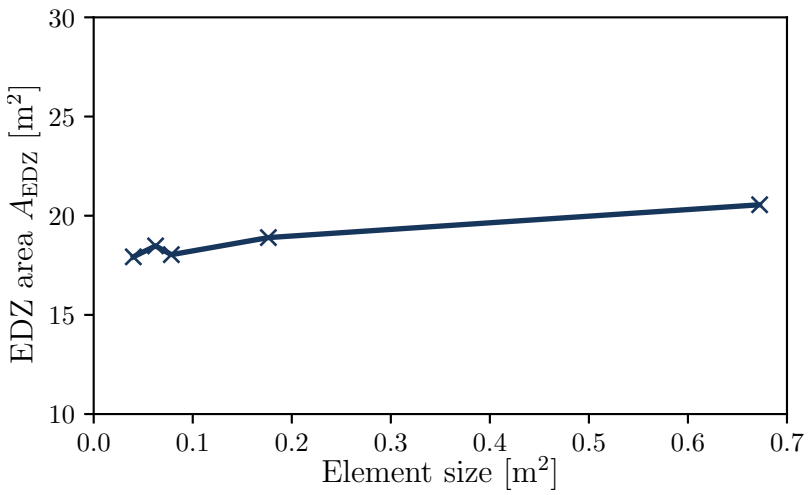

Figure 5.46.: EDZ area for different element sizes ($t = 1000$ days)

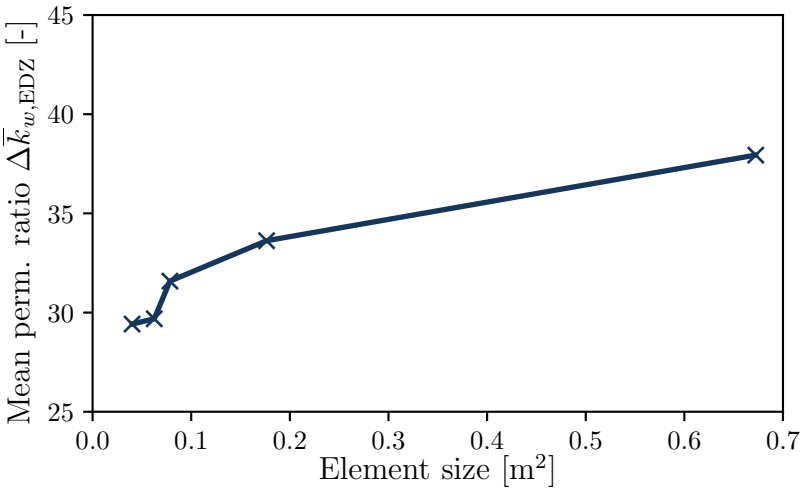

Figure 5.47.: Effect of element size on mean permeability ratio ($t = 1000$ days)

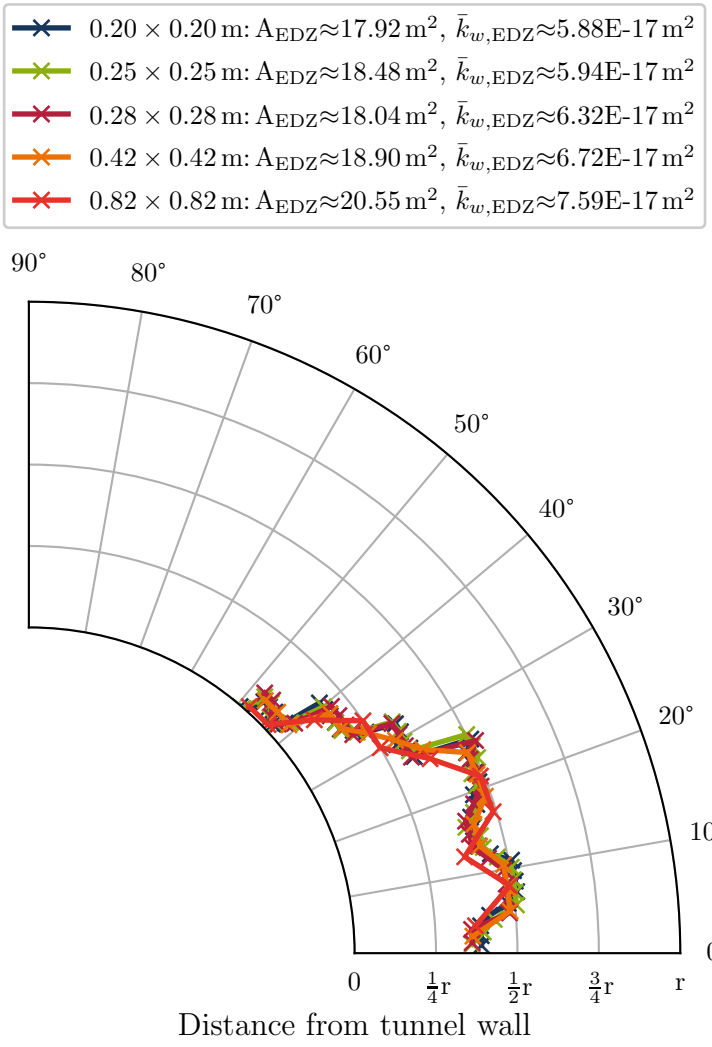

Figure 5.48.: EDZ extension for different mesh sizes ($\Delta k_{w,\mathrm{thr}} = 5$, $t = 1000$ days)

5.5.5. Effect of the shear strength of the material imperfection

In this section, the impact of the strength reduction of the material imperfection on shear strain localization is examined. As Pardoen (2015) has already noted, an imperfect element must exhibit a certain reduction in strength compared to the intact elements in order to reach plasticity earlier and trigger shear strain localization. In this research, a reduction in cohesion is considered as the material imperfection. Four different reductions in cohesion relative to the initial cohesion c_0 are investigated: $c/c_0 = 0.75$, 0.5, 0.1, and 0.01.

First, the deviatoric strains and permeability changes are presented in Figures 5.49 and 5.50. It is already evident that a reduction in cohesion to 75% of the original cohesion of 2 MPa does not lead to localized failure, as shown in Figure 5.49a. Instead, a diffuse failure is visible. However, at a reduction of 50% and more, shear bands become clearly visible, and failure is localized. Between 10% and 1% of the original cohesion, no visual differences can be observed in either the deviatoric strains (Figures 5.49c and 5.49d) or the permeability changes (Figures 5.50c and 5.50d).

For a systematic analysis, the EDZ area and mean permeability within the EDZ are calculated for all four cohesion reductions and shown in Figures 5.51 and 5.52. The results indicate similar values for the EDZ area and mean permeability across the different cohesion reductions. This is also reflected in the EDZ outer boundaries, which are depicted in Figure 5.53.

Based on the previously discussed observations, it can be concluded that a certain reduction in cohesion is necessary to induce clear localized failure. However, the magnitude of this reduction has only a marginal impact on the EDZ size and mean permeability, as long it amounts 50% or more according to Figure 5.49a. Since no significant differences are observed between cohesion ratios of $c/c_0 = 10\%$ and 1%, a reduction to 10% of the cohesion in intact elements, or 0.2 MPa, is chosen for the subsequent simulations.

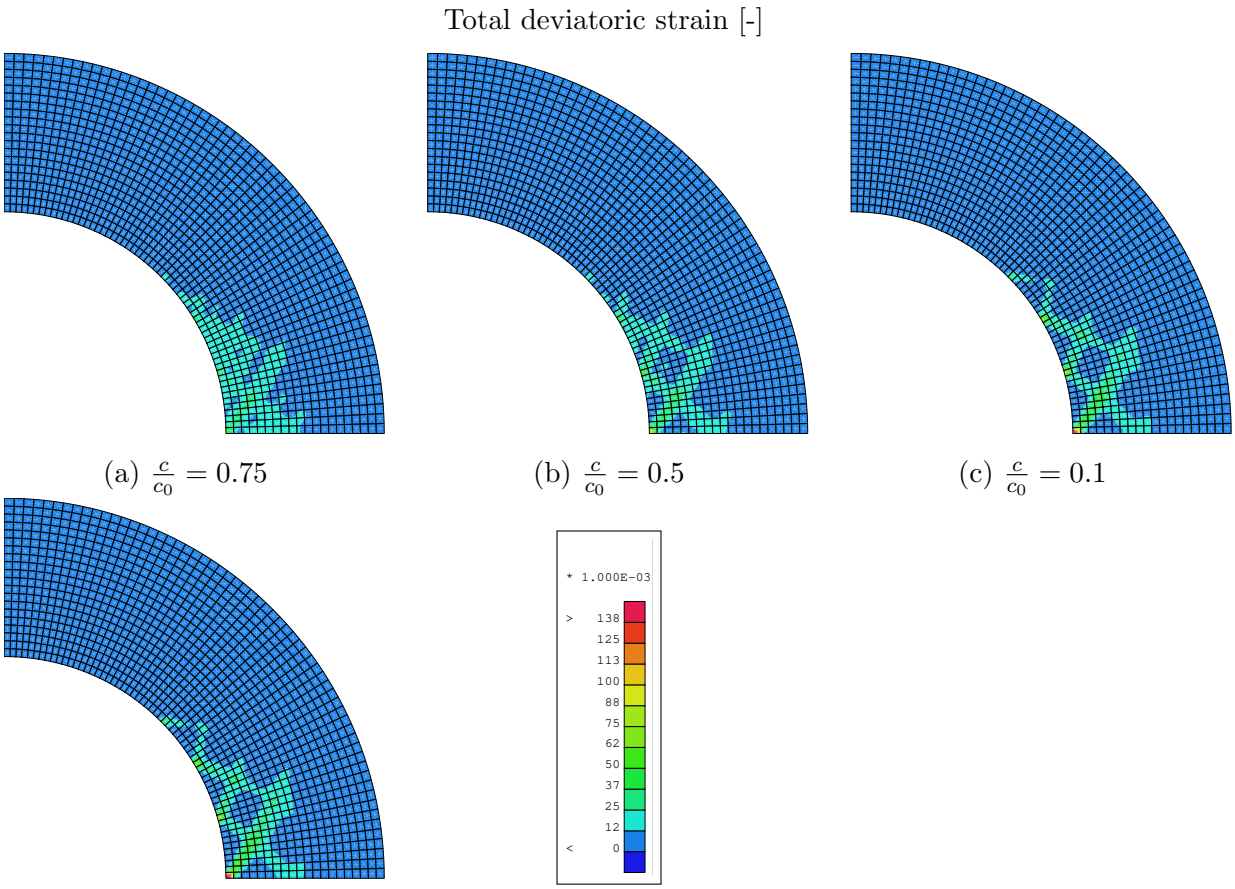

(a) $\frac{c}{c_0} = 0.75$ (b) $\frac{c}{c_0} = 0.5$ (c) $\frac{c}{c_0} = 0.1$

(d) $\frac{c}{c_0} = 0.01$

Figure 5.49.: Comparison of total deviatoric strain within the unsupported tunnel model for varying imperfection strength ($t = 1000$ days)

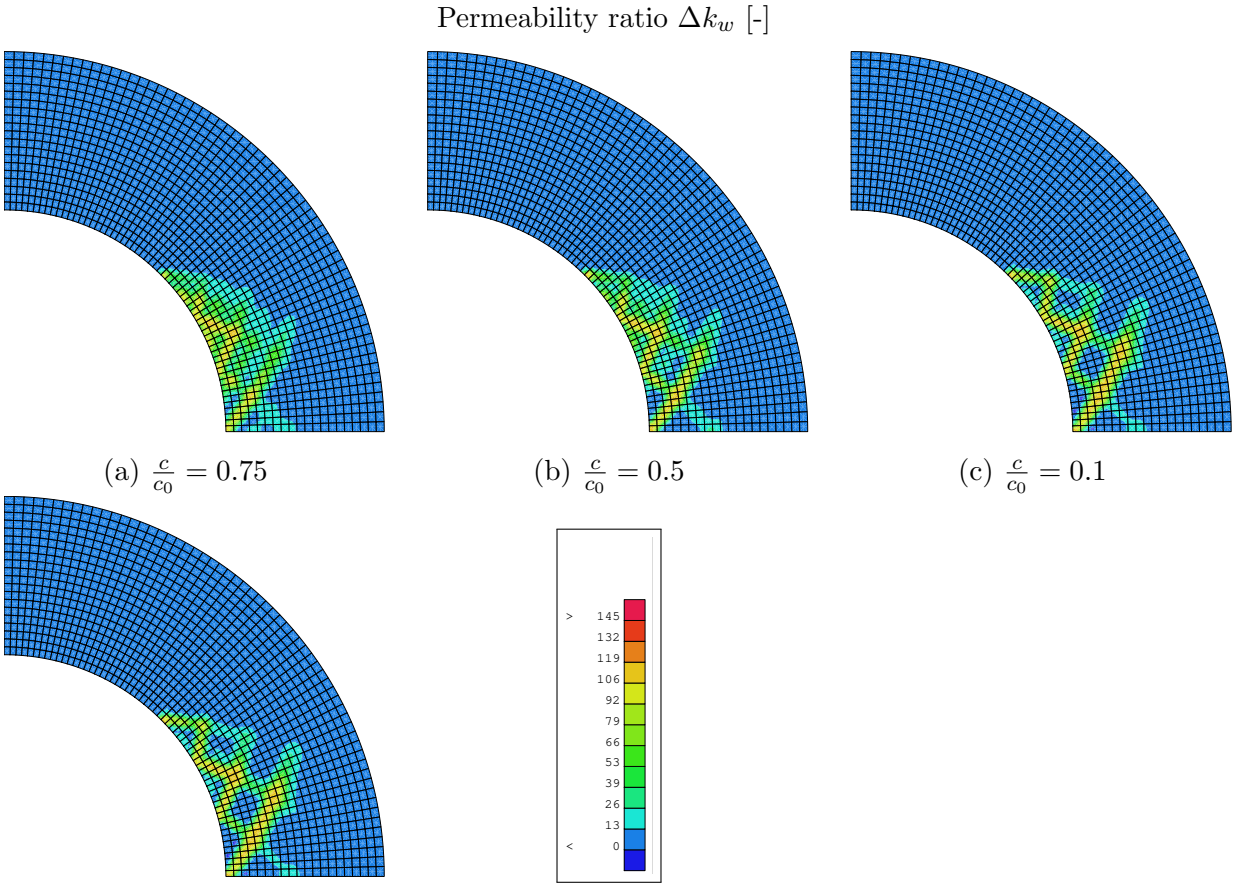

(a) $\frac{c}{c_0} = 0.75$ (b) $\frac{c}{c_0} = 0.5$ (c) $\frac{c}{c_0} = 0.1$

(d) $\frac{c}{c_0} = 0.01$

Figure 5.50.: Comparison of permeability ratio within the unsupported tunnel model for varying imperfection strength ($t = 1000$ days)

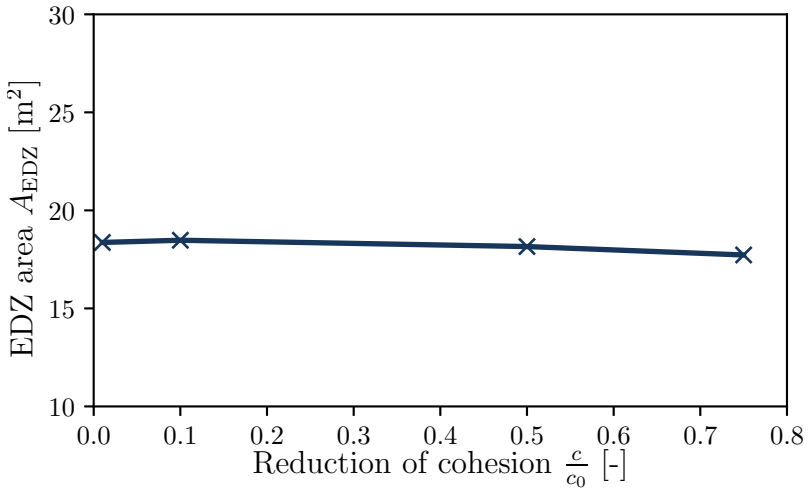

Figure 5.51.: EDZ area for varying imperfection strength ($t = 1000$ days)

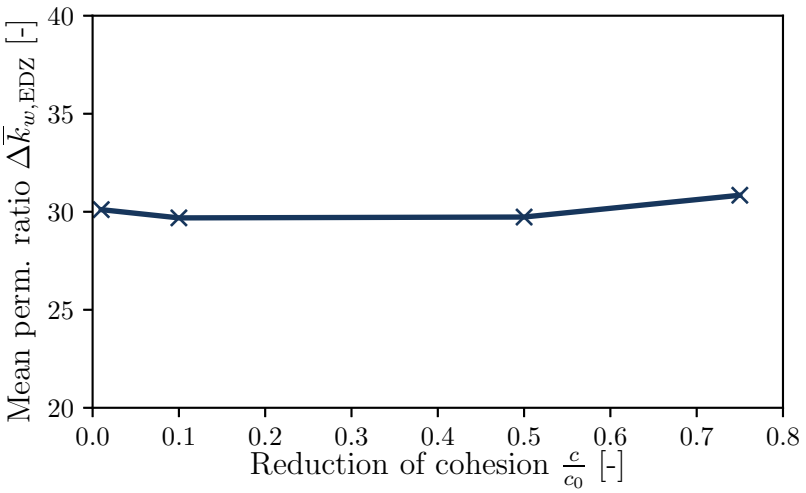

Figure 5.52.: Mean permeability ratio for varying imperfection strength ($t = 1000$ days)

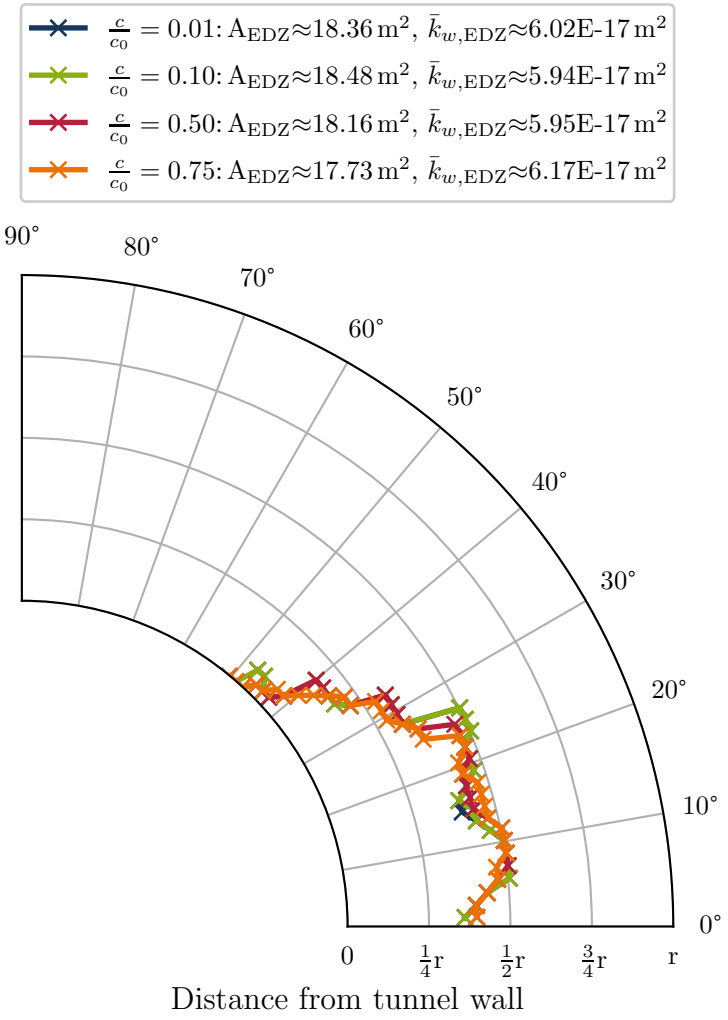

Figure 5.53.: EDZ extension for varying imperfection strength ($t = 1000$ days)

5.5.6. Effect of second gradient elastic modulus

For the chosen regularization method, the local second gradient model, the only parameter, the second gradient elastic modulus D, is analyzed regarding its influence on the EDZ area and mean permeability within the EDZ. Since the second gradient modulus acts as an internal length scale, it affects the width of the shear bands. This was already demonstrated in Section 4.3.2 for the biaxial test. Since the element sizes were altered due to the larger scale of the tunnel model compared to the biaxial test model, the second gradient elastic modulus D must also be re-examined. Therefore, four different values of D within the range of 5×10^1 to 5×10^4 N are examined.

The deviatoric strains and the mean permeability are presented in Figures 5.54 and 5.55.

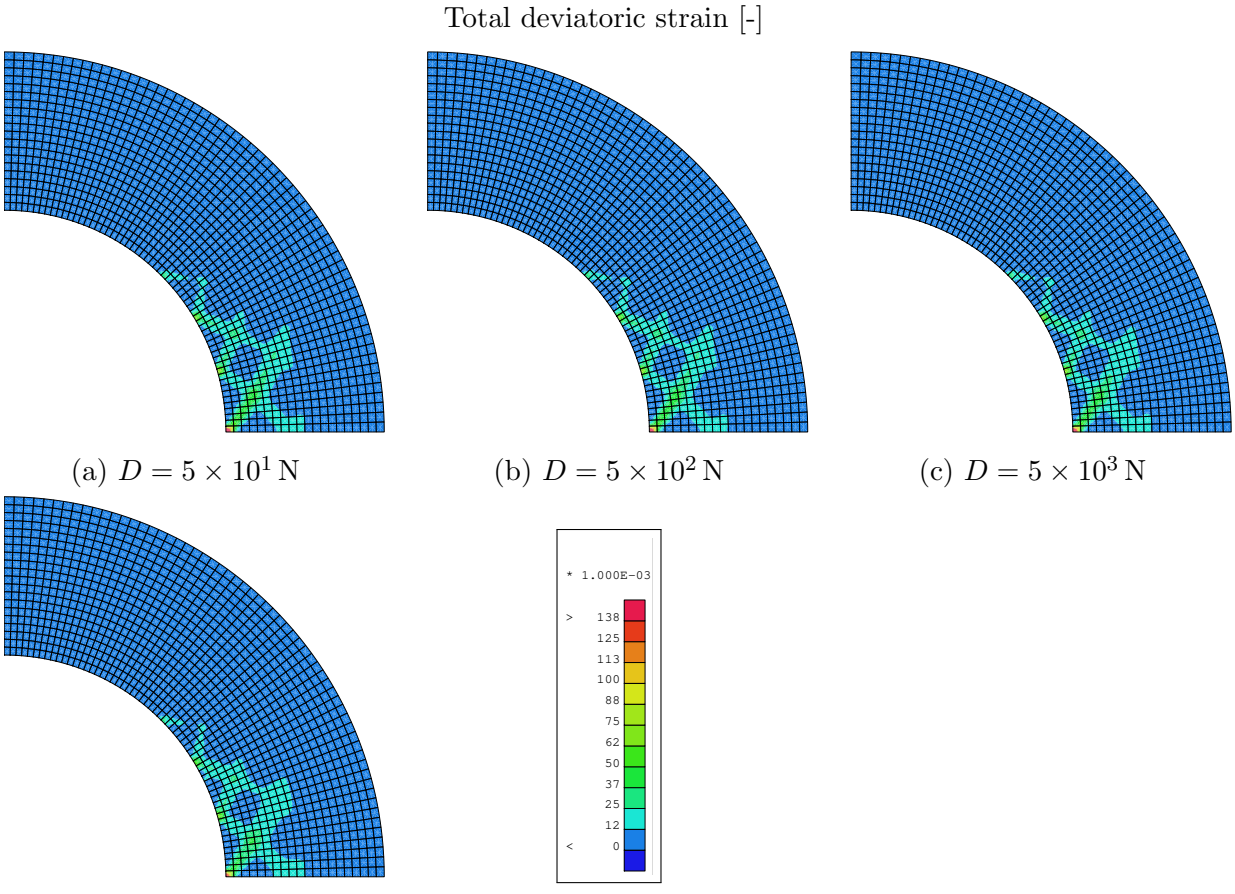

(a) $D = 5 \times 10^1$ N (b) $D = 5 \times 10^2$ N (c) $D = 5 \times 10^3$ N

(d) $D = 5 \times 10^4$ N

Figure 5.54.: Comparison of total deviatoric strain within the unsupported tunnel model for different second gradient elastic moduli ($t = 1000$ days)

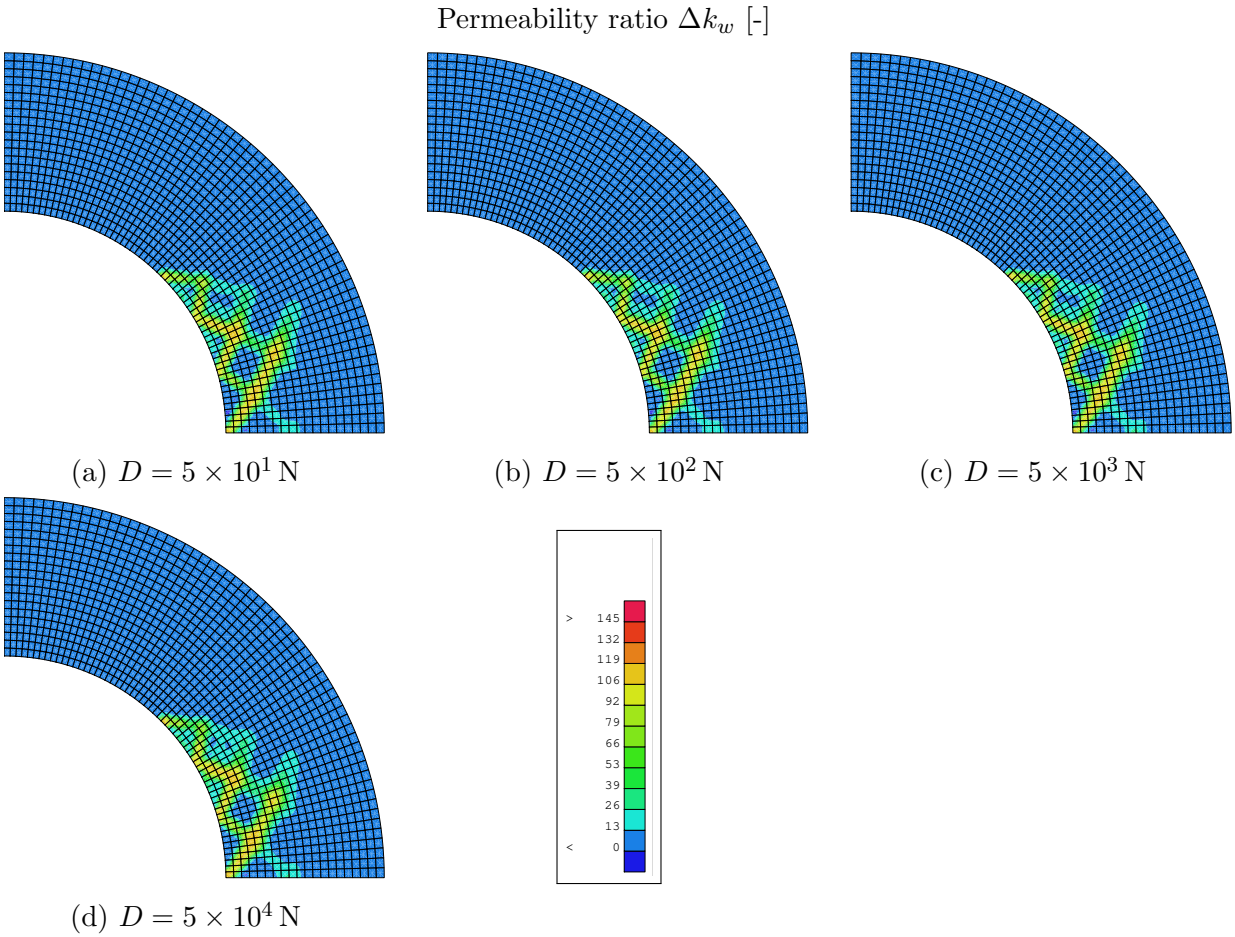

(a) $D = 5 \times 10^1$ N (b) $D = 5 \times 10^2$ N (c) $D = 5 \times 10^3$ N

(d) $D = 5 \times 10^4$ N

Figure 5.55.: Comparison of permeability ratio within the unsupported tunnel model for different second gradient elastic moduli ($t = 1000$ days)

Due to the difficulty in identifying the difference when examining the deviatoric strain and the mean permeability ratio, the plastic points are additionally shown in Figure 5.56. As can be seen there, as D increases, the width of the shear bands also increases, while the outer boundaries of the EDZ are not affected by the different values of D.

To quantify this, the EDZ area and the mean permeability increase for all four models are calculated and shown in Figures 5.57 and 5.58.

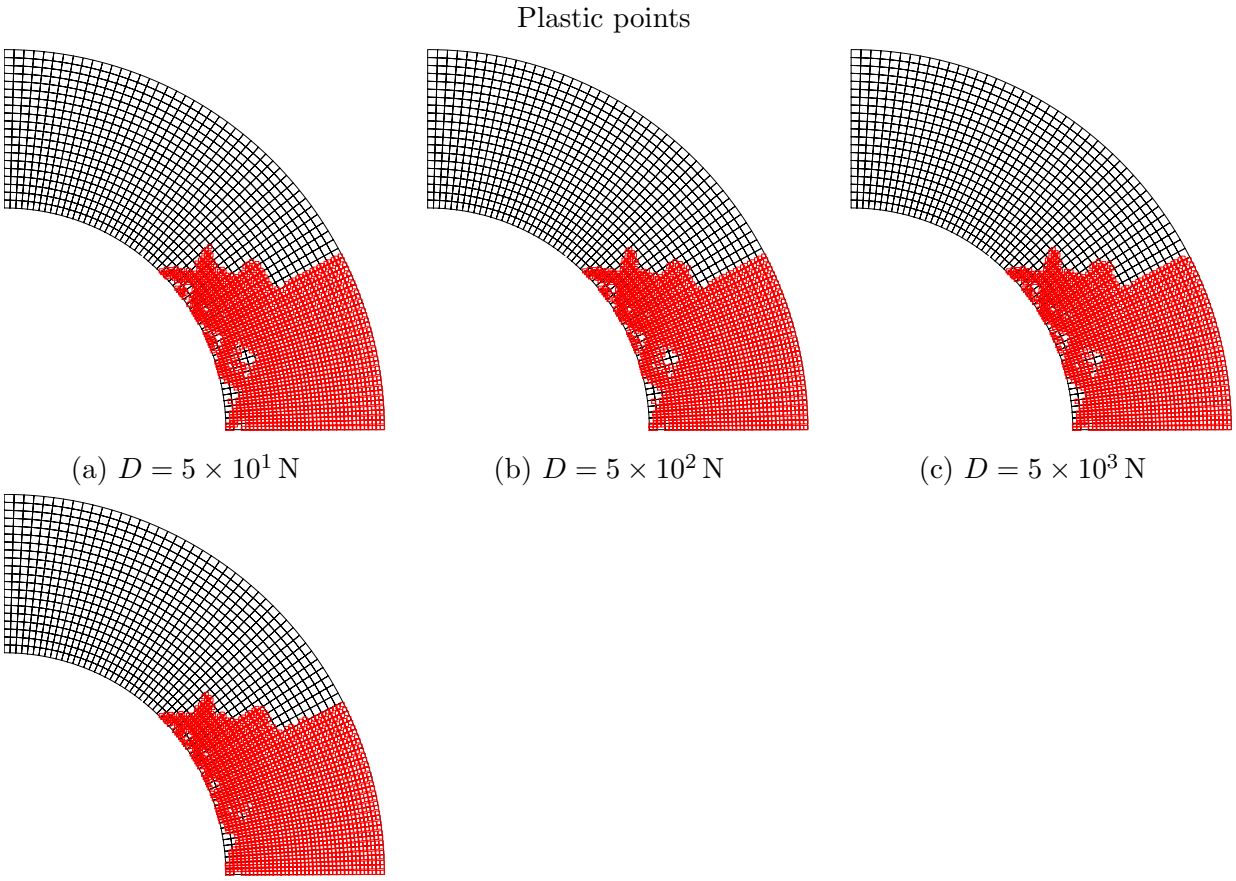

(a) $D = 5 \times 10^1$ N (b) $D = 5 \times 10^2$ N (c) $D = 5 \times 10^3$ N

(d) $D = 5 \times 10^4$ N

Figure 5.56.: Comparison of plastic points within the unsupported tunnel model for different second gradient elastic moduli ($t = 1000$ days)

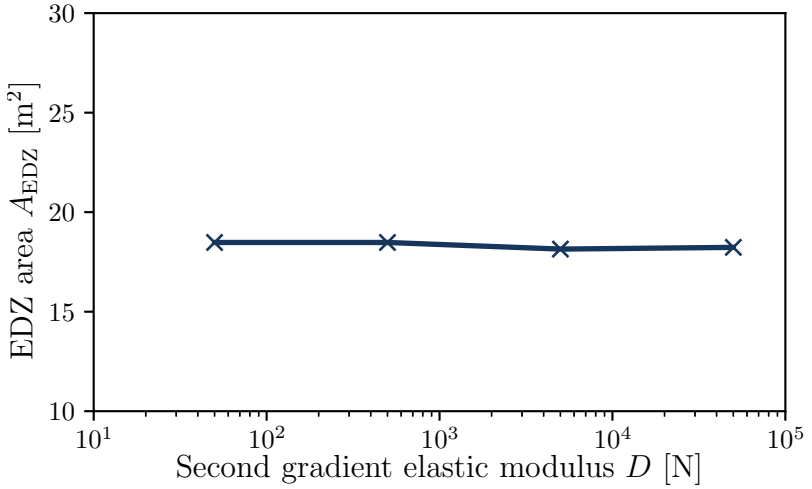

Figure 5.57.: EDZ area for different second gradient elastic moduli ($t = 1000$ days)

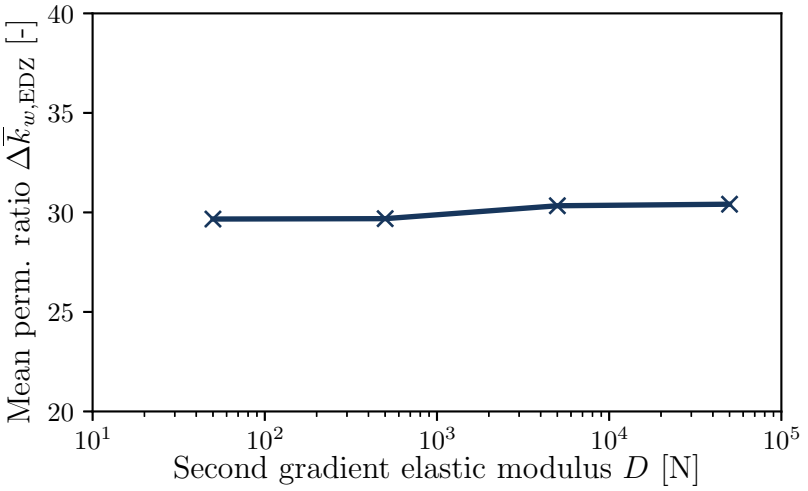

Figure 5.58.: Mean permeability ratio for different second gradient elastic moduli ($t = 1000$ days)

It is evident from Figure 5.57 that the EDZ area for all four values of D remains around $18\,\mathrm{m}^2$, and no noticeable influence on mean permeability is observed in Figure 5.58. This can be explained by the fact that while D affects the width of the shear bands, it does not affect their length, resulting in the same EDZ area, also supported by Figure 5.59, where all four models show similar EDZ outer boundaries. Additionally, it was established in previous chapters that the maximum shear strains are related to the width of the shear bands. In other words, as the shear bands become wider, the maximum deviatoric strains decrease proportionally, which in turn reduces the permeability changes. As a result, when considered across the entire EDZ area, the permeability remains practically constant.

Although the influence of D on the EDZ area and permeability has proven to be minimal, a value of $D = 500\,\mathrm{N}$ is selected for the subsequent calculations.

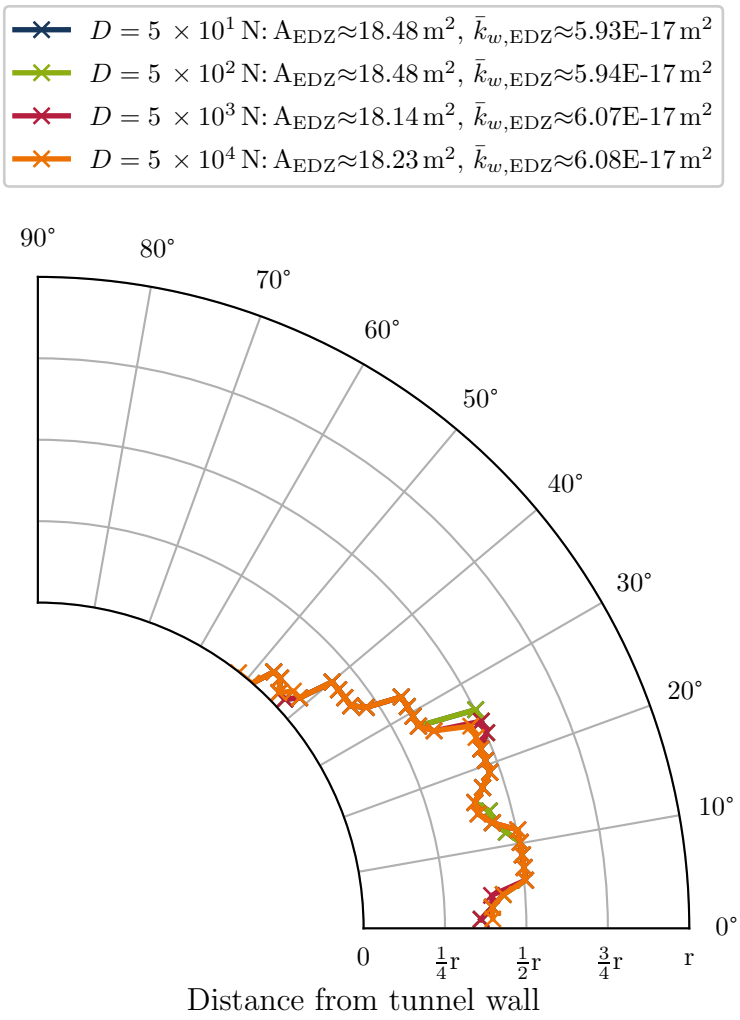

Figure 5.59.: EDZ extension for different second gradient elastic moduli ($t = 1000$ days)

5.5.7. Effect of tunnel diameter

To investigate the influence of geometric parameters on the EDZ, the tunnel diameter is examined in this parameter study with the intention to correlate it with the size of the EDZ. Three models with tunnel diameters of 6 m, 10 m, and 14 m are analyzed. As described in Section 5.5.1, the models are discretized to ensure that the element size in the tunnel nearfield remained constant between the three models, ensuring that the results are not influenced by element size.

As shown in Figures 5.60 and 5.61, the EDZ size increases with increasing tunnel diameter. For a quantitative analysis, the EDZ area and mean permeability are calculated for the three tunnel diameters and presented in Figures 5.62 and 5.63.

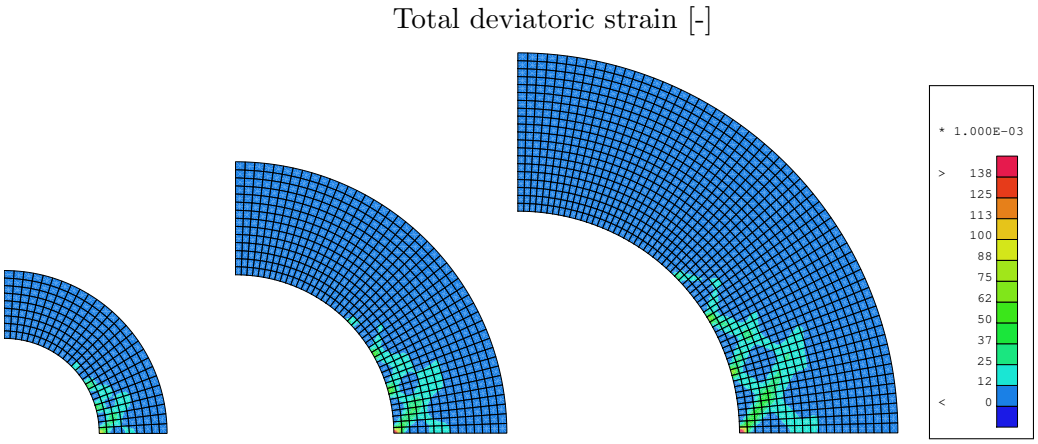

(a) $d = 6\,\mathrm{m}$ (b) $d = 10\,\mathrm{m}$ (c) $d = 14\,\mathrm{m}$

Figure 5.60.: Comparison of total deviatoric strain within the unsupported tunnel model for different tunnel diameters ($t = 1000$ days)

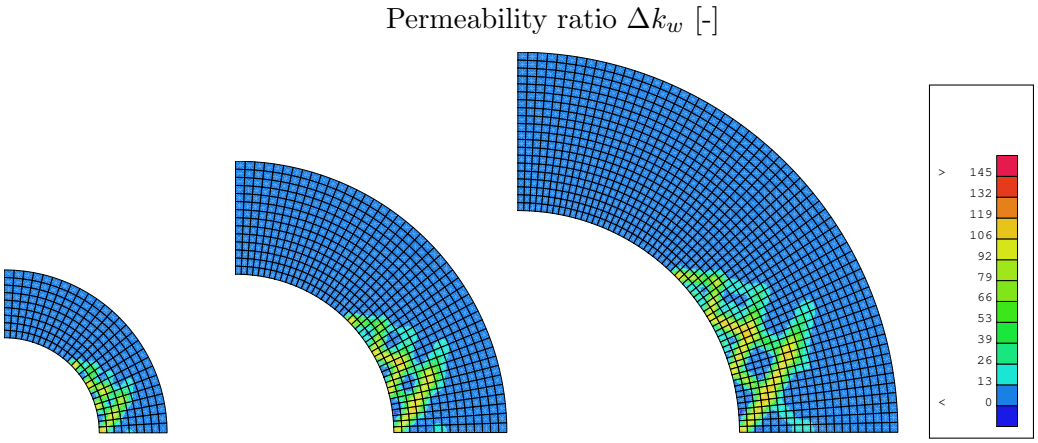

(a) $d = 6\,\mathrm{m}$ (b) $d = 10\,\mathrm{m}$ (c) $d = 14\,\mathrm{m}$

Figure 5.61.: Comparison of permeability ratio within the unsupported tunnel model for different tunnel diameters ($t = 1000$ days)

From Figures 5.60 and 5.61, the EDZ area appears as a percentage of the tunnel's nearfield region (see Figure 5.33). Therefore, the EDZ area is plotted against the square of the tunnel diameter (d^2) in Figure 5.62. The results demonstrate a linear relationship between the EDZ area and the square of the tunnel diameter. It should be mentioned that a linear trend is also observed when plotting the EDZ area over the tunnel cavity. However, the choice of d^2 is motivated by its enhanced clarity, particularly in regards to the integer values that are plotted on the x-axis. Similarly, the mean permeability is also dependent on the tunnel diameter, as the linear correlation in Figure 5.63 reveals. However, unlike the EDZ area, the mean permeability has a linear relationship with the diameter, not

with the square of the diameter. This can be attributed to the fact that the mean permeability has already been divided by the EDZ area in the calculation. Furthermore, the mean permeability decreases with increasing tunnel diameter, which can be explained by the fact that, since all three models have the same element size, the elements between the shear bands in the larger-diameter model can be better distinguished than in the smaller-diameter models, as seen in Figures 5.60a and 5.60c. This trend is similar to the results observed in the study on element size in Section 5.5.4. It should be emphasized at this point that this results from the fact that the element size was determined based on the tunnel model with a tunnel diameter of $d = 14\,\mathrm{m}$ and was not adjusted for smaller diameters in order to eliminate any influence of element size in this investigation.

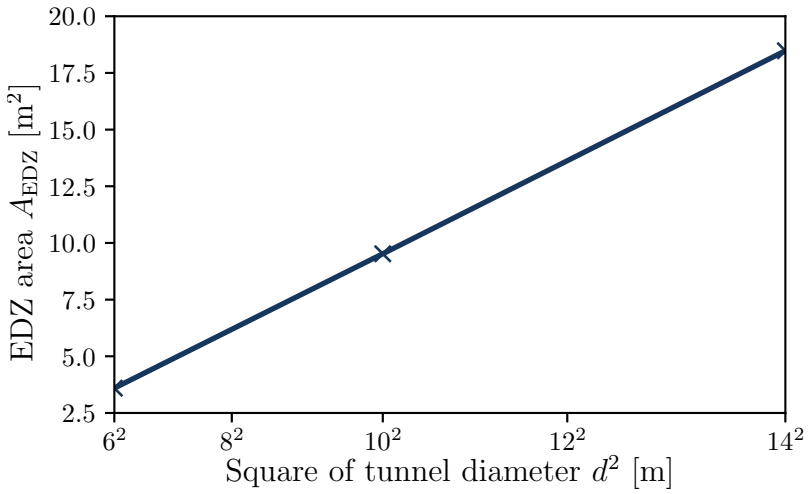

Figure 5.62.: EDZ area as a function of the square of the tunnel diameter ($t = 1000$ days)

When examining the outer boundaries of the EDZ normalized by the tunnel radius, it becomes clear that the normalized EDZ is nearly identical for all three models, as shown in Figure 5.64.

In conclusion, the tunnel diameter has the most significant influence on the EDZ area compared to the other investigated parameters, with the EDZ size being proportional to the square of the diameter.

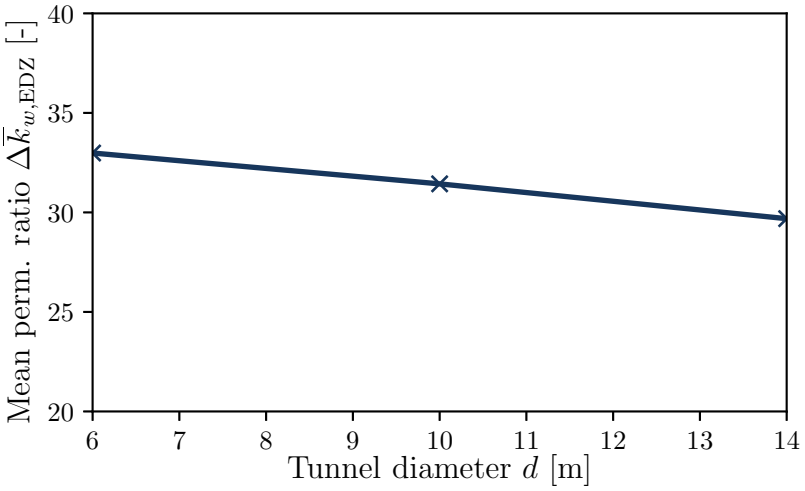

Figure 5.63.: Mean permeability ratio as a function of tunnel diameter ($t = 1000$ days)

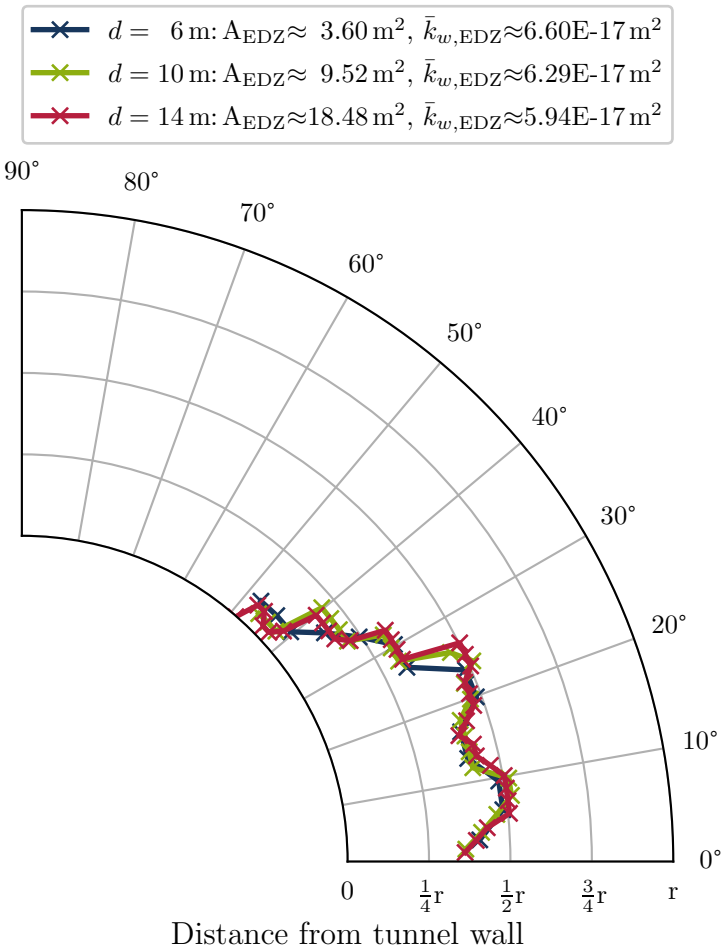

Figure 5.64.: EDZ extension for different tunnel diameters, shown in terms of distance normalized by the tunnel radius ($t = 1000$ days)

5.5.8. Conclusion of parameter study

In this parameter study, various parameters related to the mechanical constitutive model, regularization method, mesh discretization, and geometric characteristics of the tunnel model were examined with respect to their influence on the EDZ area and mean permeability ratio. Regarding element size, it was demonstrated that a sufficiently small element size is required to achieve clear shear band localization. For the second gradient modulus of the regularization method, it was found to influence the width of the shear bands but not the extent of the EDZ, meaning that this parameter has no significant effect on the EDZ area or mean permeability.

While material imperfections influence the occurrence of shear bands, they have no significant effect on the EDZ area or mean permeability. Similarly, the choice of the flow rule in the mechanical model affects the regions outside the shear bands, but not the EDZ area or mean permeability. The key parameter affecting the EDZ area is the tunnel diameter, with the EDZ area being approximately proportional to the square of the tunnel diameter.

With these findings, the next section will analyze the influence of different tunnel supports. The parameters highlighted in bold in Table 5.2 will be used for these analyses.

5.6. Comparative analysis of tunnel support strategies

After presenting the constitutive model parameters of the tunnel supports (Section 5.3.3) and the staged construction process of the supported tunnel (Section 5.3.4), this section focuses on evaluating the two tunnel support strategies, namely rigid and deformable support. It should be recalled at this point that the rigid support consists of a tunnel lining and a rigid grouting layer, whereas the deformable support uses the same tunnel lining but features a deformable grouting layer. Thus, the two support systems differ only in terms of the grouting layer. The comparison will include an analysis of their effects on the resulting EDZ and mean permeability within the EDZ, including a comparison with the unsupported tunnel model studied in the previously performed and discussed parameter study. Furthermore, the deformations of the tunnel support system are analyzed as well as the internal forces (normal force and bending moment) of the tunnel lining, to gain insights of both tunnel support strategies with the goal to evaluate their performance.

5.6.1. Saturated initial conditions

In this section, the tunnel support systems are analyzed for the initially fully saturated conditions assumed for the Belchen tunnel. In the subsequent Section 5.6.2, the same analyses is performed for initially unsaturated conditions in order to highlight the differences between the tunnel support systems more clearly.

5.6.1.1. Evaluation of the resulting EDZ and mean permeability

Since the tunnel support is constructed only after the completion of tunnel excavation, the comparison of the tunnel support strategies corresponds to the end of the simulation at $t = 1000$ days, as was the case with the unsupported tunnel model. This ensures a consistent basis for evaluating the differences in performance between the supported and unsupported scenarios. As the main growth of the EDZ occurs during the excavation of the tunnel, the extent to which the tunnel support influences this expansion is limited to the time after the end of excavation.

Initially, the deviatoric strains and the resulting permeability changes are presented in Figures 5.65 and 5.66 for all three cases as an indicator of the EDZ. Although the differences between the models are minor, a more significant extension of the EDZ is observed in the case of the unsupported tunnel, while the EDZ extend is smaller for the two supported tunnels.

For a systematic evaluation, the EDZ area and the mean permeability are calculated for all three models and displayed along with the EDZ outer boundary in Figure 5.67. Between 0° and 27°, small variations in the EDZ extension between the three scenarios are noticeable, while from 27° to 50° no changes are visible. The unsupported tunnel shows the largest EDZ area and mean permeability, followed by the deformable tunnel support, and then the rigid tunnel support.

Considering that the EDZ after the completion of excavation ($t = 4.5\,\mathrm{h}$), according to Figure 5.24, has an area of $17\,\mathrm{m}^2$ and, according to Figure 5.25, a mean permeability of 5.23E-17 m^2, the rigid support results in an increase of the EDZ area of about 1%, the deformable tunnel support in approximately 3%, and the unsupported tunnel in an 8.5% increase compared to the moment of support installation.

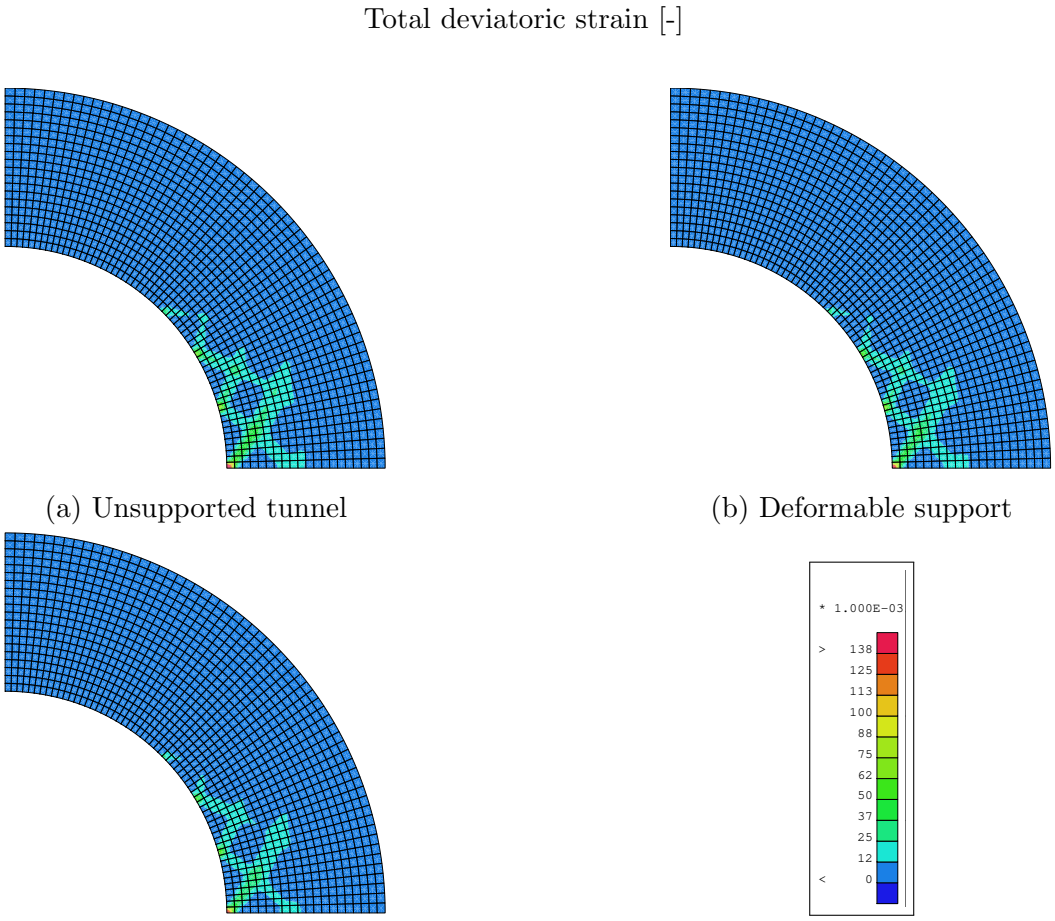

(a) Unsupported tunnel

(b) Deformable support

(c) Rigid support

Figure 5.65.: Comparison of total deviatoric strain within the numerical models of unsupported and supported tunnels, each with a tunnel diameter $d = 14\,\text{m}$ ($t = 1000$ days)

When focusing solely on the size of the EDZ, it can be summarized that the stiffer the tunnel support, the smaller the EDZ and the higher the mean permeability. However, it is important to emphasize that most of the EDZ forms during the tunnel excavation phase, on which the choice of the tunnel support has no impact.

To investigate the different tunnel supports in greater detail, additional analyses are conducted, as on the radial deformations of the tunnel support system, and on the internal forces (normal force and bending moment). This provides deeper insight into how each support strategy interacts with the surrounding clay shale and responds to the pressures induced by the excavation and swelling phenomena.

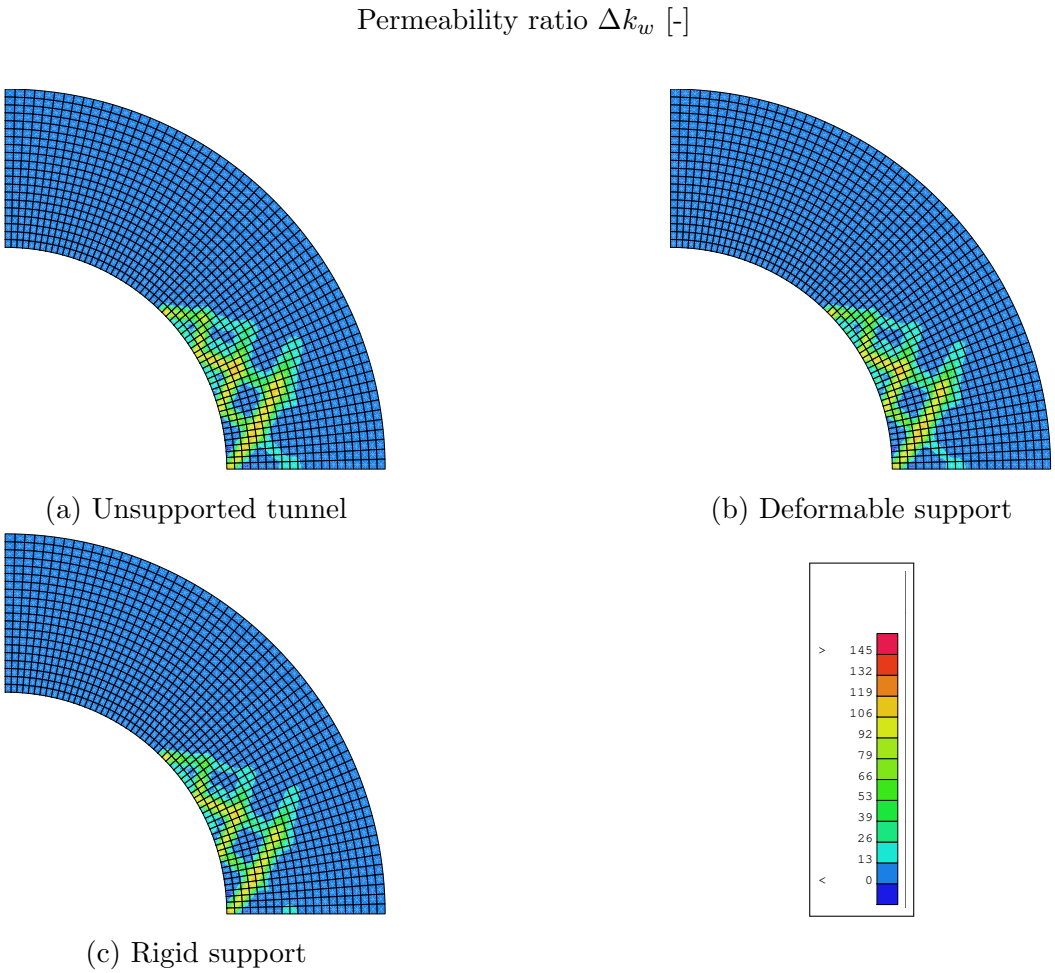

(a) Unsupported tunnel

(b) Deformable support

(c) Rigid support

Figure 5.66.: Comparison of permeability ratio within the numerical models of unsupported and supported tunnels, each with a tunnel diameter $d = 14\,\mathrm{m}$ ($t = 1000$ days)

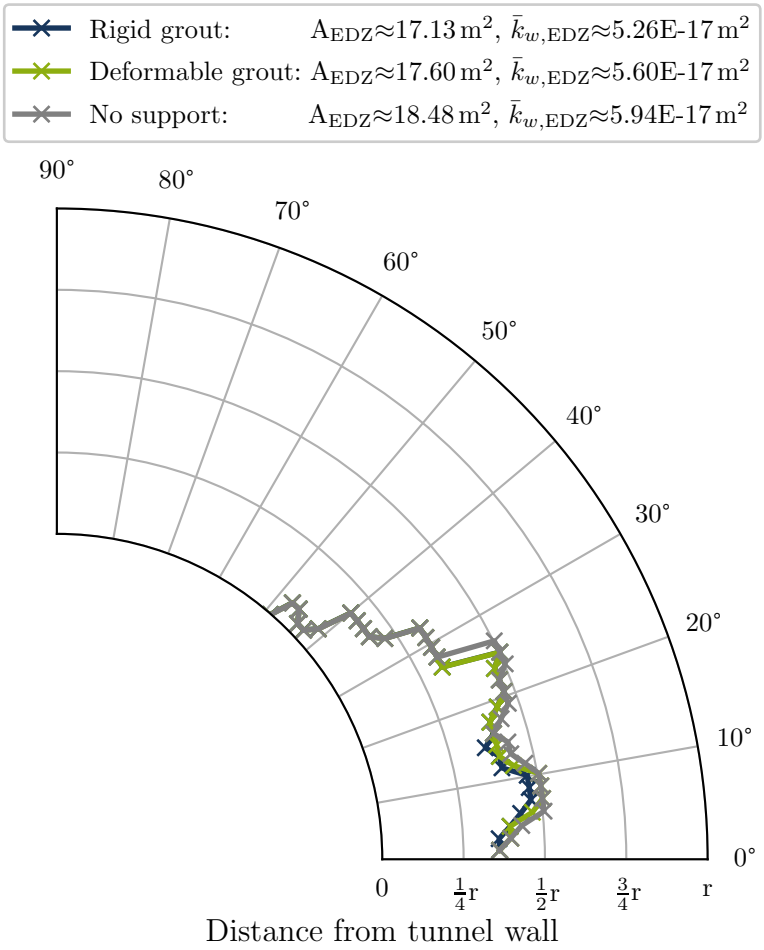

Figure 5.67.: EDZ extension for unsupported tunnel without lining and supported tunnels with deformable and rigid grouts (t = 1000 days)

5.6.1.2. Analysis of tunnel support system deformations and internal forces of tunnel lining

In this section, the impacts acting on the tunnel support system after the completion of the tunnel excavation are first elaborated. Subsequently, the deformations of the individual tunnel support components, specifically the tunnel lining and grouting, are examined to gain an understanding of the interactions between the individual tunnel support subsystems and the surrounding ground for each tunnel support strategy. Furthermore, the resulting internal forces, including normal forces and bending moments, in the tunnel lining are analyzed, as these represent critical design parameters for the tunnel support.

To interpret the tunnel support deformations and the internal forces in the tunnel lining, it is first necessary to analyze the forces acting on the tunnel support system after the tunnel support installation. Since the excavation is complete, no significant external mechanical influences are expected. Therefore, the main focus is on the hydro-mechanically coupled effects.

As already described in Section 5.4.2 for the unsupported tunnel, a negative pore water pressure, or suction, develops at the tunnel crown due to the low permeability of the Opalinus clay shale and the rapid unloading from the tunnel excavation, while at the tunnel side an excess pore water pressure develops. As shown in Figure 5.68a, a suction of approximately 1 MPa occurs at the tunnel crown immediately after the excavation (4.5 h). Additionally, an excess pore water pressure develops at the tunnel side, reaching around 5 MPa. Over time, both the suction and the excess pore water pressure decrease until finally reaching the atmospheric pressure, as seen in Figure 5.68b. The reduction in suction leads to volumetric swelling strains, as described by Equation 2.9. These volumetric strains generate forces (F_{swell}) on the tunnel support system when they are restrained from freely expanding, leading to deformations as idealized in Figure 5.69. Additionally, the reduction of the excess pore water pressure, also referred to as consolidation, at the tunnel side leads to an increase in the net mean stresses. This, in turn, results in deformations (u_x) at the tunnel side, which are also shown in Figure 5.69.

Based solely on these two processes, it can be concluded that, when considering only the modeled quarter of the tunnel, depending on the stiffness of the tunnel support, the deformation of the tunnel support system can be referred to as a rotation, as illustrated in Figure 5.69a.

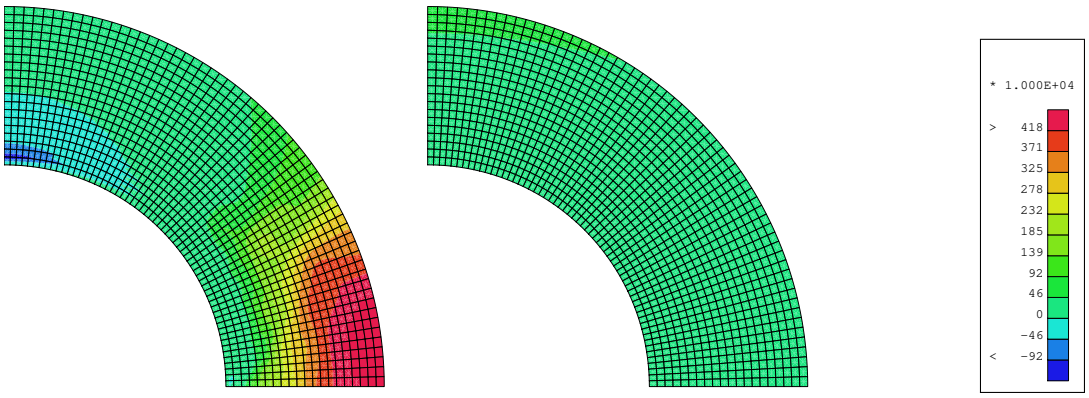

(a) End of excavation (4.5 h) (b) Long-term (1000 days)

Figure 5.68.: Comparison of pore water pressure distribution for supported tunnel model after tunnel excavation

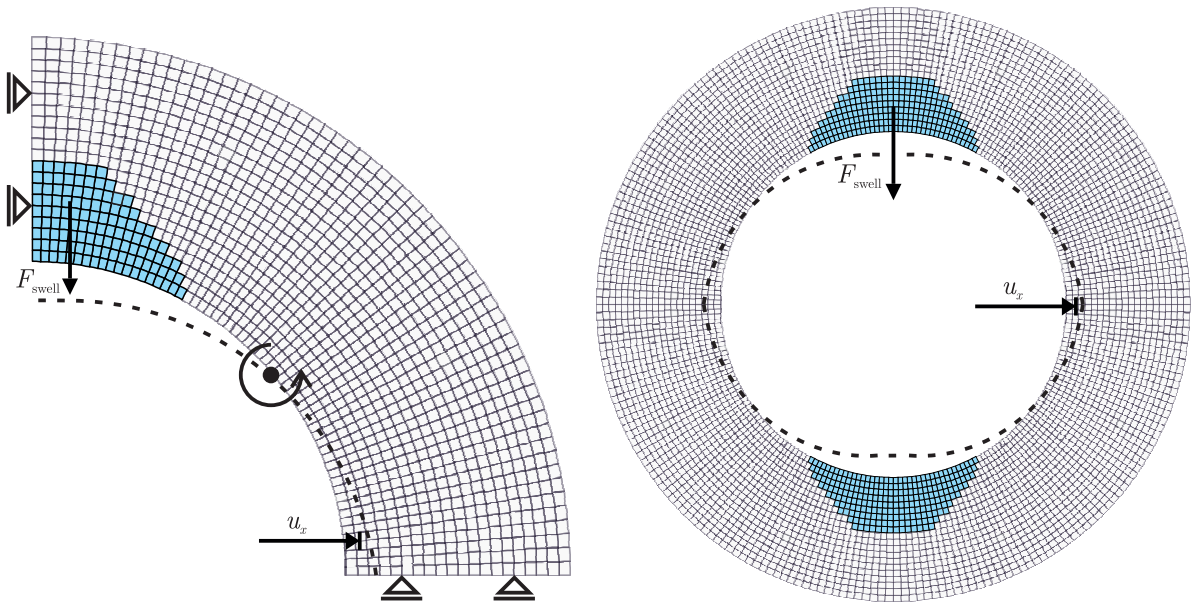

(a) Simulated quarter of the tunnel (b) Full tunnel

Figure 5.69.: Idealization of the impacts and resulting deformation of the tunnel support system for the supported tunnel

However, when constructing the full tunnel from the quarter model, this rotation manifests as tunnel ovalization, as depicted in Figure 5.69b.

After discussing the key impacts on the tunnel support system, the deformations of the tunnel support system and the internal forces can now be analyzed.

Therefore, the radial deformations of the two tunnel support strategies are assessed, starting with the radial deformations of the tunnel lining, which is analyzed beginning with

the end of excavation ($t = 4.5\,\mathrm{h}$) till 1000 days. The radial deformations are calculated based on the deformations of the tunnel lining in the x- and y-directions and are shown in Figure 5.70 for both tunnel support strategies.

Throughout the excavation process, the nodes of the tunnel lining are maintained in a fixed position, both horizontally and vertically, thereby preserving the tunnel lining's initial shape (blue line). As a reminder, in the simulation, the lining is present from the beginning but does not interact with the ground due to the use of a dummy layer between the tunnel lining and the surrounding ground. Subsequently, the fixity of the tunnel lining is released, enabling the lining to undergo deformation.

Over time, the lining at the tunnel crown moves toward the tunnel center, while at the tunnel sides it moves away from the center. This results in both a rotation and ovalization of the tunnel lining, as illustrated in Figure 5.69. Up to $t = 10$ days, the lining deformations for both scenarios are practically identical. In the final state, however, it is observed that the lining surrounded by a rigid grout layer (solid red line) deforms approximately 2.5 mm less at the crown and 1 mm less at the tunnel sides compared to the lining surrounded by a deformable grout layer (dashed red line).

The deformations of the tunnel lining can be explained by the dissipation of both, the matric suction above the tunnel crown and the excess pore water pressure at the tunnel side, generated during excavation. With increasing time the suction above the tunnel crown get dissipated which leads to volumetric strains, as depicted in Figure 5.68. The subsequent handling of volumetric swelling strains by the tunnel support system is dependent upon the deformations undergone by the tunnel support system, similar to the swelling tests presented in Section 3.4. A very rigid support leads to the development of swelling pressure, similar to the volume-constant swelling test. Conversely, a highly deformable support or the absence of any support results in swelling strains, comparable to the free swelling test. In most cases, an intermediate response occurs, similar to the deformation-controlled swelling test. The volumetric swelling strains, which are a consequence of the resaturation of the clay shale, elucidate the phenomenon of tunnel deformation at the crown.

The radial deformation at the tunnel side, on the other hand, can be attributed to two factors. First, the horizontal stresses are lower than the vertical stresses due to the anisotropic stress state, resulting in less resistance in the horizontal direction. Second, consolidation, or the dissipation of the excess pore water pressure at the tunnel side, leads to additional deformations. Due to the presence of shear bands at the tunnel side, this consolidation occurs more rapidly because of the increased permeability within the shear

bands. It should be noted that in reality the tunnel lining consists of several individual segments. These individual segments can deform and rotate among themselves to a certain extend. Due to the simplified modeling of the lining as a single volume, the bending stiffness and consequently the resulting rotation of the whole lining is overestimated.

At the first glance, the deformations of the tunnel lining suggest minimal differences between the two support systems. However, to fully understand the entire support system, it is mandatory to analyze the compression of the grout layer and the deformation of the surrounding ground, presented in the subsequent sections.

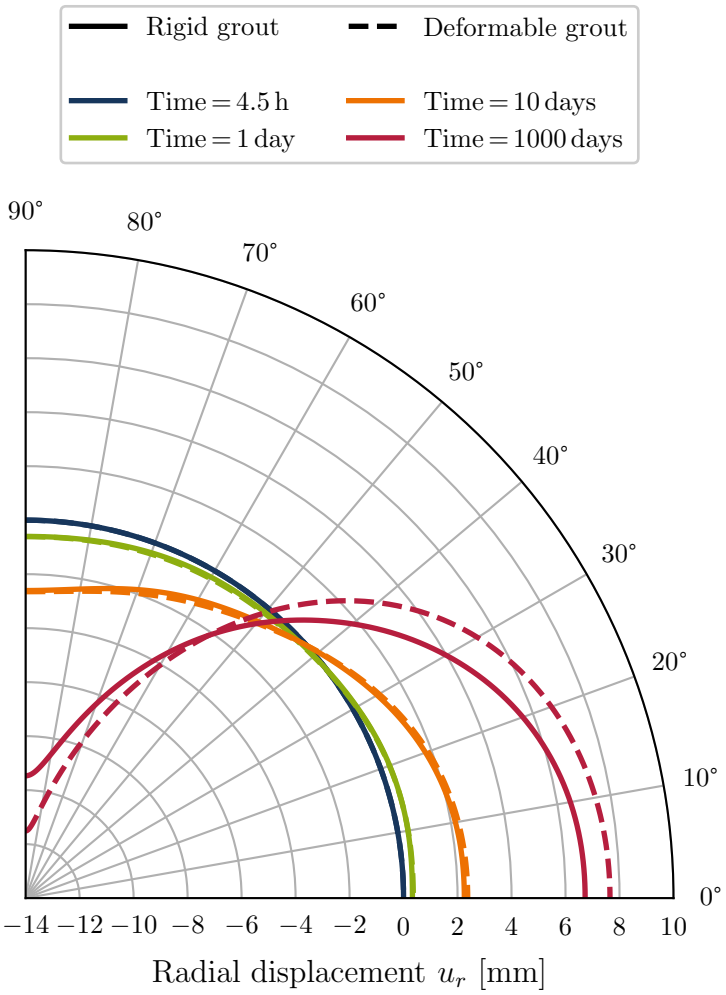

Figure 5.70.: Radial displacements of tunnel linings in supported tunnels ($t = 1000$ days)

For the grouting layer between the tunnel lining and the surrounding clay shale, the strains within the grouting layer are more relevant to analyze rather than the inner and outer displacements. The reason for this is the expectation that the deformable grout, as its name suggests, compresses rather than deforming similarly on both its inner and outer surfaces, as the tunnel lining does. Therefore, for both tunnel support strategies, the radial strains in the grouting layer are evaluated at selected time steps and are shown in Figure 5.71.

For both support strategies, zero initial radial strains are assumed, since the end of tunnel excavation, when the grout layer is activated, serves as the baseline for the evaluation. However, at $t = 1$ day (green line), relatively small positive radial strains are observed in both cases. This can be explained by the grout material being injected into the annular gap with an injection pressure, modeled as an initial stress in the grouting elements in the numerical model. Between $t = 1$ and $t = 10$ days, the strains change only slightly, but at $t = 1000$ days, a significant shift is visible for the deformable grout (dashed red line). At the tunnel side, the deformable grout compresses by approximately 1.5%, whereas no notable compression is observed at the tunnel crown. In contrast, the rigid grout remains almost undeformed.

In both tunnel scenarios, peaks in the radial strains of the grout layer can be observed at the locations of the shear bands, as shown in Figure 5.71. These peaks are comparable to the peaks in the deformations of the surrounding ground in the unsupported tunnel case, illustrated in Figure 5.13a. The reason for the peaks in the unsupported tunnel cases was attributed to the stress concentrations at the location of the shear bands, as explained earlier in Section 5.4.2, which applies here as well.

It may initially seem counterintuitive that the grout layer does not deform where the swelling occurs (at the tunnel crown), but at the tunnel side. However, this behavior can be explained, but it requires an analysis of the ground deformation at the tunnel wall, as this provides essential information to fully understand the overall behavior of both tunnel support systems.

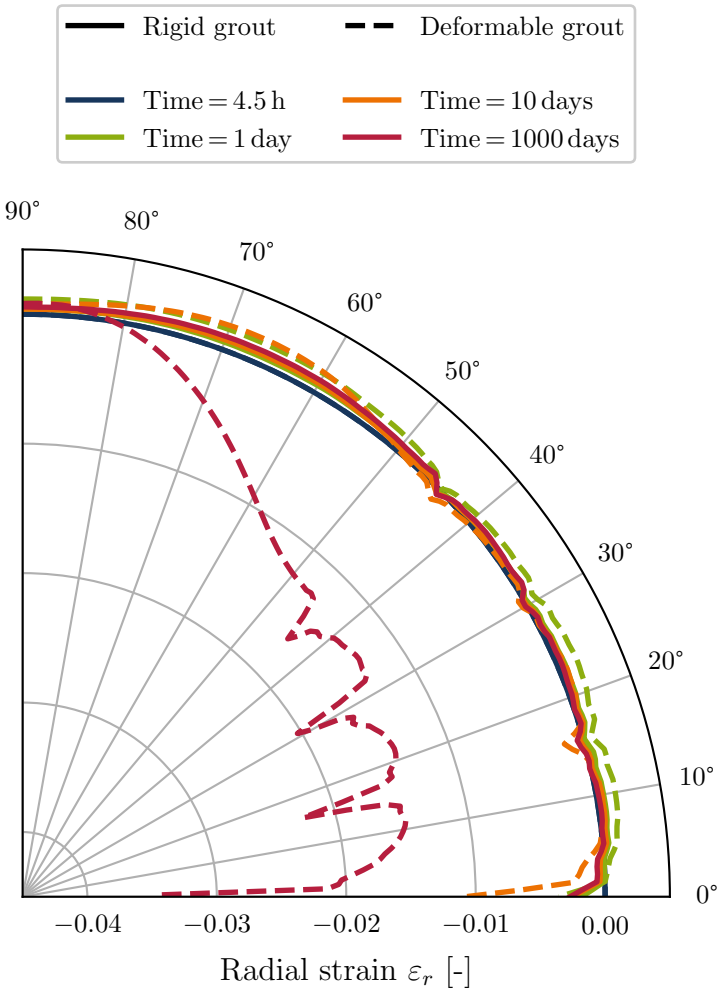

Figure 5.71.: Radial strain of the annular gap grout in supported tunnels ($t = 1000$ days)

For analyzing ground deformation at the tunnel wall, shown in Figure 5.72, zero initial deformations are assumed for $t = 4.5\,\text{h}$ (end of excavation) to isolate the effects of the two tunnel support strategies, by excluding the ground deformations occurring during the excavation process.

From the end of excavation to $t = 10$ days, both tunnel support strategies exhibit similar behavior: settlement occurs at the tunnel crown, while a deformation along the x-axis is seen at the tunnel side. The tunnel crown deformation can be explained by the reduction of the suction above the tunnel crown, which leads to swelling, resulting in crown deformation. Due to the low permeability, the suction is gradually dissipated over time, leading to increasing deformation of the tunnel crown. The deformations at the tunnel side are partly due to the anisotropic stress state, where the horizontal stress is lower than the vertical stress, thus favoring horizontal deformation where resistance is reduced. Additionally, consolidation at the tunnel side contributes to these deformations.

Comparing the radial displacements of the tunnel wall (see Figure 5.72) and the linings (see Figure 5.70) at $t = 10$ days reveals almost identical values. Given the minimal strain observed in both of the grout layers at this time, it can be concluded that the tunnel lining and the grout layer are moving as a single unit. Examining the end of the simulation at $t = 1000$ days, however, highlights differences between the two tunnel supports. For the rigid support, the tunnel support remains structurally homogeneous due to its high stiffness. This means that, with increasing swelling at the tunnel crown, the support system (lining and grout) shifts toward the tunnel center. However, because the lateral pressure on the tunnel side is lower as already explained, a rotation of the tunnel support can be observed, accompanied by a lateral displacement of the tunnel side in the x-axis direction.

In contrast, with the deformable support, the grout layer at the tunnel sides appears to have reached its yield stress threshold, leading to significant deformation. This is evident as the tunnel lining undergoes almost 8 mm displacement in the x-direction (see Figure 5.70), whereas the tunnel wall shifts by only about 4 mm (see Figure 5.72). The difference (4 mm displacement) is related to the compression of the deformable grout layer. Considering that the radial distance between the tunnel lining and the surrounding ground is approximately 15 cm after excavation, a deformation of 4 mm corresponds to the calculated radial strains of about 2% in the grouting layer, as depicted in Figure 5.71.

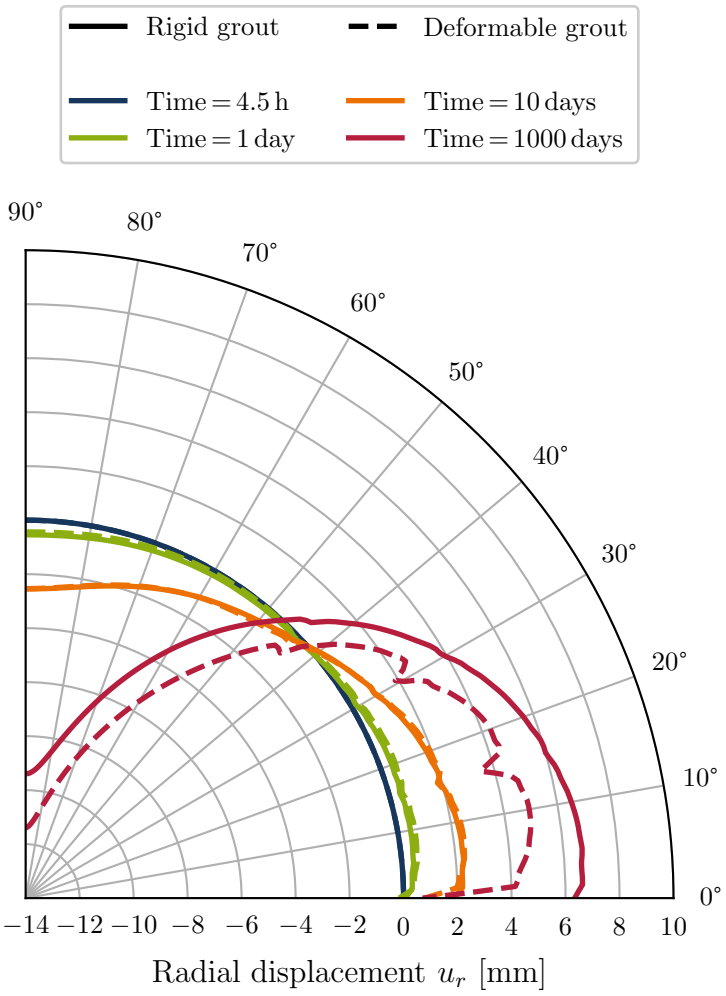

Figure 5.72.: Radial displacement of tunnel wall after excavation in supported tunnels ($t = 1000$ days)

In addition to the previously analyzed deformations, the radial stress acting on the tunnel lining provides insights into the interaction between the individual components of the tunnel support system. Analyzing this stress helps to better understand the development of internal forces within the tunnel lining, calculated in the following. For this purpose, the stress distribution along the outer surface of the tunnel lining is extracted and transformed into polar coordinates. The resulting radial stress distributions for both tunnel support scenarios are illustrated in Figure 5.73. Examining the radial stress distribution reveals stress peaks at the locations of the shear bands at about 0°, 15°, 30°, and 45°. The reasons for these peaks are the previously described stress concentrations at the location of the shear bands.

Comparing both tunnel support strategies reveals a significant reduction in radial stress for the deformable tunnel support compared to the rigid support. In the tunnel crown,

the radial stress decreased from 0.3 MPa to nearly zero, while in the tunnel sidewalls, it reduces from -1.3 MPa to -0.4 MPa.

In case of the rigid tunnel support, the larger radial stresses can be explained by the negligible deformation of the rigid grout (see Figure 5.71), despite similar overall tunnel lining deformations (see Figure 5.70). At the tunnel side, this results in compressive stresses in the tunnel lining, as the tunnel lining and the grout layer are pressed into the ground, due to the rotation initialized by the volumetric swelling strains above the tunnel crown, in addition to the consolidation at the tunnel side.

In the deformable tunnel support scenario, the compressive stresses acting on the lining at the tunnel side are reduced by the deformable grout layer. This behavior results from the ability of the grout to deform and dissipate a portion of the stresses that would otherwise transfer directly to the tunnel lining. Consequently, the deformable grout acts as a buffer, moderating the stress concentration and leading to a more uniform distribution of radial stresses acting between the tunnel support components and the surrounding ground, as can be seen in Figure 5.73.

The tensile stresses observed in the rigid tunnel support scenario at the tunnel crown can be attributed to the previously discussed rotation of the tunnel lining. The lining is pressed into the ground at the tunnel side. Since there is no interface between the lining and grout or between the grout and clay shale (nodes are shared across layer boundaries), the rotation causes extension at the tunnel crown. Due to the higher stiffness of the rigid grout and resulting limited deformation, tensile stresses are induced.

It should be noted at this point that tensile stresses or extension of the grout are not expected in reality, as the grout layer would crack or separate under tensile stresses, which represents a limitation of the modeling approach.

In contrast, the deformable grout layer expands at the tunnel crown, as shown in Figure 5.71, effectively preventing the transfer of significant tensile stresses to the tunnel lining. It should be noted that the tunnel lining also deforms due to swelling effects, meaning the observed behavior is not solely a pure rotation but rather a combination of convergence and rotation or ovalization of the tunnel lining. This dual effect explains why the radial stresses at the tunnel side are higher compared to those at the tunnel crown. The swelling-induced deformations cause the tunnel crown to move inward toward the center, while the tunnel sides experience outward movement. This uneven displacement pattern increases the compressive stresses and the consolidation of the surrounding ground at the tunnel side.

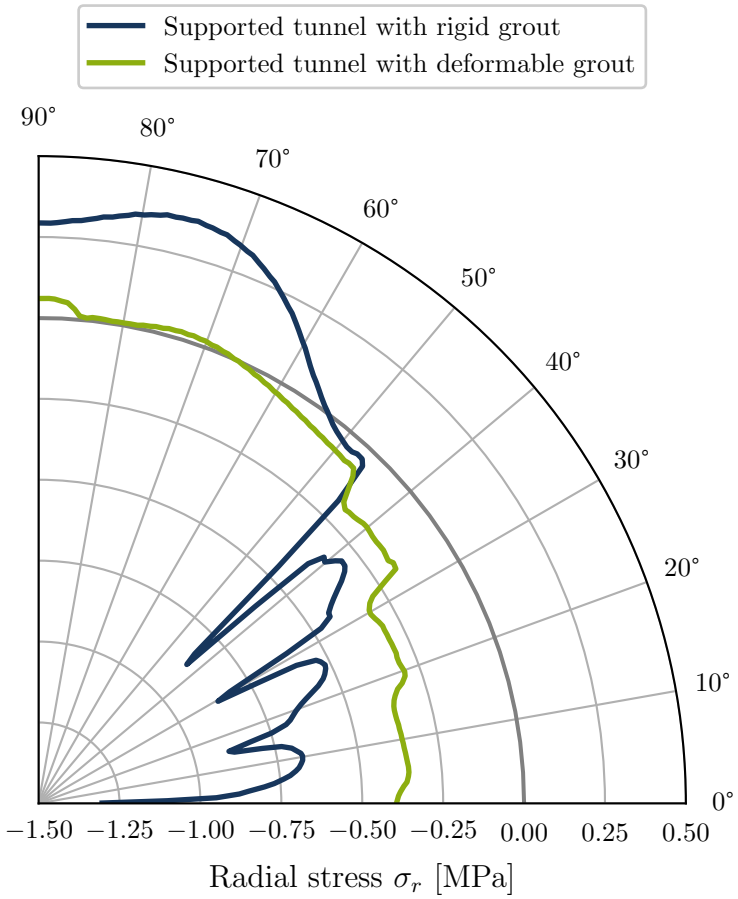

Figure 5.73.: Radial stress acting on the outer lining surface of deformable and rigid tunnel support system ($t = 1000$ days)

With the insights gained from the deformation and stress analyses, the internal forces, in this case normal forces and bending moments, of the tunnel lining are evaluated.

For that purpose, the stress linearization method (ASME, 2015) is used, which is commonly implemented in various finite element codes such as Abaqus or COMSOL. It should be noted that this method is not available in the finite element framework Lagamine used in this study. To perform this analysis, the cartesian stresses (σ_{xx}, σ_{yy}, and σ_{xy}) at all integration points of the tunnel lining are extracted, transformed into a polar coordinate system, and decomposed into membrane and bending stresses over the tunnel lining width using the previously mentioned stress linearization method. The membrane stress is then used to calculate the distribution of normal forces within the tunnel lining, while the bending stress is used to calculate the bending moments. Figure 5.74 shows the resulting distribution of normal forces in the tunnel lining for both the rigid and deformable tunnel supports.

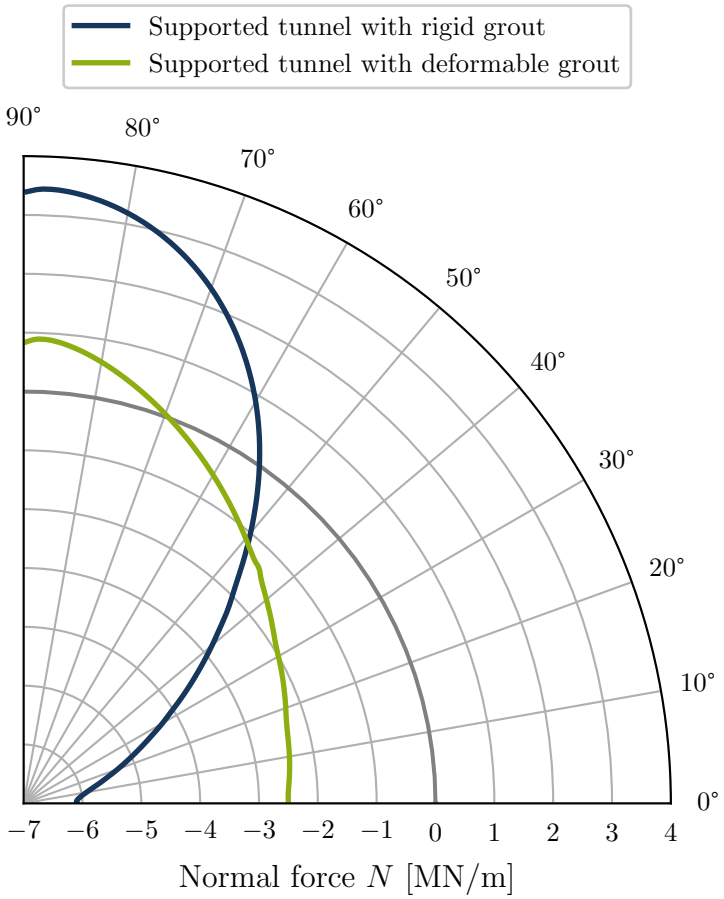

Figure 5.74.: Normal force in the linings of deformable and rigid tunnel support systems ($t = 1000$ days)

As observed, there are positive normal forces (tensile forces) at the tunnel crown and negative normal forces (compressive forces) along the tunnel side. When considering that the surrounding ground is stable, the source of the observed compressive forces at the tunnel side, is primary the swelling force F_{swell} resulting from the volumetric swelling strains of the clay shale above the tunnel crown, as depicted in Figure 5.69a. This force is primarily transferred to the vertical support, which is required due to the symmetry of the system, at the bottom of the tunnel lining, as illustrated in Figure 5.69a. The tensile forces result from the horizontal movement of the tunnel lining at the tunnel side, as highlighted in Figure 5.69a, the resulting rotation, and the associated tensile stresses between the tunnel lining, grout, and surrounding soil at the tunnel crown. It should be emphasized once again that tensile forces at the tunnel crown do not occur in reality and arise from a model simplification, as previously explained.

A comparison of the two tunnel support strategies reveals that the deformable tunnel support strategy significantly reduces the normal forces. In the tunnel crown, the normal

forces are reduced from 3.39 MN/m to 0.84 MN/m, representing a 75.3% reduction. At the tunnel sides, the normal forces decrease in absolute value from 6.11 MN/m to 2.52 MN/m, corresponding to a 58.8% reduction. Due to the higher deformation of the deformable tunnel support system compared to the rigid system, as observed in the ovalization of the tunnel lining in Figure 5.70 and the compression of the grout layer in Figure 5.71, a reduction in the radial stresses acting on the tunnel lining is observed, as already explained in the previous section. As a result of this decrease, the normal forces in the lining of the deformable tunnel support system also decrease.

Finally, the bending moments are examined. The bending moments calculated using stress linearization from the resulting bending stress are shown in Figure 5.75. As can be seen, positive bending moments occur at the tunnel crown, while negative bending moments are found at the tunnel sides. Since the bending moments have a linear relationship with the curvature of the lining, and curvature, in turn, corresponds to the second derivative of the deformation, this relationship provides a basis for explaining the distribution of the bending moments.

The positive bending moments in the tunnel crown can be explained by the deformation of the tunnel lining towards the tunnel center in this region. Negative bending moments are found at the tunnel side, as here the deformation occurs in the opposite direction, away from the tunnel center. The fact that the absolute values of the bending moment are higher in the tunnel crown than at the tunnel side for both support strategies can also be explained by the lining deformations illustrated in Figure 5.70. As shown, the deformations and the curvature of the tunnel lining in the tunnel crown are significantly larger than at the sides, which aligns with the observed bending moment distribution.

When comparing the two support strategies, it becomes apparent that in the tunnel crown and at the tunnel sides the deformable tunnel support exhibits higher bending moments than the rigid support. However, in some central sections, the opposite trend can also be observed. This can be explained by the fact that the tunnel lining deforms slightly more with the deformable tunnel support, compared to the rigid tunnel support, as shown in Figure 5.70.

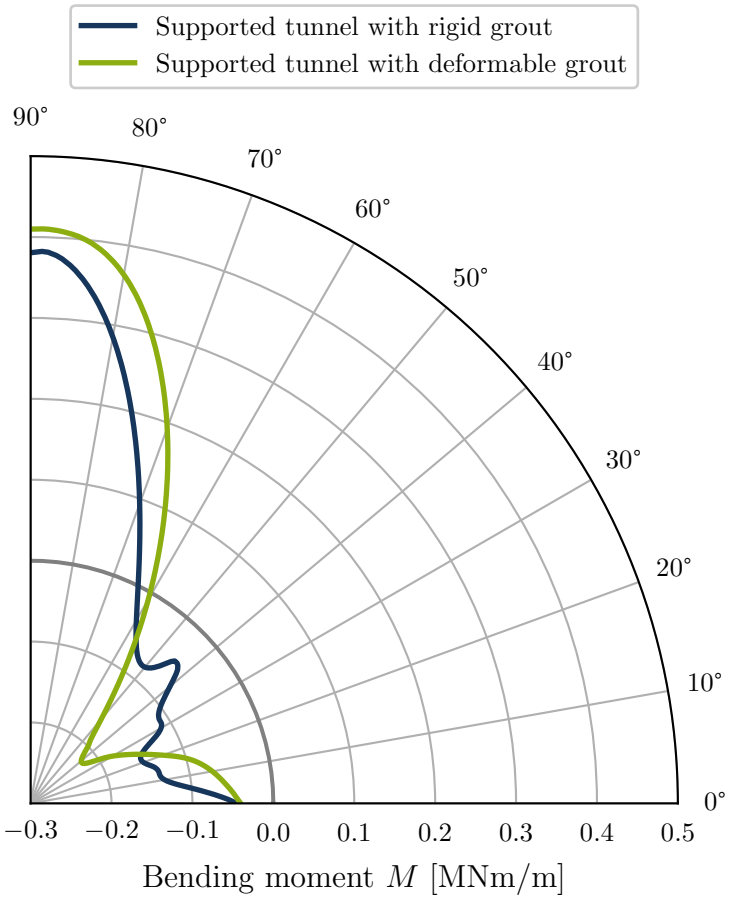

Figure 5.75.: Bending moment in the linings of deformable and rigid tunnel support system ($t = 1000$ days)

5.6.2. Unsaturated initial conditions

As shown in the previous section, the differences between the rigid and deformable tunnel support systems are minor in case of initially saturated conditions. It should be emphasized once more that the initial degree of saturation in the surrounding Opalinus clay shale at the Belchen tunnel remains unknown. Therefore, the previous simulations assumed fully saturated initial conditions based on observations from the Mont Terri Rock Laboratory, where Opalinus clay shale occurs at a similar depth.

Under these initially saturated conditions, the volume increase of the surrounding clay shale acting on the tunnel support is attributed solely to mechanical swelling. This swelling results from the unloading of the clay shale during excavation in combination with its low permeability.

Since larger differences between the tunnel support systems are expected for initially unsaturated conditions due to the swelling associated with the saturation of Opalinus clay shale, additional simulations are conducted assuming such initial conditions. Therefore, an initial suction $s = 35\,\mathrm{MPa}$ is set in all elements of the Opalinus clay shale within the numerical model.

5.6.2.1. Evaluation of the resulting EDZ and mean permeability

To investigate the influence of the tunnel support system on the EDZ, the permeability ratio at the end of the simulation ($t = 1000$ days) is shown in Figure 5.76. As the figure indicates, the EDZ extent is greatest for the unsupported tunnel, followed by the tunnel with deformable support. The rigid support results in the smallest EDZ extent, and the shear bands are shorter compared to the other two cases. This can be attributed to the reduced tunnel wall convergence resulting from the rigid support, which will be examined in greater detail in the following section.

To quantify the EDZ area and to highlight the differences of the various tunnel support systems, the temporal evolution of the EDZ area for each tunnel support strategy is calculated and depicted in Figure 5.77. A common feature among all models is that the main EDZ growth occurs after excavation, in contrast to the initially saturated model where most EDZ growth takes place during excavation, as shown in Figure 5.28. These differences result from the fact that under initially saturated conditions, the unloading caused by the tunnel excavation is already sufficient to induce plastic deformations in the form of shear bands during the excavation phase. In contrast, under initially unsaturated conditions, the yield surface in $p - q$ space is larger compared to the initially saturated case. As a result, the unloading caused by the tunnel excavation alone is not sufficient to trigger plastic deformations. In this case, the formation of shear bands is caused by the reduction in suction following saturation after the tunnel excavation, which leads to wetting-induced softening.

Up to approximately 10 h, the EDZ areas for all three support strategies are nearly identical, with an EDZ area of about $A_{\mathrm{EDZ}} = 8\,\mathrm{m}^2$. Beyond this point, the unsupported tunnel and the tunnel with deformable support exhibit continuous growth of the EDZ area, which appears linear in the logarithmic plot. In contrast, the tunnel with rigid support shows a slower increase in EDZ area. At the end of the simulation ($t = 1000$ days), the EDZ areas of the unsupported tunnel and the tunnel with deformable support are $A_{\mathrm{EDZ}} = 60\,\mathrm{m}^2$ and $A_{\mathrm{EDZ}} = 56\,\mathrm{m}^2$, respectively. The EDZ area for the tunnel with rigid support is less then half, with an area of $A_{\mathrm{EDZ}} = 26\,\mathrm{m}^2$.

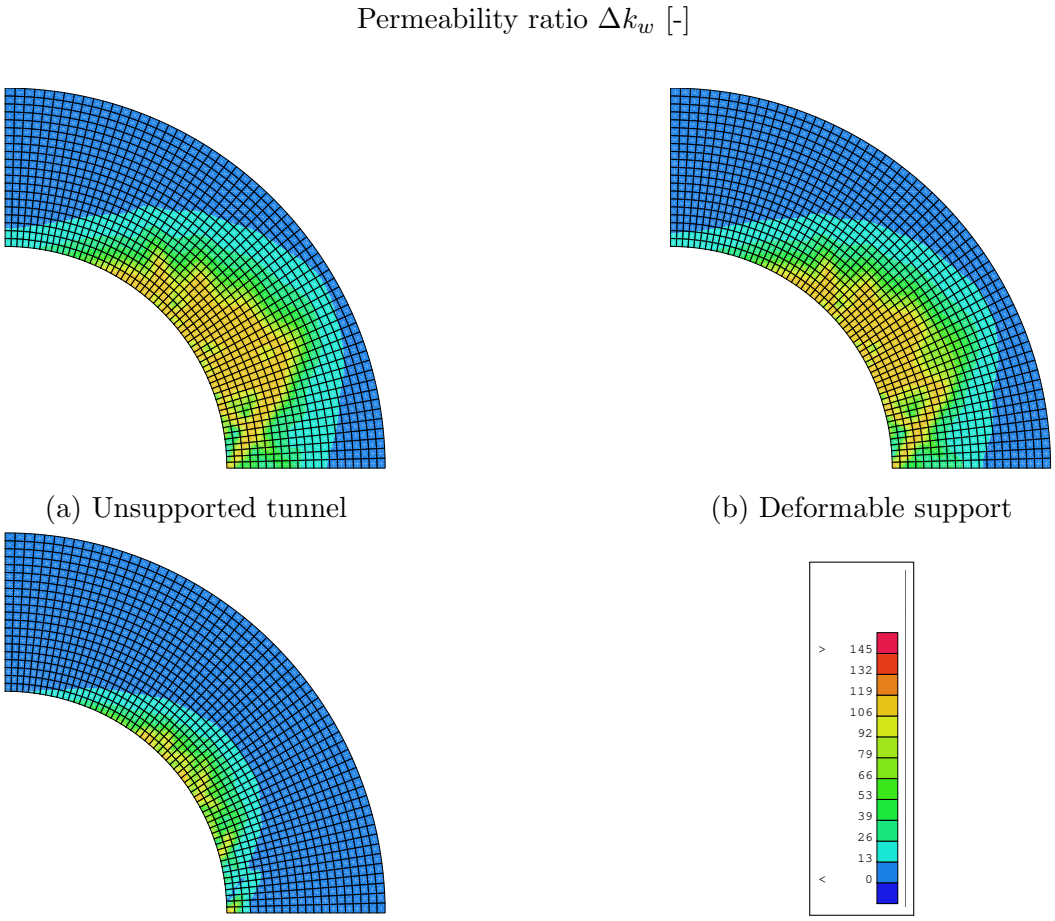

(a) Unsupported tunnel

(b) Deformable support

(c) Rigid support

Figure 5.76.: Comparison of permeability ratio within the initially unsaturated ($s = 35\,\text{MPa}$) numerical models of unsupported and supported tunnels, each with a tunnel diameter $d = 14\,\text{m}$ ($t = 1000$ days)

Although the development of the EDZ is not yet fully completed after 1000 days under initially unsaturated conditions, the simulation time frame and all previously defined parameters, particularly those controlling the permeability increase as a function of shear strains and the threshold used to evaluate the EDZ, are not adjusted for the initially unsaturated tunnel simulations in order to maintain comparability with the previously studied simulations under saturated initial conditions.

In addition to the EDZ area, the temporal evolution of the mean permeability ratio is calculated and illustrated in Figure 5.78. In all cases, the mean permeability ratio increases rapidly during excavation and then decreases until reaching an equilibrium value. The explanation follows the same reasoning as discussed in Section 5.4.7. During the EDZ growth process, the calculated EDZ area initially consists of non-contiguous elements with

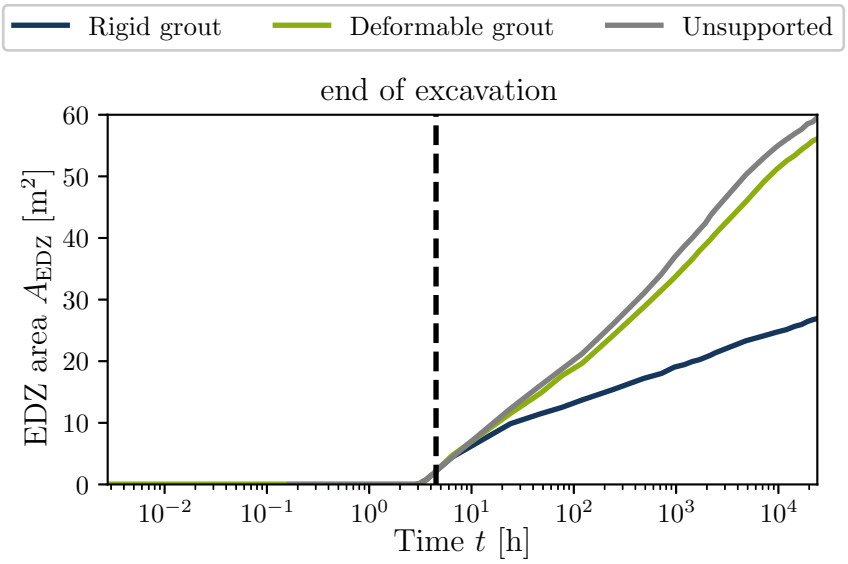

Figure 5.77.: Comparison of the temporal evolution of the EDZ area within the initially unsaturated ($s = 35\,\mathrm{MPa}$) numerical models of unsupported and supported tunnels

increased permeability. Once the shear bands are fully developed, the EDZ area also includes elements between the shear bands that do not exhibit increased permeability, leading to an overall reduction in the mean permeability.

Comparing the different tunnel support strategies, it becomes evident that the unsupported tunnel results in the highest mean permeability ratio, followed by the tunnel with deformable support and then the tunnel with rigid support. This is consistent with the previously analyzed EDZ areas.

While the EDZ is an important quantity, and it can already be concluded that the rigid support results in the smallest EDZ area and the lowest permeability increase within the EDZ, the tunnel support systems themselves are at least equally important to examine. Therefore, the following section evaluates the deformations of the individual components of the tunnel support system as well as the internal forces within the tunnel lining.

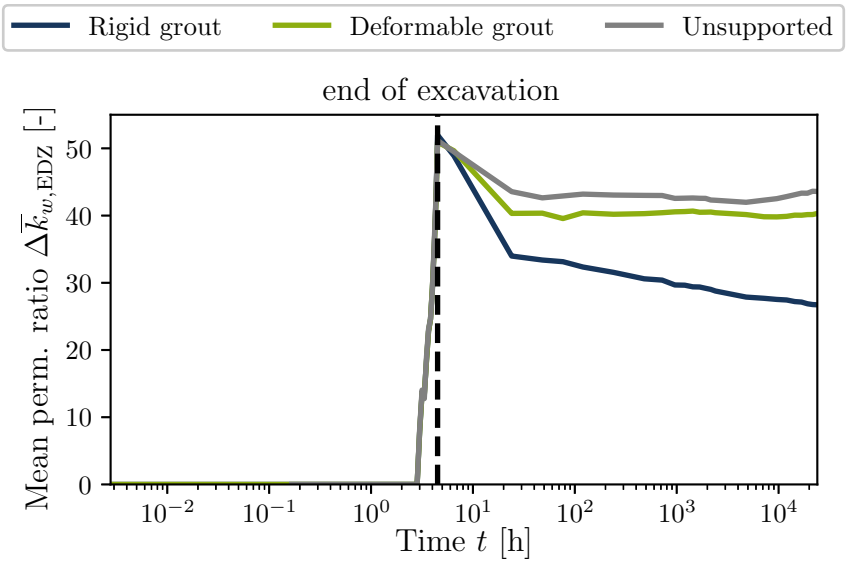

Figure 5.78.: Comparison of the temporal evolution of the mean permeability ratio within the initially unsaturated ($s = 35\,\mathrm{MPa}$) numerical models of unsupported and supported tunnels

5.6.2.2. Analysis of tunnel support system deformation and internal forces of tunnel lining

Before evaluating the deformation of the tunnel support systems and the internal forces within the tunnel lining, it is essential to analyze the loads acting on the tunnel support. This provides the foundation for understanding the resulting deformations and internal forces. Particularly important under initially unsaturated conditions is the pore water pressure distribution after the tunnel excavation, as the saturation level of these elements governs the magnitude of swelling acting on the tunnel support system.

Figure 5.79a shows the pore water pressure distribution after tunnel excavation ($t = 4.5\,\mathrm{h}$). It can be observed that almost all elements in the near-field of the tunnel remain at their initial suction level of approximately 35 MPa. Two exceptions are present. A small zone of elements at the tunnel crown shows a further increase in suction to around 38 MPa, while some elements at the tunnel side exhibit a slight reduction in suction to approximately 33 MPa. These variations can be explained by the initial anisotropic stress state, which leads to ovalization of the tunnel wall during excavation. Combined with the low permeability, the elements at the tunnel crown tend to expand volumetrically, resulting in increased suction. In contrast, elements at the tunnel side exhibit the opposite behavior. This phenomenon was also observed in the tunnel model with initially saturated conditions, as discussed in the previous section.

The elements near the tunnel wall are already close to full saturation. This is a consequence of the prescribed pore water pressure boundary condition at the tunnel wall, which is applied during and after excavation, as previously described in Section 5.3.2. As a result, saturation of the Opalinus clay shale proceeds from the tunnel wall toward the surrounding clay shale. The main difference between the previously studied initially saturated case and the currently analyzed initially unsaturated case lies in the higher suction levels after excavation, which lead to a greater reduction in suction during the saturation phase. This results in larger volumetric deformations, which are acting on the tunnel support system.

Since the EDZ is expected to develop primarily at the tunnel side, as observed in the previously studied cases, the increased permeability in this zone accelerates resaturation, leading to a faster reduction of suction and thus causing the elements within the EDZ to swell more rapidly. This behavior is illustrated in Figure 5.79b.

After analyzing the pore water pressure distribution, indicating the impacts acting on the tunnel support system, the deformations of the tunnel support are now evaluated. For this purpose, the temporal evolution of the radial deformations of the tunnel lining is examined for both scenarios, rigid and deformable support, as shown in Figure 5.80. The evaluation is carried out at four specific times: 4.5 h, 1 day, 10 days, and 1000 days.

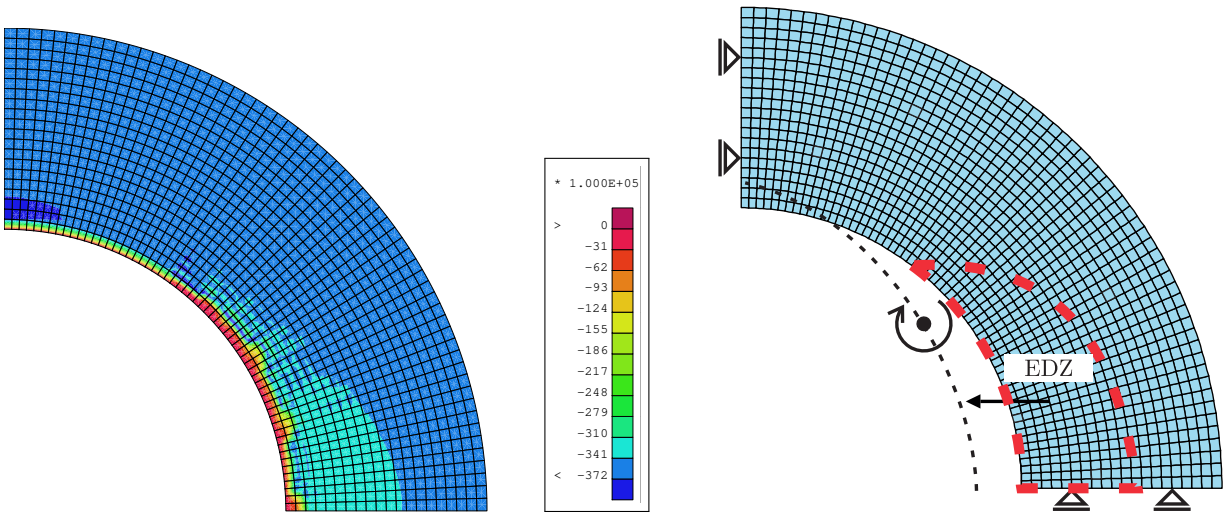

Figure 5.79.: Pore water pressure distribution at the end of excavation (left) and idealization of the impacts and resulting deformation of the tunnel support system (right) for the initially unsaturated tunnel model

In the case of the rigid support, the tunnel lining is directly affected by swelling, which begins at the tunnel side due to the increased permeability in the EDZ. As a result, radial deformation of the tunnel lining occurs from the tunnel side toward the tunnel center. Due to the rigidity of the tunnel support, radial deformation at the tunnel crown directed outward is also observed, as illustrated in Figure 5.80. Once the maximum radial deformation at the tunnel crown is reached after almost 10 days, these deformations begin to decrease over time. This behavior is related to the delayed onset of swelling at the tunnel crown compared to the tunnel side. The highest radial deformations are observed at an angle of almost 20 degrees, which can be attributed to the highly localized failure in the clay shale, leading to also localized swelling in this region.

For the deformable support, a different deformation pattern is observed. Initially, an ovalization of the tunnel lining due to stress anisotropy is evident after 1 day, with the tunnel side deforming away from the tunnel center and the tunnel crown deforming toward the tunnel center. This indicates that the swelling is initially fully absorbed by the grout, which undergoes deformation, as will be discussed in more detail in the following.

Starting at around 10 days, deformation patterns similar to those in the rigid support case emerge. This can be explained by the increasing swelling of the Opalinus clay shale, which eventually causes the grout layer to transfer deformations to the tunnel lining.

Overall, both tunnel support systems show similar final deformations of the tunnel lining, with the deformable case resulting in approximately 1 mm higher deformation at the tunnel crown and about 5 mm lower deformation at the tunnel side compared to the rigid support case.

To understand the deformation behavior of the entire tunnel support system, it is necessary to analyze the deformation of the grouting layer. Since the grout is located between the tunnel lining and the Opalinus clay shale, radial strains are the relevant quantity to be examined. These are shown for both tunnel support systems at selected time instances in Figure 5.81.

As illustrated in Figure 5.81, the rigid grout deforms negligibly, leading to the conclusion that all swelling-induced deformations are transferred directly to the tunnel lining.

In contrast, the deformable grout shows progressive deformation over time, reaching radial strains of approximately 25% to 35% at the end of the simulation at $t = 1000$ days.

The peaks in radial strain observed at 0, 17, 30 and 45 degrees correspond to the locations of the imperfect elements, where stress and strain concentrations occur.

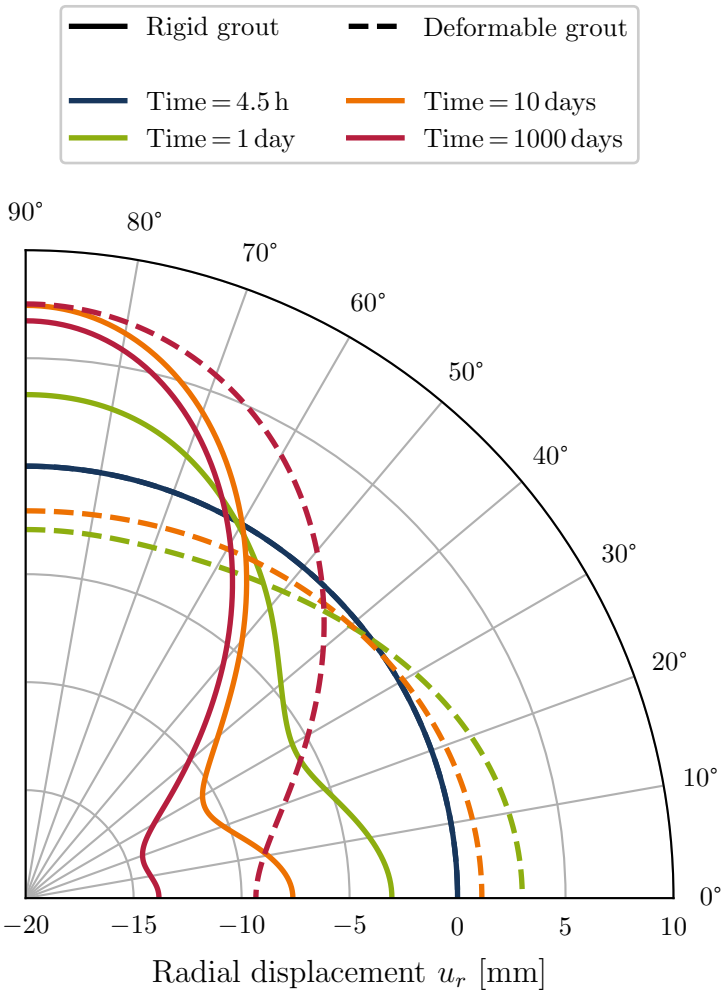

Figure 5.80.: Radial displacements of tunnel linings in supported tunnels for initially unsaturated conditions

Finally, the radial deformation of the tunnel wall must be examined to understand where swelling is prevented, leading to the buildup of swelling pressure, and where swelling is allowed, resulting in swelling-induced deformation. For that purpose, the increment of radial displacements after tunnel excavation was analyzed at four time instances for both tunnel support systems and is shown in Figure 5.82.

For the tunnel with rigid support, lower overall deformations are observed due to the high rigidity of the support system. Figure 5.82 shows displacements of approximately -15 mm at the tunnel side and about 5 mm at the tunnel crown. The deformation at the tunnel crown away from the tunnel center can be explained by the deformation of the tunnel lining. As previously established, the stiffness of the rigid tunnel support is so high that the swelling acting at the tunnel side leads to an ovalization of the tunnel lining. As a

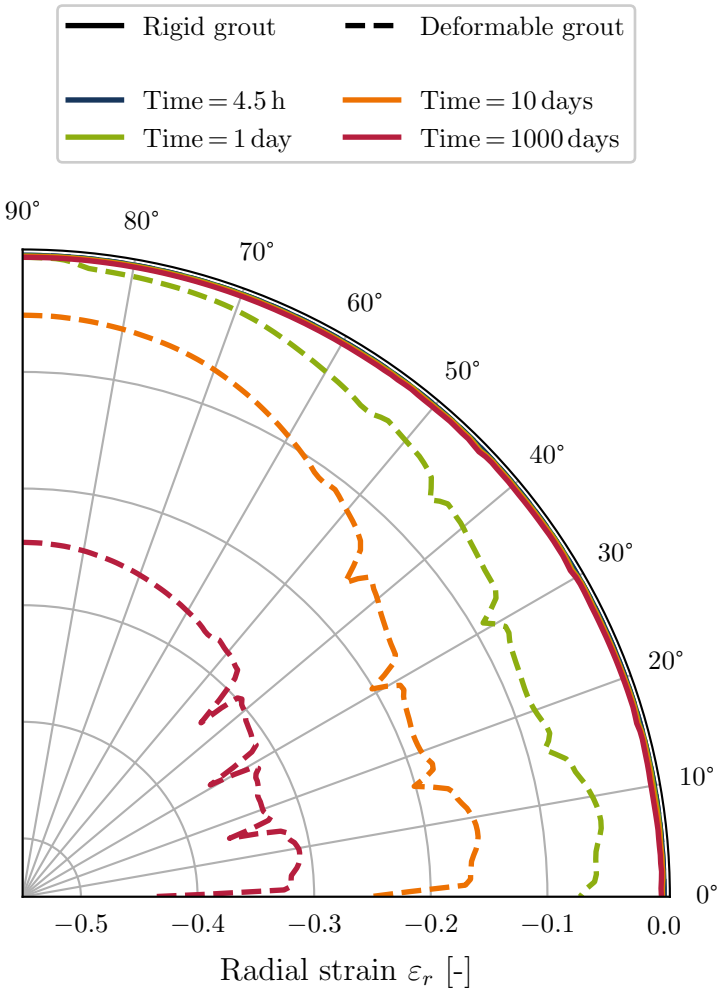

Figure 5.81.: Radial strain of the annular gap grout in supported tunnels for initially unsaturated conditions

result, the tunnel lining at the tunnel crown is pushed into the surrounding Opalinus clay shale.

In contrast, the tunnel with deformable support exhibits significantly higher deformations, with nearly -75 mm at the tunnel side and approximately -35 mm at the tunnel crown. This leads to the conclusion that swelling-induced volumetric deformations are allowed in this case, unlike in the tunnel with rigid support.

In addition to the deformations, the internal forces are a crucial factor for the design of the tunnel support system. Therefore, the normal forces and bending moments in the tunnel lining are evaluated in the following. First, the normal forces in the tunnel lining are analyzed for both tunnel support systems at the end of the simulation (t = 1000 days), which are depicted in Figure 5.83.

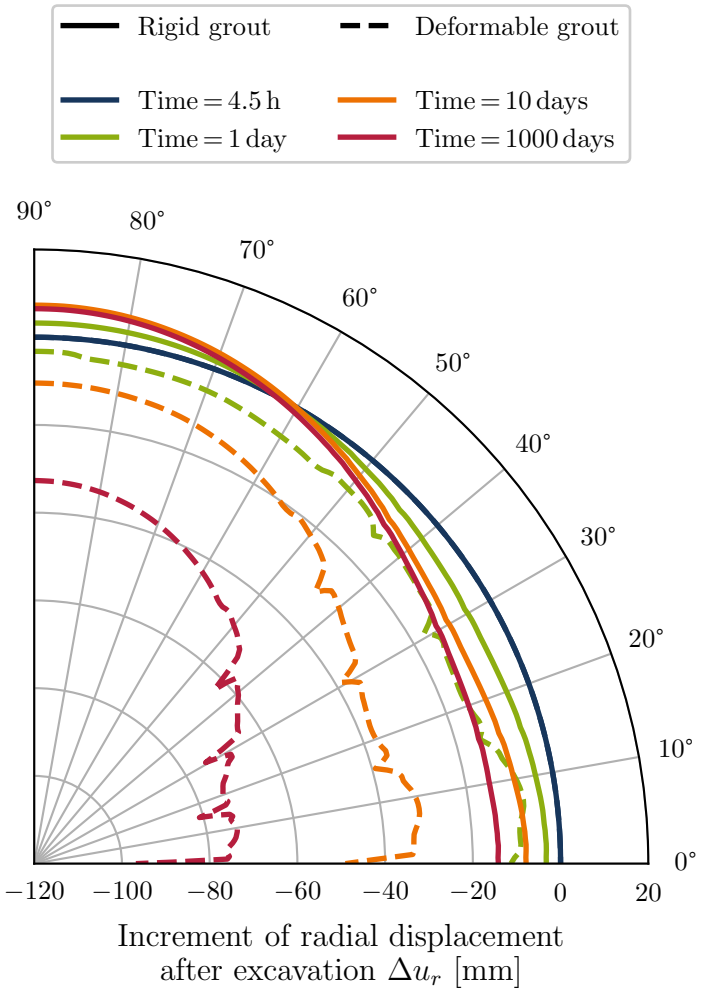

Figure 5.82.: Radial displacement of tunnel wall after excavation in supported tunnels for initially unsaturated conditions

When comparing the rigid and deformable tunnel supports, it becomes evident that the deformable support significantly reduces the normal forces. At the tunnel side, the absolute values of the normal forces are reduced from -47 MN/m to -4 MN/m, and at the tunnel crown from -24 MN/m to -3 MN/m. This corresponds to an approximate 90% reduction, underlining the effectiveness of the deformable support.

In addition to the normal forces, the bending moments are another important parameter, shown for both tunnel support systems in Figure 5.84. A comparison of the two systems reveals that the absolute values of the bending moments are generally reduced when using the deformable tunnel support.

For the deformable support, the deformation of the tunnel crown away from the tunnel center results in negative bending moments, while at the tunnel side the opposite occurs.

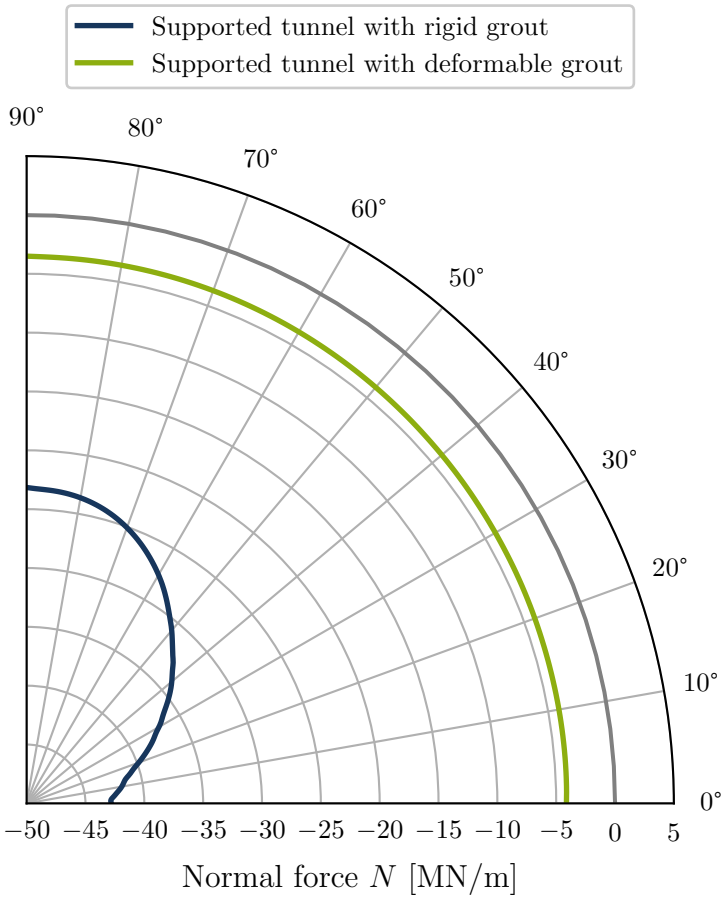

Figure 5.83.: Normal force in the linings of deformable and rigid tunnel support systems for initially unsaturated conditions ($t = 1000$ days)

The larger deformation at the tunnel side leads to slightly higher bending moments in this area compared to the tunnel crown.

In the case of the rigid tunnel support, the distribution of bending moments is more difficult to interpret due to the more complex tunnel lining deformations observed in Figure 5.80. Accordingly, the second derivative of the deformation, the curvature line, which has a linear relationship with the bending moment, is also complex. Therefore, the curvature line of the tunnel lining for the rigid support was evaluated and is presented in Figure 5.85. As shown, a similar pattern to the previously determined bending moment distribution emerges.

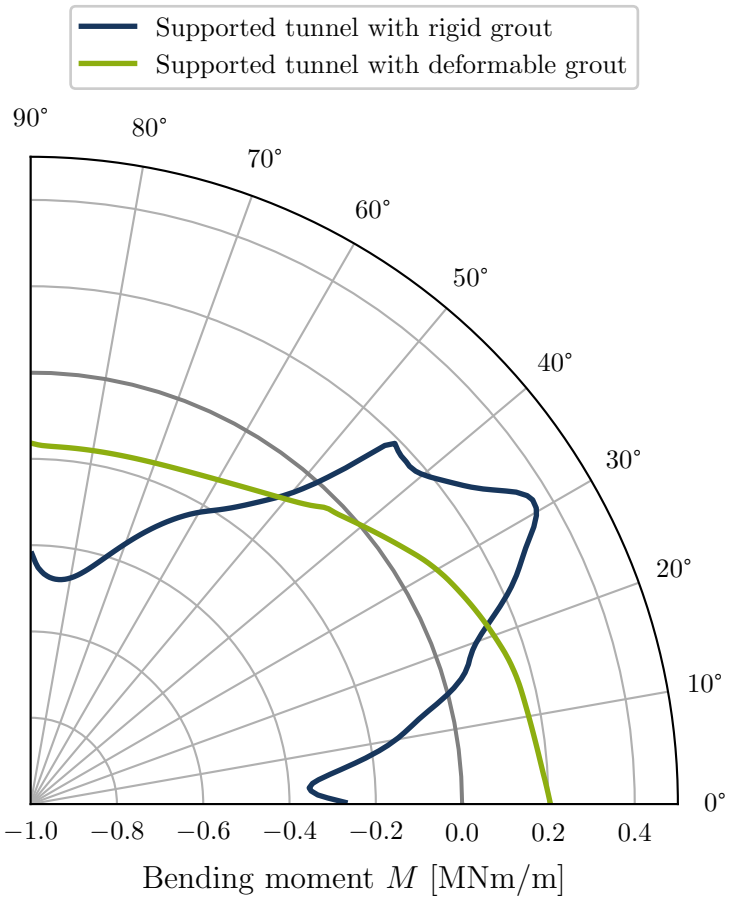

Figure 5.84.: Bending moment in the linings of deformable and rigid tunnel support systems for initially unsaturated conditions ($t = 1000$ days)

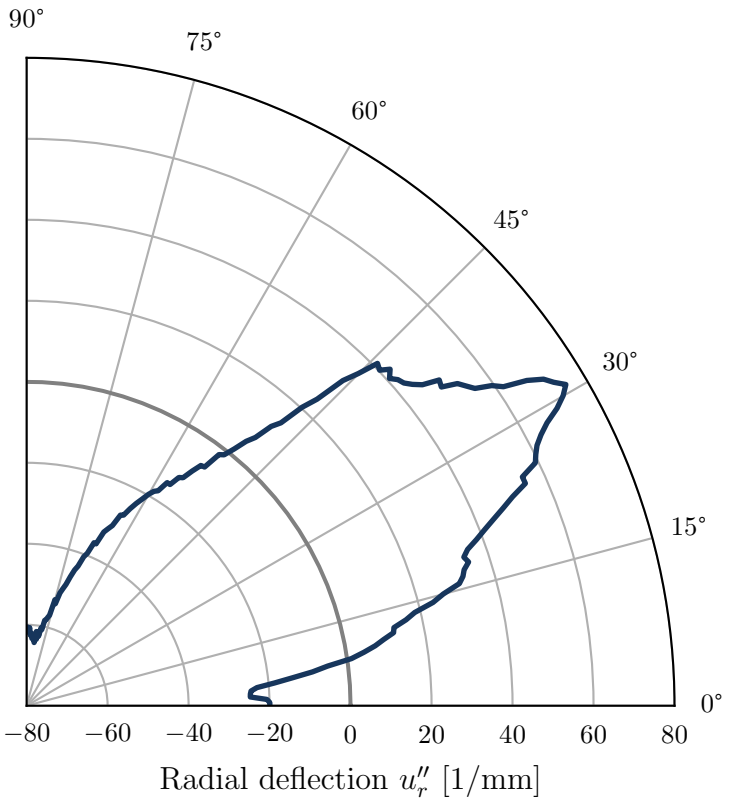

Figure 5.85.: Deflection of the lining of rigid tunnel support system for initially unsaturated conditions ($t = 1000$ days)

5.6.3. Evaluation of the tunnel support strategies and conclusion

After examining the two tunnel support strategies in terms of their influence on the EDZ size as well as their overall behavior and interaction with the surrounding clay shale, a final evaluation of the support systems is presented.

It was shown that the initial degree of saturation has a significant impact on the temporal evolution of the EDZ. In the initially fully saturated case, the EDZ forms primarily during excavation, whereas in the unsaturated case, it develops mainly during the saturation phase, when wetting-induced softening occurs.

For both initial saturation conditions, the rigid tunnel support consistently results in the smallest EDZ size among all investigated support strategies, with this effect being especially pronounced under initially unsaturated conditions. Furthermore, the rigid support leads to the lowest deformations, as was expected. However, this comes at the cost of high internal normal forces within the tunnel lining, requiring a considerable material investment to achieve the necessary stiffness.

The deformable tunnel support, in contrast, exhibits greater deformation and a larger EDZ than the rigid support. In the fully saturated case, the resulting EDZ is moderately smaller than in the unsupported tunnel, while in the unsaturated case, the EDZ size approaches that of the unsupported scenario. Despite this, the final lining deformations are very similar for both support systems, with the greatest difference observed under unsaturated conditions, where the deformable support yields 5 mm lower deformations at the tunnel side.

Of particular note is the compressibility of the deformable grout, which substantially reduces the radial stresses transferred to the tunnel lining and thereby significantly lowers the normal forces. This effect was especially evident in the unsaturated case and has the potential to reduce the required material for the tunnel lining, offering both ecological and economic advantages. However, to enable such optimization, the bending moments must be carefully assessed. While they remain within a similar range for both initial saturation conditions, a reduction in lining material could increase them and affect the structural performance.

Overall, the deformable tunnel support represents a promising approach for mechanized tunneling in swelling clay shales, particularly under partially saturated conditions.

5.7. Modified convergence-confinement method

As concluded in the previous section, under initially saturated conditions, the tunnel support has only a minor influence on the formation of the EDZ, since the EDZ develops primarily during tunnel excavation. Since the previous simulations assumed a linear convergence-confinement curve during excavation, this approach represents a simplification compared to real-world observations. In reality, surface settlement profiles along the excavation direction often exhibit a distinct s-shape, which similarly translates into a s-shaped convergence-confinement curve. Given the significant role excavation plays in the development of the EDZ, it is essential to evaluate whether a more realistic convergence-confinement curve impacts the EDZ size and characteristics, such as the mean permeability.

This section, therefore, aims to refine the simulation by developing a more representative convergence-confinement curve and assessing its effect on these aspects. Given the absence of surface settlement data due to the reference tunnel's considerable depth, due to the high overburden preventing any measurable surface deformations, an alternative data source must be identified. While a 3D tunnel excavation model could provide these information, the lack of a 3D implementation of the Barcelona Basic Model (BBM) in the finite element code Lagamine, in addition to the high computational cost of a fully coupled 3D simulation, renders this approach unfeasible. Instead, a 2D axisymmetric tunnel model is developed. This model, while ensuring computational efficiency, is employed to extract data along the tunnel excavation direction, which is subsequently used to construct the convergence-confinement curve.

The following section introduces the 2D axisymmetric model of the tunnel excavation, including its geometry, boundary conditions, and excavation strategy. To enable progressive tunnel excavation in the axisymmetric model and to address computational instabilities in the hydro-mechanically coupled simulation, it was necessary to use an internal force reduction method. This method is validated by comparing selected model results with an identical simulation in the finite element code Plaxis 2D, where a comparable reduction method is already implemented.

Once validated, the longitudinal displacement profile (LDP) from the axisymmetric model and the ground reaction curve (GRC) from the plane strain model are extracted and subsequently used to construct an updated convergence-confinement curve. Lastly, a comparison of the resulting EDZ obtained using the linear and the modified convergence-confinement curves in the plane strain model is conducted.

5.7.1. 2D axisymmetric model

As previously noted, an axisymmetric model is developed to maintain computational efficiency while simulating realistic tunnel advancement in 2D. This model provides radial convergence of the tunnel wall as a function of the excavation progress, termed the longitudinal displacement profile (LDP) subsequently used in Section 5.7.3 to constructed a modified convergence-confinement curve.

The 2D axisymmetric model has the dimensions of 100 m x 70 m, with mesh discretization and boundary conditions highlighted in Figure 5.86a. The initial stresses are applied via load conditions at the model boundaries, consistent with the approach used in the plane strain model. The values of the initial stresses as well as the initial pore water pressure vary between the individual simulations and are detailed for each model in the respective sections, along with further explanations. The degrees of freedom for temperature and air pressure in all model nodes are fixed at $T = 20°\text{C}$ and atmospheric pressure $P_a = 100\,\text{kPa}$, aligning with the conditions of the plane strain tunnel model.

The same constitutive models and parameters (see Table 3.5) as in the plane strain model, described in Section 5.3, are applied here, with one exception: the second gradient model could not be employed, as it is only implemented for 2D plane strain conditions in the chosen finite element code Lagamine. Therefore, the MWAT 2D elements used for the laboratory tests are applied for these simulations as well.

The progressive excavation process in the plane strain model was simulated by applying an initial load inside the tunnel, corresponding to the initial stress level at the start of the simulation. During excavation, this load was gradually reduced, following the convergence-confinement method. In contrast, the axisymmetric model implements a different approach, where the stepwise tunnel excavation process is represented in 16 individual excavation phases, where each phase involves deactivating a soil slice with a radius of 7 m and a thickness of 2 m, as depicted in Figure 5.86b. Each excavation phase is assumed to last 4.5 h, consistent with the duration used in the plane strain model.

Since mechanized tunneling involves gradual excavation, the internal forces of the excavated elements are gradually reduced to zero until they are fully deactivated during excavation. This approach, also employed in other finite element codes such as Plaxis 2D, allows for a smoother simulation of tunnel excavation and addresses computational stability issues that can arise from abrupt element deactivation. Since the precise implementation of this method in finite element codes like Plaxis is not publicly disclosed, the following section benchmarks the implementation by directly comparing the Lagamine

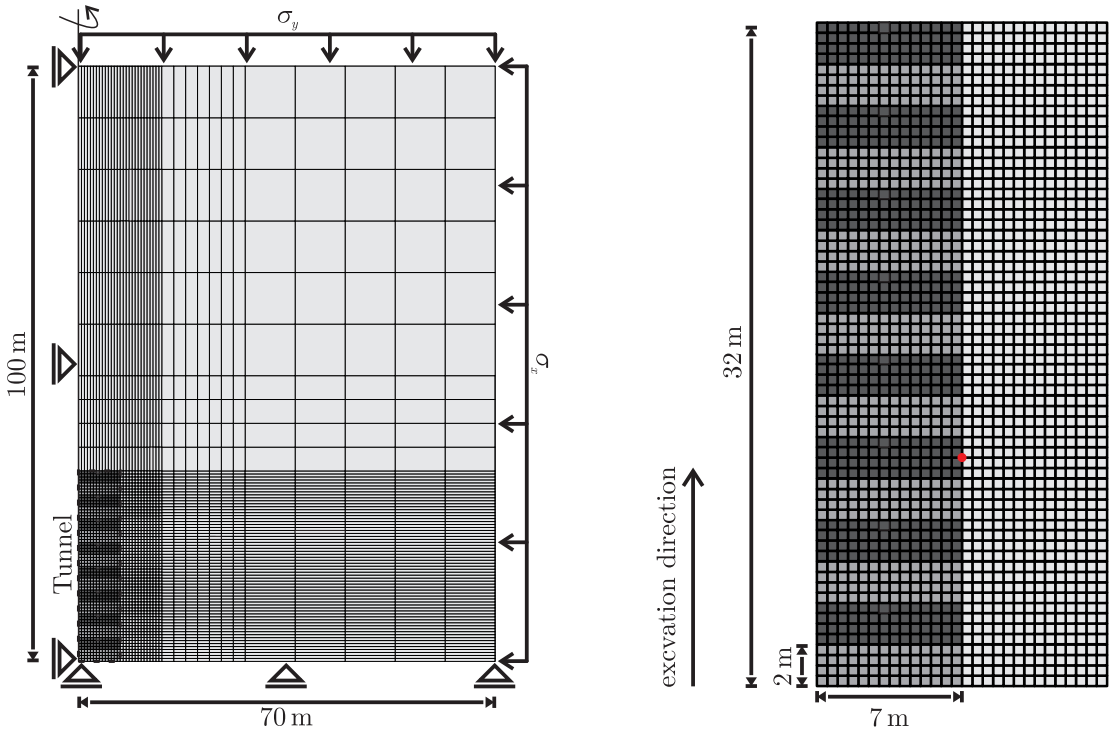

(a) Full model (b) Magnified area around tunnel excavation

Figure 5.86.: Schematic illustration of the axisymmetric tunnel model

model with an identical Plaxis model. The benchmarking specifically evaluates the longitudinal displacement profile (LDP) and the pore water pressure evolution during tunnel excavation. It should be noted that the internal force reduction method was already implemented in Lagamine. However, it needed to be adapted for use with the MWAT 2D elements and constitutive laws employed in this study. As the implementation had not been sufficiently validated and a full validation is out of scope of this thesis, it was decided to specifically carry out the validation only for the use case required within the scope of this work.

5.7.2. Validation of internal force reduction method

As previously mentioned, to enable a progressive tunnel excavation in the axisymmetric model, the internal forces of each element within the excavation slice are reduced from their current value to zero, representing complete deactivation, over a specified time span, in this case 4.5 h.

To validate this approach, an identical axisymmetric model is also created in Plaxis 2D. Initially, a purely mechanical scenario with an isotropic initial stress of $\sigma_x = \sigma_y = 7\,\mathrm{MPa}$

in conjunction with a linear elastic constitutive model is considered as the simplest case. The used parameters of the linear elastic constitutive model are presented in Table 5.3. Since the objective of the axisymmetric model is to determine tunnel convergence or radial displacements over time or with tunnel advancement, the radial displacement of the central node within the 6th excavation slice at the tunnel wall is evaluated throughout the excavation process. The 6th excavation slice is selected to minimize the influence of boundary effects on the results. This node is hereafter referred to as the reference node and is highlighted in red in Figure 5.86b.

Figure 5.87 illustrates the results for both the Lagamine and Plaxis 2D models, showing an almost identical model response. In this figure, the displacements u_x are plotted over time and as a function of the distance of the reference node to the tunnel (excavation) face x.

The model complexity is progressively increased by transitioning from an initial isotropic stress state ($\sigma_x = \sigma_y = 7\,\text{MPa}$) to an initial anisotropic stress state ($\sigma_x = 14\,\text{MPa}$, $\sigma_y = 7\,\text{MPa}$). Additionally, the model evolves from a purely mechanical approach, where pore water pressure is not considered, to a hydro-mechanically coupled scenario that incorporates the Van Genuchten soil-water characteristic curve (SWCC). The initial pore water pressure is set to match that of the plane strain tunnel model, with $p_{w,\text{initial}} = 2\,\text{MPa}$. Regarding the constitutive model, the complexity moves from linear elasticity to an elasto-plastic framework, specifically employing the Mohr-Coulomb model, with the corresponding parameters presented in Table 5.4.

It should be noted that the Barcelona Basic Model (BBM) implementation in Plaxis differs from that in the Lagamine finite element code. For instance, the Plaxis implementation does not incorporate cohesion, which is essential for modeling overconsolidated clay rocks such as Opalinus clay shale. Therefore, the Mohr-Coulomb model is selected for validation purposes, while the BBM is used in the final simulations.

Figure 5.88 presents the longitudinal displacement profile (LDP) obtained from both Lagamine and Plaxis models, and Figure 5.89 illustrates the development of pore water pressure over time or with TBM advancement. For the LDP, the radial displacements in both models are almost identical. Regarding pore water pressure, both models demonstrate an initial increase prior to excavation, aligning with in-situ observations from tunneling in London clay (Wan et al., 2019) and overcoring experiments in Opalinus clay (Khaledi et al., 2021). During excavation, the pore water pressure drops due to unloading around the tunnel. In low-permeability Opalinus clay, this unloading occurs nearly undrained, leading to the development of negative pore pressures.

The Plaxis results indicate slightly higher negative pore water pressures post-excavation. However, the outcomes are in a generally good agreement, validating the internal force reduction method applied.

Table 5.3.: Parameters of the linear elastic constitutive model

Parameter	Symbol	Unit	Value
Young's modulus	E	GPa	5
Poisson's ratio	ν	-	0.3

Table 5.4.: Parameters of the Mohr-Coulomb model

Parameter	Symbol	Unit	Value
Young's modulus	E	GPa	5
Poisson's ratio	ν	-	0.3
Friction angle	φ	degree	35
Cohesion	c	MPa	1
Dilatancy angle	ψ	degree	5

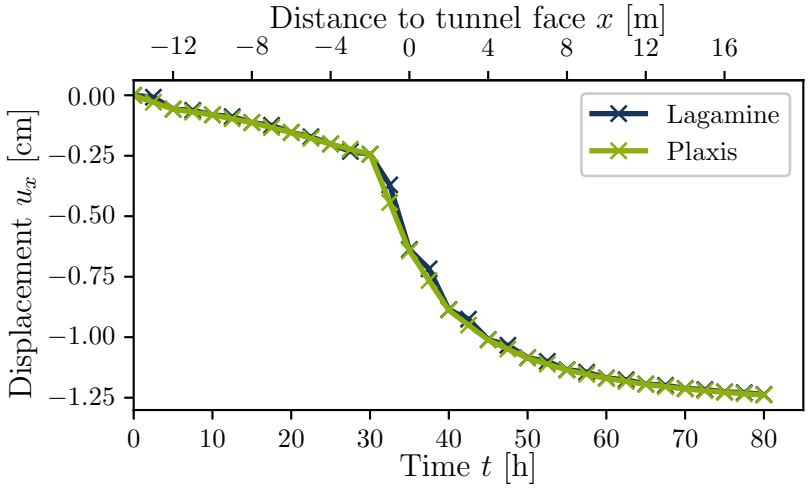

Figure 5.87.: Comparison of longitudinal displacement profile (LDP) from axisymmetric models in Lagamine and Plaxis 2D using linear elastic constitutive model

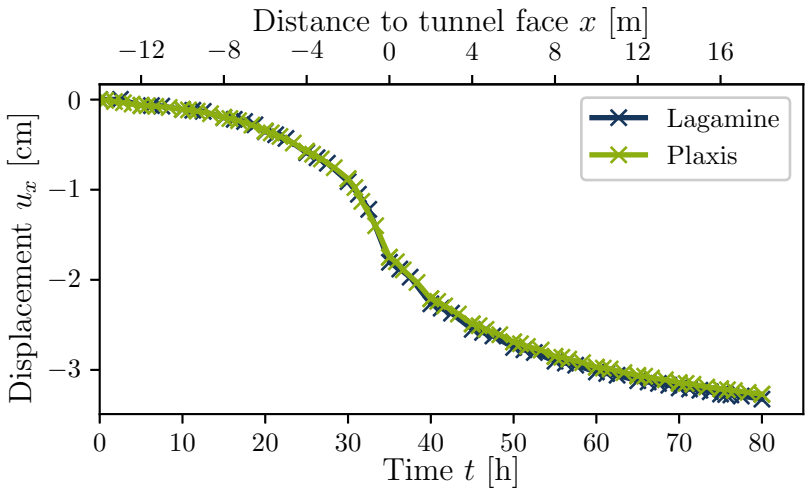

Figure 5.88.: Comparison of longitudinal displacement profile (LDP) from axisymmetric models in Lagamine and Plaxis 2D using Mohr-Coulomb constitutive model

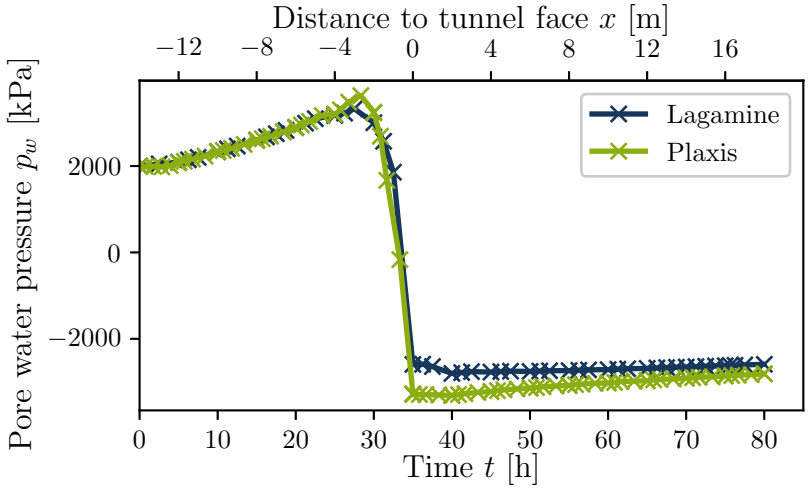

Figure 5.89.: Comparison of temporal evolution of pore water pressure from axisymmetric models in Lagamine and Plaxis 2D using Mohr Coulomb constitutive model

5.7.3. Construction of the convergence-confinement curve

As explained in Section 2.3.2.1, the longitudinal displacement profile (LDP) and the ground reaction curve (GRC) are used to construct the deconfinement ratio as a function of tunnel advancement, hereafter referred to as the convergence-confinement curve. However, a remaining limitation of the axisymmetric model is the absence of an anisotropic stress state around the tunnel wall, as was used in the plane strain model, where the initial stress state was set to 14 MPa vertical and 7 MPa horizontal. It should be emphasized

here that, although an anisotropic stress state can be assumed in the axisymmetric model, σ_x remains constant along the entire tunnel wall due to the position of the symmetry axis.

Consequently, two initial isotropic stress states, $\sigma_x = \sigma_y = 14\,\text{MPa}$ and $\sigma_x = \sigma_y = 7\,\text{MPa}$ are considered in both the axisymmetric model (to obtain the LDP) and the plane strain model (to obtain the GRC). The objective is, first, to analyze the extent to which the initial stress state influences the resulting convergence-confinement curve and, second, to identify an appropriate convergence-confinement curve for the given anisotropic stress condition as considered in the plane strain model.

During simulations with the axisymmetric model and the Barcelona Basic Model (BBM) as the constitutive model, several numerical instabilities are observed. These instabilities stem from the different parameters compared to the Mohr-Coulomb model leading to more deformation and pore water pressure generation. To enhance computational stability, the pore water pressure is controlled at every node within the slice currently being excavated. A python script is developed to facilitate this: it stores the pore water pressure of each node in the upcoming excavation slice at the end of the current slice's excavation, and then, during excavation, linearly decreases the pore water pressure from this stored value to atmospheric pressure (100 kPa). By controlling the pore water pressure during excavation, all previously observed numerical instabilities were resolved.

For both initial stress states, radial displacements and pore water pressures at the reference node are extracted from the axisymmetric model and presented in Figures 5.90 and 5.91, respectively. The only difference between the two models is the initial stress state. The model with 14 MPa initial stress exhibits greater displacements and a more pronounced pore water pressure peak compared to the 7 MPa model. This behavior results from the higher initial stresses leading to a greater increment of stress reduction during tunnel excavation. With all other boundary conditions remaining the same, this larger stress reduction increment inevitably results in greater deformation.

No significant differences are observed in the LDP between the 7 MPa and 14 MPa models throughout most of the excavation process. However, towards the end of the excavation, as shown in Figure 5.90, the differences become more pronounced. This delay is attributed to the low permeability of the material. Stress changes are initially accommodated by the buildup of pore water pressure, which delays the transfer of these changes in the form of effective stress to the solid skeleton. This also explains why the pore water pressure peak is higher in the model with an initial stress of 14 MPa compared to the 7 MPa model, as shown in Figure 5.91.

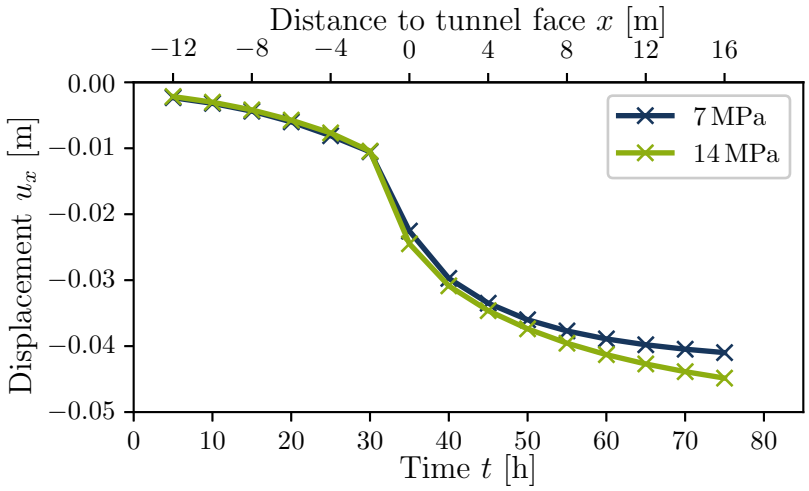

Figure 5.90.: Longitudinal displacement profile (LDP) from axisymmetric model using Barcelona Basic Model with both isotropic initial stresses

Nonetheless, the trends in both models are comparable and almost independent of the initial stress state. These trends include the characteristic s-shaped settlement pattern that develops as the tunnel excavation progresses, as well as the buildup of a pore water pressure peak ahead of the TBM, which rapidly dissipates upon reaching the excavation front. The reduction of pore water pressure to atmospheric pressure (100 kPa) is imposed during the excavation process, as in the plane strain model. This pressure is then maintained at a constant value post-excavation. Consequently, no negative pore water pressures are observed, in contrast to the results obtained with the Mohr-Coulomb model in the previous section. The control of pore water pressure in the excavated slices is necessary to ensure stable convergence of the numerical model utilizing the BBM as the constitutive model.

To construct the evolution of the deconfinement ratio $(1 - \lambda)$ with tunnel advancement, radial displacements as a function of the deconfinement ratio are required. For this, the plane strain model introduced in Section 5.3 is employed with two modifications.

First, the initial stress is adjusted to $\sigma_x = \sigma_y = 14\,\text{MPa}$ and $\sigma_x = \sigma_y = 7\,\text{MPa}$ respectively to match the axisymmetric model's conditions. Second, the local second gradient model is omitted to enable a direct comparison with the axisymmetric model, where this model is unavailable. Due to the isotropic stress state, radial displacements are uniform at every point along the tunnel wall. The radial displacements are extracted at the node located at the tunnel crown and the resulting ground reaction curves are shown in Figure 5.92 for both initial stress states.

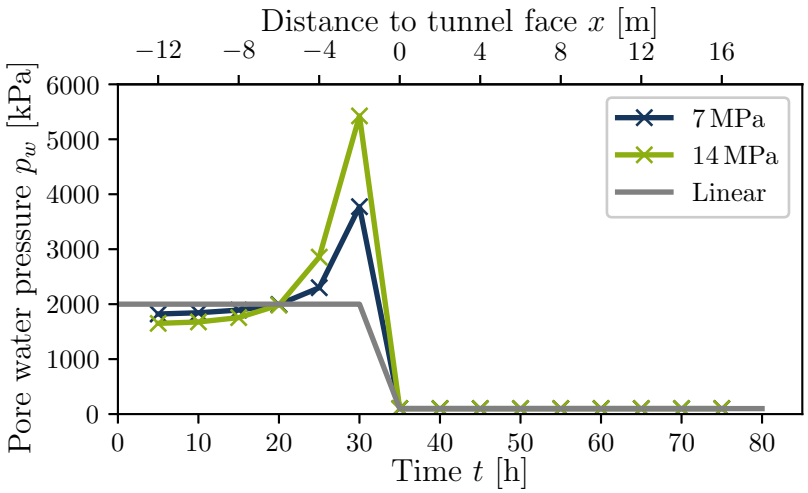

Figure 5.91.: Temporal evolution of pore water pressure from axisymmetric model using Barcelona Basic Model with both isotropic initial stresses

Similar to the axisymmetric model, the 14 MPa isotropic initial stress case results in higher deformations compared to the 7 MPa stress case. As seen in Figure 5.92, the relationship between deconfinement ratio and radial displacement appears linear for the model with an initial stress state of 7 MPa. However, in the 14 MPa stress scenario, this linear relationship holds only until a deconfinement ratio of about $1 - \lambda = 0.4$, below which the radial displacements increase more sharply. This behavior suggests the onset of plastic failure at lower deconfinement ratios for the 14 MPa initial stress model.

To construct the curve of the deconfinement ratio over time or as a function of tunnel advancement, each point on the LDP curve for the initial stress states of 7 MPa and 14 MPa is used to interpolate a deconfinement ratio that corresponds to the same radial deformation observed on the GRC, following the approach illustrated in Figure 2.16.

Due to the low permeability and rapid excavation, the increase in pore water pressure prior to excavation has minimal impact on the results, as the process occurs almost undrained. Therefore, the pore water pressure increase due to tunnel advancement is disregarded, meaning the peak effect is neglected. Instead, the reduction from the initial pore water pressure $p_{w,0} = 2$ MPa to the final pore water pressure equal to the atmospheric pressure is assumed to be linear, as depicted in Figure 5.91 (gray curve). The resulting deconfinement ratios, derived from $p_{w,0}/p_w$, along with the deconfinement ratio for the two initial stress states, are shown in Figure 5.93. The appendix C presents a comparison of the resulting EDZ areas and mean permeability for different approaches to the pore water pressure profile prior to excavation.

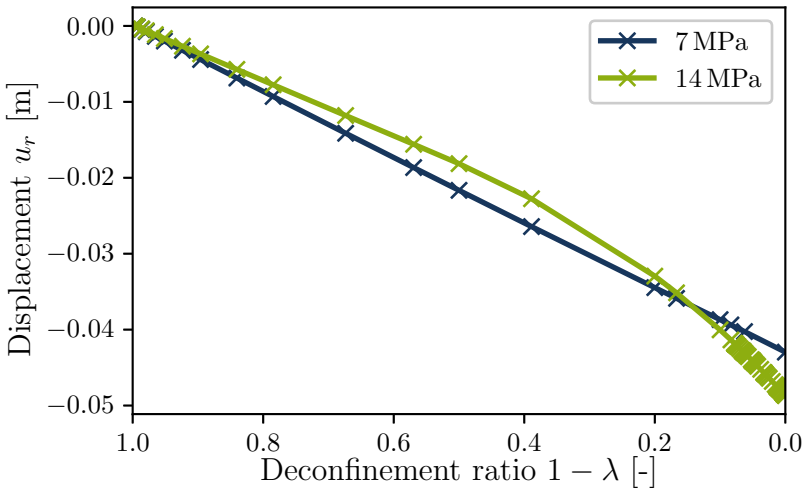

Figure 5.92.: Ground reaction curve (GRC) from plane strain model using Barcelona Basic Model for both isotropic initial stress states

As seen in Figure 5.93, the two deconfinement ratio curves for the different initial stress states exhibit minimal differences. From the beginning until approximately $x = -4\,\mathrm{m}$ (equivalent to two tunnel segments) before the TBM reaches the examined tunnel segment, the curves are nearly identical. Minor deviations occur between $x = -4\,\mathrm{m}$ and $x = +6\,\mathrm{m}$, though they disappear further along the curve. Thus, it can be concluded that the initial stress state has only a minor impact on the curve of the deconfinement ratio. Consequently, an average of the two curves is computed and applied in the subsequent 2D plane strain tunnel model calculations using the local second gradient model and anisotropic initial stress conditions. It should be noted at this point that the resulting temporal evolution of the deconfinement ratio during tunnel excavation does not reduce to zero, as was the case in previous simulations assuming a linear convergence-confinement curve. Instead, a small residual value of 0.034 remains.

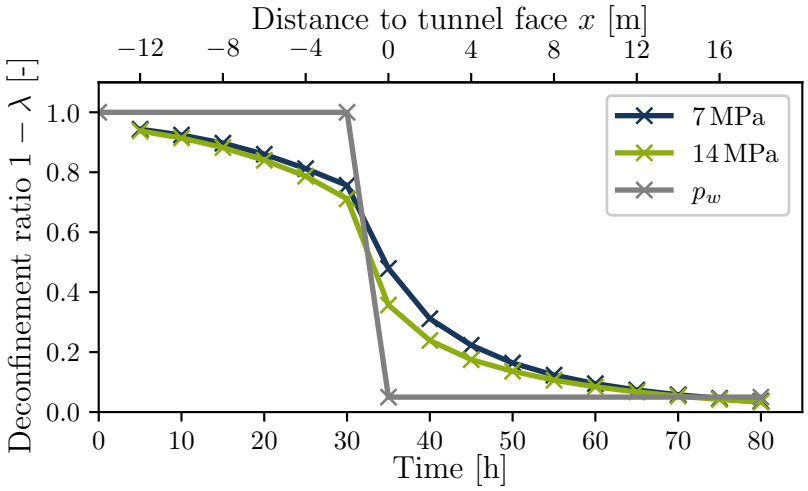

Figure 5.93.: Resulting temporal evolution of the deconfinement ratios for pore water pressure and both isotropic initial stress states

5.7.4. Resulting excavation damaged zone using modified convergence-confinement method

Following the previous section, where the modified convergence-confinement curve was constructed using an axisymmetric model, an average of the two convergence-confinement curves resulting from two different initial stress states (7 MPa and 14 MPa) is computed. This averaged curve is then applied as the boundary condition for the tunnel wall in the plane strain model with an anisotropic initial stress state of $\sigma_x = 7\,\text{MPa}$ and $\sigma_y = 14\,\text{MPa}$. The analysis first focuses on the temporal evolution of the resulting excavation damaged zone (EDZ) and subsequently compares these findings with the results from the model that employed a linear convergence-confinement curve, as utilized in earlier sections, such as the parameter study.

For the EDZ analysis, the temporal evolution of total deviatoric strains is first examined, as shown for selected time steps in Figure 5.94. As seen in this figure, no deviatoric strains appear until the excavation front ($x = 0\,\text{m}$ and $t = 1.5$ days) is reached. When the TBM reaches the reference node, two of the four imperfect elements show deviatoric strains, though no shear strain localization is yet evident as depicted in Figure 5.94c.
As excavation progresses, initial shear bands begin to form (see Figure 5.94d), and by the end of excavation at $t = 3.3$ days (Figure 5.94e), a distinct EDZ has developed.

In addition to the time steps during excavation (Figures 5.94a to 5.94e), further post-excavation time steps (Figures 5.94f to 5.94h), as examined in Section 5.4, are also eval-

uated. It is observed that the EDZ continues to develop over time, with quantification to be conducted in the subsequent analysis.

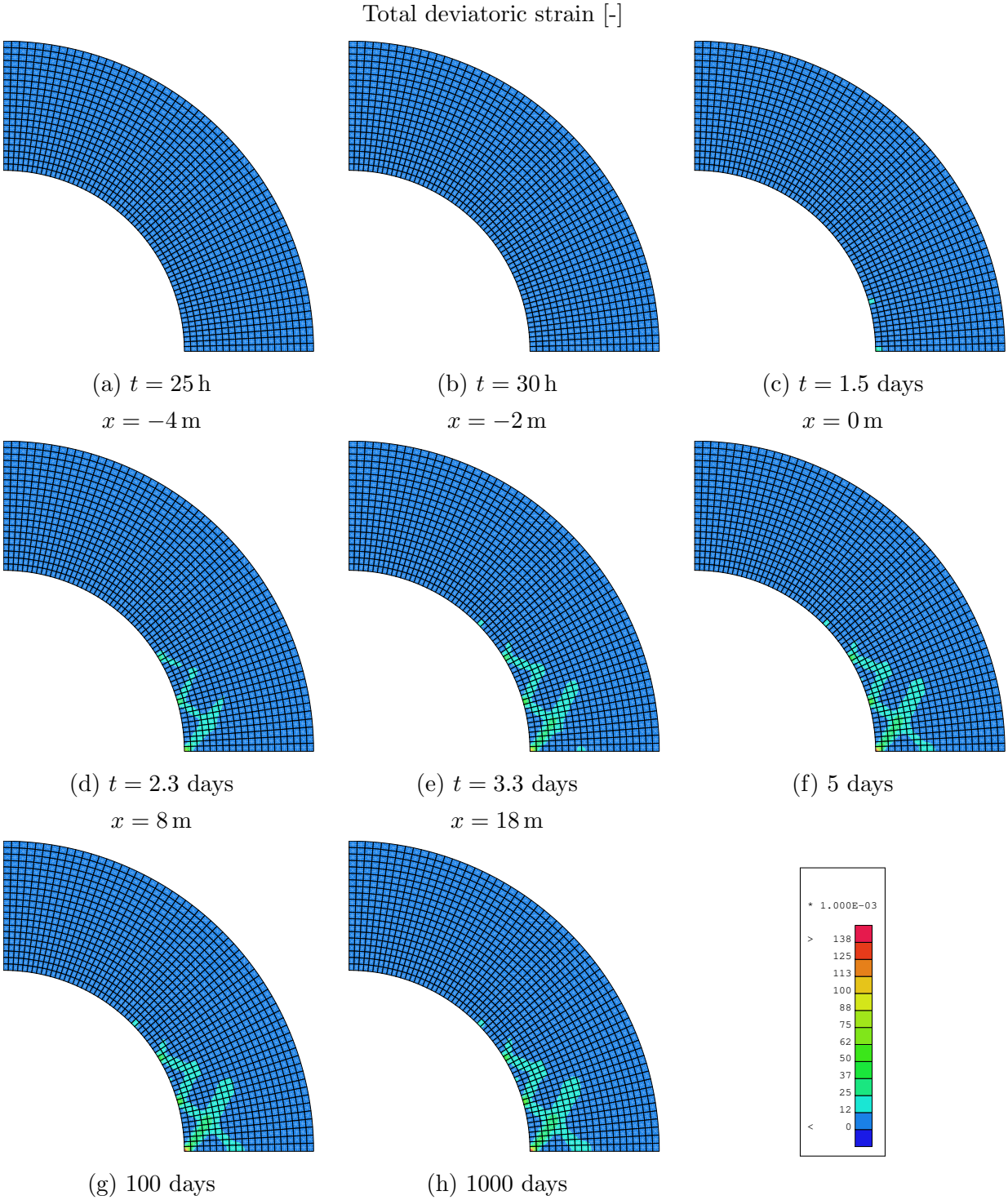

(a) $t = 25\,\mathrm{h}$, $x = -4\,\mathrm{m}$ (b) $t = 30\,\mathrm{h}$, $x = -2\,\mathrm{m}$ (c) $t = 1.5$ days, $x = 0\,\mathrm{m}$

(d) $t = 2.3$ days, $x = 8\,\mathrm{m}$ (e) $t = 3.3$ days, $x = 18\,\mathrm{m}$ (f) 5 days

(g) 100 days (h) 1000 days

Figure 5.94.: Development of total deviatoric strain within numerical model of unsupported tunnel employing modified convergence-confinement curve

Additionally, the temporal evolution of plastic points is analyzed to gain a better understanding of the plastic zone, which partially overlaps with the EDZ. The plastic points for the selected time steps are shown in Figure 5.95. Unlike the deviatoric strains, plasticity is observed as early as 25 h, or approximately 4 m distance from the reference node to the excavation front ($x = -4$ m), where two of the four imperfect elements reached plasticity (see Figure 5.95a).

Over time, the plastic zone expands, reaching its maximum at the end of excavation ($t = 3.3$ days) illustrated in Figure 5.95e. As previously discussed in Section 5.4, the plastic zone is notably larger than the area where shear bands appear. This was attributed to the excess pore water pressure in Section 5.4, which is also the case here. From the end of excavation ($t = 3.3$ days) to $t = 5$ days post-excavation, the plastic zone decreases (see Figures 5.95e and 5.95f), corresponding to the reduction in pore water pressure, which had increased during excavation due to tunnel ovalization, a result of the anisotropic initial stress state. Between $t = 5$ days and $t = 1000$ days, the plastic zone remains nearly constant (see Figures 5.95f to 5.95h).

Although the plastic zone is a significant result of the calculation it does not directly equate to the EDZ, as plastic deformations may increase permeability, but not to the same extent as the permeability increase associated with shear strain localization or shear bands, which can indicate the presence of fractures or other damage. Therefore, in the following, the permeability ratio is again employed to quantify the extent of the EDZ.

Figure 5.96 illustrates the temporal evolution of the permeability ratio. Similar to the deviatoric strains, changes in permeability begin at $t = 1.5$ days, coinciding with reaching the TBM face ($x = 0$ m), where permeability increases by approximately $\Delta k_w = 10$ in three of the four imperfect elements, as can be seen in Figure 5.96c. In the subsequent time step, the formation of the EDZ is significantly progressed (Figure 5.96d) and continues to increase further, as depicted in Figures 5.96e through 5.96h. Within the shear bands, a peak permeability increase of approximately $\Delta k_w = 100$ is observed.

Since permeability is coupled to deviatoric strains in this simulation, the permeability ratio behaves analogously to the shear band development (see Figure 5.94). This relationship highlights the direct impact of shear band formation on permeability increase, with the largest changes occurring along these zones of concentrated strain.

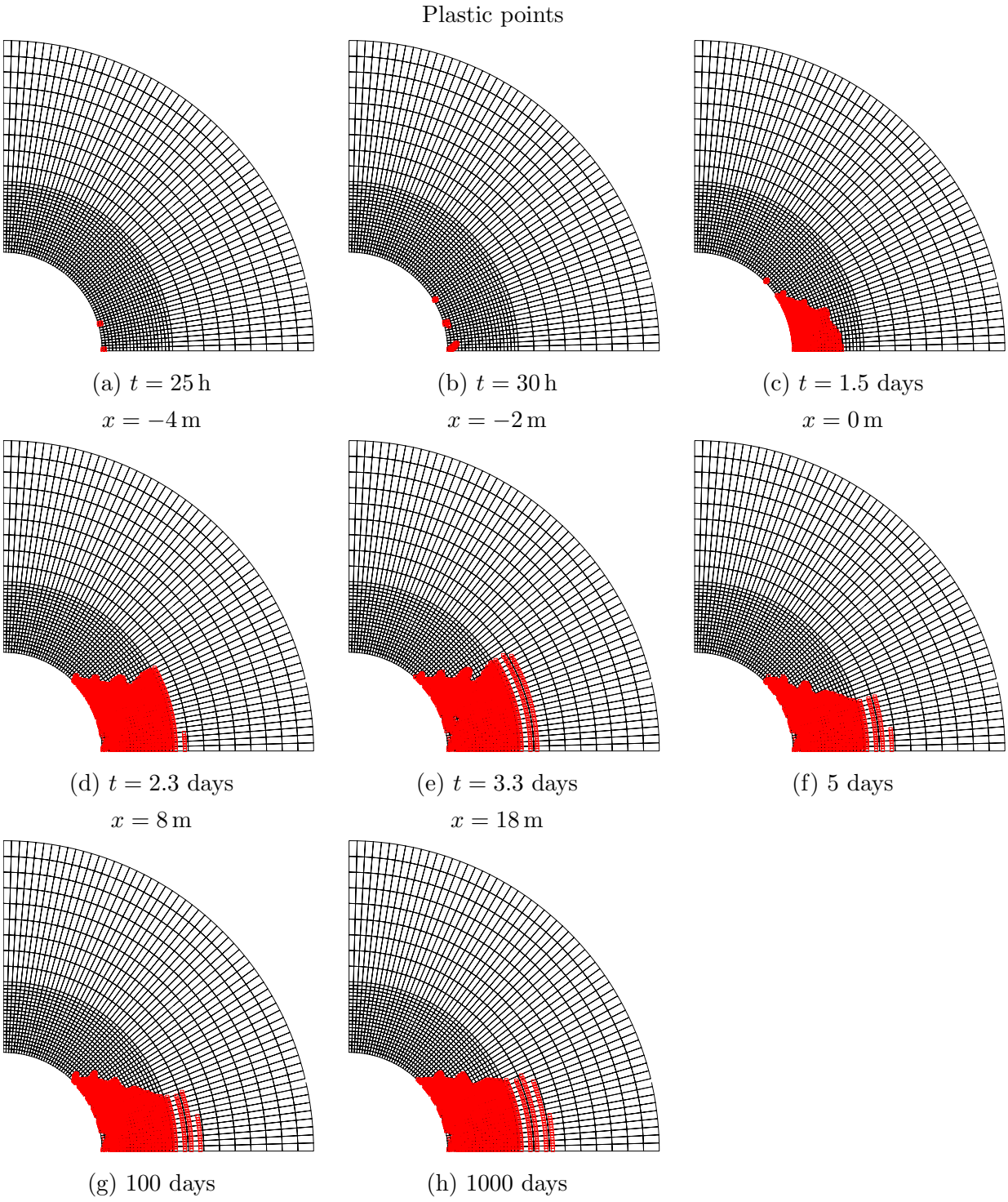

(a) $t = 25\,\mathrm{h}$ $x = -4\,\mathrm{m}$ (b) $t = 30\,\mathrm{h}$ $x = -2\,\mathrm{m}$ (c) $t = 1.5$ days $x = 0\,\mathrm{m}$

(d) $t = 2.3$ days $x = 8\,\mathrm{m}$ (e) $t = 3.3$ days $x = 18\,\mathrm{m}$ (f) 5 days

(g) 100 days (h) 1000 days

Figure 5.95.: Development of plastic points within numerical model of unsupported tunnel employing modified convergence-confinement curve

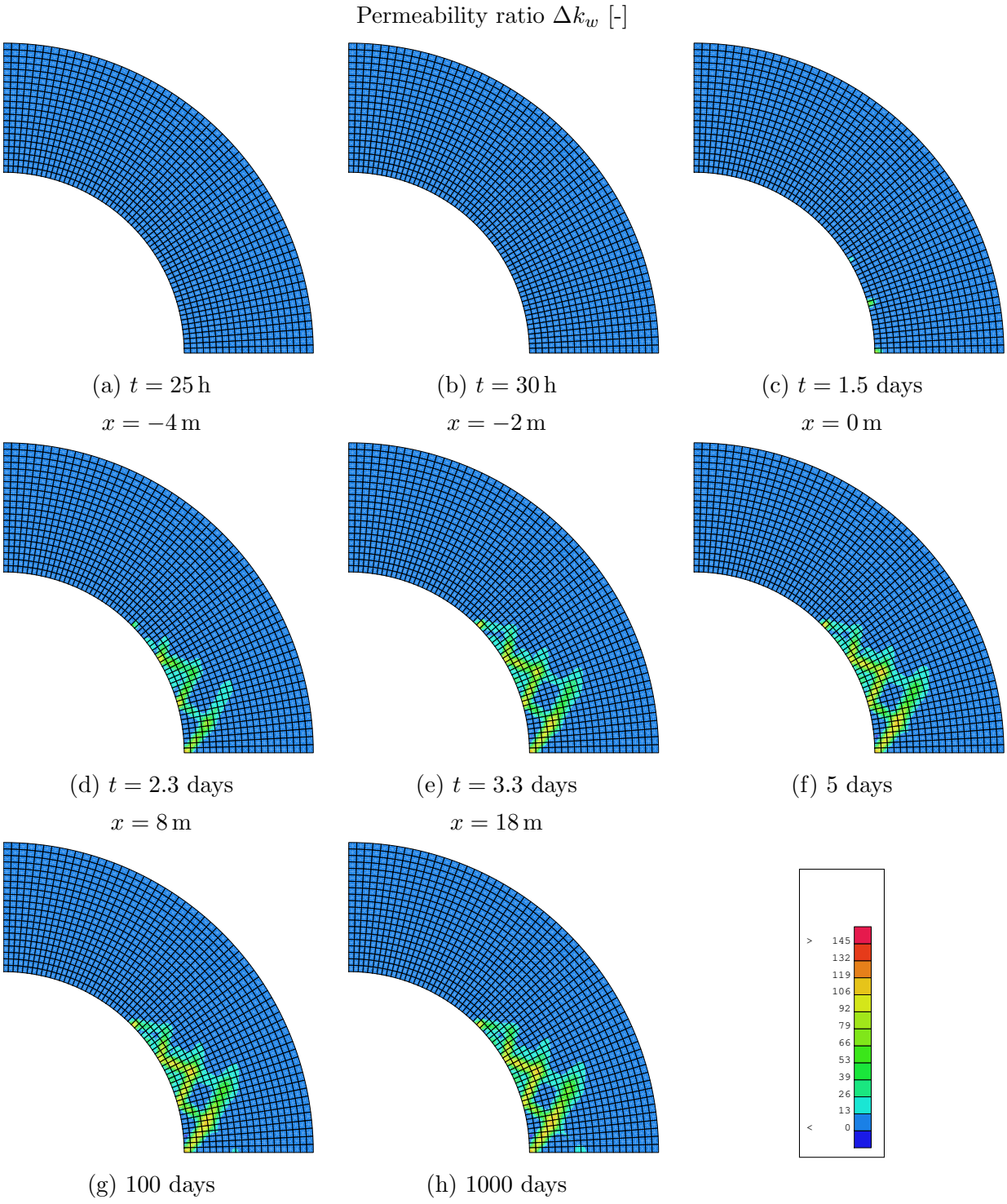

(a) $t = 25\,\mathrm{h}$ $x = -4\,\mathrm{m}$

(b) $t = 30\,\mathrm{h}$ $x = -2\,\mathrm{m}$

(c) $t = 1.5$ days $x = 0\,\mathrm{m}$

(d) $t = 2.3$ days $x = 8\,\mathrm{m}$

(e) $t = 3.3$ days $x = 18\,\mathrm{m}$

(f) 5 days

(g) 100 days

(h) 1000 days

Figure 5.96.: Development of permeability ratio within numerical model of unsupported tunnel employing modified convergence-confinement curve

Based on the permeability ratio and a permeability ratio threshold of 5, as selected in Section 5.4.6, both the extent of the EDZ and the mean permeability ratio within the EDZ are determined across the entire calculation period, as shown in Figures 5.97 and 5.98.

The EDZ begins to form at $t = 1.5$ days and expands steadily in size with increasing time and TBM advancement, as illustrated in Figure 5.97. The most significant increase occurs between $t = 1.5$ days ($A_{\mathrm{EDZ}} = 0\,\mathrm{m}^2$) and the end of the excavation at $t = 3.3$ days ($A_{\mathrm{EDZ}} = 13.20\,\mathrm{m}^2$), where $t = 1.5$ days indicated the time when the TBM arrives at the reference point. In the model with linear convergence-confinement curve, the main growth was also observed during the excavation process, where a greater EDZ size $A_{\mathrm{EDZ}} \approx 17\,\mathrm{m}^2$ was determined.

Between the end of the excavation and $t = 5$ days, the EDZ size increases only slightly. However, a noticeable secondary increase occurs between $t = 5$ days and $t = 100$ days. This can be explained by the dissipation of excess pore water pressure in the formation at the tunnel side, which leads to an increase in effective stresses. This rise in effective stresses, in turn, promotes further softening and strain localization, ultimately leading to an increase in the EDZ area.

Similar to the findings in Section 5.4, a maximum value is approached towards the end of the simulation ($t = 1000$ days), with the EDZ size stabilizing at $A_{\mathrm{EDZ}} = 16.19\,\mathrm{m}^2$.

Similar to the increase in EDZ area, the mean permeability ratio also rises from approximately $\Delta k_w = 1$ at $t = 1.5$ days to around $\Delta k_w = 25$ at $t = 3.3$ days, marking the end of the excavation (see Figure 5.98). Afterwards, the mean permeability ratio continues to increase, though not at the same rate as the EDZ area. A closer examination of Figure 5.98 reveals a slight decrease in mean permeability ratio between 5 and 100 days, contrasting with the increase in the EDZ area. This discrepancy can be attributed to the expansion of the EDZ, which now includes regions that do not experience remarkable permeability increases (e.g., areas between shear bands). Therefore, an increase in EDZ area does not necessarily result in a higher mean permeability ratio.

In addition, the temporal progression of the identified EDZ outer boundary is illustrated in Figure 5.99. Also in this representation it is clearly evident that the largest increase in the EDZ area occurs within the first 3.3 days, which corresponds to the tunnel excavation. After the end of the excavation, only a marginal increase is observed.

Following the analysis of the temporal progression of the EDZ using the model with the modified convergence-confinement curve, this model is compared with the model employ-

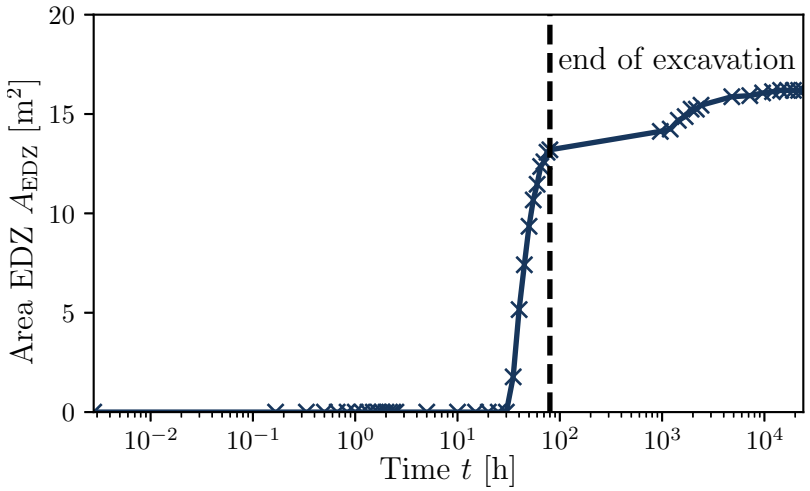

Figure 5.97.: Temporal evolution of the EDZ area for the numerical model of unsupported tunnel employing modified convergence-confinement curve

ing the linear convergence-confinement curve used in the parameter study. The comparison is conducted at $t = 1000$ days after the start of the excavation, as the EDZ has reached its maximum extent by this time and is expected to stabilize without further significant increase. For this purpose, the three key parameters, deviatoric strains, plastic points, and permeability ratio, are presented side by side in Figure 5.100.

Considering the deviatoric strains shown in Figures 5.100a and 5.100d, it is evident that the extent of the EDZ is larger in the model with the linear convergence-confinement curve compared to the one with the modified convergence-confinement curve. This difference is also reflected in the permeability ratio. Although the distribution of plastic points varies between the models, the distinction is less pronounced.

For a quantitative comparison, the EDZ area and the mean permeability are calculated for both models and displayed in Figure 5.101, along with the outer boundaries of the EDZ. It becomes apparent that the EDZ size is reduced by approximately 2 m^2, or 12%, in the model incorporating the modified convergence-confinement curve. Additionally, the permeability is also lower by 0.5E-17 m^2. A primary reason for this difference is that in the model with the linear convergence-confinement curve, the tunnel support pressure was unloaded to a deconfinement ratio of 0, while the modified convergence-confinement curve only reduced the deconfinement ratio to 0.034.

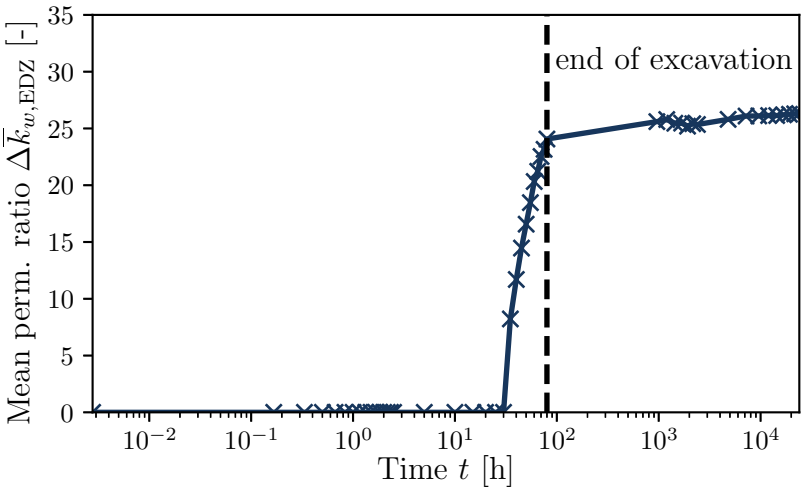

Figure 5.98.: Temporal evolution of mean permeability ratio within the EDZ for the numerical model of unsupported tunnel employing modified convergence-confinement curve

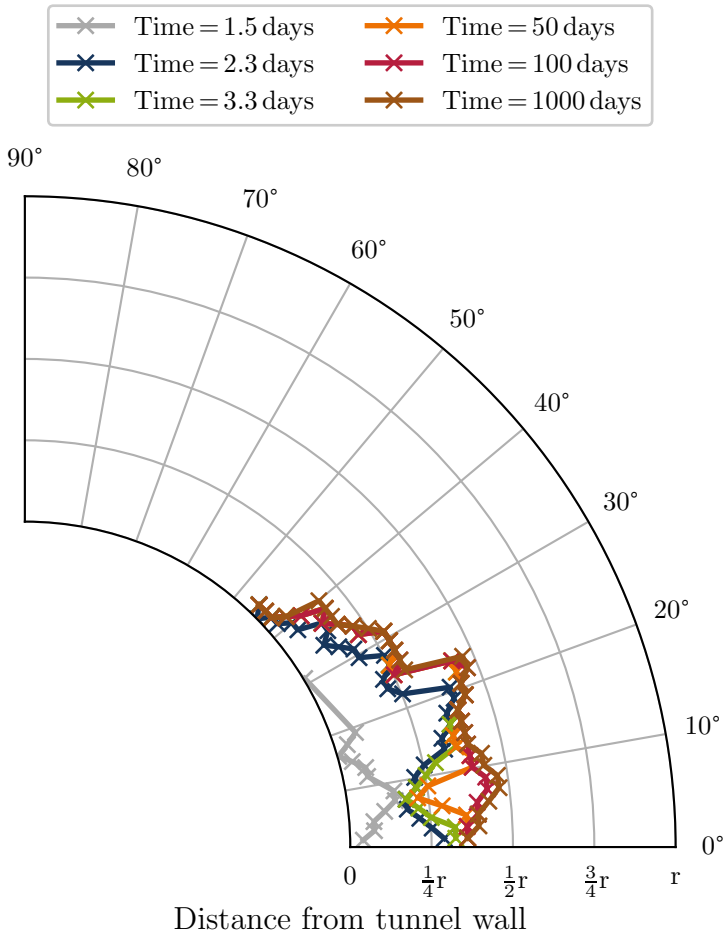

Figure 5.99.: Temporal evolution of EDZ extension for the numerical model of unsupported tunnel employing modified convergence-confinement curve

Linear convergence-confinement curve

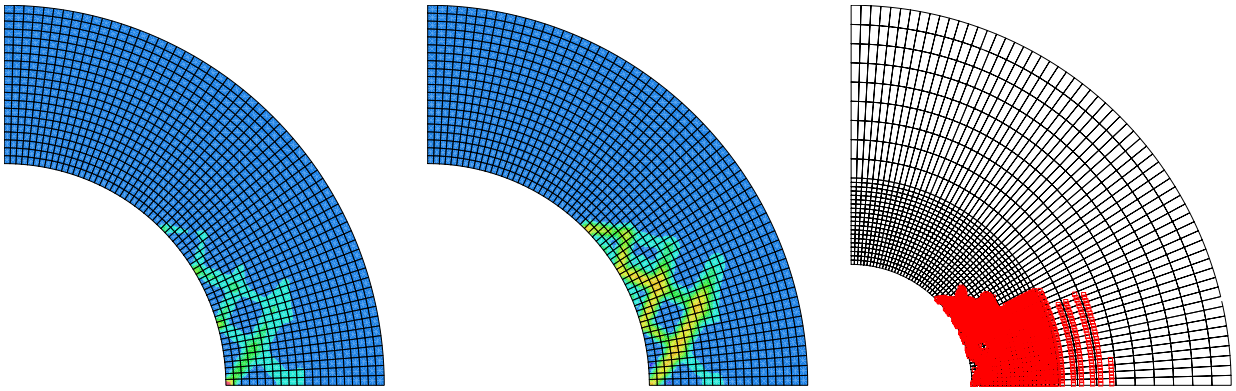

(a) Deviatoric strain (b) Permeability ratio (c) Plastic points

Modified convergence-confinement curve

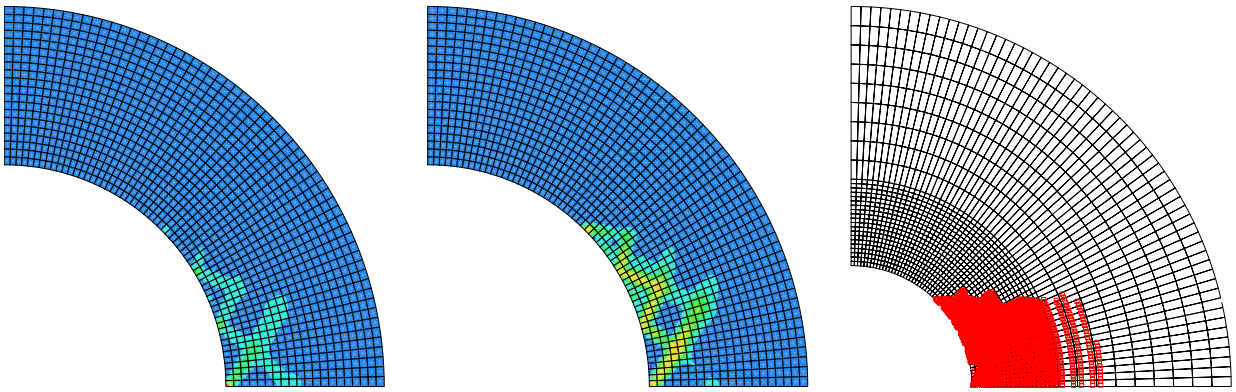

(d) Deviatoric strain (e) Permeability ratio (f) Plastic points

Figure 5.100.: Comparison of key results between the modified and linear convergence-confinement models ($t = 1000$ days)

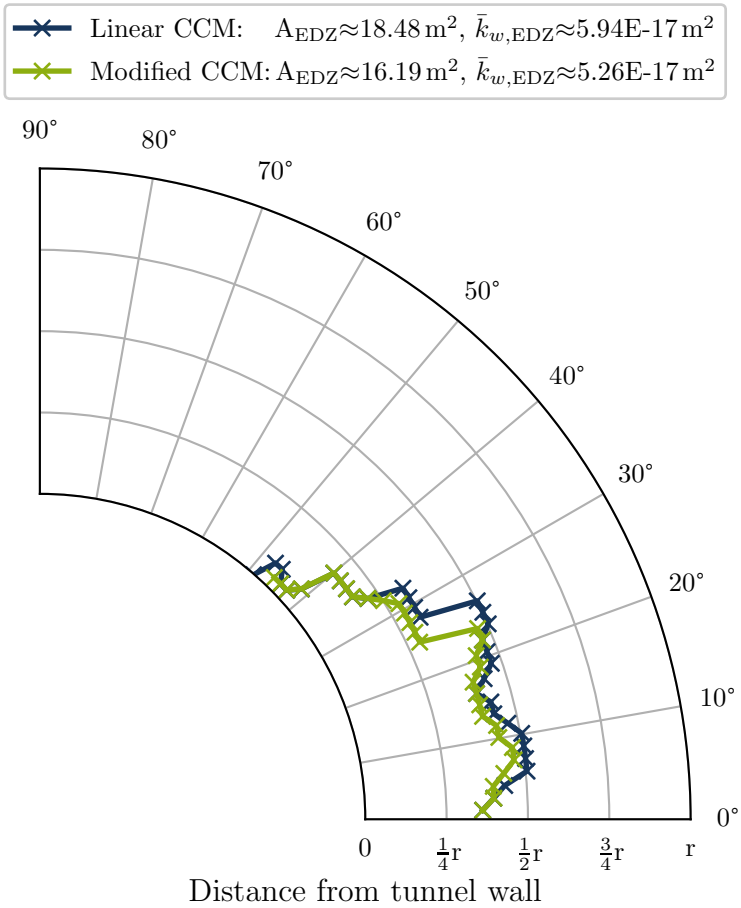

Figure 5.101.: Comparison of the EDZ extend for the modified and linear convergence-confinement models ($t = 1000$ days)

5.8. Conclusion

This chapter began with an explanation of the numerical models and the simulation method used for tunnel excavation. Subsequently, various metrics were evaluated for their suitability in systematically assessing the size of the EDZ. Although plastic points initially appeared promising, the plastic zone was larger than the region where shear bands occur. This discrepancy was due to an additional zone influenced by pore water pressure changes, which also induced plasticity. Therefore, the permeability ratio was ultimately considered as the metric for systematically evaluating the EDZ size. Determining a threshold value was necessary to distinguish between the EDZ and the surrounding area.

The next question addressed was the timing of the EDZ evaluation. It was found that the majority of the EDZ forms during excavation but that the EDZ continues to grow afterward. To analyze the most unfavorable case, it was decided to evaluate the EDZ at the end of the simulation, where the greatest EDZ size was observed.

A parameter study was then conducted on the unsupported tunnel. It was shown that the number and strength of imperfect elements had little effect on the EDZ size. As in the previous chapter, a sufficiently small element size was required to distinguish between shear bands and areas adjacent to them. Regarding the second gradient elastic modulus, it was confirmed, as previously observed, that it influences shear band thickness, but ultimately not EDZ size. Finally, the tunnel diameter was analyzed, revealing that the square of the tunnel diameter has a linear relationship with the EDZ size.

After analyzing the unsupported tunnel in the parameter study, two tunnel support strategies were investigated: a rigid support and a deformable support, each under different initial saturation conditions. In both cases, the rigid support resulted in the smallest EDZ size. For initially saturated conditions, the deformable support led to a slightly larger EDZ, while under initially unsaturated conditions, the EDZ size was similar to that of the unsupported tunnel. A detailed assessment of both support strategies followed, focusing on the deformations of individual components and their interaction with the surrounding Opalinus clay shale. The rigid support showed minimal deformation but caused significantly higher stresses. In contrast, the deformable support, due to its compressible grout layer, accommodated swelling pressures through deformation. This effect was particularly visible under initially unsaturated conditions. These findings highlight the deformable support as a promising alternative to rigid support systems, especially in cases where significant swelling is expected.

Another key finding was that the tunnel support has limited influence on the EDZ size, for initially saturated conditions, as the EDZ primarily grows during tunnel excavation. Consequently, the linear convergence-confinement curve approach was compared with a modified approach to investigate the impact of a more realistic convergence-confinement curve on EDZ size. For this purpose, an axisymmetric tunnel model was developed to provide information about the excavation process along the excavation direction. Comparing the linear convergence-confinement curve with the modified approach revealed a smaller EDZ size in the latter case. This underscores the importance of accurately modeling the mechanized tunnel excavation process, as it has an influence on the development of the EDZ.

6. Conclusions and recommendations

6.1. Summary

This study analyzed the hydro-mechanical behavior of clay shales during mechanized tunneling, with a focus on swelling clay shale formations. The research was motivated by a central question posed by the Collaborative Research Center 837 "Interaction Modeling in Mechanized Tunneling" which aimed to address the challenges of mechanized tunnel excavation through such geotechnically complex formations. The central question of this research was: How could a mechanized tunnel drive be successfully realized through swelling clay shale formations, which presented unique challenges due to their hydro-mechanical properties? To answer this, the study required a comprehensive analysis of the coupled hydro-mechanical behavior of the material and the development of realistic models to simulate tunneling processes in these formations.

Given the complexity of swelling clays, the research employed both experimental and numerical approaches to understand the interactions between the soil and tunnel construction processes. However, only the numerical investigations were conducted as part of this thesis.

The first step was to derive the hydro-mechanical properties of Opalinus clay, a representative clay shale formation, through an extensive literature review and experimental investigations conducted at Ruhr University Bochum (RUB). The focus was on determining the mechanical and hydraulic properties that govern the behavior of swelling clay shales during tunneling.

The mechanical properties were quantified based on laboratory tests, including oedometer and triaxial tests, conducted outside the scope of this thesis. These tests enabled the calibration of key parameters such as compressibility, shear strength, and stress-strain behavior under different loading conditions, providing insights into the soil's response to mechanical forces during tunneling operations. Similarly, the hydraulic properties were determined through permeability tests and water retention curve measurements, offering

essential data on the clay shale's ability to retain and transmit water. As these tests were not performed as part of this thesis, detailed test protocols and methodologies are not included.

The hydro-mechanical properties obtained from these laboratory experiments were used to simulate swelling tests under tunneling-relevant boundary conditions. One of the key achievements of this study was the successful calibration of a single parameter set, that could represent the swelling behavior under all investigated boundary conditions.

Shear strain localization in Opalinus clay was subsequently studied using numerical models of a biaxial test featuring well-defined boundary conditions. Stress paths were analyzed to understand their impact on strain localization, supported by a parameter study of critical model parameters. Furthermore, methods for predicting the increased permeability of the excavation damaged zone (EDZ) were examined in detail.

These findings were applied to tunnel-scale modeling, focusing on the formation and evolution of the EDZ during mechanized tunnel excavation. A case study illustrated the application of numerical models to simulate excavation processes. The influence of various model parameters and tunnel support systems on the EDZ was systematically evaluated, and a modified modeling approach for tunnel excavation was introduced and assessed for its impact on EDZ development.

6.2. Conclusions

In this thesis, various aspects of the hydro-mechanical behavior of clay shales during mechanized tunnel excavation were investigated, with the focus varying depending on the chapter. The main findings of this work are listed chronologically as follows:

- During the parameter calibration, the Barcelona Basic Model effectively replicated the mechanical behavior of Opalinus clay shale. For hydraulic modeling, the van Genuchten model successfully characterized the water retention properties, while a modified Kozeny-Carman model accurately captured the porosity-dependent permeability.
- Modeling the swelling tests demonstrated the necessity of precise knowledge of the boundary conditions, particularly deformations, as minor deformations significantly influence swelling pressure. Utilizing the Barcelona Basic Model for expansive soils enabled the successful simulation of all conducted swelling tests under varying deformation boundary conditions with a single parameter set.

- Laboratory data from biaxial tests on Opalinus clay revealed pronounced brittle behavior. Simulations using the Barcelona Basic Model with a local second gradient extension provided reasonable agreement, offering deeper insights and highlighting highly localized shear failure.
- Detailed analyses of conditions leading to shear strain localization in the Barcelona Basic Model revealed two critical stress path scenarios: one associated with mechanical softening in highly overconsolidated clay when the stress path enters plasticity, and another where an initially unsaturated soil undergoes saturation, causing hydraulic softening.
- For the local second gradient model, a sufficiently small element size was determined to be essential to adequately distinguish between regions inside and outside the shear band. Additionally, the second gradient parameter, D, was found to control the shear band thickness by acting as an internal length scale, facilitating mesh-independent localization.
- Among various approaches to linking permeability with shear strain localization, the strategy of correlating permeability to equivalent deviatoric strains produced the most reliable results and was exclusively adopted for the tunnel model.
- The permeability ratio, as defined in this thesis, represents the ratio between the increased permeability within the Excavation Damaged Zone (EDZ) and the initial permeability of the rock mass. This ratio proved to be a robust indicator for systematically determining the size of the EDZ. In contrast, relying solely on the plastic zone tended to overestimate the EDZ size due to the inclusion of regions where plasticity arises solely from pore water pressure changes.
- A parameter study using the tunnel model indicated that the incorporated material imperfections, intended to evoke shear strain localization, influenced the position of the shear bands but had no measurable effect on the EDZ size. Among the variables analyzed, tunnel diameter emerged as the most significant factor influencing the EDZ size, which was found to correlate approximately with the square of the tunnel diameter..
- Comparative analysis of two potential tunnel support systems revealed that rigid supports minimized deformation and EDZ size while inducing the highest normal forces in the tunnel lining. In contrast, deformable supports exhibited slightly greater EDZ sizes but similar lining deformations, while decreasing normal forces in the tunnel lining. Both systems were effective in limiting EDZ expansion com-

pared to an unsupported tunnel. However, it was observed that most EDZ growth occurs during excavation, limiting the overall impact of tunnel support systems in this regard.

- Incorporating results from a two-dimensional axisymmetric model enabled a more realistic simulation of tunnel excavation. This approach resulted in a smaller predicted EDZ, underscoring the importance of accurately modeling the excavation process.

6.3. Outlook and recommendations for further studies

Although this thesis has examined the hydro-mechanical behavior of clay shales during tunneling from various perspectives, this research field still offers opportunities for further studies. The following are identified by the author as potentially valuable areas for future research:

- Although a parameter set for Opalinus clay was derived using the experiments conducted at RUB, the intermediate states during saturation or, more generally, during changes in suction could not be fully validated. To address this, it would be beneficial to repeat the laboratory experiments under various constant suction conditions. This approach would enable better modeling of the transition from unsaturated to saturated states and provide valuable insights for a more detailed understanding of soil behavior.

- Opalinus clay, as well as other sedimentary clay shales, exhibit strongly anisotropic behavior, particularly with regard to swelling, as demonstrated in this thesis. This anisotropic behavior cannot be adequately captured using the Barcelona Basic Model (BBM). Therefore, a potential avenue for further study could involve extending the BBM to account for anisotropy.

- In this study, only two-dimensional finite element calculations were performed, as the constitutive models used are implemented exclusively in 2D in the chosen software. However, tunnel excavation is inherently a three-dimensional problem. To examine water transport along the tunnel or potential cross-connections between tunnel tubes in more detail, a 3D simulation is required. It is therefore proposed to transfer the EDZ sizes and mean permeability determined in this work into a 3D model and simulate without additional regularization techniques. This approach

would significantly reduce the computational time of the 3D model while maintaining a realistic representation of the EDZ. To implement this, either the BBM would need to be extended to three dimensions within Lagamine, or an alternative finite element framework should be used that already includes a three-dimensional implementation of the BBM or another constitutive model suitable for capturing the hydro-mechanical behavior of Opalinus clay shale.

- The derivation of the convergence-confinement curve using an axisymmetric model, as conduced in this study, could also be further refined. It is proposed to validate this approach using real surface settlement data from a shallow tunnel. Additionally, the scope of the axisymmetric model could be expanded by incorporating both face pressure and grouting pressure into the analysis.

- In this study, two potential tunnel support strategies were examined under different uniform initial saturation conditions. A possible extension of this work could explore non-uniform initial conditions, such as a tunnel cross-section that includes vertical, horizontal, or inclined layers that are partially unsaturated. This would allow for an analysis of tunnel support performance under locally acting swelling pressures. Furthermore, future studies could focus on optimizing tunnel support systems to identify the most effective tunnel design for a range of geological and hydro-mechanical scenarios.

- Lastly, temperature effects could be incorporated into the tunnel simulation, as it is well established in the literature that temperature significantly influences the swelling behavior of clay shales. Therefore, a further study could investigate the heat generated during the hydration of the concrete lining or examine seasonal temperature fluctuations and their impact on the behavior of the tunnel support system and the surrounding geomaterial.

Bibliography

Aifantis, E. C. (1984), 'On the Microstructural Origin of Certain Inelastic Models', *Journal of Engineering Materials and Technology* **106**(4), 326–330.

Alabdullah, J. and Schanz, T. (2010), Testing Unsaturated Soil for Plane Strain Conditions: A New Double-Wall Biaxial Device, PhD thesis, Professur Bodenmechanik, Weimar.

Alonso, E. E., Gens, A. and Josa, A. (1990), 'A constitutive model for partially saturated soils', *Géotechnique* **40**(3), 405–430.

Alonso, E. E. and Olivella, S. (2008), Modelling Tunnel Performance in Expansive Gypsum Claystone, *in* '12th International Conference of International Association for Computer Methods and Advances in Geomechanics', Goa, India, pp. 891–910.

Alonso, E. and Ramon, A. (2013), 'Heave of a railway bridge induced by gypsum crystal growth: Field observations', *Géotechnique* **63**(9), 707–719.

Alshibli, K. A., Batiste, S. N. and Sture, S. (2003), 'Strain Localization in Sand: Plane Strain versus Triaxial Compression', *Journal of Geotechnical and Geoenvironmental Engineering* **129**(6), 483–494.

Amann, F., Wild, K. M., Loew, S., Yong, S., Thoeny, R. and Frank, E. (2017), 'Geomechanical behaviour of Opalinus Clay at multiple scales: Results from Mont Terri rock laboratory (Switzerland)', *Swiss Journal of Geosciences* **110**(1), 151–171.

Amstad, C. and Kovári, K. (2001), *Untertagbau in Quellfähigem Fels: Forschungsauftrag 52/94, 5408.01*, Département Fédéral de l'environnement, Des Transports, de l'énergie et de La Communication, Office Fédéral Des Routes, VSS.

Anagnostou, G. (1993), 'A model for swelling rock in tunnelling', *Rock Mechanics and Rock Engineering* **26**(4), 307–331.

Anagnostou, G. (2007), The one-step solution of the advancing tunnel heading problem, *in* 'EURO:TUN 2007 : ECCOMAS Thematic Conference on Computational Methods in Tunneling', Vienna, Austria.

Anagnostou, G., Pimentel, E. and Serafeimidis, K. (2010), 'Swelling of sulphatic claystones – some fundamental questions and their practical relevance', *Geomechanics and Tunnelling* **3**(5), 567–572.

Antonioli, B. (2018), Mechanical Properties of Gap Grout Installed in the TBM-excavated New Belchen A2 Highway Tunnel, B.Sc. Thesis, Department of Earth Sciences, ETH Zurich.

Arson, C. and Gatmiri, B. (2012), 'Thermo-hydro-mechanical modeling of damage in unsaturated porous media: Theoretical framework and numerical study of the EDZ', *International Journal for Numerical and Analytical Methods in Geomechanics* **36**(3), 272–306.

Arthur, J. R. F., Dunstan, T., Al-Ani, Q. A. J. L. and Assadi, A. (1977), 'Plastic deformation and failure in granular media', *Géotechnique* **27**(1), 53–74.

ASME (2015), 'Boiler and Pressure Vessel Code Section VIII: Rules for Construction of Pressure Vessels Division 2: Alternative Rules'.

Baille, W., Tripathy, S. and Schanz, T. (2010), 'Swelling pressures and one-dimensional compressibility behaviour of bentonite at large pressures', *Applied Clay Science* **48**(3), 324–333.

Bastiaens, W., Bernier, F., Buyens, M., Demarche, M., Li, X., Linotte, J.-M. and Verstricht, J. (2003), The extension of the HADES Underground Research facility at Mol, Belgium - The construction of the connecting gallery, EURIDICE Report 03-294.

Berdugo, I., Alonso, E., Romero, E. and Gens, A. (2009*a*), 'Tunnelling and swelling in Triassic sulphate-bearing rocks, Part I-case studies from Baden-Württemberg', *Epsilon* **12**.

Berdugo, I., Alonso, E., Romero, E. and Gens, A. (2009*b*), 'Tunnelling and swelling in Triassic sulphate-bearing rocks. Part II-case studies from Jura Mountains', *Epsilon* **12**.

Bertrand, F. and Collin, F. (2017), 'Anisotropic modelling of Opalinus Clay behaviour: From triaxial tests to gallery excavation application', *Journal of Rock Mechanics and Geotechnical Engineering* **9**(3), 435–448.

Bésuelle, P., Chambon, R. and Collin, F. (2006), 'Switching deformation modes in post-localization solutions with a quasibrittle material', *Journal of Mechanics of Materials and Structures* **1**(7), 1115–1134.

Bésuelle, P., Desrues, J. and Raynaud, S. (2000), 'Experimental characterisation of the localisation phenomenon inside a Vosges sandstone in a triaxial cell', *International Journal of Rock Mechanics and Mining Sciences* **37**(8), 1223–1237.

Blümling, P., Bernier, F., Lebon, P. and Derek Martin, C. (2007), 'The excavation damaged zone in clay formations time-dependent behaviour and influence on performance assessment', *Physics and Chemistry of the Earth, Parts A/B/C* **32**(8-14), 588–599.

Bock, H. (2001), Rock mechanics analyses and synthesis (RA experiment): Data report on rock mechanics, Mont Terri Technical Report, TR 2000-02, International Consultants for Quality Control and Safety Management in Geotechnical Engineering (Q+S Consult), Germany.

Bock, H. (2009), RA experiment: Updated review of the rock mechanics properties of the Opalinus clay of the Mont Terri URL based on laboratory and field testing, Mont Terri Technical Report, TR 2008-04, International Consultants for Quality Control and Safety Management in Geotechnical Engineering (Q+S Consult), Germany.

Bossart, P., Meier, P. M., Moeri, A., Trick, T. and Mayor, J.-C. (2002), 'Geological and hydraulic characterisation of the excavation disturbed zone in the Opalinus Clay of the Mont Terri Rock Laboratory', *Engineering Geology* **66**(1-2), 19–38.

Bossart, P. and Thury, M. (2011), 'Characteristics of the Opalinus clay at Mont Terri', *Reports of the Swiss Geological Survey* **3**, 25.

Bossart, P. and Thury, M., eds (2008), *Mont Terri Rock Laboratory Project: Programme 1996 to 2007 and Results*, number 3 *in* 'Reports of the Swiss Geological Survey', Swiss Geological Survey, Wabern.

Brinkgreve, RBJ., Engin, E. and Swolfs, WM. (2017), 'Plaxis 2D manual'.

Butscher, C., Breuer, S. and Blum, P. (2018), 'Swelling laws for clay-sulfate rocks revisited', *Bulletin of Engineering Geology and the Environment* **77**(1), 399–408.

Butscher, C., Mutschler, T. and Blum, P. (2016), 'Swelling of Clay-Sulfate Rocks: A Review of Processes and Controls', *Rock Mechanics and Rock Engineering* **49**(4), 1533–1549.

Carman, P. (1997), 'Fluid flow through granular beds', *Chemical Engineering Research and Design* **75**, S32–S48.

Casagrande, A. (1936), The determination of preconsolidation load and its practical significance, *in* 'Proceedings of the First International Conference on Soil Mechanics and Foundation Engineering', Cambridge, pp. 60–64.

Cerfontaine, B., Dieudonné, A., Radu, J., Collin, F. and Charlier, R. (2015), '3D zero-thickness coupled interface finite element: Formulation and application', *Computers and Geotechnics* **69**, 124–140.

Chambon, R. and Caillerie, D. (1999), 'Existence and uniqueness theorems for boundaryvalue problems involving incrementally non linear models', *International Journal of Solids and Structures* **36**(33), 5089–5099.

Chambon, R., Caillerie, D. and El Hassan, N. (1998), 'One-dimensional localisation studied with a second grade model', *European Journal of Mechanics - A/Solids* **17**(4), 637–656.

Chambon, R., Caillerie, D. and Matsuchima, T. (2001), 'Plastic continuum with microstructure, local second gradient theories for geomaterials: Localization studies', *International Journal of Solids and Structures* **38**(46-47), 8503–8527.

Chapuis, R. P. and Aubertin, M. (2003), 'On the use of the Kozeny-Carman equation to predict the hydraulic conductivity of soils', *Canadian Geotechnical Journal* **40**(3), 616–628.

Charlier, R. (1987), Approche unifiée de quelques problèmes non linéaires de mécanique des milieux continus par la méthode des éléments finis (grandes déformations des métaux et des sols, contact unilatéral de solides, conduction thermique et écoulements en milieu poreux), PhD thesis, Université de Liège.

Christ, F. (2025), Experimental Investigations on the Hydro-Mechanical Behaviour of Clay Shales for Tunnelling Relevant Boundary Conditions, PhD thesis, Ruhr Universität Bochum.

Christ, F. and Lavasan, A. A. (2024), Influence of volumetric boundary conditions on the water-retention behaviour of reconstituted and intact clay shales, *in* 'XVIII European Conference on Soil Mechanics and Geotechnical Engineering', Lisbon.

Christ, F., Schoen, M., Lavasan, A. and Wichtmann, T. (2025), 'Hydro-mechanical behaviour of Opalinus powder considering controlled volumetric deformations [Unpublished manuscript]'.

Collin, F. (2003), Couplages thermo-hydro-mécaniques dans les sols et les roches tendres partiellement saturés, PhD thesis, ULiège - Université de Liège.

Collin, F., Chambon, R. and Charlier, R. (2006), 'A finite element method for poro mechanical modelling of geotechnical problems using local second gradient models', *International Journal for Numerical Methods in Engineering* **65**(11), 1749–1772.

Collin, F., Levasseur, S. and Chambon, R. (2009), 'Numerical post failure methods in multiphysical problems', *European Journal of Environmental and Civil Engineering* **13**(7-8), 983–1004.

Corbetta, F. (1990), Nouvelles méthodes d'étude des tunnels profonds : calculs analytiques et numériques, PhD thesis, Ecole National Supérieure des Mines de Paris.

Corman, G. (2024), Hydro-Mechanical Modelling of Gas Transport Processes in Clay Host Rocks in the Context of a Nuclear Waste Repository, PhD thesis, ULiège - Université de Liège.

Cosserat, E. and Cosserat, F. (1909), 'Théorie des Corps déformables', *Nature* **81**(2072), 67–67.

Coulomb, C. A. (1773), 'Essai sur une application des règles de maximis et minimis à quelques problèmes de statique, relatifs à l'architecture', *Académie Royale des Sciences* **7**, 343–382.

Crisci, E., Ferrari, A., Giger, S. B. and Laloui, L. (2019), 'Hydro-mechanical behaviour of shallow Opalinus Clay shale', *Engineering Geology* **251**, 214–227.

De Borst, R. and Mühlhaus, H.-B. (1992), 'Gradient-dependent plasticity: Formulation and algorithmic aspects', *International Journal for Numerical Methods in Engineering* **35**(3), 521–539.

Dedecker, F., Cundall, P., Billaux, D. and Groeger, T. (2007), 'Evaluation of damage-induced permeability using a three-dimensional Adaptive Continuum/Discontinuum Code (AC/DC)', *Physics and Chemistry of the Earth, Parts A/B/C* **32**(8-14), 681–690.

Desrues, J. (1984), La localisation de la déformation dans les milieux granulaires, Theses, Université Joseph-Fourier - Grenoble I.

Desrues, J. (2005), 'Hydro-mechanical coupling and strain localization in saturated porous media', *Revue Européenne de Génie Civil* **9**(5-6), 619–634.

Desrues, J., Chambon, R., Mokni, M. and Mazerolle, F. (1996), 'Void ratio evolution inside shear bands in triaxial sand specimens studied by computed tomography', *Géotechnique* **46**(3), 529–546.

Desrues, J. and Viggiani, G. (2004), 'Strain localization in sand: An overview of the experimental results obtained in Grenoble using stereophotogrammetry', *International Journal for Numerical and Analytical Methods in Geomechanics* **28**(4), 279–321.

Deutsche Gesellschaft für Geotechnik e. V. (DGGT), ed. (2022), *Empfehlungen des Arbeitskreises Versuchstechnik Fels*, 1 edn, Wiley.

Diederichs, M. S. (2003), 'Manuel Rocha Medal Recipient Rock Fracture and Collapse Under Low Confinement Conditions', *Rock Mechanics and Rock Engineering* **36**(5), 339–381.

Diederichs, M. S. (2007), 'The 2003 Canadian Geotechnical Colloquium: Mechanistic interpretation and practical application of damage and spalling prediction criteria for deep tunnelling', *Canadian Geotechnical Journal* **44**(9), 1082–1116.

Dieudonne, A.-C. (2016), Hydromechanical Behaviour of Compacted Bentonite: From Micro-Scale Analysis to Macro-Scale Modelling, PhD thesis, ULiège - Université de Liège.

Einstein, H. H. (1996), 'Tunnelling in difficult ground — Swelling behaviour and identification of swelling rocks', *Rock Mechanics and Rock Engineering* **29**(3), 113–124.

Eurocode 2: Bemessung und Konstruktion von Stahlbeton- und Spannbetontragwerken - Teil 1-1: Allgemeine Bemessungsregeln und Regeln für den Hochbau (2011).

Farahmand, K. and Diederichs, M. S. (2021), 'Calibration of coupled hydro-mechanical properties of grain-based model for simulating fracture process and associated pore pressure evolution in excavation damage zone around deep tunnels', *Journal of Rock Mechanics and Geotechnical Engineering* **13**(1), 60–83.

Favero, V., Ferrari, A. and Laloui, L. (2016), 'On the hydro-mechanical behaviour of remoulded and natural Opalinus Clay shale', *Engineering Geology* **208**, 128–135.

Ferrage, E. (2016), 'Investigation of the Interlayer Organization of Water and Ions in Smectite from the Combined Use of Diffraction Experiments and Molecular Simulations. A Review of Methodology, Applications, and Perspectives', *Clays and Clay Minerals* **64**(4), 348–373.

Finno, R. J., Harris, W. W., Mooney, M. A. and Viggiani, G. (1996), 'Strain Localization and Undrained Steady State of Sand', *Journal of Geotechnical Engineering* **122**(6), 462–473.

Finno, R. J., Harris, W. W., Mooney, M. A. and Viggiani, G. (1997), 'Shear bands in plane strain compression of loose sand', *Géotechnique* **47**(1), 149–165.

García-Fontanet, A. (1998), Coupled Phenomena in Unsaturated Porous Media with Discontinuities. Theoretical and Numerical Modelling, PhD thesis, Universitat Politècnica de Catalunya.

Gens, A. and Alonso, E. E. (1992), 'A framework for the behaviour of unsaturated expansive clays', *Canadian Geotechnical Journal* **29**(6), 1013–1032.

Gens, A. and Sánchez, M. (2010), Long-term performance of engineered barrier systems PEBS, Deliverable (DN: D3. 5-2), European Commission.

Germain, P. (1973), 'The Method of Virtual Power in Continuum Mechanics. Part 2: Microstructure', *SIAM Journal on Applied Mathematics* **25**(3), 556–575.

Giger, S. B., Marschall, P., Lanyon, B. and Martin, C. D. (2015), 'Hydro-mechanical response of Opalinus Clay during excavation works - a synopsis from the Mont Terri URL', *Geomechanics and Tunnelling* **8**(5), 421–425.

Golshani, A., Oda, M., Okui, Y., Takemura, T. and Munkhtogoo, E. (2007), 'Numerical simulation of the excavation damaged zone around an opening in brittle rock', *International Journal of Rock Mechanics and Mining Sciences* **44**(6), 835–845.

Grob, H. (1972), Schwelldruck im Belchentunnel, *in* 'Internationales Symposium für Untertagbau', Luzern, pp. 99–119.

Hadamar, J. (1904), 'Leçons sur la Propagation des Ondes et les Équations de l'Hydrodynamique', *Nature* **71**(1835), 196–197.

Han, C. and Vardoulakis, I. G. (1991), 'Plane-strain compression experiments on water-saturated fine-grained sand', *Géotechnique* **41**(1), 49–78.

Hanafy, E. A. and Emery, J. J. (1980), Advancing face simulation of tunnel excavations and lining placement, *in* 'Underground Rock Engineering, 13th Canadian Rock Mechanics Symposium'.

Heidkamp, H. and Katz, C. (2002), Soils with swelling potential - Proposal of a final state formulation within an implicit integration scheme and illustrative FE-calculations, *in* 'Proceedings of the 5th World Congress on Computational Mechanics', Vienna, Austria.

Henke, KF., Kaiser, W. and Nagel, D. (1975), 'Geomechanische Untersuchungen im Gipskeuper', *Strassenbau und Strassenverkehrstechnik* **184**, 149–169.

Hill, R. (1958), 'A general theory of uniqueness and stability in elastic-plastic solids', *Journal of the Mechanics and Physics of Solids* **6**(3), 236–249.

Hoefsloot, F. and Verweij, A. P. (2006), 4D grouting pressure model PLAXIS, *in* 'Geotechnical Aspects of Underground Construction in Soft Ground. Proceedings of the 5th International Conference of TC 28 of the ISSMGE', pp. 529–534.

Huder, J. and Amberg, G. (1970), 'Quellung in Mergel, Opalinuston und Anhydrit', *Schweizerische Bauzeitung / Revue polytechnique suisse* **88**(43), 975–980.

ISRM (1979), 'Suggest methods for determining water content, porosity, density, absorption and related properties and swelling and slake-durability index properties', *International Journal of Rock Mechanics and Mining Sciences Abstracts* **16**, 141–156.

ISRM (1981), *International Society for Rock Mechanics, Rock Characterisation: Testing and Monitoring - ISRM Suggested Methods*, Pergamon Press, Oxford.

ISRM (1989), 'Suggested methods for laboratory testing of argillaceous swelling rocks', *International Journal of Rock Mechanics and Mining Sciences Abstracts* **26**(5), 415–426.

ISRM (1999), 'Suggested methods for laboratory testing of swelling rocks.', *International Journal of Rock Mechanics and Mining Sciences* **36**(3), 291–306.

Jenq, Y. S. (1988), 'Mixed-mode fracture of concrete', *International Journal of Fracture* (38), 123–142.

Katzenbach, R. and Breth, H. (1981), Nonlinear 3-D analysis for NATM in Frankfurt Clay, *in* 'Proceedings of the International Conference on Soil Mechanics and Foundation Engineering, 10th'.

Khaledi, K., Hamdi, P., Winhausen, L., Jalali, M., Jaeggi, D. and Amann, F. (2021), 'Unloading induced absolute negative pore pressures in a low permeable clay shale', *Engineering Geology* **295**, 106451.

Kiehl, J. R. (1990), Ein dreidimensionales Quellgesetz und seine Anwendung auf den Felshohlraumbau, *in* 'Sonderheft der Zeitschrift Geotechnik, Vorträge zum 9. Nationalen Felsmechanik Symposium'.

Kirschke, D. (1996), 'Neue Versuchstechniken und Erkenntnisse zum Anhydritschwellen', *Taschenbuch für den Tunnelbau, Verlag Glückauf GmbH, Essen.* pp. 203–225.

Kleinert, K. and Einsele, G. (1978), Sohlhebungen in Straßeneinschnitten in anhydritführendem Gipskeuper, *in* '3. Nationale Tagung über Felsmechanik', Vol. 3, Aachen, pp. 103–124.

Kotronis, P. and Collin, F. (2005), Implementation of path following techniques into the finite element code LAGAMINE, Research Report Rapport Interne Géomac/3S-R.

Kotronis, P., Collin, F., Bésuelle, P., Chambon, R. and Mazars, J. (2007), Local Second Gradient Models and Damage Mechanics: 1D Post-Localization Studies in Concrete Specimens, *in* 'Bifurcations, Instabilities, Degradation in Geomechanics', Springer Berlin Heidelberg, Berlin, Heidelberg, pp. 127–142.

Kovári, K., Amstad, C. and Anagnostou, G. (1987), Tunnelbau in quellfähigem Gebirge, *in* 'Probleme mit Wasser im Fels- und Untertagbau / L'eau dans les massifs rocheux et dans les ouvrages souterrains', Vol. 115 of *Mitteilungen der Schweizerischen Gesellschaft für Boden- und Felsmechanik / Publications de la Société de Mécanique des Sols et des Roches*, Schweizerische Gesellschaft für Boden- und Felsmechanik, Zürich, pp. 19–26.

Kozeny, J. (1927), 'Über kapillare Leitung des Wassers im Boden', *Sitzungsberichte der Akademie der Wissenschaften in Wien* **136**, 271.

Kraehenbuehl, F., Stoeckli, H., Brunner, F., Kahr, G. and Mueller-Vonmoos, M. (1987), 'Study of the water-bentonite system by vapour adsorption, immersion calorimetry and X-ray techniques: I. Micropore volumes and internal surface areas, following Dubinin's theory', *Clay Minerals* **22**(1), 1–9.

Labiouse, V., Sauthier, C. and You, S. (2014), 'Hollow Cylinder Simulation Experiments of Galleries in Boom Clay Formation', *Rock Mechanics and Rock Engineering* **47**(1), 43–55.

Lavasan, A. A. and Schanz, T. (2017), Numerical investigation of hydromechanical interactions at the tail void of bored tunnels due to grouting, *in* 'Geotechnical Aspects of Underground Construction in Soft Ground', Taylor & Francis Group, London, pp. 161–169.

Lee, C., Lee, J. and Kim, G.-Y. (2021), 'Numerical analysis of coupled hydro-mechanical and thermo-hydro-mechanical behaviour in buffer materials at a geological repository for nuclear waste: Simulation of EB experiment at Mont Terri URL and FEBEX at Grimsel test site using Barcelona basic model', *International Journal of Rock Mechanics and Mining Sciences* **139**, 104663.

Lee, K. M. and Rowe, R. K. (1991), 'An analysis of three-dimensional ground movements: The Thunder Bay tunnel', *Canadian Geotechnical Journal* **28**(1), 25–41.

Lei, Q., Latham, J.-P., Xiang, J. and Tsang, C.-F. (2017), 'Role of natural fractures in damage evolution around tunnel excavation in fractured rocks', *Engineering Geology* **231**, 100–113.

Lenoir, N., Bornert, M., Desrues, J., Bésuelle, P. and Viggiani, G. (2007), 'Volumetric Digital Image Correlation Applied to X-ray Microtomography Images from Triaxial Compression Tests on Argillaceous Rock', *Strain* **43**(3), 193–205.

Levasseur, S., Charlier, R., Frieg, B. and Collin, F. (2010), 'Hydro-mechanical modelling of the excavation damaged zone around an underground excavation at Mont Terri Rock Laboratory', *International Journal of Rock Mechanics and Mining Sciences* **47**(3), 414–425.

Levasseur, S., Collin, F., Charlier, R. and Kondo, D. (2013), 'A micro–macro approach of permeability evolution in rocks excavation damaged zones', *Computers and Geotechnics* **49**, 245–252.

Lisjak, A., Tatone, B. S. A., Mahabadi, O. K., Grasselli, G., Marschall, P., Lanyon, G. W., Vaissière, R. D. L., Shao, H., Leung, H. and Nussbaum, C. (2016), 'Hybrid Finite-Discrete Element Simulation of the EDZ Formation and Mechanical Sealing Process Around a Microtunnel in Opalinus Clay', *Rock Mechanics and Rock Engineering* **49**(5), 1849–1873.

Liu, J., Elsworth, D. and Brady, B. (1999), 'Linking stress-dependent effective porosity and hydraulic conductivity fields to RMR', *International Journal of Rock Mechanics and Mining Sciences* **36**(5), 581–596.

Lyapunov, A. M. (1992), 'The general problem of the stability of motion', *International Journal of Control* **55**(3), 531–534.

Mader, T., Schreter, M. and Hofstetter, G. (2022), 'On the Influence of Direction-Dependent Behavior of Rock Mass in Simulations of Deep Tunneling Using a Novel Gradient-Enhanced Transversely Isotropic Damage–Plasticity Model', *Applied Sciences* **12**(17), 8532.

Madsen, F. T. and Müller-Vonmoos, M. (1989), 'The swelling behaviour of clays', *Applied Clay Science* **4**(2), 143–156.

Maidl, B., Herrenknecht, M., Maidl, U. and Wehrmeyer, G. (2011), *Maschineller Tunnelbau im Schildvortrieb*, 1 edn, Wiley.

Mandel, J. (1966), Conditions de Stabilité et Postulat de Drucker, *in* 'Rheology and Soil Mechanics / Rhéologie et Mécanique Des Sols', Springer Berlin Heidelberg, Berlin, Heidelberg, pp. 58–68.

Martin, C. D., Kaiser, P. K. and McCreath, D. R. (1999), 'Hoek-Brown parameters for predicting the depth of brittle failure around tunnels', *Canadian Geotechnical Journal* **36**(1), 136–151.

Martin, C. and Lanyon, G. (2003), 'Measurement of in-situ stress in weak rocks at Mont Terri Rock Laboratory, Switzerland', *International Journal of Rock Mechanics and Mining Sciences* **40**(7-8), 1077–1088.

Marwan, A. (2019), Computational Analysis of Segmental Linings in Mechanized Tunneling, PhD thesis, Ruhr University Bochum.

Massat, L., Cuisinier, O., Bihannic, I., Claret, F., Pelletier, M., Masrouri, F. and Gaboreau, S. (2016), 'Swelling pressure development and inter-aggregate porosity evolution upon hydration of a compacted swelling clay', *Applied Clay Science* **124–125**, 197–210.

Matsushima, T., Chambon, R. and Caillerie, D. (2002), 'Large strain finite element analysis of a local second gradient model: Application to localization', *International Journal for Numerical Methods in Engineering* **54**(4), 499–521.

Mindlin, R. D. (1964), 'Micro-structure in linear elasticity', *Archive for Rational Mechanics and Analysis* **16**(1), 51–78.

Mokni, M. and Desrues, J. (1999), 'Strain localization measurements in undrained plane-strain biaxial tests on Hostun RF sand', *Mechanics of Cohesive-frictional Materials* **4**(4), 419–441.

Möller, S. C. (2006), *Tunnel induced settlements and structural forces in linings*, Mitteilung des Instituts für Geotechnik Stuttgart Heft Nr. 54, Inst. für Geotechnik, Stuttgart.

Mousivand, M., Maleki, M., Nekooei, M. and Mansoori, M. R. (2017), 'Application of Convergence–Confinement Method in Analysis of Shallow Non-circular Tunnels', *Geotechnical and Geological Engineering* **35**(3), 1185–1198.

Panet, M. (1995), *Le calcul des tunnels par la méthode convergence-confinement*, Presses de l'École nationale des ponts et chaussées.

Panet, M. and Sulem, J. (2022), *Convergence-Confinement Method for Tunnel Design*, Springer Tracts in Civil Engineering, Springer International Publishing.

Pardoen, B. (2015), Hydro-Mechanical Analysis of the Fracturing Induced by the Excavation of Nuclear Waste Repository Galleries Using Shear Banding, PhD thesis, ULiège - Université de Liège.

Pardoen, B., Levasseur, S. and Collin, F. (2015), 'Using Local Second Gradient Model and Shear Strain Localisation to Model the Excavation Damaged Zone in Unsaturated Claystone', *Rock Mechanics and Rock Engineering* **48**(2), 691–714.

Pardoen, B., Seyedi, D. and Collin, F. (2015), 'Shear banding modelling in cross-anisotropic rocks', *International Journal of Solids and Structures* **72**, 63–87.

Pardoen, B., Talandier, J. and Collin, F. (2016), 'Permeability evolution and water transfer in the excavation damaged zone of a ventilated gallery', *International Journal of Rock Mechanics and Mining Sciences* **85**, 192–208.

Peerlings, R., Geers, M., De Borst, R. and Brekelmans, W. (2001), 'A critical comparison of nonlocal and gradient-enhanced softening continua', *International Journal of Solids and Structures* **38**(44-45), 7723–7746.

Peerlings, R. H. J., De Borst, R., Brekelmans, W. A. M. and De Vree, J. H. P. (1996), 'Gradient enhanced damage for quasi-brittle materials', *International Journal for Numerical Methods in Engineering* **39**(19), 3391–3403.

Perras, M. A. and Diederichs, M. S. (2016), 'Predicting excavation damage zone depths in brittle rocks', *Journal of Rock Mechanics and Geotechnical Engineering* **8**(1), 60–74.

Pijaudier-Cabot, G. and Bažant, Z. P. (1987), 'Nonlocal Damage Theory', *Journal of Engineering Mechanics* **113**(10), 1512–1533.

Pimentel, E. (2007), A laboratory testing technique and a model for the swelling behavior of anhydritic rock, *in* '11th ISRM Congress', Lisbon, Portugal.

Pimentel, E. (2015), 'Existing Methods for Swelling Tests – A Critical Review', *Energy Procedia* **76**, 96–105.

Pimentel, E. and Anagnostou, G. (2013), 'New Apparatus and Experimental Setup for Long-Term Swelling Tests on Sulphatic Claystones', *Rock Mechanics and Rock Engineering* **46**(6), 1271–1285.

Plückelmann, S. and Breitenbücher, R. (2020), 'Verformungsverhalten von Betonen mit ausgeprägtem plastischen Stauchvermögen', *Beton- und Stahlbetonbau* **115**(12), 994–1005.

Renz, T., Ziegler, M. and Loew, S. (2019), 'Investigations in the new TBM-excavated Belchen highway tunnel. In-situ and laboratory data analyses (Part 3)', *ENSI Research and Experience Report 2018* (ENSI-AN-10577), 315–325.

Rice, J. (1976), Localization of plastic deformation, *in* 'Proceedings of the 14th International Congress on Theoretical and Applied Mechanics', Delft.

Riks, E. (1979), 'An incremental approach to the solution of snapping and buckling problems', *International Journal of Solids and Structures* **15**(7), 529–551.

Roger, V., Desrues, J. and Viggiani, G. (1998), Experiments on strain localisation in dense sand under isochoric conditions, *in* 'Localization and Bifurcation Theory for Soils and Rocks Proceedings of the Fourth International Workshop', Gifu, Japan.

Roscoe, K. and Burland, J. (1968), On the generalized stress-strain behaviour of wet clay, *in* 'Engineering Plasticity', Cambridge, pp. 535–609.

Rothfuchs, T., Jockwer, N. and Zhang, C.-L. (2007), 'Self-sealing barriers of clay/mineral mixtures – The SB project at the Mont Terri Rock Laboratory', *Physics and Chemistry of the Earth, Parts A/B/C* **32**(1-7), 108–115.

Rudnicki, J. and Rice, J. (1975), 'Conditions for the localization of deformation in pressure-sensitive dilatant materials', *Journal of the Mechanics and Physics of Solids* **23**(6), 371–394.

Salehnia, F. (2015), From Some Obscurity to Clarity in Boom Clay Behavior: Analysis of Its Coupled Hydro-Mechanical Response in the Presence of Strain Localization, PhD thesis, ULiège - Université de Liège.

Sánchez, M., Gens, A. and Olivella, S. (2010), 'Effect of thermo-coupled processes on the behaviour of a clay barrier submitted to heating and hydration', *Anais da Academia Brasileira de Ciências* **82**(1), 153–168.

Shah, R., A. Lavasan, A., Peila, D., Todaro, C., Luciani, A. and Schanz, T. (2018), 'Numerical Study on Backfilling the Tail Void Using a Two-Component Grout', *Journal of Materials in Civil Engineering* **30**(3), 04018003.

Shen, B. and Barton, N. (1997), 'The disturbed zone around tunnels in jointed rock Masses', *International Journal of Rock Mechanics and Mining Sciences* **34**(1), 117–125.

Snow, D. T. (1969), 'Anisotropie Permeability of Fractured Media', *Water Resources Research* **5**(6), 1273–1289.

Sridharan, A., Rao, A. and Puvvadi, S. (1986), 'Swelling pressure of clays', *Geotechnical Testing Journal* **9**, 24–33.

Steiner, W. (1993), 'Swelling rock in tunnels: Rock characterization, effect of horizontal stresses and construction procedures', *International Journal of Rock Mechanics and Mining Sciences & Geomechanics Abstracts* **30**(4), 361–380.

Sulem, J. (2010), 'Bifurcation theory and localization phenomena', *European Journal of Environmental and Civil Engineering* **14**(8-9), 989–1009.

Tao, M., Hong, Z., Peng, K., Sun, P., Cao, M. and Du, K. (2019), 'Evaluation of Excavation-Damaged Zone around Underground Tunnels by Theoretical Calculation and Field Test Methods', *Energies* **12**(9), 1682.

Tatsuoka, F., Nakamura, S., Huang, C.-C. and Tani, K. (1990), 'Strength Anisotropy and Shear Band Direction in Plane Strain Tests of Sand', *Soils and Foundations* **30**(1), 35–54.

Tatsuoka, F., Sakamoto, M., Kawamura, T. and Fukushima, S. (1986), 'Strength and Deformation Characteristics of Sand in Plane Strain Compression at Extremely Low Pressures', *Soils and Foundations* **26**(1), 65–84.

Thakur, V. (2007), Strain Localization in Sensitive Soft Clays, PhD thesis, Norwegian University of Science and Technology, Trondheim, Norway.

Thewes, M. and Budach, C. (2009*a*), Grouting of the annular gap in shield tunneling – an important factor for minimization of settlements and for production performance, *in* 'Proceedings of the ITA-AITES World Tunnel Congress'.

Thewes, M. and Budach, C. (2009*b*), 'Mörtel im Tunnelbau: Stand der Technik und aktuelle Entwicklungen zur Verfüllung des Ringspaltes bei Tunnelvortriebsmaschinen', *Bauportal* **121**(12), 706–711.

Thury, M. F. and Bossart, P. J. (1999), *Mont Terri Rock Laboratory: Results of the Hydrogeological, Geochemical and Geotechnical Experiments Performed in 1996 and 1997*, Landeshydrologie und -geologie, Bern.

Toupin, R. A. (1962), 'Elastic materials with couple-stresses', *Archive for Rational Mechanics and Analysis* **11**(1), 385–414.

Triantafyllidis, N. (1980), 'Bifurcation phenomena in pure bending', *Journal of the Mechanics and Physics of Solids* **28**(3-4), 221–245.

Van Genuchten, M. Th. (1980), 'A Closed-form Equation for Predicting the Hydraulic Conductivity of Unsaturated Soils', *Soil Science Society of America Journal* **44**(5), 892–898.

Van Marcke, P. and Bastiaens, W. (2010), 'Excavation induced fractures in a plastic clay formation: Observations at the HADES URF', *Journal of Structural Geology* **32**(11), 1677–1684.

Vardoulakis, I. (1981), 'Bifurcation analysis of the plane rectilinear deformation on dry sand samples', *International Journal of Solids and Structures* **17**(11), 1085–1101.

Vardoulakis, I., Goldscheider, M. and Gudehus, G. (1978), 'Formation of shear bands in sand bodies as a bifurcation problem', *International Journal for Numerical and Analytical Methods in Geomechanics* **2**(2), 99–128.

Wan, M. S. P., Standing, J. R., Potts, D. M. and Burland, J. B. (2019), 'Pore water pressure and total horizontal stress response to EPBM tunnelling in London Clay', *Géotechnique* **69**(5), 434–457.

Wheeler, S. J., Gallipoli, D. and Karstunen, M. (2002), 'Comments on use of the Barcelona Basic Model for unsaturated soils', *International Journal for Numerical and Analytical Methods in Geomechanics* **26**(15), 1561–1571.

Wileveau, Y. and Bernier, F. (2008), 'Similarities in the hydromechanical response of Callovo-Oxfordian clay and Boom Clay during gallery excavation', *Physics and Chemistry of the Earth, Parts A/B/C* **33**, 343–349.

Witherspoon, P. A., Wang, J. S. Y., Iwai, K. and Gale, J. E. (1980), 'Validity of Cubic Law for fluid flow in a deformable rock fracture', *Water Resources Research* **16**(6), 1016–1024.

Wittke-Gattermann (2004), 'Computation of strains and pressures for tunnels in swelling rocks', *Tunnelling and Underground Space Technology* **19**(4-5), 422–423.

Wittke, W. (2014), *Rock Mechanics Based on an Anisotropic Jointed Rock Model (AJRM)*, Verlag Ernst & Sohn, Berlin.

Xu, H. and Arson, C. (2014), 'Anisotropic damage models for geomaterials: Theoretical and numerical challenges', *International Journal of Computational Methods* **11**(02), 1342007.

Xu, X., Zhou, Y., Zhu, C., Zeng, C. and Guo, C. (2022), 'An Analytical Model for the Excavation Damage Zone in Tunnel Surrounding Rock', *Minerals* **12**(10), 1321.

Yu, H.-D., Chen, W.-Z., Jia, S.-P., Cao, J.-J. and Li, X.-L. (2012), 'Experimental study on the hydro-mechanical behavior of Boom clay', *International Journal of Rock Mechanics and Mining Sciences* **53**, 159–165.

Zervos, A., Papanastasiou, P. and Vardoulakis, I. (2001), 'Modelling of localisation and scale effect in thick-walled cylinders with gradient elastoplasticity', *International Journal of Solids and Structures* **38**(30-31), 5081–5095.

Zhang, C., Rothfuchs, T., Moog, H., Dittrich, J. and Müller, J. (2004), Thermo-hydro-mechanical and geochemical behaviour of the Callovo-Oxfordian Argillite and the Opalinus clay, Technical Report, GRS - 202, Society for Plant and Reactor Safety (GRS), Germany.

Zhao, Z., Guo, T., Li, S., Wu, W., Yang, Q. and Chen, S. (2020), 'Effects of joint surface roughness and orientational anisotropy on characteristics of excavation damage zone in jointed rocks', *International Journal of Rock Mechanics and Mining Sciences* **128**, 104265.

Ziegler, M., Alimardani Lavasan, A. and Loew, S. (2022), 'Stress evolution around a TBM tunnel in swelling clay shale over four years after excavation', *Tunnelling and Underground Space Technology* **128**, 104649.

Ziegler, M. and Loew, S. (2017), 'Investigations in the new TBM-excavated Belchen highway tunnel. Program, design and installations (Part 1)', *ENSI Research and Experience Report* (ENSI-AN-9961), 281–288.

A. Appendix A

In this appendix, the reversible wetting-drying line κ_s for volume constant conditions is derived. During volumetric swelling the elastic volumetric strains due to suction change $d\epsilon^e_{v,s}$ are prevented and therefore a swelling pressure is build up. It is assumed that $d\epsilon^e_{v,p} = d\epsilon^e_{v,s}$. By knowing this pressure change and the slope of the unloading-reloading line κ the reversible wetting-drying line κ_s can be derived as:

$$d\epsilon_v = d\epsilon^e_{v,p} + d\epsilon^e_{v,s} \tag{A.1}$$

$$\kappa \cdot \frac{dp}{p} - \kappa_s \cdot \frac{ds}{s + u_{\text{atm}}} \quad | \quad x = s + u_{\text{atm}} \tag{A.2}$$

$$\kappa \cdot \int_{p_\text{A}}^{p_\text{B}} \frac{1}{p} dp - \kappa_s \cdot \int_{s_\text{A}}^{s_\text{B}} \frac{1}{x} dx \tag{A.3}$$

$$\kappa \cdot [\ln(p)]_{p_\text{B}}^{p_\text{A}} - \kappa_s \cdot [\ln(s + u_{\text{atm}})]_{s_\text{B}}^{s_\text{A}} \tag{A.4}$$

$$\kappa \cdot \ln\left(\frac{p_\text{B}}{p_\text{A}}\right) - \kappa_s \cdot \ln\left(\frac{s_\text{B} + u_{\text{atm}}}{s_\text{A} + u_{\text{atm}}}\right) \tag{A.5}$$

$$\kappa_s = \kappa \cdot \frac{\ln(p_\text{B}) - \ln(p_\text{A})}{\ln\left(s_\text{A} + u_{\text{atm}}\right) - \ln\left(s_\text{B} + u_{\text{atm}}\right)} \tag{A.6}$$

It has to be noted that this derivation is only valid for true volume constant conditions $\Delta u = 0$ and only within the elastic domain. As the force measurement in the laboratory involves small deformation of the load cell this boundary condition has to be considered for the evaluation. In addition, swelling tests are commonly performed in oedometric cells without measurement of the radial stress, therefore an estimation of K_0 (e.g., with Jaky's formula) is needed in order to calculate the mean stress p.

B. Appendix B

In this appendix the Young's modulus E as well the Poisson's ratio ν are derived from linear elasticity theory for biaxial compression boundary conditions. First with linear elasticity theory the following relationships between strain and stress increments are obtained:

$$\begin{aligned}
\Delta\varepsilon_{11} &= \frac{1}{E} \cdot (\Delta\sigma_{11} - \nu \cdot (\Delta\sigma_{22} + \Delta\sigma_{33})) \\
\Delta\varepsilon_{22} &= \frac{1}{E} \cdot (\Delta\sigma_{22} - \nu \cdot (\Delta\sigma_{11} + \Delta\sigma_{33})) \\
\Delta\varepsilon_{33} &= \frac{1}{E} \cdot (\Delta\sigma_{33} - \nu \cdot (\Delta\sigma_{11} + \Delta\sigma_{22}))
\end{aligned}$$

Considering the boundary conditions of the biaxial test $\Delta\varepsilon_{33} = 0$ and $\Delta\sigma_{22} = 0$ the equations can be simplified:

$$\begin{aligned}
\Delta\varepsilon_{11} &= \frac{1}{E} \cdot (\Delta\sigma_{11} - \nu \cdot \Delta\sigma_{33}) \\
\Delta\varepsilon_{22} &= \frac{1}{E} \cdot (-\nu \cdot (\Delta\sigma_{11} + \Delta\sigma_{33})) \\
0 &= \frac{1}{E} \cdot (\Delta\sigma_{33} - \nu \cdot \Delta\sigma_{11})
\end{aligned}$$

Solving the system of linear equations for the Young's modulus E leads to:

$$E = \frac{\Delta\sigma_{11}}{\Delta\varepsilon_{11}} \cdot (1 - \nu^2) \tag{B.1}$$

Solving the equations for the Poisson's ratio ν and considering that $\varepsilon_v = \Sigma\varepsilon_{ii}$ results in:

$$\nu = \frac{\Delta\varepsilon_v - \Delta\varepsilon_{11}}{\Delta\varepsilon_v - 2\Delta\varepsilon_{11}} \tag{B.2}$$

C. Appendix C

In Section 5.7.3, various curves of pore water pressure development were extracted from the axisymmetric model (see Figure 5.91). While the characteristic pore water pressure peak was identified, it was decided not to include this as a predefined boundary condition , as it was assumed that the low permeability of Opalinus clay shale and the rapid excavation process render its effect negligible. Nevertheless, in additional simulations the influence of the temporal evolution of pore water pressure is compared for all three cases in terms of the EDZ area and permeability ratio, as illustrated in Figures C.1 and C.2, respectively. The various curves of pore water pressure development shown in Figure 5.91 are applied as predefined pore water pressures at the tunnel wall of the plane strain tunnel model.

As evident from the resulting evolution of the EDZ area and the permeability ratio within the EDZ, the temporal evolution of pore water pressure applied in the simulation during tunnel excavation has almost no influence on the results. Therefore, the choice of a linear pore water pressure decrease during excavation is validated as justified.

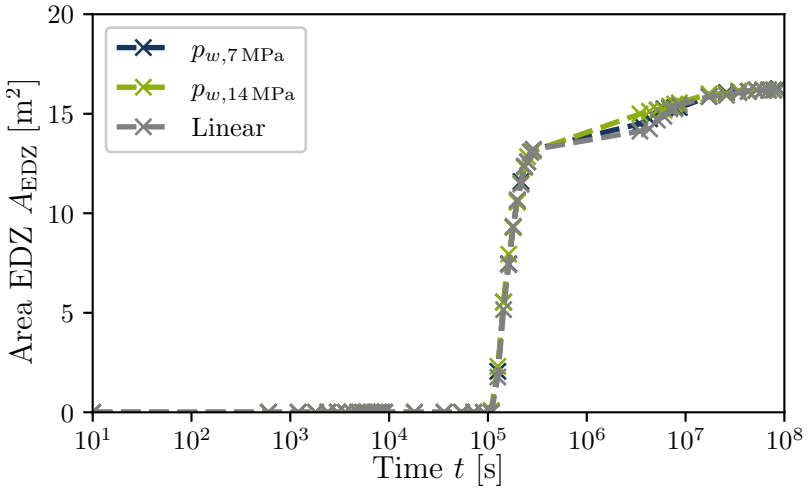

Figure C.1.: Comparison of simulations with different pore-water pressure evolutions at the tunnel wall during excavation in terms of the EDZ area

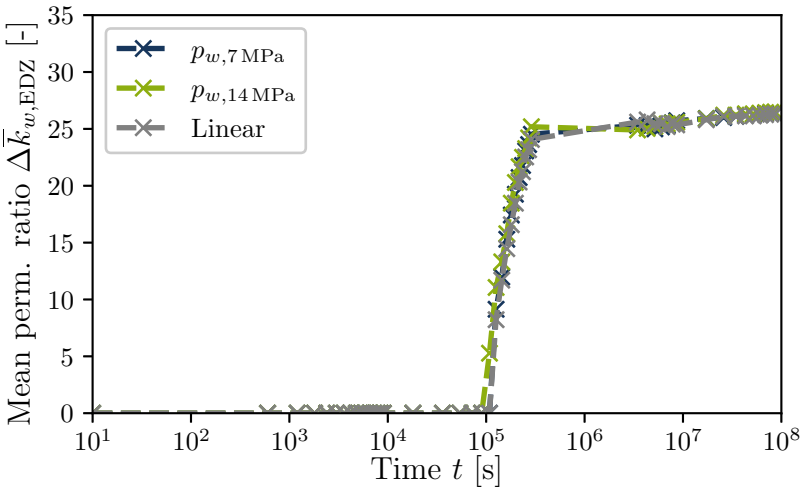

Figure C.2.: Comparison of simulations with different pore-water pressure evolutions at the tunnel wall during excavation in terms of permeability ratio

Schriftenreihe des Instituts für Grundbau, Wasserwesen und Verkehrswesen der Ruhr-Universität Bochum

Herausgeber: H.L. Jessberger

1 (1979) **Hans Ludwig Jessberger**
Grundbau und Bodenmechanik an der Ruhr-Universität Bochum

2 (1978) **Joachim Klein**
Nichtlineares Kriechen von künstlich gefrorenem Emschermergel

3 (1979) **Heinz-Joachim Gödecke**
Die Dynamische Intensivverdichtung wenig wasserdurchlässiger Böden

4 (1979) **Poul V. Lade**
Three Dimensional Stress-Strain Behaviour and Modeling of Soils

5 (1979) **Roland Pusch**
Creep of soils

6 (1979) **Norbert Diekmann**
Zeitabhängiges, nichtlineares Spannungs-Verformungsverhalten von gefrorenem Schluff unter triaxialer Belastung

7 (1979) **Rudolf Dörr**
Zeitabhängiges Setzungsverhalten von Gründungen in Schnee, Firn und Eis der Antarktis am Beispiel der deutschen Georg-von-Neumayer- und Filchner-Station

8 (1984) **Ulrich Güttler**
Beurteilung des Steifigkeits- und Nachverdichtungsverhaltens von ungebundenen Mineralstoffen

9 (1986) **Peter Jordan**
Einfluss der Belastungsfrequenz und der partiellen Entwässerungs-möglichkeiten auf die Verflüssigung von Feinsand

10 (1986) **Eugen Makowski**
Modellierung der künstlichen Bodenvereisung im grundwasserdurchströmten Untergrund mit der Methode der finiten Elemente

11 (1986) **Reinhard A. Beine**
Verdichtungswirkung der Fallmasse auf Lastausbreitung in nichtbindigem Boden bei der Dynamischen Intensivverdichtung

12 (1986) **Wolfgang Ebel**
Einfluss des Spannungspfades auf das Spannungs-Verformungsverhalten von gefrorenem Schluff im Hinblick auf die Berechnung von Gefrierschächten

13 (1987) **Uwe Stoffers**
Berechnungen und Zentrifugen-Modellversuche zur Verformungsabhängigkeit der Ausbaubeanspruchung von Tunnelausbauten in Lockergestein

14 (1988) **Gerhard Thiel**
Steifigkeit und Dämpfung von wassergesättigtem Feinsand unter Erdbebenbelastung

15 (1991) **Mahmud Thaher**
Tragverhalten von Pfahl-Platten-Gründungen im bindigen Baugrund,
Berechnungsmodelle und Zentrifugen-Modellversuche

Schriftenreihe des Instituts für Grundbau der Ruhr-Universität Bochum

Herausgeber: H.L. Jessberger

16 (1992) **Rainer Scherbeck**
Geotechnisches Verhalten mineralischer Deponieabdichtungsschichten
bei ungleichförmiger Verformungswirkung

17 (1992) **Martin M. Bizialiele**
Torsional Cyclic Loading Response of a Single Pile in Sand

18 (1993) **Michael Kotthaus**
Zum Tragverhalten von horizontal belasteten Pfahlreihen aus langen Pfählen in Sand

19 (1993) **Ulrich Mann**
Stofftransport durch mineralische Deponieabdichtungen:
Versuchsmethodik und Berechnungsverfahren

20 (1992) **Festschrift anlässlich des 60. Geburtstages von**
Prof. Dr.-Ing. H. L. Jessberger
20 Jahre Grundbau und Bodenmechanik an der Ruhr-Universität Bochum

21 (1993) **Stephan Demmert**
Analyse des Emissionsverhaltens einer Kombinationsabdichtung im Rahmen der
Risikobetrachtung von Abfalldeponien

22 (1994) **Diethard König**
Beanspruchung von Tunnel- und Schachtausbauten in kohäsionslosem Lockergestein
unter Berücksichtigung der Verformung im Boden

23 (1995) **Thomas Neteler**
Bewertungsmodell für die nutzungsbezogene Auswahl von Verfahren zur Altlastensanierung

24 (1995) **Ralph Kockel**
Scherfestigkeit von Mischabfall im Hinblick auf die Standsicherheit von Deponien

25 (1996) **Jan Laue**
Zur Setzung von Flachfundamenten auf Sand unter wiederholten Lastereignissen

26 (1996) **Gunnar Heibrock**
Zur Rissbildung durch Austrocknung in mineralischen Abdichtungsschichten
an der Basis von Deponien

27 (1996) **Thomas Siemer**
Zentrifugen-Modellversuche zur dynamischen Wechselwirkung zwischen Bauwerken
und Baugrund infolge stoßartiger Belastung

28 (1996) **Viswanadham V. S. Bhamidipati**
Geosynthetic Reinforced Mineral Sealing Layers of Landfills

29 (1997) **Frank Trappmann**
Abschätzung von technischem Risiko und Energiebedarf bei Sanierungsmaßnahmen für Altlasten

30 (1997) **André Schürmann**
Zum Erddruck auf unverankerte flexible Verbauwände

31 (1997) **Jessberger, H. L. (Herausgeber)**
Environment Geotechnics, Report of ISSMGE Technical Committee TC 5 on Environmental Geotechnics

Schriftenreihe des Instituts für Grundbau und Bodenmechanik der Ruhr-Universität Bochum

Herausgeber: Th. Triantafyllidis

32 (2000) **Triantafyllidis, Th. (Herausgeber)**
Boden unter fast zyklischer Belastung: Erfahrung und Forschungsergebnisse (Workshop)

33 (2002) **Christof Gehle**
Bruch- und Scherverhalten von Gesteinstrennflächen mit dazwischenliegenden Materialbrücken

34 (2003) **Andrzej Niemunis**
Extended hypoplastic models for soils

35 (2004) **Christiane Hof**
Über das Verpressankertragverhalten unter kalklösendem Kohlensäureangriff

36 (2004) **René Schäfer**
Einfluss der Herstellungsmethode auf das Verformungsverhalten von Schlitzwänden in weichen bindigen Böden

37 (2005) **Henning Wolf**
Zur Scherfugenbänderung granularer Materialien unter Extensionsbeanspruchung

38 (2005) **Torsten Wichtmann**
Explicit accumulation model for non-cohesive soils under cyclic loading

39 (2008) **Christoph M. Loreck**
Die Entwicklung des Frischbetondruckes bei der Herstellung von Schlitzwänden

40 (2008) **Igor Arsic**
Über die Bettung von Rohrleitungen in Flüssigböden

41 (2009) **Anna Arwanitaki**
Über das Kontaktverhalten zwischen einer Zweiphasenschlitzwand und nichtbindigen Böden

Schriftenreihe des Lehrstuhls für Grundbau, Boden- und Felsmechanik der Ruhr-Universität Bochum

Herausgeber: T. Schanz

42 (2009) **Yvonne Lins**
Hydro-Mechanical Properties of Partially Saturated Sand

43 (2010) **Tom Schanz (Herausgeber)**
Geotechnische Herausforderungen beim Umbau des Emscher-Systems
Beiträge zum RuhrGeo Tag 2010

44 (2010) **Jamal Alabdullah**
Testing Unsaturated Soil for Plane Strain Conditions: A New Double-Wall Biaxial Device

45 (2011) **Lars Röchter**
Systeme paralleler Scherbänder unter Extension im ebenen Verformungszustand

46 (2011) **Yasir Al-Badran**
Volumetric Yielding Behavior of Unsaturated Fine-Grained Soils

47 (2011) **Usque ad finem**
Selected research papers

48 (2012) **Muhammad Ibrar Khan**
Hydraulic Conductivity of Moderate and Highly Dense Expansive Clays

49 (2014) **Long Nguyen-Tuan**
Coupled Thermo-Hydro-Mechanical Analysis: Experimental and Back Analysis

50 (2014) **Tom Schanz (Herausgeber)**
Ende des Steinkohlenbergbaus im Ruhrrevier: Realität und Perspektiven für die Geotechnik
Beiträge zum RuhrGeo Tag 2014

51 (2014) **Usque ad finem**
Selected research papers

52 (2014) **Houman Soleimani Fard**
Study on the Hydro-Mechanical Behavior of Fiber Reinforced Fine Grained Soils,
with Application to the Preservation of Historical Monuments

53 (2014) **Wiebke Baille**
Hydro-Mechanical Behaviour of Clays - Significance of Mineralogy

54 (2014) **Qasim Abdulkarem Jassim Al-Obaidi**
Hydro-Mechanical Behavior of Collapsible Soils

55 (2015) **Veselin Zarev**
Model Identification for the Adaption of Numerical Simulation Models -
Application to Mechanized Shield Tunneling

56 (2015) **Meisam Goudarzy**
Micro and Macro Mechanical Assessment of Small and Intermediate Strain
Properties of Granular Material

57 (2016) **Oliver Detert**
Analyse einer selbstregulierenden interaktiven Membrangründung für Schüttkörper auf geringtragfähigen Böden

58 (2016) **Yang Yang**
Analyses of Heat Transfer and Temperature-induced Behaviour in Geotechnics

59 (2016) **Alborz Pourzargar**
Application of suction stress concept to partially saturated compacted soils

60 (2017) **Hanna Haase**
Multiscale Analysis of Clay-Polymer Composites for Geoenvironmental Applications

61 (2017) **Kavan Khaledi**
Constitutive modeling of rock salt with application to energy storage caverns

62 (2017) **Nina Silvia Müthing**
On the consolidation behaviour of fine-grained soils under cyclic loading

63 (2017) **Elham Mahmoudi**
Probabilistic analysis of a rock salt cavern with application to energy storage systems

64 (2017) **Negar Rahemi**
Evaluation of liquefaction behavior of sandy soils using critical state soil mechanics and instability concept

65 (2018) **Chenyang Zhao**
Numerical Modeling of Mechanized Tunnel Excavation:
Effects of Sub-systems and Advanced Process Simulation

66 (2018) **Tom Schanz (Herausgeber)**
Innovationen im Spezialtiefbau und in der Umweltgeotechnik
Beiträge zum RuhrGeo Tag 2018

67 (2019) **Linzhi Lang**
Hydro-Mechanical Behaviour of Bentonite-Based Materials Used for Disposal of Radioactive Wastes

68 (2019) **Usama Al-Anbaki**
Hydraulic Interaction of Soil and Nonwoven Geotextiles under Unsaturated Conditions

69 (2019) **Abhishek Rawat**
Coupled Hydro-mechanical Behavior of a Compacted Bentonite-Sand Mixture: Experimental and Numerical Investigations

Schriftenreihe des Lehrstuhls für Bodenmechanik, Grundbau und Umweltgeotechnik der Ruhr-Universität Bochum

Herausgeber: T. Wichtmann

70 (2019) **Mahmoud Qarmout**
Tunnel face stability using Kinematical Element Method (KEM)

71 (2021) **Raoul Hölter**
Optimal Experimental Design in Geotechnical Engineering

72 (2022) **Wolfgang Lieske**
Impact of polymer constitution on the hydro-mechanical behaviour of modified bentonite for the application in geotechnical and geoenvironmental engineering

73 (2022) **Patrick Staubach**
Contributions to the numerical modelling of pile installation processes and high-cyclic loading of soils

74 (2022) **Lingyun Li**
On the hydromechanical behaviour of loess and its effect on slope stability under rainfall infiltration

75 (2022) **Debdeep Sarkar**
Influence of particle characteristics on the behaviour of granular materials under static, cyclic and dynamic loading

76 (2023) **Torsten Wichtmann (Herausgeber)**
Umbau des Emscher-Systems - Geotechnische Erfahrungen
Beiträge zum RuhrGeo Tag 2023

77 (2023) **Abbas Farhat**
Fluidization and erosion of cemented granular materials. Experimental characterization and micromechanical simulation

78 (2023) **Andrea Geppetti**
Experimental and numerical investigations on the behaviour of tailing storage facilities under seismic loading

79 (2023) **Mohammad Hassan Sanayei**
Micromechanical modelling for the analysis of piping erosion in cemented soils for suction-assisted offshore foundations

80 (2024) **Christoph Schmüdderich**
Contributions to the stability assessment of slopes subjected to seismic loading

81 (2024) **Thomas Barciaga**
Constitutive modeling of natural clay with application to mechanized tunneling

82 (2024) **Cristian Rodriguez**
Contributions to the modelling of large deformations of soils: A particle-based approach

83 (2025) **Florian Christ**
Experimental investigations on the hydro-mechanical behaviour of clay shales for tunnelling relevant boundary conditions

84 (2025) **Alireza Jebeli**
On the influence of a heterogeneous pore structure on collapse behavior of sandy soils

85 (2025) **Maximilian Schoen**
Numerical analysis of tunnel excavation in swellable clay shales